Effect of subcrystalline domains, grain boundaries and hetero-interfaces on the carrier transport in perovskite solar cells

Dissertation

zur Erlangung des Grades

“Doktor der Naturwissenschaft”

Im Promotionsfach Chemie

am Fachbereich Chemie, Pharmazie, Geographie und Geowissenschaften

der Johannes Gutenberg-Universität Mainz

Ilka Maria Hermes

geboren in Hannover

Mainz, 2021

Die vorliegende Arbeit wurde in der Zeit von August 2014 bis November 2021 am Max-Planck-Institut für Polymerforschung in Mainz unter Anleitung von [redacted] angefertigt.

Mainz, 30. November 2021

Dekan:

1. Berichterstatter:

2. Berichterstatter:

Tag der mündlichen Prüfung:

https://www.youtube.com/watch?v=AEB6ibtdPZc

Table of content

Abbreviations

Photovoltaic	PV
Power conversion efficiency	*PCE*
Silicon	Si
Gallium Arsenide	GaAs
Perovskite solar cells	PSC
Photoluminescence	PL
Ultraviolet	UV
Visible	vis
Infrared	IR
Air mass	AM
Hole transport layer	HTL
Electron transport layer	ETL
Short circuit	SC
Open circuit	OC
Maximum power point	*mpp*
Fill factor	*FF*
Methylammonium lead iodide	$MAPbI_3$
2,2',7,7'-tetrakis-(N,N-di-p-methoxyphenyl-amine)-9,9'-spirobifluorene	SpiroOMeTAD, spiro
X-ray diffraction	XRD
Piezoresponse force microscopy	PFM
$Pb_{(1-x)}Zr_xTiO_3$	PZT
$Pb_{(1-x)}Sr_xTiO_3$	PST
$BaTiO_3$	BTO
Dimethyl sulfoxide	DMSO
Dimethyl formamide	DMF
Formamidinium	FA
Atomic force microscopy	AFM
Scanning tunneling microscopy	STM
Scanning prove microscopy	SPM
Electrostatic force microscopy	EFM
Kelvin probe force microscopy	KPFM
Proportional gain	P gain
Integral gain	I gain
Conductive atomic force microscopy	CAFM
Amplitude modulation	AM
Lock-in amplifier	LIA
Dual amplitude resonance tracking	DART
Contact potential difference	CPD
Frequency modulation	FM

Continuous wave	CW
Scanning electron microscopy	SEM
Focused ion beam	FIB
$BiFeO_3$	BFO
Energy-dispersive x-ray spectroscopy	EDX
Self-assembled monolayer	SAM
Transmission electron microscopy	TEM
Electron backscattered diffraction	EBDS

Abstract

The climate crisis and ever-rising energy demand require clean, sustainable and affordable solutions for electricity generation. Perovskite solar cells (PSC), based on the perovskite compound methylammonium lead iodide ($MAPbI_3$), offer high power conversion efficiencies of 25.5% and low production costs. By reducing losses in the charge carrier extraction, the efficiency of PSCs can push towards the radiative efficiency limit. Particularly the impact of local morphological features in the absorber and heterointerfaces on charge carrier dynamics is of great interest to further optimize PSCs. In this work, I explored how boundary structures on different lengths scales – from subcrystalline domains to grain boundaries in polycrystalline $MAPbI_3$ films to heterointerfaces in PSCs – affect the charge carrier transport.

First, I studied a periodic subcrystalline domain pattern within $MAPbI_3$ grains via piezoresponse force microscopy (PFM) and 2D x-ray diffraction for in-depth structural characterization. In-situ PFM across $MAPbI_3$'s phase transition temperature and during the application of mechanical stress revealed the ferroelastic nature of the domains, while simultaneously demonstrating routes for strain engineering. Finally, the correlation of the domain pattern with spatial and time-resolved photoluminescence (PL) microscopy showed that the photocarrier diffusion depends on the orientation of the domain walls.

Furthermore, I investigated the impact of grain boundaries on the charge carrier drift and diffusion via conductive atomic force microscopy (CAFM) and spatial and time-resolved PL microscopy. CAFM measurements allowed the determination of single grain boundary resistances. Moreover, CAFM and PL results indicate that grain boundaries act as semitransparent barriers to the inter-grain carrier transport. Here, the transparency appeared to depend on the boundary morphology, including density and contact area. I observed a similar effect for PL-photons that become trapped in the $MAPbI_3$ film due to internal reflection: Dense grain boundaries with large contact areas seemed to facilitate photon propagation with minimal outcoupling as required for efficient light management in PSCs.

Lastly, I studied the influence of different electron transport layers (ETL) on the photocarrier extraction using Kelvin probe force microscopy (KPFM) on PSC cross sections with and without illumination. The charge distribution resolved via KPFM indicates that mobile iodide ions released at the $MAPbI_3$ / ETL interface degrade the organic hole transport layer. This degradation likely increases the interfacial resistance and defect density, resulting in losses in the charge carrier extraction.

Ultimately, this work suggests that targeted control of boundary structures within the $MAPbI_3$ absorber and stabilization of heterointerfaces will improve carrier extraction and thereby contribute to PSCs' reaching their full potential.

Zusammenfassung

Die Klimakrise und der stetig wachsende Energiebedarf erfordern saubere, nachhaltige und kostengünstige Lösungen um Elektrizität zu gewinnen. Perowskit Solarzellen (PSC) basieren auf dem Perowskit-Material Methylammonium Bleiiodid ($MAPbI_3$) und ermöglichen einen hohen Wirkungsgrad von 25.5% bei gleichzeitig niedrigen Produktionskosten. Um die theoretische Obergrenze des Wirkungsgrades von PSCs zu erreichen, müssen unter anderem Verluste in der Ladungsträgerextraktion reduziert werden. Vor allem der Einfluss lokaler morphologischer Eigenschaften in der Absorberschicht und der Grenzflächen auf den Ladungsträgertransport ist von großem Interesse für die Optimierung der PSCs. Im Rahmen dieser Arbeit habe ich untersucht, wie sich Grenzstrukturen unterschiedlicher Größenordnungen – von subkristallinen Domänen über Korngrenzen in $MAPbI_3$ Dünnschichten bis zu Grenzflächen in PSCs – auf den Ladungsträgertransport auswirken.

Dafür habe ich zunächst periodische, subkristalline Domänen in $MAPbI_3$ Körnern mit piezoelektrischer Rasterkraftmikroskopie (PFM) und 2D Röntgenbeugung strukturell charakterisiert. In-situ PFM Messungen über den Phasenübergang und während der Anwendung einer mechanischen Last offenbarten den ferroelastischen Charakter der Domänen. Zudem verdeutlichen die Ergebnisse der in-situ Messungen, wie die Domänenanordnung über externe Last gezielt manipuliert werden kann. Die Korrelation der Domänenstruktur mit räumlich und zeitlich aufgelösten Photolumineszenz (PL) Messungen zeigte schließlich, dass die Orientierung der Domänenwände die Ladungsträgerdiffusion beeinflusst.

Des Weiteren habe ich die Wirkung von Korngrenzen auf Ladungsträgerdrift und -diffusion mit Leitfähigkeitsrasterkraftmikroskopie (CAFM) sowie räumlich und zeitlich aufgelösten PL-Messungen untersucht. Die CAFM Messungen erlaubten die Bestimmung des Widerstandes einzelner Korngrenzen. Darüber hinaus weisen CAFM- und PL-Ergebnisse darauf hin, dass Korngrenzen als halbdurchlässige Barrieren auf Ladungsträger wirken. Ihre Durchlässigkeit hängt dabei von der Morphologie der Korngrenze ab, einschließlich ihrer Dichte und Kontaktfläche. Einen ähnlichen Effekt habe ich für PL-Photonen beobachtet, die durch innere Reflexion in $MAPbI_3$ Filmen eingeschlossen sind: Dichte Korngrenzen mit großer Kontaktfläche ermöglichen Photonentransport mit minimaler Auskopplung für effizientes Photonenmanagement in PSCs.

Abschließend habe ich den Einfluss unterschiedlicher Elektronentransportschichten (ETL) auf die Ladungsträgerextraktion durch Kelvin Sonden Rasterkraftmikroskopie (KPFM) auf PSC Querschnitten abgebildet. Die KPFM-Ladungsverteilungen deuten darauf hin, dass mobile Iodid Ionen, die an der $MAPbI_3$ / ETL Grenzfläche freigesetzt werden, mit der organischen Lochtransportschicht reagieren und dadurch den Grenzflächenwiderstand erhöhen. Der erhöhte Widerstand kann zu Verlusten in der Ladungsträgerextraktion führen.

Diese Arbeit zeigt, dass eine gezielte Kontrolle von Grenzstrukturen in der $MAPbI_3$-Schicht sowie eine Stabilisierung der Transportschichten eine verbesserte Ladungsträgerextraktion ermöglichen und damit zu der weiteren Optimierung von PSCs beitragen können.

1 Fundamentals

1.1 Introduction

Following the 2015 world climate summit in Paris, 191 countries agreed to limit global warming to well below 2 °C above pre-industrial levels in an effort to mitigate the climate crisis.[1] Yet, four years later in 2019, 80% of the worldwide energy consumption still stemmed from the combustion of fossil fuels: Oil, gas and coal.[2] Main product of fossil fuel combustion is the greenhouse gas CO_2. CO_2 transmits the solar radiation that reaches the earth, but absorbs infrared radiation reemitted by the earth, which heats up the lower parts of the atmosphere and, thereby, directly contributes to global warming.[3] In an effort to reduce CO_2 emission, modern technology uses electrical power instead of fossil fuel combustion, most prominently in electric cars. The growing awareness for the climate crisis in the population, reduced operational cost and government incentives led to an almost exponential rise in the amount of electric cars in Germany and worldwide over the last ten years.[4–6] However, in order for electric mobility to make an actual impact on the overall CO_2 emissions, the increased electricity demand has to be met with sustainable concepts over the more traditional coal and gas power stations.

Sustainable technologies for electricity generation use water power, wind or solar irradiance.[7] For the latter, the yearly average power density of the irradiance at the earth surface lies between 100 W/m² in high latitudes and 300 W/m² in areas close to the equator.[8] The abundant access and unlimited supply in the foreseeable future make solar power an indispensable component in the long overdue revision of the worldwide energy industry. Established concepts for solar power conversion are solar thermal systems and solar cells. In solar thermal systems, solar irradiance heats fluids, whose thermal energy is then transformed to electrical energy e.g., via steam turbines.[9] Solar cells on the other hand, generate electricity directly from the sunlight via the photovoltaic (PV) effect.[3,8] Requirements and working mechanism of solar cells in general will be introduced in Chapter 1.2.

Improvement of the performance of solar cells, expansion to new application fields and optimization of production processes require continuous research on new compositions, materials and architectures for solar cells. By now, a variety of different solar cells exists, each adjusted for their respective area of application. For example, gallium arsenide (GaAs) solar cells that are used in spacecrafts allow high power conversion efficiencies (*PCE*, Chapter 1.2.4.3, Equation 1.16), good radiation resistance and low weight.[8] Commercial solar cells, based on mono- or polycrystalline silicon (Si), were improved in architecture and material design for light incoupling, longevity and affordability. However, the inherent disadvantage of Si solar cells, namely their weak absorption, necessitates new solutions for commercial solar cells.[3] Here, thin film perovskite solar cells (PSCs), which use hybrid organic-inorganic perovskite absorbers based on methylammonium lead iodide ($MAPbI_3$), offer strong absorption of visible light and low production cost due to solution processing.[10] Moreover, combining PSCs with commercial Si solar cells to tandem cells facilitates *PCE*s of close to 30% as of 2021.[11] An introduction of material properties, composition and architecture of PSCs are given in Chapter 1.3.

Extensive research allowed optimizing the properties of the perovskite absorber and solar cell architecture over the past ten years for a *PCE* that approaches monocrystalline Si solar cells.[11–17] To facilitate a strategic and targeted tuning of material and device parameters that enhance performance, solar cell research requires a variety of accurate characterization techniques. Particularly, correlative studies on the impact of morphological and local phenomena on the charge carrier behavior in PSCs demand a combination of high-resolution optoelectronic, electrical and structural measurements methods. The fundamentals of the techniques used in this work are presented in Chapter 1.4.

Following the introduction of fundamental solar cell and PSC properties as well as the methodology used, I will summarize the scope and aim of my work in detail in Chapter 2. In short, I studied the influence three boundary structures at different lengths scales on charge carrier dynamics in $MAPbI_3$ thin films and PSCs: Subcrystalline twin domains, grain boundaries and heterointerfaces to charge extraction layers. Accordingly, the results section in Chapters 3, 4 and 5 is organized in three parts. Chapter 3 focuses on the subcrystalline domain structure that is present in single grains of polycrystalline $MAPbI_3$. Here, I investigated the domains' structure, nature and their response on the external triggers heat, mechanical force and electric fields, which show the ferroelastic character of the domains. A correlation of the domain arrangement with the photocarrier diffusion revealed that the domain walls affect diffusive carriers. In Chapter 4, I explored the impact of grain boundaries on the charge carrier drift and diffusion. My findings indicate that grain boundaries act as semitransparent barriers on the charge carrier transport. The transparency appeared to depend on the grain boundary morphology. Chapter 5 contains a study on the effect of heterointerfaces on the charge carrier extraction in PSCs. Data suggests that the partial degradation of the organic hole transport layer increases the series resistance of the cells and thereby limits the charge carrier extraction. Finally, I will summarize all conclusions in Chapter 6 and give an outlook on subsequent research based on this work.

1.2 Photovoltaics

The working mechanism of solar cells, in which solar energy is directly transformed to electrical energy, is based on the PV effect. The PV effect entails the absorption of photons, consequent excitation of bound electrons and the spatial separation of excited electrons from their vacancies, which are called holes, via a built-in potential asymmetry. Well-performing solar cells require absorber materials with suitable electronic properties to absorb light in the visible region of the solar spectrum, facilitate long-range charge carrier transport and, ideally, loss-free charge extraction to the external circuit.[8]

1.2.1 Photovoltaic effect

In the PV effect, a material absorbs photons from the visible region of the solar spectrum. Photons with sufficient energy excite electrons to higher energy states, which leads to the formation of holes in the ground state. A build-in potential asymmetry spatially separates electron-hole pairs, introducing a photovoltage. The consequent extraction of the charge carriers on opposite sides of the absorber to an external circuit generates a photocurrent.[8] Besides the spatial charge carrier

separation via the potential asymmetry, the PV effect requires an energetic separation of electrons and holes. Here, the band gap of semiconductors acts as forbidden region between excited and ground state, which facilitates the required energetic separation between electrons and holes. Thereby, the band gap prevents the immediate relaxation of electrons into their ground states via recombination with the respective holes.[3] Hence, to identify of suitable absorber materials for solar cells, their electronic band structure is decisive.

1.2.2 Electronic band structure

To derive the allowed energy states of electrons in a solid, electrons are best described as waves instead of particles. According to the wave-particle duality, which is a concept in quantum mechanics, electrons simultaneously exhibit particle and wave characteristics. The de Broglie relation connects particle and wave properties via: $\lambda = h/p,$ with the wavelength λ, the particle impulse p and the Planck constant h. Therefore, a wave function Ψ that is the solution of the Schrödinger equation describes the dynamics of electrons:[18]

$$-\frac{\hbar}{2m_e}\frac{\mathrm{d}^2\Psi}{\mathrm{d}x^2} + V(x)\Psi = E\Psi$$

Equation 1.1: Schrödinger equation.

, with the potential energy *V(x)* at position *x*, the electron mass m_e, the electron energy *E* and the reduced Planck constant $\hbar = h/2\pi$. For a free electron in one dimension, the solution of the Schrödinger equation (Equation 1.1) is a plane wave in the form of

$$\Psi = \mathrm{e}^{\mathrm{i}kx}$$

Equation 1.2: Electron wave function Ψ.

along x direction, with the wavenumber k that depends on the wavelength via $k = 2\pi/\lambda$. At an electron energy $E = \hbar^2k^2/2m_e$ and no limitations for k, a free electron can occupy all energies *E*.[18]

However, in crystalline solids, the periodically arranged positive atom cores with a lattice spacing a perturb the electron dynamics. The atom cores interact with the electrons via Coulomb forces, forming a periodic potential landscape *V(x)* (Figure 1.1a).[19] In agreement with Bragg's law, electrons are reflected by the crystal lattice planes at $k = \pi/a$ or $\lambda = 2a$, which causes a superposition of incident and reflected wave and, therefore, a standing-wave electron behavior:[19,20]

$$\Psi_{\pm} = e^{\mathrm{i}\pi x/a} \pm e^{-\mathrm{i}\pi x/a}$$

Equation 1.3: Electron wave functions $\Psi_{\pm}$ in crystalline solids.

From the wave functions in Equation 1.3, we derive probability densities $|\Psi_+|^2$ and $|\Psi_-|^2$, depicted in Figure 1.1b. The distribution of the probability densities along *x* shows that electrons with wave function Ψ_+ mainly accumulate between atom cores and those with Ψ_- accumulate at atom cores. Since the periodic potential *V(x)* in crystals features minima at the position of positive atom cores due to Coulomb interactions and maxima in between the cores (Figure 1.1a), the

potential energy of electrons with Ψ_- becomes lower than the energy of electrons with Ψ_+.[19] In the dispersion relation between electron energy E and wavenumber k – a parabola for the free electrons in Equation 1.2 (Figure 1.1c) – the different energies of electrons with Ψ_+ and Ψ_- introduce a splitting of the energy levels at certain k. The split energy levels form energy gaps between allowed energy levels (Figure 1.1d). Due to Bragg's law, these energy gaps occur at integer multiples n to $k = \pi/a$ and $k = -\pi/a$. Solutions of Schrödinger equation (Equation 1.1) that consider the periodic potential of a crystalline solid are called Bloch wave functions (Equation 1.4). Bloch wave functions accurately describe the dynamics of the electrons in the crystal lattice:[19,20]

$$\Psi(x) = e^{ikx} \cdot u(x)$$

Equation 1.4: Bloch electron wave function Ψ with perodic potential $u(x)$.

Here, the plane wave e^{ikx} is analogous to the wave function of a free electron (Equation 1.2). The periodic function $u(x)$ exhibits the same periodicity as the atom cores in the crystal lattice: $u(x) = u(x + a)$. Energy regions, for which no solutions to the Schrödinger equation in form of Bloch wave functions exist, are energy gaps with the width E_g (Figure 1.1d).[20]

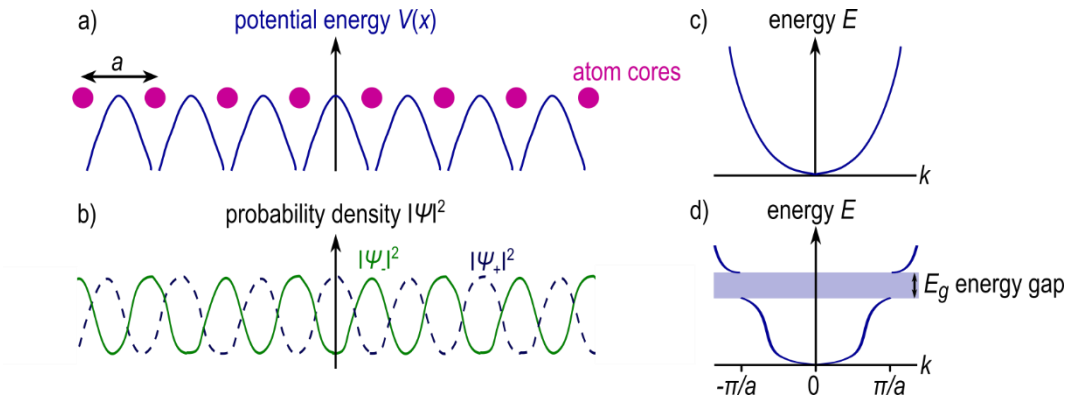

Figure 1.1: a) Periodic electron potential $V(x)$ in crystalline solid caused by Coulomb interactions between positive atom cores and electrons. Atom cores are displayed in pink and the potential energy $V(x)$ in blue. b) Probability densities $|\Psi_+|^2$ and $|\Psi_-|^2$ showing the accumulation of electrons with wave function Ψ_+ (blue dashed line) between the atom cores and electrons with wave function Ψ_- (green solid line) at atom cores. The superposition of a) and b) leads to lower energies for electrons with Ψ_-.[19] c) Parabolic dispersion relation between electron energy E and wavenumber k of free electrons. d) Dispersion relation for electrons in a periodic crystal potential with a splitting of the energy levels at $k = \pi/a$ and $k = -\pi/a$, which introduces an energy gap with the width E_g.[20]

With energy gaps as forbidden regions, electrons instead occupy the allowed continuous energy states, which are named energy bands.[8,19] The widths of these energy bands ΔE_n depend on the interaction strength between electrons and atom cores: The strong Coulomb interaction between positive atom cores and inner-shell electrons causes a large energy difference between Ψ_+ and Ψ_- and thus a large energy gap, which is also called band gap. Accordingly, energy bands are narrow. For outer-shell electrons, inner-shell electrons screen the Coulomb potential from the atom cores. Therefore, the band gap decreases until the energy bands overlap.[3] The presence and width E_g of the band gap between the highest occupied energy band, the valence band, and the lowest unoccupied energy band, the conduction band, determines whether solids are classified as metallic conductor, semiconductor or insulator.[3,8,19,20]

Metallic conductors do not have a band gap. Here, either the valance and conduction band overlap, or the valence band is only partially filled. The occupation probability of the available energy states at thermal equilibrium is described by the Fermi-Dirac statistics, which generally apply to fermions in multi-particle systems (Chapter 1.2.3.2, Equation 1.6). Here, the highest occupied energy state at $T = 0$ K is called Fermi energy E_f.[20] In metals, electrons close to the Fermi energy move freely through the material. This delocalization of electrons leads to a high electrical conductivity, which decreases with temperature, as thermal oscillations of atom cores, so-called phonons, scatter the electrons inelastically.[18,21] Despite their high electrical conductivity, metals are not suited as light-absorbers in solar cells, because excited electrons continuously loose energy by inelastic phonons scattering within periods as short as picoseconds. Therefore, the lifetime of excited electrons in metals is not sufficient to extract charge carriers and generate an electrical current.[3]

For insulators as well as for semiconductors, electrons fill the valence band entirely since the Fermi energy lies within in the band gap that separates the valence and conduction band.[3,8,18] In insulators, band gaps are large: Around 9 eV for sodium chloride and up to 12 eV for lithium fluoride.[22] Thus, insulators display a low conductivity. Additionally, their band gaps are too wide for photons in the visible light range to excite electrons, which makes insulators not applicable as light-absorbing materials in solar cells.[3,8,18]

On the other hand, semiconductors with band gaps between 0.5 and 3.0 eV are generally suited as light-absorbers in solar cells. Photons from the visible light range at 420 – 700 nm and the infrared up to 2500 nm have sufficient energy to excite electrons across the semiconductor band gap.[18] Moreover, in semiconductors, the continuous relaxation of excited electrons via phonon-scattering is only possible until electrons reach the lower edge of the conduction band. For complete relaxation to the ground state, the electrons would have to lose the entire gap energy E_g in one single step by emitting photoluminescence (PL). However, this radiative relaxation process has a low probability, as it requires the presence of a hole at the same position. Thus, the band gap in semiconductors increases the lifetime of excited electrons to up to several microseconds.[3,8] The optical absorption and the conductivity in semiconductors are discussed in following.

1.2.3 Semiconductors as solar cell light absorbers

1.2.3.1 Optical absorption

Macroscopically, the Beer-Lambert law describes the exponential attenuation of intensity I with respect to the initial intensity I_0, as the light travels through an absorber with thickness l and a uniform absorption coefficient α:

$$I = I_0 e^{-\alpha l}$$

Equation 1.5: Beer-Lambert law.

According to Equation 1.5, two parameters can boost the optical absorption: An increase in the layer thickness l and/or choosing an absorber material with a high optical absorption coefficient α.[8,18] The absorption coefficient α is determined by the probability with which a photon is absorbed

by exciting an electron to a higher energy state. This probability depends on photon energy as well as the density of occupied electron states in the valence band and unoccupied electron states in the conduction band at the given wavelength. The inverse of the absorption coefficient, the penetration depth $L_\gamma = 1/\alpha$, serves as measure for the required material thickness for efficient absorption.[3,20]

For a suitable solar cell absorber, the absorption onset ideally features a sharp defined absorption edge, which is called Urbach tail. The wavelength of the onset is given by band gap energy E_g of the light-absorber and should be below the high intensity regions of the solar spectrum.[3] The sun emits radiation in a wide energy range, from the ultraviolet to near infrared. By the time the sunlight reaches the surface of the earth, its spectral intensity fluctuates strongly due to an increased absorption of certain wavelengths by atmospheric gases. Generally, the spectral composition of light emitted by the sun is illustrated by plotting the irradiance, the spectral power density in W/m², against the photon energy in nm. The solar irradiance spectrum at an air mass (AM) of 1.5 considers the partial absorption of sunlight in the atmosphere as well as an incident radiation angle of 48 ° and is the standard to evaluate of solar cell performance (Figure 1.2a).[23] The solar irradiance reaches its maximum in the blue-green region of the visible light – a region that should be covered by the absorption range of a suitable solar cell light-absorber.[8]

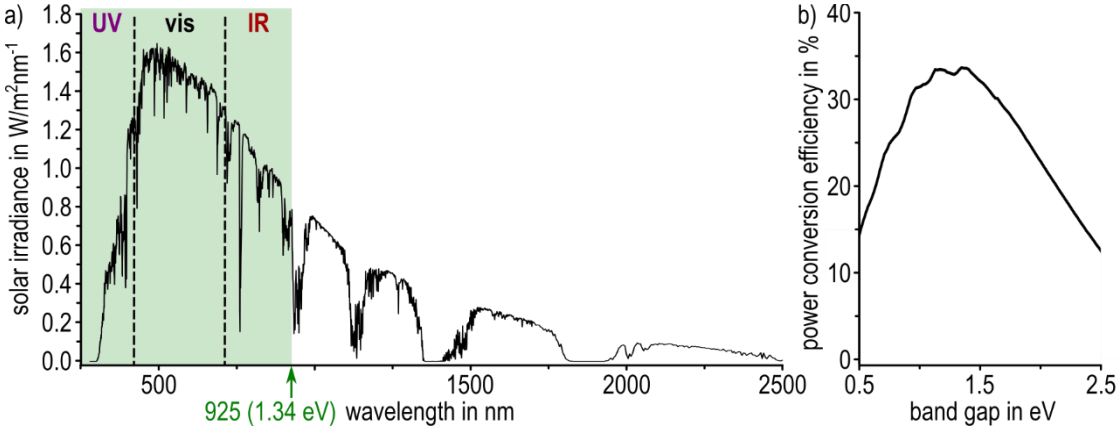

Figure 1.2: a) The solar irradiance spectrum at air mass 1.5 plotted from data by the American Society for Testing and Materials.[23] The absorption region of an ideal solar cell light-absorber with a band gap and absorption onset of 1.34 eV (~925 nm)[24] is shaded light green. b) Radiative efficiency limit versus band gap energy for the standard solar irradiance at AM 1.5 as displayed in a.[24,25]

In the ideal absorber, all photons with energy E greater than the band gap energy E_g are absorbed, while photons with lower energy are transmitted or reflected.[3] To increase the absorption, it may seem feasible to choose materials with the lowest possible band gap energy E_g. However, too narrow band gaps implicate significant losses of surplus energy from above-band gap photons, as excited electrons relax to the lower edge of the conduction band. On the other hand, too high band gap energies substantially limit the absorption, since all sub-band gap photons are excluded.[8] To determine the optimal band gap energy for efficient absorption, Shockley[26] and Queisser derived the *PCE* for a range of band gap energies.[24] For the solar irradiance spectrum at 1.5 AM (Figure 1.2a), a maximum *PCE* of ~33.5% can be reached at a band gap of 1.34 eV, defined as radiative efficiency limit of solar cells (Figure 1.2b).[25,27,28] Due to the relatively broad maximum,

suitable semiconductors with band gap energies E_g between 1 and 1.5 eV can potentially facilitate high solar cells performances.[3]

1.2.3.2 Conductivity of semiconductors

The intrinsic conductivity of pure semiconductors originates from a thermal excitation of electrons from the valance band into the conduction band. For a material in thermodynamic equilibrium, Fermi-Dirac statistics quantitatively describe the occupation probability P of energy states by electrons:[8,18,20]

$$P = \frac{1}{e^{(E-E_f)/k_BT} + 1}$$

Equation 1.6: Fermi-Dirac statistics with the occupation probability *P*.

Here, k_BT is the thermal energy. At $T = 0$ K, electrons occupy all energy states up to the Fermi energy E_f, which is located in the center of the band gap for intrinsic semiconductors. Above 0 K atom cores transfer their thermal energy to electrons via phonon scattering and excite them above the Fermi energy, with $P = 0.5$ at E_f (Figure 1.3a). If the exponential tail of the Fermi-Dirac distribution (Equation 1.6) expands over the band gap, electrons close to the Fermi energy can overcome the band gap, move into the conduction band and thereby generate an equal number of holes in the valance band.[8,18]

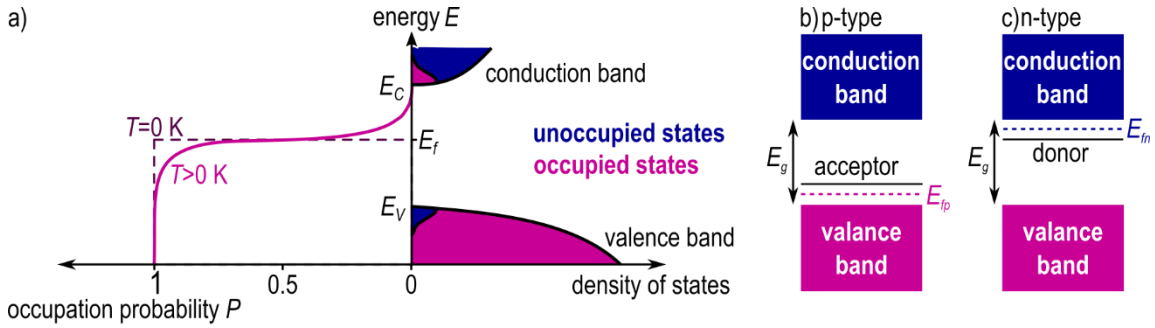

Figure 1.3: a) On the left, the occupation probability *P* plotted against the electron energy *E* at $T = 0$ K (violet dashed line) and at elevated temperatures $T > 0$ K (pink solid line) according to Fermi-Dirac. The respective occupation of density of states of valence and conduction band, with the band edge energies E_V and E_C, respectively is shown on the left: Occupied states in red, unoccupied states in blue. Fermi energy E_f lies in the center of the band gap at $P = 0.5$ for intrinsic semiconductors.[8,19] b) Band structure for *p*-type doped semiconductor with formation of acceptor band over the valance band in the band gap E_g and shift of the Fermi energy E_{fp} to lower energies. c) Band structure for *n*-type doped semiconductor with formation of donor band under the conduction band in the band gap E_g and shift of the Fermi energy E_{fn} to higher energies.[19]

In an electric field, these free electrons and holes become subject to a drift with velocity v, whose magnitude is directly proportional to the charge carrier mobility μ_i. The mobility is given as: $\mu_i = q\tau_c/m_i^*$, with charge q, mean free time τ_c and the effective charge carrier mass m_i^*. The mobilities electrons and holes μ_e and μ_h, in an electric field define the material's conductivity σ via:

$$\sigma = c_e q\mu_e + c_h q\mu_h$$

Equation 1.7: Conductivity σ in dependence of hole and electron mobility μ_e and μ_h.

with the electron and hole concentration c_e and c_h.[20] Due to the dependence of the charge carrier concentrations c_i on band gap energy E_g, the conductivity of intrinsic semiconductors in dark can vary by several orders of magnitude. For example, Germanium with a band gap of 0.74 eV has a room temperature conductivity of $2 \cdot 10^{-2}$ $Ohm^{-1}cm^{-1}$, whereas GaAs with a band gap of 1.42 eV has a room temperature conductivity of 10^{-8} $Ohm^{-1}cm^{-1}$.[8]

To improve the conductivity of semiconductors, a small amount of material atoms can be exchanged for dopant atoms with a lower or higher number of valence electrons. This exchange, called doping, increases the charge carrier concentration in the semiconductor. Doping with an acceptor – an element with less valence electrons than the semiconductor – introduces additional holes as positive charge carriers and is called *p*-type doping. *P*-doped semiconductors possess an additional narrow acceptor band within the band gap close to the valence band for the excitation of electrons (Figure 1.3b). Here, holes are majority and electrons minority charge carriers. On the other hand, doping with a donor – an element with more valence electrons than the semiconductor – increases the electron density and is called *n*-type doping. *N*-doping with excess electrons leads to the formation of a narrow donor band close to the conduction band, from which electrons are readily excited (Figure 1.3c). In *n*-doped semiconductors, electrons are the majority and holes minority charge carriers. In both cases, the overall conductivity increases due to the higher carrier concentration (Equation 1.7). The additional inner band gap states in doped semiconductors introduce a shift of the Fermi energy to lower or higher energies in *p*-type or *n*-type doping, respectively.[8,18,19] Even without extrinsic doping, semiconductors can exhibit slight *p*-type or *n*-type doping due to self-doping via broken bonds, crystal impurities or defects at grain boundaries and surfaces in polycrystalline compounds or monocrystalline materials.[8]

1.2.3.3 Dynamics of photogenerated charge carriers

Photogeneration

In solar cells, the most important process to introduce mobile charge carriers in the absorbing semiconductor is photogeneration: The concentration of electrons in the conduction band and holes in the valance band, significantly rises with the absorption of sufficiently energetic photons, which enhances the conductivity (Equation 1.7).[3,8] Depending on the dielectric properties of the absorber, the photogenerated electron-hole pair is either bound by coulomb forces and acts as quasi-particle, which is called exciton, or dissociates to free photocarriers. Most inorganic semiconductors have sufficiently high dielectric constants to effectively screen the coulomb forces between electron and hole, so that excitons readily dissociate into free charge carriers at room temperature.[29]

Diffusion

Without an electric field as driving force, the movement of free photocarriers in the light-absorber is governed by diffusion. Photocarrier diffusion ensues from a concentration gradient e.g., when a focused illumination source only locally generates a high carrier concentration, whereas other areas remain dark and consequently display low carrier concentrations. The diffusion process follows a random walk motion, until the concentration across the absorber becomes uniform.[3,18] To quantify the photocarrier diffusion in thin absorber layers, which are present in thin film solar cells,

the diffusion probability *P(d, t)* can be approximated via a 2D diffusion equation in form of a normalized Gaussian function (Chapters 3.2.2 and 4.1.2):

$$P(d,t) = \frac{1}{4\pi Dt} \cdot e^{-\frac{d^2}{4Dt}}$$

Equation 1.8: Diffusion probability *P(d,t)* in two dimensions.

where *P(d, t)* is the probability that a carrier diffused a certain distance *d* from its origin within a given time *t*. *P(d, t)* depends on the temperature- and material-specific diffusion constant *D* as measure for the diffusion rate. For the 2D diffusion within the thin absorber, *D* is defined as:

$$D = \frac{d^2}{4\tau_{Diff}}$$

Equation 1.9: Diffusion constant *D* in two dimensions.

with the average diffusion time τ_{Diff}.[30] For a suitable solar cell absorber, the average distance photocarriers diffuse before they recombine should exceed the absorber thickness to enable the extraction of charges at the respective contacts.[8] This diffusion length L_D depends on the diffusion constant *D* and the recombination lifetime τ of the charges:[31]

$$L_D = \sqrt{D\tau}$$

Equation 1.10: Diffusion length L_D.

Recombination

The recombination lifetime τ is the average time between electron excitation into the conduction band and relaxation into the valence band, where the electron recombines with a hole. Without charge extraction via contact layers, all photocarriers necessarily recombine sometime after their generation. Generally, various mechanisms facilitate a recombination of electron and hole. Some adverse recombination mechanisms can be reduced by material or device improvement but others are inevitable. The former includes trap-assisted recombination, the latter radiative and Auger recombination. Depending on the number of particles partaking in the recombination, the mechanisms are classified as monomolecular (trap-assisted), bimolecular (radiative) or trimolecular recombination (Auger). Due to the dependence on the number of involved particles, the governing recombination mechanism changes with the charge carrier density i.e., the trimolecular Auger recombination mainly occurs at high carrier densities.[8,32] All mechanisms exhibit characteristic lifetimes τ_i that contribute to the total recombination lifetime τ_{tot} as $1/\tau_{tot} = \sum_i 1/\tau_i$.[3]

In trap-assisted recombination, a localized crystal defect or impurity immobilizes a hole or an electron, which subsequently is either released via thermal excitation or recombines with its counterpart while captured. The defects or impurities form additional energy states in the band gap: Energy states close to the valance band capture holes and energy states close to the conduction band capture electrons. States located close to the band edges are called trap states, while mid-band gap energy states that can capture either charge carrier are called recombination centers.[3,8] The additional energy states in the band gap allow electron relaxation via phonon release, which makes

trap-assisted recombination nonradiative.[3] Trap-assisted recombination occurs in the bulk material, but increasingly takes place on surfaces or grain boundaries of polycrystalline light-absorbers. At these positions, the symmetry of the crystal is reduced and broken bonds or other crystal defects form.[8] Since real absorber systems contain some amount of crystal defects, trap-assisted recombination is generally present in solar cells. However, controlled crystallization minimizes the concentration of bulk defects and passivation of surfaces and/or grain boundaries partially prevents interfacial defects. Therefore, optimized preparation procedures can significantly reduce trap-assisted recombination.[3]

Spontaneous emission of photons, which is called radiative recombination, occurs for band-to-band transitions, where electrons relax directly from the conduction into the valance band. Here, the wavelength of emission corresponds to the band gap of the absorber.[33] Radiative recombination is a bimolecular process and depends on the concentration of electrons and holes. Therefore, radiative recombination requires higher charge carrier densities than trap-assisted recombination.[3] Without the extraction of photocarriers e.g., in an isolated absorber film without contact layers, the emission of photons is utilized to characterize the charge carrier dynamics of the material, including diffusion length L_D (Equation 1.10) and carrier lifetime τ via PL spectroscopy and microscopy (Chapters 1.4.2.2, 3.2.2, 4.1.2 and 4.2).[3,34,35] For a full solar cell under operation, the continuous extraction of charge carriers reduces the influence of radiative recombination on the performance.[8] However, semiconductors with sharp absorption onset and broad emission spectrum, like GaAs and hybrid perovskites, allow the reabsorption of photons from radiative recombination in a process that is called photon recycling.[27,36,37] By reducing the outcoupling probability of the emitted photons from the absorber layer via photon management (Chapters 1.3.2.1 and 4.2), photon recycling can contribute to higher solar cell performances.[27,38]

1.2.4 Solar cells

1.2.4.1 Electrical current

To generate an electrical current from solar cells, a driving force needs to separate and extract photogenerated holes and electrons on opposite sides of the absorber to the contact layers, where they enter the external electrical circuit. Relevant forces are a gradient in the electrical potential due to a build-in electric field, introducing a drift current (Chapter 1.2.3.2, Figure 1.4a), and a concentration gradient causing a diffusion current (Chapter 1.2.3.3, Figure 1.4b).[3]

For the drift current, an electric field, with the field strength E_{el}, generates a potential gradient for electrons in the conduction band and holes in the valance band. Consequently, both carriers flow in opposite directions with the velocity v to minimize their energy (Chapter 1.2.3.2). The carrier mobility μ_i quantitatively describes the charge carrier drift in an electric field via:

$$\mu_i = \frac{|v|}{E_{el}} = \frac{q\tau_c}{m_i^*}$$

Equation 1.11: Charge carrier mobility μ_i.

With the mean free time τ_c and the effective mass m_i^* of the respective charge carriers.[20] The resulting drift current density $j_{Drift,\,i}$ is directly proportional to the charge carrier mobility μ_i via

charge q, charge carrier concentration c_i and the electric field E, but can also be expressed by the conductivity σ_i (Equation 1.7):

$$j_{Drift,i} = \mu_i \cdot q c_i E = \sigma_i E$$

Equation 1.12: Current density of drift $j_{Drift,\,i}$, depending on the charge carrier mobility μ_i.

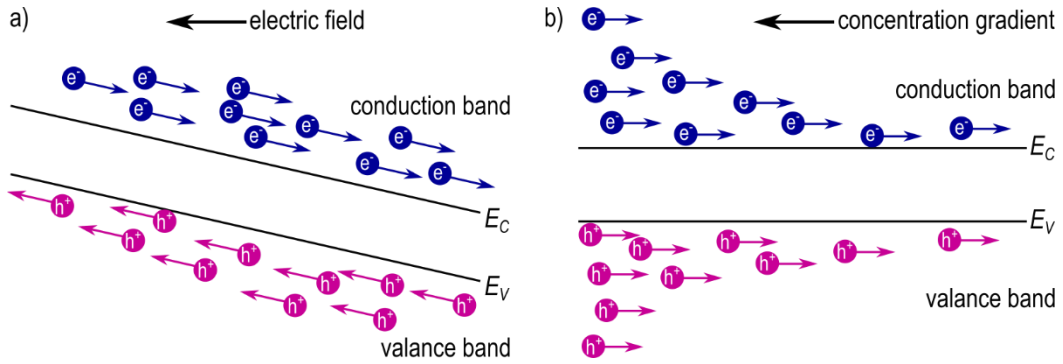

Figure 1.4: a) Schematic representation of drift current at uniform carrier concentrations with an electric field as driving force introducing a gradient in the band edge energies of valance band E_V and conduction band E_C. The direction of the hole and electron flow are indicated by the arrows. b) Schematic representation of diffusion current without electric field with a concentration gradient as driving force. The energies of the band edges E_V and E_C stay constant. The direction of the hole and electron flow are indicated by the arrows: A net current is only generated for unbalanced hole and electron concentrations.[3,8]

In the absence of an electric field and presence of a nonuniform carrier concentration, the concentration gradient dc_i/dx drives the charge carriers motion depending on their diffusion constant D_i (Equation 1.9). D_i relates to the charge carrier mobility μ_i via the Einstein equation:

$$D_i = \mu_i \frac{k_B T}{q}$$

Equation 1.13: Einstein equation realting the diffusion constant D_i to the charge carrier mobility μ_i.

with the thermal energy $k_B T$.[31] An electrical current is generated when hole and electron concentrations are unbalanced e.g., in doped semiconductors. The consequent diffusion current density $j_{Diff,\,i}$ is given as:[3]

$$j_{Diff,i} = -qD_i \cdot \frac{dc_i}{dx}$$

Equation 1.14: Current density of diffusion $j_{Diff,\,i}$, depending on the charge carrier diffusion constant D_i and the concentration gradient.

Ultimately, the total electrical current generated in a solar cell is a combination of drift and diffusion currents in Equation 1.12 and Equation 1.14.[3,8]

1.2.4.2 Architecture

An effective separation of the charge carriers to generate a photocurrent or a photovoltage requires a build-in electric field across a solar cell. This build-in field can be introduced by assembling an array of materials with a gradient in their work functions (Figure 1.5a). The work

function Φ_W represents the work necessary to excite an electron from the Fermi energy E_f above the vacuum level E_{vac}:[3,8]

$$\Phi_W = E_{vac} - E_f$$

Equation 1.15: Work function Φ_W.

A junction between the materials with a work function difference $\Delta\Phi_W$ leads to an alignment of their Fermi levels, which generates a gradient in the vacuum level E_{vac} and band edge energies E_C and E_V. Consequently, electrons in the conduction band flow from one material to the other to reduce their potential energy V by $\Delta V = \Delta\Phi_W$. To achieve a separation of electrons and holes, the junction needs to extract photocarriers in opposite directions.[8]

In homojunctions – most prominent are *pn*-junctions in Si solar cells – differently doped layers of the same semiconductor are brought into contact (Figure 1.5b). With the lower Fermi energy in the *p*-doped region and the higher Fermi energy in the *n*-doped region (Figure 1.3b and c), an alignment of the Fermi energies leads to the formation of a build-in potential step ΔV. During the alignment of Fermi energies, electrons as majority carriers from the *n*-doped side diffuse to the *p*-doped side and holes as majority carriers from the *p*-doped side diffuse to the *n*-doped side due to a concentration gradient. Consequently, holes and electrons recombine the region around the junction, which depletes the interface of majority charge carriers and leaves behind ionized dopants with negative charge on the *p*-doped side and positive charge on the *n*-doped side. This depletion region around the junction introduces the potential step ΔV, which extracts photogenerated electrons from the *p*-doped into the *n*-doped side and photogenerated holes from the *n*-doped into the *p*-doped side.[3,8,39]

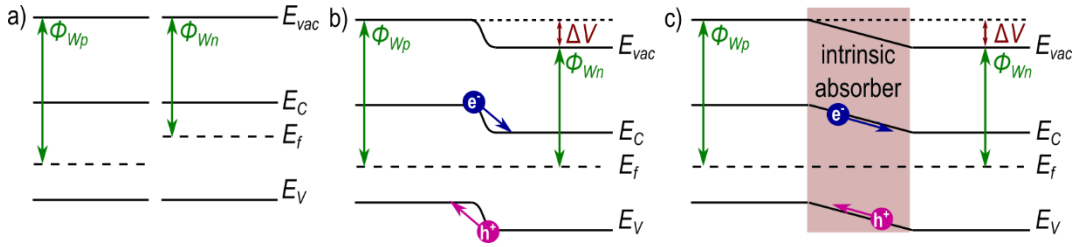

Figure 1.5: a) Electronic band structure of two isolated materials with different work functions Φ_{Wp} and Φ_{Wn} with vacuum energy E_{vac}, band edges of the conduction band E_C, valance band E_V and Fermi energy E_f. The material on the left is *p*-doped, the material on the right is *n*-doped. b) Schematic of *pn*-junction: A connection leads to the alignment of Fermi energies, a gradient in E_{vac} and the band edges E_C and E_V. Thus, a build-in electric field forms across the space charge region with potential energy step of ΔV. c) Schematic of *pin*-junction with an intrinsic absorber layer sandwiched between an *n*-type and a *p*-type layer, acting as electron and hole transport layer, respectively. The alignment of Fermi energies of *n*-type and *p*-type layer leads to the formation of a constant electric field in the intrinsic absorber.[8]

Another architecture to achieve a build-in field is the *pin*-junction, for which an intrinsic absorber layer is sandwiched between a *p*-doped and an *n*-doped region. Upon establishing the junction, the Fermi-levels of *p*- and *n*-doped region align, but now the resulting build-in field spans over the intrinsic layer in the center (Figure 1.5c). Typically, a *pin*-architecture is used in heterojunctions consisting of different materials, where the majority of the photocarriers are generated in intrinsic absorber, but have relatively short diffusion lengths. Here, the wide build-in field is advantageous, as the field drives photogenerated holes and electrons out of the intrinsic

absorber layer towards the *p*-type hole transport layer (HTL) and the *n*-type electron transport layer (ETL), respectively.[3,8] For a maximum current output, the width of the intrinsic layer has to be adjusted, to provide a sufficiently strong electric field, yet still be thick enough to absorb most of the incident light as given by the penetration depth L_λ (Chapter 1.2.3.1). For that reason, thin-film solar cells, based on *pin*-junctions, employ absorber materials with low penetration depths, so that layer thicknesses in or below the single-digit micrometer scale suffice for efficient light absorption as well as for providing a build-in field (Chapter 1.3.2.3).[3]

Disadvantages of *pin*-junctions include a possible electric field neutralization and interfacial traps. The former effect occurs when very high carrier densities or mobile ions are present in the absorber: The electronic or ionic carriers can form depletion regions at the interfaces to the *p*- and *n*-type semiconductors and screen the build-in field within the intrinsic absorber (Chapter 1.3.1.2, Figure 1.11). Here, diffusion becomes the governing carrier transport mechanism. Therefore, current generation requires diffusion lengths in the range of the layer thickness for the carriers to reach the *pi* or *in* junction, where they are extracted. Regarding the latter interface phenomenon: Heterointerfaces often contain traps or recombination centers and therefore considerably affect the shunt resistance of solar cells. Hence, efficient *pin*-solar cells often require a passivation of internal interfaces to reduce interfacial recombination, maintain a high shunt resistance and thereby a high open circuit voltage.[8] Moreover, poor stability of the charge transport layers with respect to mobile ions in the intrinsic semiconductor can lead to an interfacial material degradation. This degradation can increase the series resistance of the cell, which lowers the current (Chapters 1.2.4.3 and 5.1).

1.2.4.3 Characterization of solar cells

Key parameter to evaluate the performance of solar cells is the *PCE*, which is the ratio of the electrical power P_{PV} generated per power of the incident solar power P_{sol}:

$$PCE = \frac{P_{PV}}{P_{sol}}$$

Equation 1.16: Definition of *PCE*.

The electrical power of a solar cell P_{PV} is the product of photocurrent I und photovoltage V:

$$P_{PV} = I * V$$

Equation 1.17: Electrical power P_{PV} of solar cell.

To compare different solar cells, it is common to use the area-normalized photocurrent density j instead of total photocurrent I. The photocurrent density depends on the generation of mobile charges as well as their collection via the transfer layer and/or electrodes and reaches its maximum j_{SC} in short circuit conditions at zero voltage. The photovoltage, which is defined as the internal potential difference between the solar cell electrodes under illumination, reaches its maximum V_{OC} in open circuit conditions at zero photocurrent.[40] By sweeping an external voltage applied to an illuminated solar cell and tracking the current density from short to open circuit, a current-voltage (*j*-*V*) curve is recorded (Figure 1.6a). This curve allows identifying and calculating all relevant solar

cells parameters: The j_{SC}, the V_{OC}, the *PCE*, the maximum power point (*mpp*) and the fill factor (*FF*). The *mpp* marks the point of maximal power generation, where the cell should be operated.

$$P_{mpp} = V_{mpp} * j_{mpp} = P_{PV}$$

Equation 1.18: Power of solar cell P_{PV} at *mpp*.

The *FF* quantifies the quality of a solar cell by comparing the power P_{PV} at the *mpp* (blue area in Figure 1.6a) with the product of j_{SC} and V_{OC} (yellow area in Figure 1.6a):

$$FF = \frac{j_{mpp}V_{mpp}}{j_{SC}V_{OC}}$$

Equation 1.19: Definition of the solar cell fill factor *FF*.

By combining Equation 1.16 – Equation 1.19 , the *PCE* can now be expressed as:[8,40]

$$PCE = \frac{j_{SC}V_{OC}FF}{P_{sol}}$$

Equation 1.20: *PCE* in dependence of j_{SC}, V_{OC}, *FF* and P_{sol}.

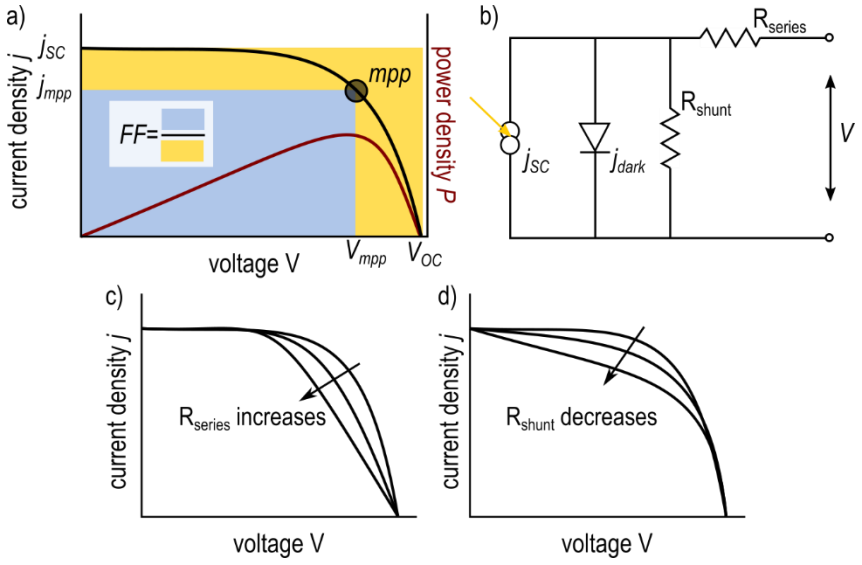

Figure 1.6: a) *j-V* curve showing the recorded current density *j* in black as the voltage is swept from 0 V to open circuit conditions under one sun illumination (100 mW/cm²) with short circuit current j_{SC} at 0 V and open circuit voltage V_{OC}. The power density is shown in dark red, the maximum power point (*mpp*) is highlighted by the black circle, the current j_{mpp} and voltage V_{mpp} at the *mpp* are marked on their respective axis. Fill factor *FF* is calculated by dividing the blue area below the curve (j_{mpp}*V_{mpp}) by yellow area (j_{SC}*V_{OC}).[8,40] b) Equivalent solar cell circuit with series and shunt resistance R_{series} and R_{shunt}, respectively, and the dark current density j_{dark}.[8] c) Schematic of the impact of an increasing series resistance R_{series}.[8] d) Schematic of the impact of a decreasing shunt resistance R_{shunt}.[8]

Internal resistive losses in the solar cell change the shape of the *j-V* curve and affect particularly the *FF* and therefore the *PCE*. There are two types of resistance relevant for solar cell operation: The series resistance R_{series}, which is attributed to interface resistance as well as the bulk resistance of the constituent layers, and the shunt or leakage resistance R_{shunt}, which decreases with increased recombination and a poor selectivity of the transfer layers (Figure 1.6b). A high series resistance impairs the *FF* of the cell by lowering the current output at high voltages (Figure 1.6c), thus the bulk

materials and their interfaces need to be optimized for maximal conductivity (Chapter 5.1). On the other hand, a low shunt resistance reduces the current output at lower voltages (Figure 1.6d). In order to avoid current reduction via shunts, the traps and recombination center density at interfaces or grain boundaries should be minimal.[8,40]

1.3 Perovskite solar cells

Today´s most successful PV technologies are solar cells based on the inorganic absorbers Si and GaAs. Decades of research improved both systems to reach efficiencies of 26.1% for single-crystalline Si and 29.1% for thin-film GaAs solar cells, which is close to their theoretical limit of 29% and 31%, respectively.[8,11] Crystalline Si exhibits a well-suited band gap of 1.1 eV, high carrier mobilities of 500 cm^2/Vs for holes and 1500 cm^2/Vs for electrons as well as diffusion lengths in the range of 100 µm. However, the material's optical absorption is weak and thus efficient photocurrent generation requires absorber thicknesses of several 100 µm. Moreover, the absorption onset of Si is rather flat and leads to a reduced absorption of red light.[8] With a band gap of 1.42 eV,[8] GaAs is close to the ideal absorber for solar cells, according to the radiative efficiency limit (Chapter 1.2.3.1).[24] A strong optical absorption allows using GaAs in thin film architectures with film thicknesses in the single-digit micrometer range. Additionally, the carrier mobilities between 300 cm^2/Vs for holes and 5000 cm^2/Vs for electrons are high and facilitate an efficient charge carrier extraction. However, limited Ga resources and the manufacturing costs for GaAs solar cells, which are up to 10 times higher than for Si solar cells, restrict their commercial utilization.[8,41]

On the search for suitable and affordable alternatives for established solar cell absorbers, researchers have started to implement the hybrid organic-inorganic perovskite methylammonium lead iodide $MAPbI_3$ in solar cells, called PSCs.[12] This material has a band gap of 1.55-1.60 eV, which can be tuned to higher energies by exchanging the iodide ions for bromide or chloride.[42,43] It is a strong optical absorber, so that layer thicknesses of a few hundred nanometers suffice for efficient photocurrent generation. Furthermore, $MAPbI_3$ exhibits a sharp absorption onset, which leads to a strong absorption over a wide spectral range.[44] With measured values varying between 1 and 160 cm^2/Vs, the carrier mobility is orders of magnitude lower than in the inorganic absorbers GaAs and Si. On the other hand, diffusion lengths of up to 1 µm for polycrystalline films facilitate the diffusion of carriers across the full layer thickness, which is required for sufficient charge extraction.[45,46] The solution-based film formation enables a cheap and low-temperature fabrication and allows printing large absorber areas.[47]

Owing to the advantageous properties of the hybrid perovskite absorber, PSCs have seen an astonishing increase in *PCE* within the ten years of their discovery. When Kojima *et al.* first implemented $MAPbI_3$ as light absorbing dye in solar cells in 2009, they reached a *PCE* of 3.81%. However, the group used an organic electrolyte solution as HTL, in which the hygroscopic perovskite quickly decomposed and the photovoltaic performance decayed quickly.[12] Three years after $MAPbI_3$´s initial implementation, researchers from the groups of Michael Grätzel in Lausanne and Henry Snaith in Oxford simultaneously published studies on all solid state PSCs with efficiencies of 9.7% and 10.9%, respectively. Both groups used the solid HTL 2,2',7,7'-tetrakis-(N,N-di-p-methoxyphenyl-amine)-9,9'-spirobifluorene (SpiroMeOTAD), which greatly enhanced the

lifetime and performance of their solar cells.[13,14] Since 2012, researchers publish new record efficiencies of PSCs on a regular basis with the most recent value of 25.5% certified *PCE,* surpassing the commercially used multicrystalline Si solar cells (23.3%).[11]

1.3.1 $MAPbI_3$ perovskite structure

Perovskite solar cells are named after the crystal structure of their light absorber $MAPbI_3$, which belongs to a large material class that is based on the mineral perovskite $CaTiO_3$. The general perovskite composition is ABX_3 and consists of a large cation A, a small cation B and an anion X. The crucial factor for a material to crystallize in a perovskite structure is the size relation between the constituent ions. The tolerance factor $\tau_{Perovskite}$ considers the relation of the ionic radii r_A, r_B and r_X via:

$$\tau_{Perovskite} = \frac{r_A + r_X}{\sqrt{2}(r_B + r_X)}$$

Equation 1.21: Tolerance factor $\tau_{Perovskite}$ in dependence of ionic radii.

If $\tau_{Perovskite}$ lies between 1 and 0.9, the compound will crystallize in a cubic perovskite structure, whereas lower values will lead to a distortion to reduced symmetry structures.[21] For $MAPbI_3$ with ionic radii of r_{MA}=0.18 nm, r_{Pb}=0.12 nm and r_I=0.22 nm, the tolerance factor is 0.83, which entails a tetragonal room temperature structure.[48] Here, the MA^+ cation (A) occupies the cuboctahedral gap between corner-connected PbI_6 (BX_6) octahedra as inorganic crystal framework (Figure 1.7a).[49]

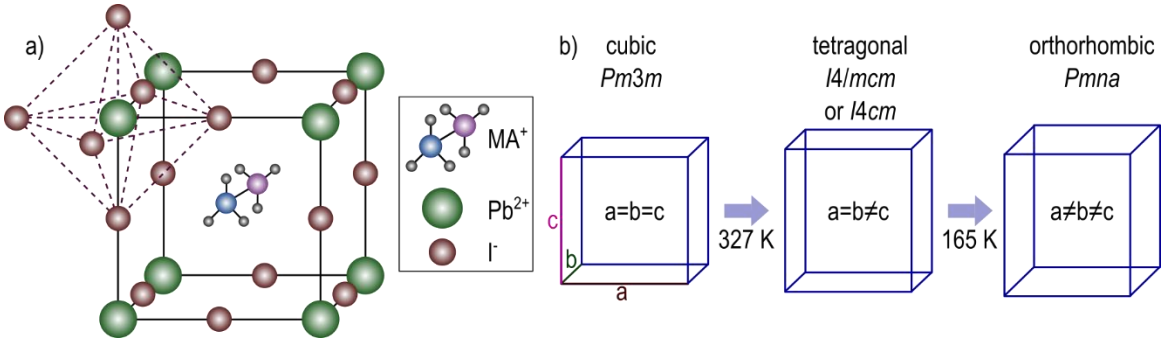

Figure 1.7: a) Methylammonium (MA) lead iodide ($MAPbI_3$) perovskite crystal structure. The PbI_6 octahedra are indicated by dashed lines, MA^+ cations occupy cuboctahedral gaps of the inorganic network.[50] b) Phase transitions of $MAPbI_3$ from cubic to tetragonal to orthorhombic at their characteristic temperatures including the according space groups.[49,51–55]

Crystalline $MAPbI_3$ undergoes two phase transitions at their characteristic temperatures (Figure 1.7b). Above 327 K, $MAPbI_3$ crystallizes in a cubic structure with a $Pm\bar{3}m$ symmetry, below 165 K, in an orthorhombic structure with a *Pnma* symmetry and between 165 and 327 K in a tetragonal phase.[49,51–55] For the latter, studies on the crystal symmetry are inconclusive: While some assign the tetragonal phase to a non-polar $I4/mcm$ space group[52,54,56,57] others report on a polar $I4cm$ space group.[51,53,54,58] According to simulations by Quarti *et al.* and diffraction measurements by Breternitz *et al.,* the formation of the non-polar $I4/mcm$ and the polar $I4cm$ space group mainly depends on the orientation of the MA^+ ion. This is because a preferential orientation of the asymmetric MA^+ ions cancels the inversion symmetry of the unit cells and slightly changes the structure of the inorganic framework to an $I4cm$ space group.[59,60] The symmetry relation between

cubic and tetragonal phase determines whether the tetragonal room temperature phase will be ferroic: A transition from the cubic $Pm\bar{3}m$ to the $I4cm$ structure predicts a ferro*electric* as well as ferro*elastic* tetragonal phase, while the transition to $I4/mcm$ classifies solely as ferro*elastic*.[61] As I will show in Chapter 3.2.2, the presence of ferroic properties in room temperature tetragonal $MAPbI_3$ could affect the charge carrier transport within the perovskite absorber significantly.[35,59,62–68] Hence, I will introduce some basics of ferroelectrics and ferroelastics in the following subchapter.

1.3.1.1 Ferroics

General

Ferroic phase transitions at a critical temperature T_c lower the point group symmetry of the unit cell in a crystalline compound from a non-ferroic high-symmetry prototype phase to a ferroic low-symmetry phase.[69,70] From the loss of symmetry during a ferroic phase transition follows that the ferroic phase can exist in two or more equally stable orientation states when no external fields are applied.[70,71] The application of an electric/magnetic field or mechanical stress changes the energy relation between the orientation states and causes them to switch into the according lowest energy state.[61,69,71] The three primary ferroics are:[69–71]

1) Ferromagnets are materials with a spontaneous magnetization vector.
2) Ferroelectrics are materials with a spontaneous electric polarization vector.
3) Ferroelastics are materials with a spontaneous internal strain tensor.

Herein, I will only focus on ferroelectricity and ferroelasticity as possible properties of the tetragonal $MAPbI_3$ phase at room temperature.

A spontaneous electric polarization in ferroelectric materials requires a polar point group symmetry and therefore a loss in center-symmetry.[61,69,72] The microscopic origin for the electrical polarization can be twofold: First, a displacive phase transition causes a shift in the equilibrium position of ions in the lattice. For example, an off-centering of the center-ion leads to a loss of inversion symmetry and introduces a spontaneous polarization in the unit cell (Figure 1.8a).[61,72] Second, an order-disorder phase transition increases the order from the parent to the ferroic phase e.g., by suppressing the isotropic rotation of dipolar constituent ions. A collective alignment of the dipolar ions then introduces a spontaneous polarization in the ferroelectric phase (Figure 1.8b).[61] The origin of ferroelasticity, on the other hand, is a change of the crystal class during the phase transition (Figure 1.8c). Expanding unit cell parameters introduce an internal strain in the ferroelastic phase characterized by a second rank tensor.[61]

Symmetry relations between the parent phase and the ferroic phase dictate the number of accessible orientation states. A ferroelectric phase transition from a cubic $Pm\bar{3}m$ to a tetragonal $I4cm$ phase results in six equally likely orientation states for the electrical polarization orientated parallel and antiparallel to the *c*-axis along all three spatial directions. Figure 1.8a and b depict two 180° states of the overall six possible polarization orientation states. The simultaneous ferroelastic phase transition leads to three stable orientation states, where the *c*-axis is aligned along all three spatial directions (Figure 1.8c). The additional ferroelectric polarization changes by 90° between the three ferroelastic states.[61,70] The phase transition from $Pm\bar{3}m$ to a tetragonal $I4/mcm$ phase on

the other hand includes solely three ferroelastic states without electrical polarization (Figure 1.8c).[61]

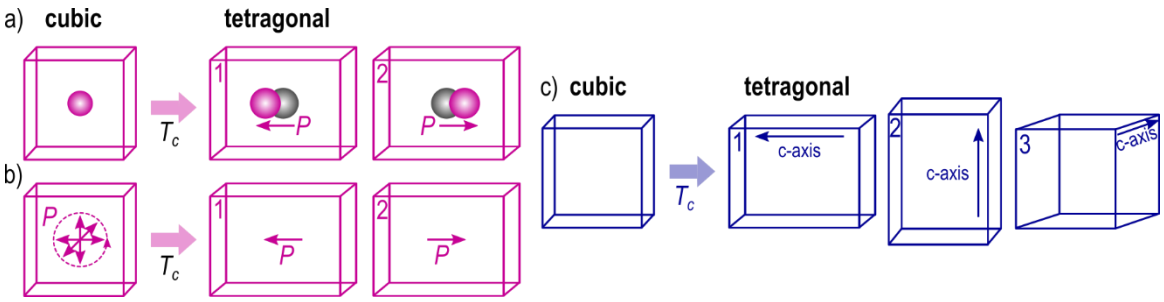

Figure 1.8: a) Schematic illustration of a displacive ferro*electric* phase transition at the critical temperature T_c from a centrosymmetric parent phase (here cubic) to a lower-symmetry ferro*electric* phase (here tetragonal) with the two exemplary stable orientation states 1 and 2. For example, an off-centering of a positive center-ion relative to a negative lattice introduces an electrical polarization *P* with opposite orientations 1 and 2. b) Order-disorder ferro*electric* phase transition: A preferential orientation of a dipolar center-ion introduces an electrical polarization *P* with opposite orientations for the exemplary ferroelectric orientation states 1 and 2, while the dynamic disorder in the cubic phase suppresses a polarization. c) Schematic illustration of ferro*elastic* phase transition at the critical temperature T_c from a high symmetry crystal class (here cubic) to a low symmetry ferro*elastic* crystal class (here tetragonal), which results in three stable orientation states (1, 2 and 3) that differ in the orientation of the c-axis and their internal strain tensor.

States with the same polarization/strain orientation arrange in domains, also called transformational twins. Domain walls, which act as subcrystalline boundaries, separate domains with different orientations (grey line in top row of Figure 1.9a and b).[61] Without external electric field/mechanical stress, all allowed orientation states are energetically degenerate.[61,69,70] The random distribution of domains with different orientation states of microscopic polarization/strain leads to a macroscopic compensation of polarization/strain: As-grown ferroelectric/-elastic materials exhibit no macroscopic polarization/strain (top row Figure 1.9a and b). However, the application of a field/uniaxial stress cancels the degeneracy of the orientation states and lowers the energy for one state selectively.[61] If the field/stress is sufficiently strong, other orientation states will switch into the lowest energy state on timescales of picoseconds to nanoseconds and introduce a non-zero macroscopic polarization/strain (Figure 1.9a and b). Upon removing the field/stress, most of the domains remain aligned and maintain a remnant macroscopic polarization/strain. Now, only the application of a reverse field/stress can re-establish a zero macroscopic polarization/strain (coercive field/stress). Ferroelectric/-elastic hysteresis plots describe the relation between external field/stress and the macroscopic polarization/strain (Figure 1.9c).[61,69,70]

Ferroelectric domain walls can exhibit electronic properties that differ significantly from the bulk behavior and could be harnessed for photovoltaic applications.[61,73,74] As internal interfaces, domain walls have higher energies than the bulk material due to electrostatic contributions.[61] The electrostatic energy increases in particular for those domain walls, where the positive or negative direction of the polarization of adjacent domains points towards their shared interface. These domain walls are called head-to-head (positive, Figure 1.9a) or tail-to-tail (negative) walls, respectively.[74] These domain walls consequently carry a bound charge that depends on the magnitude of the polarization and the angle between the polarization vectors of both adjacent domains: Either 180° or 90° for the ferroelectric and –elastic *I*4*cm* space group.[61] Charged 180° or 90° domain walls will occur only if electronic or ionic charge carriers compensate the bound charge

of the wall.[61,74,75] The compensation of the domain wall charge by free electronic carriers can introduce quasi-metallic domain wall conductivities that are up to 13 orders of magnitude higher than the bulk conductivity.[74,76] However, since most ferroelectrics are insulators, their intrinsic electronic carrier concentrations often do not suffice to compensate for charged domain walls.[61] Here, above band gap photoexcitation or doping can artificially stabilize charged domain walls by increasing the free carrier concentration.[75,76] Furthermore, antiparallel 180° or 90° head-to-tail domain walls can carry a weak charge if the polarization angle between the adjacent domains slightly deviates from 180° or 90°. This deviation often occurs in ferroelectric and –elastic materials to compensate elastic mismatches between domains. Due to the lower domain wall charge than head-to-head or tail-to-tail orientations, these domain walls display a higher stability.[61,77] For $MAPbI_3$ as semiconducting perovskite, the higher intrinsic carrier density promises a more effective stabilization of charged ferroelectric domain walls, if present. This stabilization by free charge carriers could not only lead to increased domain walls conductivities over the bulk, but also to a selective localization of carriers. A selective localization can lower the photocarrier recombination, which is advantageous for photovoltaic applications.[62]

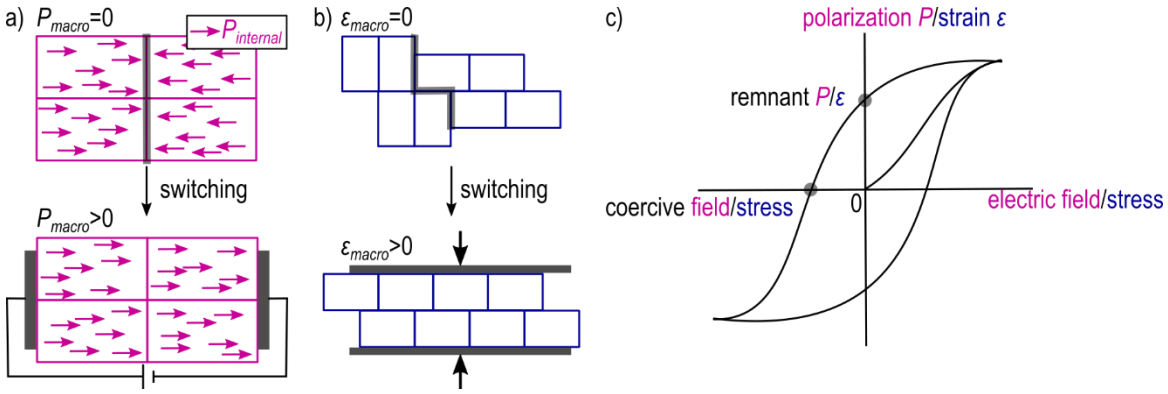

Figure 1.9: a) Simplified schematic of ferro*electric* domains before and after switching with an electric field, resulting in a net macroscopic electrical polarization P_{macro}. A 180° positively charged head-to-head domain wall is shown in grey. b) Simplified schematic of ferro*elastic* domains before and after switching with a mechanical stress (bold black arrows), resulting in a net macroscopic strain ε_{macro}. Domain wall is shown in grey. In real sample systems, domain walls likely exhibit structural imperfections. c) Ferroelectric and -elastic hysteresis loop, showing the material's electrical polarization P and strain ε during the application of an electric field or mechanical stress. The remnant polarization/strain and coercive field/stress are marked by the grey circles.

For purely ferroelastic domain walls as expected for the $I4/mcm$ space group of $MAPbI_3$, the typical periodic lamellar arrangement of ferroelastic domains is dictated by elastic contributions to the domain wall energy.[78] Depending on the magnitude of the strain mismatch between neighboring domains given by the unit cell dimensions, ferroelastic domain walls can exhibit a complex internal structure with significant deviations from the bulk structure. These structural inhomogeneities manifest in local displacements of ions in the lattice introducing energy sinks and crystal defects, but can also lead to a local polarization, called flexoelectricity.[68,73,79] Furthermore, due to their irregular structure, ferroelastic domain walls can act as preferential localization for dopants in the lattice, which in turn increases the local conductivity.[79] Consequently, purely ferroelastic domain walls may be beneficial for carrier transport in solar cell absorbers.[68,80]

On the other hand, the local change of the crystalline order at ferroelectric and ferroelastic domain walls can introduce defects or energetic barriers. Hence, domain walls as subcrystalline boundaries could act as non-radiative recombination centers,[81,82] or inhibit the charge carrier transport in certain directions and introduce anisotropic charge carrier dynamics.[35]

Ferroic nature of $MAPbI_3$

Due to the symmetry relation between the cubic and tetragonal structure of $MAPbI_3$, the potential existence of ferroelectric and/or –elastic domains is investigated since 2013. Stoumpos *et al.* were first to suggest ferroelectricity in the perovskite based on the crystal structure. Moreover, they reported on crystallographic twins introduced by crystalline strain during the phase transition, based on x-ray diffraction (XRD).[51] Nevertheless, up until today, the presence of ferroelectricity remains disputed,[35,67,83–91] since only the polar *I*4*cm* space group allows for a ferroelectric polarization.[61] Structurally, ferroelectricity could originate from a displacive phase transition via the displacement of MA^+ or Pb^{2+} ions relative to the anion lattice and/or an order-disorder transition via the collective alignment of MA^+ ions, which exhibit a dipole moment of 2.3 D.[59,62,67] However, most studies argue that the dipolar MA^+ cation is too mobile within the unit cell at room temperature for a long-range collective alignment and that ionic displacements in the lattice are random, without long-range directionality.[92–96]

The first report on an experimental observation of ferroelectric domains resolved via piezoresponse force microscopy (PFM) in 2014,[97] sparked vivid discussions in the PSC and ferroelectric community. While some subsequent studies confirmed the presence of ferroelectricity by means of PFM, macroscopic switching experiments and second harmonic generation,[83,86,87,89,90,98,99] others assigned the previous observations to mechanical and electrostatic crosstalk.[85,88,91,94,96,100–103] The ambiguity of the experimental results mainly stems from $MAPbI_3$'s semiconducting nature and ionic conductivity: High leakage currents and redistribution of mobile ions can counteract on ferroelectric signals or result in false positives in ferroelectric switching experiments.[67]

On the other hand, the ferroelastic nature of tetragonal $MAPbI_3$ is widely accepted,[67,84,85,88,104–107] since symmetry relations predict ferroelasticity for the centrosymmetric *I*4/*mcm* as well as the non-centrosymmetric *I*4*cm* space group.[61,108] Indeed, in our 2016 study on textured $MAPbI_3$ films with micrometer-sized crystallites, we observed a distinct periodic structure in the material's piezoresponse (Figure 1.1Figure 1.10a and b, Chapter 3.1.1).[84] This structure is reminiscent of ferroelastic twin domains known from classic ferroelectric and -elastic perovskites like $Pb_{(1-x)}Zr_xTiO_3$ (PZT),[109] $Pb_{(1-x)}Sr_xTiO_3$ (PST)[110] or $BaTiO_3$ (BTO).[61] Subsequently, researchers resolved the same domain structure via transmission electron microscopy,[111] polarized light microscopy,[104,107] PFM[85,86,89,91,112] and different diffraction techniques.[60,105,106] The observed disappearance of the domain structure above the cubic-tetragonal phase transition temperature,[111,112] as well as the domains' mechanical switchability confirmed their ferroelastic nature.[104,105]

$MAPbI_3$'s ferroelasticity is thought to originate from change of the lattice parameters during the cubic-tetragonal phase transition.[60,67,84,86,106,111] Here, the deformation of the unit cell introduces a spontaneous strain that depends on the a/c lattice parameter ratio and can be further enhanced by

using Cl-containing precursors.[106] Literatures values for the lattice strain in tetragonal $MAPbI_3$ range between 0.15 and 1%.[64,67,81,106]

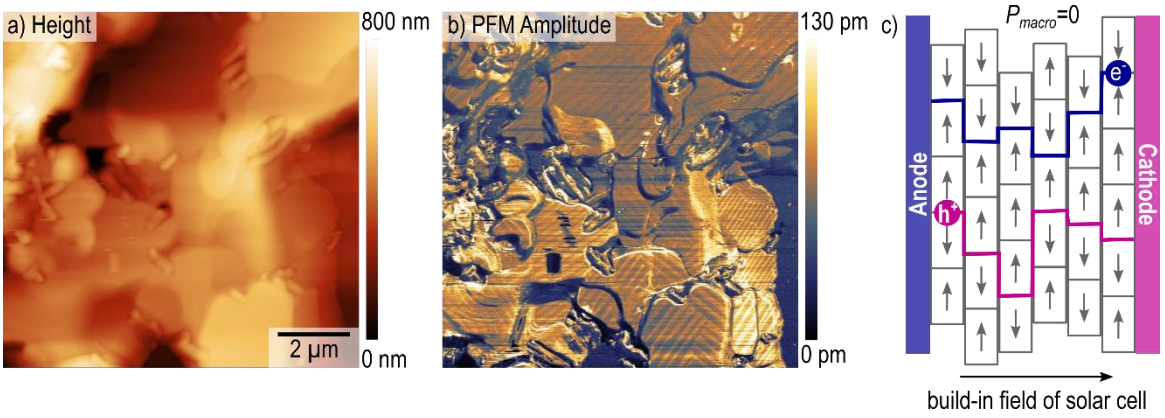

Figure 1.10: a) and b) PFM measurement on $MAPbI_3$ film with a preferential (110) crystal orientation parallel to the film surface. a) Topography signal, b) piezoresponse amplitude with distinct periodic pattern, characteristic for ferroelastic domains in tetragonal crystal systems.[84] Reprinted with permission from J. Phys. Chem. C 2016, 120, 10, 5724–5731. Copyright 2016 American Chemical Society. c) Proposed model of selective carrier pathways along ferroelectric domains walls. A random distribution of polarization orientations may lead to charged head-to-head or tail-to-tail domains walls in a macroscopically unpolarized material. In the build-in electric field of the solar cell, the carriers would be transported selectively through the absorber to their according contacts, which lowers recombination rates.[62]

Possible consequences of the material's ferroic nature on charge carrier dynamics and extraction have been proposed early on. Some studies suggested that a macroscopic ferroelectric polarization across the $MAPbI_3$ absorber is responsible for the peculiar hysteresis in the *j-V* curves of PSCs .[113–115] However, Beilsten-Edmands *et al.* showed that if present, a ferroelectric polarization of $MAPbI_3$ does not suffice to cause the observed magnitude of this anomalous *j-V* hysteresis.[92] Following their finding, the focus shifted to exploring the effect of domain walls on charge carriers. Here, multiple theory groups modeled the domain wall influence on the transport properties in macroscopically unpolarized $MAPbI_3$.[62–65,68,80,93,116–118] Frost *et al.* were first to propose that charged ferroelectric domain walls serve as carrier-specific pathways due to positive head-to-head or negative tail-to-tail polarization orientations (Figure 1.10a).[62] While Frost *et al.* only considered 180° charged ferroelectric domain walls, following publications investigated 90° charged and neutral domain walls,[63,64] disordered nanoscopic (8-100 nm) ferroelectric and antiferroelectric domains[65,93] and purely ferroelastic domain walls.[68,80] Interestingly, the studies showed that most domain wall configurations lead to a charge-specific localization of carriers at domain walls due an inhomogeneous potential landscape – even for neutral heat-to-tail ferroelectric and purely ferroelastic walls.[62–65,68,80,93,116–118] It was suggested that the attraction from "uncharged" ferroelectric domain walls on charge carriers originates from small deviations of the polarization angle between adjacent domains.[63,64] For purely ferroelastic domain walls, the charge localization at domain walls stems from a strain-induced electrical polarization at the position of the domain walls, called flexoelectric effect (Chapter 3.2.2).[68] Ultimately, the selective localization of charges entails lower recombination rates and increased diffusion lengths, thereby directly affecting the device performance.[62–65,68,80,93,116–118] Moreover, the switchablity of ferroic domains upon external stimuli opens the door for domain engineering to facilitate optimized charge extraction (Chapter 3.1.3.2).

1.3.1.2 Ion dynamics

$MAPbI_3$'s structural flexibility expands from switchable ferroic properties to highly mobile ions that can freely rearrange due to the material's mixed ionic and electronic conductivity.[119–121] As mentioned in the previous chapter, polar center-ion MA^+, positioned in the cuboctahedral gap in the inorganic Pb-I lattice, displays a high rotational degree of freedom. Literature values of the activation energies for the MA^+ rotation at room temperature range between 10 – 40 meV,[59,122,123] and researchers reported on reorientations on the time scale of picoseconds.[59,95,121,122,124] The high degree of rotational freedom of the polar MA^+ molecule prevents its contribution to a possible ferroelectric polarization in the $MAPbI_3$ crystal lattice.[92–96] However, the orientational disorder of MA^+ is thought to influence the extent of ion migration in the material by facilitating the accommodation of mobile ionic interstitials in the cuboctahedral of the lattice.[125] Moreover, the molecules dipole of 2.3 D[59,62,67] could stabilize mobile ions or ion vacancies via electrostatic screening.[126]

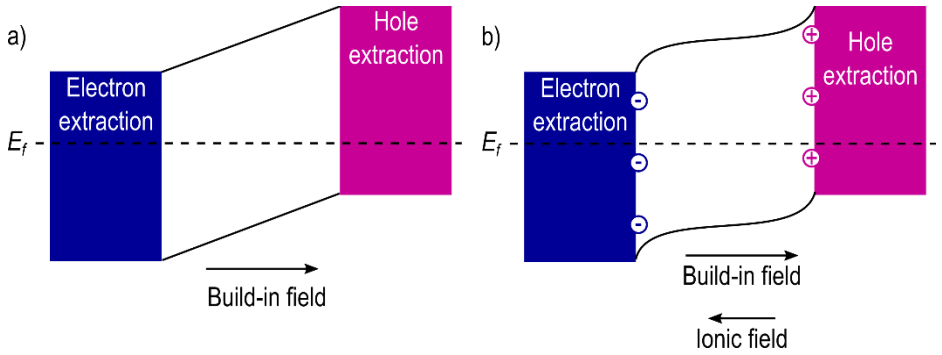

Figure 1.11: a) Schematic potential distribution across *pin*-junction in the absence of mobile ions, with electron extraction via *n*-doped ETL and hole extraction via p-doped HTL in the build-in field due to the constant electric field. b) Schematic potential distribution across *pin*-junction in presence of mobile ions/ion vacancies: Ions or ion vacancies accumulate at the interfaces to the extraction layers and counteract the build-in field.[127,128]

The presence of mobile ions in $MAPbI_3$ has significant consequences for charge carrier dynamics and the performance of PSCs. Most importantly, the redistribution of ions and ion vacancies in the build-in field of the solar cell counteracts the internal field and therefore lowers the carrier extraction (Figure 1.11). Since this ionic field depends in the biased state of the device, it contributes to the anomalous hysteresis observed in the *j-V* characteristics of PSCs:[121,124,129–133] In short circuit conditions, ions and/or ion vacancies form space charge layers at the interfaces to the extraction layers and impede the carrier extraction. In open voltage conditions, the ionic field dissipates via diffusion.[132] Due to this dissipation of the ionic field, the reverse bias sweep in the *j-V* curve, from open circuit to short circuit, yields a higher photocurrent than the forward sweep – the hallmark of *j-V* hysteresis in PSCs.[113]

Aside from hysteresis, the high ion mobility of ions in $MAPbI_3$ and related absorber materials can increase non-radiative recombination[134] and lower the overall device stability. Several studies suggested the degradation of contact layers due to the infiltration of halide ions, including our 2018 study in Chapter 5.1. For example, Ag-electrodes have been shown to react with iodide to AgI, which reduces the charge collection.[135] Additionally, researchers observed a diffusion of mobile iodide or MA^+ ions into the *p*-doped organic hole transport material SpiroOMeTAD. Here, a redox reaction

between iodide and SpiroOMeTAD reduces the materials conductivity and therefore, impedes the hole extraction from the absorber (Chapter 5.1).[136–138] Moreover, ion migration can cause destabilization and degradation of perovskite absorber itself by decreasing the crystallinity or via phase separation in perovskites that use a mixture of different halides anions.[139]

Migrating species in $MAPbI_3$ are likely iodide ions and/or their vacancies with activation energies in the range of 0.1 and 0.6 eV and fast dynamics in the microsecond regime.[124,130–133] Possible migration pathways are grain boundaries,[133,134,140] lattice distortions[133] or bulk transport via vacancies or interstitials.[125,131,141] While iodide and iodide vacancies are generally believed to govern ion migration phenomena, mobile MA^+ ions and vacancies have also been observed. MA^+ ions and vacancies feature higher activation energies than I^- ions and vacancies ranging between 0.4 – 1.1 eV and slower migration dynamics with time scales in the millisecond regime.[130,133,142]

Besides ion mobility, $MAPbI_3$ also displays a high versatility in its chemical composition. Particularly on the site of halide anions, bromide or chloride can readily replace the iodide or vice versa.[42] Researcher utilize halide exchange to tune optical properties, like the band gap. Here, a gradual replacement of iodide with bromide increases the band gap and shifts the absorption onset to lower wavelengths, which is required for a combination of PSCs and Si solar cells in tandems PV with a wider absorption range.[42] Moreover, the flexible ion replacement is employed for film preparation. Several studies found that the use of chloride as precursor material improves the crystallinity, crystal size and texture in polycrystalline $MAPbI_3$ films without chloride being incorporated in the final film.[143–145] Instead, chloride is thought to form a preliminary perovskite lattice with high crystallinity and preferential out-of-plane grain orientation, called texture. Subsequently, iodide replaces chloride via fast anion exchange, maintaining the quality of the chloride lattice, while MA^+ and Cl^- evaporates.[106,146] The exchange of the smaller Cl^- with the bigger I^- can also increase the density of ferroelastic domains to compensate for the internal strain caused by larger anions.[106]

1.3.1.3 Polycrystalline $MAPbI_3$

Generally, polycrystalline $MAPbI_3$ thin films form from solutions of PbI_2 or $PbCl_2$ and MAI in organic, polar solvents like dimethyl sulfoxide (DMSO) or dimethyl formamide (DMF).[147] The thin film deposition from the precursor solutions occurs either in a one-step or sequential routine via spin coating or chemical vapor deposition.[147–149] In the final thermal annealing step, elevated temperatures of up to 100 °C promote the crystallization of $MAPbI_3$ via intercalation of the organic cations in the inorganic PbI_2 lattice.[147] The environment during the annealing step affects the film quality. Annealing in the presence of solvent vapor and/or controlled humidity improves the crystallinity and grain size, but can reduce surface coverage.[150–152] In solvent annealing with DMF vapor, Shen *et al.* proposed that DFM molecules intercalate the PbI_2 lattice instead of MA^+ and prevent a fast, uncontrolled $MAPbI_3$ precipitation. The slow evaporation of DMF at 100 °C leads to a controlled substitution with MA^+ ions, which facilitates slower crystallization rates to achieve high crystallinity and large grain sizes.[153] For humidity-assisted annealing, researchers suggested that a controlled amount of moisture leads to the formation monohydrates $MAPbI_3{\cdot}H_2O$ at grain boundaries. These monohydrates lower the activation energy for grain coalescence and thus enable crystal growth.[152,154]

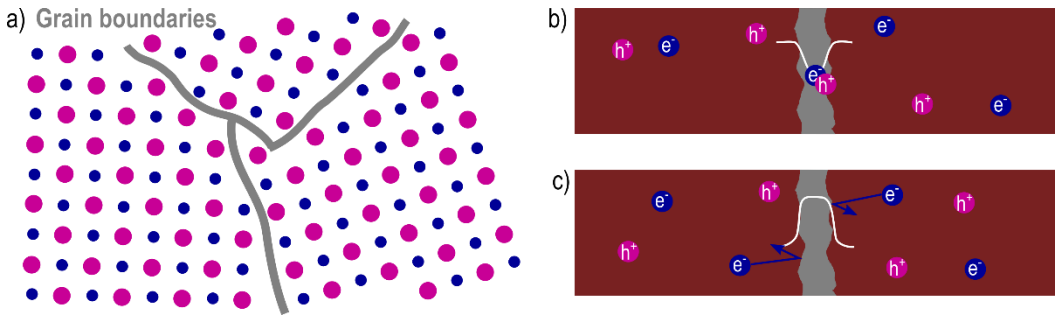

Figure 1.12: a) Grain boundaries in polycrystalline $MAPbI_3$ films introducing local lattice mismatches and dangling bonds. b) Grain boundary serving as non-radiative recombination site. c) Grain boundary inhibiting the inter-grain charge transport by acting as electrostatic potential barrier.[155]

Achieving high crystallinity, texture and large grain sizes during the $MAPbI_3$ thin film formation is desirable since these morphological features impact the optoelectronic properties of the material:[147] A high crystal quality minimizes non-radiative recombination at defect sites and facilitates a high V_{OC}; [156] Textured $MAPbI_3$ films, which is formed preferentially during chloride-assisted preparation, can enhance the charge carrier extraction,[157] likely due to a facet dependence of the photocurrent;[158] An increase of crystal size in polycrystalline $MAPbI_3$ films consequently reduces the density of grain boundaries. Grain boundaries are presumably obstructive for the device performance.[147] As internal interfaces within the absorber layer, they host a variety of crystal defects, including dangling bonds, lattice dislocations, uncompensated charges and impurities (Figure 1.12a). Due to the crystalline disorder, researchers suggested grain boundaries to act as sites of increased non-radiative recombination (Figure 1.12b),[159] pathways for migrating ions[133] or electrostatic barriers for photocarriers (Figure 1.12 c, Chapter 4).[34,160]

1.3.2 $MAPbI_3$ as solar cell light absorber

1.3.2.1 Optical properties

Among others, the success of PSCs is attributed to their optical properties including a high absorption coefficient around 10^4 cm^{-1}, which is in the magnitude of GaAs – an established photovoltaic.[44] A 280 nm thick $MAPbI_3$ film already suffices to absorb 80% of incident light.[95] With a band gap of 1.5 – 1.6 eV,[95] $MAPbI_3$ approaches the optimal light-absorber predicted by Shockley[26] and Queisser.[24] This band gap corresponds to an absorption onset around 800 nm. Hence, $MAPbI_3$'s absorption range covers the full visible light spectrum (Chapter 1.4.2.3, Figure 1.25b) and features a sharp onset with an Urbach tail as low as 15 meV, which indicates a high degree of order.[44,161] During absorption, photons excite electrons from the valence band that consists of antibonding states between 5p iodide orbitals and 6s lead orbitals into the conduction band, which is formed from antibonding states between the 5p iodide orbitals and the 6p lead orbitals.[162] With iodide contributing to the band edge states, a partial anion exchange with Cl^- or Br^- directly tunes band gap and absorption range, as does a replacement of lead.[42] Since the organic cation is not associated with band edge states, it has no direct influence on the band gap. However, the organic cation can modify the band gap indirectly by changing the lead-halide bond angles.[51,162,163] For example, exchanging MA^+ with formamidinium (FA^+) lowers the band gap by 0.07 to 0.09 eV and leads to an increase in the absorption range by 40 – 50 nm.[42]

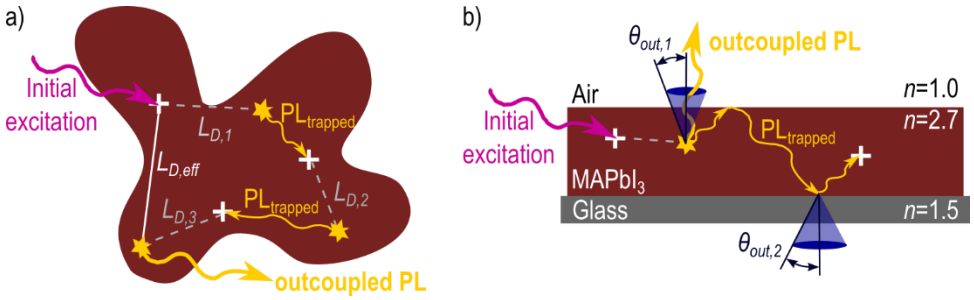

Figure 1.13: a) Photon recycling in $MAPbI_3$ grain: Upon the initial excitation with an absorption event marked by the white cross, the photocarriers diffuse over a diffusion length $L_{D,1}$ until they radiatively recombine at the position of the yellow star. The emitted photon becomes trapped in the grain and travels a certain distance before being reabsorbed at a new absorption site, and so on. After several emission and reabsorption events the PL photon is outcoupled. The diffusion lengths $L_{D,I}$ and the travelled distance of the trapped PL photons contribute to the efficient diffusion lengths $L_{D,eff}$.[164] b) Trapped PL in a $MAPbI_3$ film caused by a mismatch of the refractive indices n of the ambient environment, $MAPbI_3$, and the exemplary glass substrate. The large mismatches lead to narrow escape cones with an angle $\theta_{out,i}(n)$. All PL outside the escape cone is reflected internally at the interface to substrate or the surface and can be reabsorbed.[38]

$MAPbI_3$'s emission spectrum shows a maximum at ~765 nm with a relatively broad distribution, which is caused by interactions of photocarriers with phonons. The broad PL spectrum combined with the sharp absorption onset create ideal conditions for photon recycling (Chapter 1.2.3.3).[37] In photon recycling, PL emitted during radiative recombination remains in the material and is reabsorbed to generate new photocarriers. The path travelled by the trapped PL and the photocarrier diffusion of all recycling events increases the diffusion length to an effective value $L_{D,eff}$, which improves the charge carrier extraction by facilitating larger transport distances (Figure 1.13a).[37,164] Furthermore, Kirchartz *et al.* found that the increase in photocarrier concentration due to photon recycling benefits the open circuit voltage with a rise of 50 – 80 mV depending on the degree of light outcoupling.[165] Light outcoupling from the $MAPbI_3$ layer mainly depends on the difference of the refractive indices n between the environment or top layer, $MAPbI_3$ and the substrate or back contact. With a refractive index of 2.7 for $MAPbI_3$,[166] the escape cone at the air interface has an angle $\theta_{out,1}$ of 22°. All photons with incident angle above 22° will be reflected at the interface and therefore, remain confined in the absorber layer (Figure 1.13b).[167] For the $MAPbI_3$ / glass interface, the critical angle of the escape cone $\theta_{out,2}$ is 35°.[168] The total outcoupling probability of photons in $MAPbI_3$ is given as 8 – 30%,[38,167–169] depending on the contribution of light scattering.[168] Hence, to minimize the light outcoupling and thereby increase the reabsorption probability, optical scattering centers, for example at grain boundaries, should be avoided (Chapter 4.2).

1.3.2.2 Dynamics of photogenerated carriers

Mobility

The charge carrier mobility μ_i in semiconducting absorber determines the drift current of a solar cell (Equation 1.12) and therefore aids to evaluate the suitability of absorber materials. For $MAPbI_3$, electron and hole mobilities are in the same order of magnitude and thus facilitate an ambipolar charge transport.[170] Literature values for the mobilities range between 0.4 and 71 cm^2/Vs in thin films and 2.5 and 160 cm^2/Vs in single crystals.[46] While these values appear large in comparison with organic PV materials (0.1 – 15 cm^2/Vs), they are substantially smaller than in established inorganic PV materials. For example, GaAs displays electron mobilities in the range of 5000 cm^2/Vs

and hole mobilities of 300 cm²/Vs,[8] and Si exhibits charge carrier mobilities of 1500 cm²/Vs for electrons and 500 cm²/Vs for holes.[171] Limitations to the carrier mobility in $MAPbI_3$ appear to arise from phonon interactions, which effectively scatter charge carriers and thereby reduce their mobility.[46,171] However, $MAPbI_3$'s long diffusion lengths and recombination lifetimes compensate for low mobilities to allow for efficient charge transport throughout the absorber layer.[46]

Besides inevitable lattice interactions, morphological boundary structures in $MAPbI_3$ thin films and PSCs could impact the carrier mobility. Among those, Warwick *et al.* suggested that ferroelastic domain walls increase the carrier mobility by introducing a local intrinsic carrier drift due to flexoelectricity, which can introduce localized in-plane polarization at domain walls.[68] In our 2020 study in Chapter 3.2.2, we indeed observed indication of a domain wall polarization. On the other hand, grain boundaries likely lower the carrier mobility by acting as scattering centers and/or electrostatic barriers. An improvement in the crystallinity and increase in the grain size can mitigate the detrimental impact of grain boundaries by reducing the amount of scattering centers/electrostatic barriers.[172,173] In Chapter 4.1.1, we investigated the influence of grain boundaries on the lateral conductivity. We found that single grain boundaries introduce significant resistances in the giga-ohm regime and thus act as substantial barriers for the charge carrier drift. Finally, the charge carrier extraction across ETL and HTL likely reduces the carrier mobility compared to the absorber layer: Grill *et al.* observed a mobility decrease by three orders of magnitude after charge carriers pass through the extraction layers. Particularly, the HTL appears to limit the carrier mobility.[174] This finding is in agreement with our 2018 study in Chapter 5.1, where a seemingly reduced conductivity of the HTL impeded the hole extraction and lead to a positive charging of the absorber layer.

Diffusion

In the absence of an electric field, the charge dynamics in the absorber layer are characterized by the diffusion constant D and the diffusion length L_D, which describe the charge carrier motion in a concentration gradient (Chapter 1.2.3.2). A common technique to measure D and L_D is PL microscopy (Chapter 1.4.2.2). Here, it is important to consider that the carrier diffusion lengths detected in PL microscopy can be overestimated due to photon recycling as depicted in Figure 1.13a. For $MAPbI_3$, especially after chloride-assisted crystallization, several groups reported diffusion lengths in the range of several micrometers.[45,175] These extensive diffusion lengths likely originate from the low trap density in bulk $MAPbI_3$.[176] Literature values for diffusion constants in $MAPbI_3$ range between 0.8 and 3.3 cm²/s.[34,177,178]

Like the mobility, the charge carrier diffusion can be altered by boundary structures on different lengths scales in polycrystalline $MAPbI_3$. For example, we observed that ferroelastic twin domains walls introduce an anisotropy in diffusion constants: The diffusion constant measured parallel to the domain walls was $D_{\parallel} = 1.9 \pm 0.1$ cm²/s and the diffusion constant perpendicular to the domain walls gave $D_{\perp} = 1.2 \pm 0.1$ cm²/s (Chapter 3.2.2). Moreover, the charge carrier diffusion reacts particularly sensitive to the presence of grain boundaries: Several studies observed that grain boundaries act as barriers for diffusive charge carriers and thereby limit the inter-grain carrier diffusion.[34,173,180–184] Among these reports, Ciesielski *et al.* and DeQuilettes *et al.* found that some grain boundaries can block the inter-grain carrier diffusion entirely.[34,160] The latter suggested that

a facet dependence determines the transparency of grain boundaries.[160] In Chapter 4.1.2, we investigated the inter-grain carrier diffusion to find that the given grain boundary morphology appeared to determine the grain boundary transparency for photocarriers.

Recombination

The governing recombination mechanism in $MAPbI_3$ under AM1.5 illumination, which corresponds to a charge carrier density of 10^{15} – 10^{16} cm^{-3}, is trap-mediated monomolecular recombination (Chapter 1.2.3.3).[32] Since a majority of the defects in PSCs are relatively shallow trap states that charge carriers can readily escape, recombination lifetimes reach up to several microseconds.[184] The distribution of traps across the $MAPbI_3$ layer is not homogeneous. Instead, traps appear to accumulate at the position of grain boundaries,[185] but more importantly at the heterointerfaces to the charge transport layers (Chapter 5.1).[182,184,186] This interfacial nonradiative recombination mainly contributes to losses in the open circuit voltage in PSCs.[186] In bulk grains, strain and local crystal misorientations also lead to an increase recombination losses,[81,82] whereas ferroelastic twin domains seem to be benign for nonradiative recombination (Chapter 3.2.2).[107]

1.3.2.3 Architecture of perovskite solar cells

PSCs are constructed in a *pin*-architecture, with $MAPbI_3$ as intrinsic semiconductor absorber positioned between a HTL and a ETL, connected to a metal electrode via the HTL and a transparent oxide electrode via the ETL.[187–189] Here, the alignment of the band edges of absorber and transport layer is crucial to facilitate a high charge selectivity. A selective hole extraction requires a small positive offset $\Delta E_{V,HTL}$ from the valance band edge of the absorber to the HTL and a large positive offset in the conduction band $\Delta E_{C,HTL}$. The large offset in the conduction band effectively blocks electrons. For the selective electron extraction, the conduction band edge of the absorber is slightly higher than in the ETL $\Delta E_{C,ETL}$, while the valance band features a large negative offset to prevent hole extraction $\Delta E_{V,ETL}$ (Figure 1.14a).[48,190,191] Typically, PSCs employ either metal oxides, particularly TiO_2, as ETL and the organic compound SpiroMeTAD as HTL.[48] However, TiO_2 has been linked to a higher concentration of mobile ions in the $MAPbI_3$ active layer as well as interfacial trap states and low conductivity.[190,192–196] These mobile ions are one of the main origins in the *j-V* hysteresis in PSCs (Figure 1.14b).[121,124,129–133] Furthermore, iodide ions are thought to lower the conductivity of the HTL SpiroMeOTAD: The p-doped material could react irreversibly with iodide, which would lower the materials hole conductivity and impedes the overall charge carrier extraction (Chapter 5.1).[137,141,197] Studies have shown that fullerene-based ETLs decrease the magnitude of hysteresis, likely by reducing defect sites that could contribute to the formation of free ion-vacancy pairs (Chapter 5.1).[192–194,198]

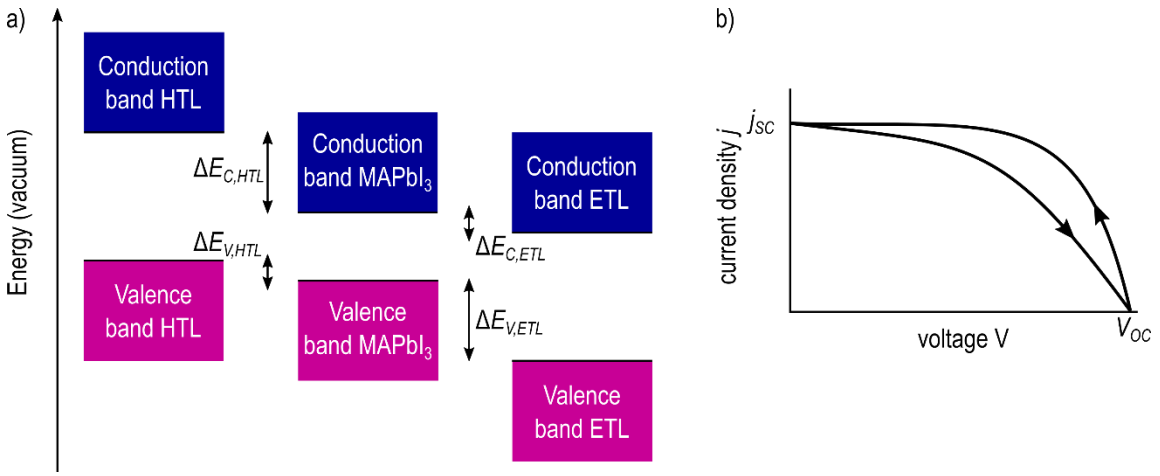

Figure 1.14: a) Band alignment between extraction layers and $MAPbI_3$ absorber with suitable band offsets ΔE between HTL, absorber and ETL to allow high selectivity in the charge extraction. b) Schematic of *j-V* hysteresis in PSC, with reduced *FF* in the forward bias scan and increased *FF* in the reverse bias scan.

1.4 Characterization methods

1.4.1 Atomic force microscopy

To investigate structural influences on optoelectronic properties of solar cell absorbers, the local sample morphology needs to be correlated to the electrical behavior in real space. Atomic force microscopy (AFM) can access a range of electromechanical and electrical surface properties with a nanometer resolution and link them to the simultaneously recorded sample topography.[188–193] With their invention of scanning tunneling microscopy (STM) in 1982, Binnig and Rohrer paved the way to a new class of microscopy methods: Scanning probe microscopy (SPM).[194] Based on the Nobel Prize winning STM, Binnig, Quate and Gerber developed AFM in 1986, which allows characterization of conductive and nonconductive samples alike.[195]

In AFM, an atomically sharp tip attached to a cantilever scans a sample surface and interacts with the surface via short- and long-range forces. These tip-sample forces cause a deformation of the cantilever, which acts as a spring-like force-sensor. Forces perpendicular to the surface induce a vertical deflection Δz that follows Hooke's law:

$$\Delta z = \frac{F}{k}$$

Equation 1.22: Hooke's law.

with the tip-sample interaction force F and the spring constant of the cantilever k.[193,196] Most commonly, an optical beam deflection method detects the force-induced cantilever motion.[197] Here, a laser beam focused on the reflective backside coating of the cantilever is reflected onto a four-quadrant photodiode. By comparing the intensity I_i of the reflected laser beam detected by each quadrant, the AFM records the cantilever motion as the tip scans the surface and thus the surface topography.[193]

1.4.1.1 Tip-sample forces

The forces that contribute to the tip-sample interaction exhibit different distance dependences ranging between the single-digit Angstrom-scale and several hundreds of nanometers.[198] Short-range repulsive forces arise at distances below one nanometer when the atomic orbitals of tip and sample interact. Due to the quantum mechanical Pauli principle, which forbids two electrons to occupy the same state, the overlap of orbitals leads to a strong repulsion.[18,193] The Pauli repulsion is not a force in the traditional sense, but rather a direct consequence of the anti-symmetry requirement of electrons as stated by Pauli.[199]

At distances above one nanometer, tip-sample forces are dominated by attractive van der Waals forces, which originate from ever-present dipole-dipole interactions, and electrostatic forces for charged or conductive tip-sample systems. In van der Waals forces, especially the London dispersion contributes to the attraction between tip and sample. The dispersion force stems from a fluctuation of the electron density around the atomic core, which causes transient dipoles in a non-polar molecule. These transient dipoles can induce dipoles in adjacent molecules and the consequent attractive interaction between the two dipoles lowers the potential energy of the system.[18,193,200]

Electrostatic forces arise for interactions between charged dielectric tips and samples, conductive tips and dielectric samples and vice versa, as well as for the interaction between conductive tips and samples with different potentials. Localized charges in dielectric tips and samples, which can originate from sample cleaving, ion sputtering or previous electrification, lead to coulomb forces. Likewise, if either the tip or the sample is conductive, electrostatic coulomb interactions are caused by the presence of localized charges in the dielectric component or stem from an induced polarization of the insulator by the conductor. Electrostatic interactions between two conductive or semiconducting materials originate from their different surface potential due to an external electric field or different work functions Φ_i.[193] Electrical AFM methods, such as electrostatic force microscopy (EFM) or Kelvin probe force microscopy (KPFM, Chapter 1.4.1.6), utilize these electrostatic interaction forces between tip and sample to image localized charging or the surface potential, respectively.[201] Ultimately, the governing tip-sample interaction depends on the AFM operational mode.

1.4.1.2 Contact mode AFM

During contact mode AFM, the tip scans the sample surface in direct contact. Here, the Pauli repulsion dominates the tip-sample interactions, introducing an upward bending of the cantilever, which is called deflection. Via the spring constant of the cantilever k, the deflection is directly proportional to the normal tip-sample force (Equation 1.22). While the cantilever-tip system scans the sample surface, the four-quadrant photodiode detects the deflection at each pixel and feeds the signal into a PI-feedback system. The feedback compares the cantilever deflection to a preset value, which is called setpoint, and multiplies the deviation or error signal with a proportional (P) and an integral (I) gain. The PI-feedback controller uses the error multiplied by the gains to readjust the tip-sample distance via a piezo-scanner to maintain a constant deflection and constant force. Common piezo-scanners used in AFM allow for accurate tip positioning in z on the picometer scale. From the output signal of the feedback control, a topographic and a deflection image are generated

(Figure 1.15a). The deflection image corresponds to the error signal of the PI-feedback. In ideal AFM scans, this image would feature a minimal contrast. However, in real measurements, where the feedback can react too slow or overdrive, the deflection channel often shows fine surface structures with high sensitivity.[193]

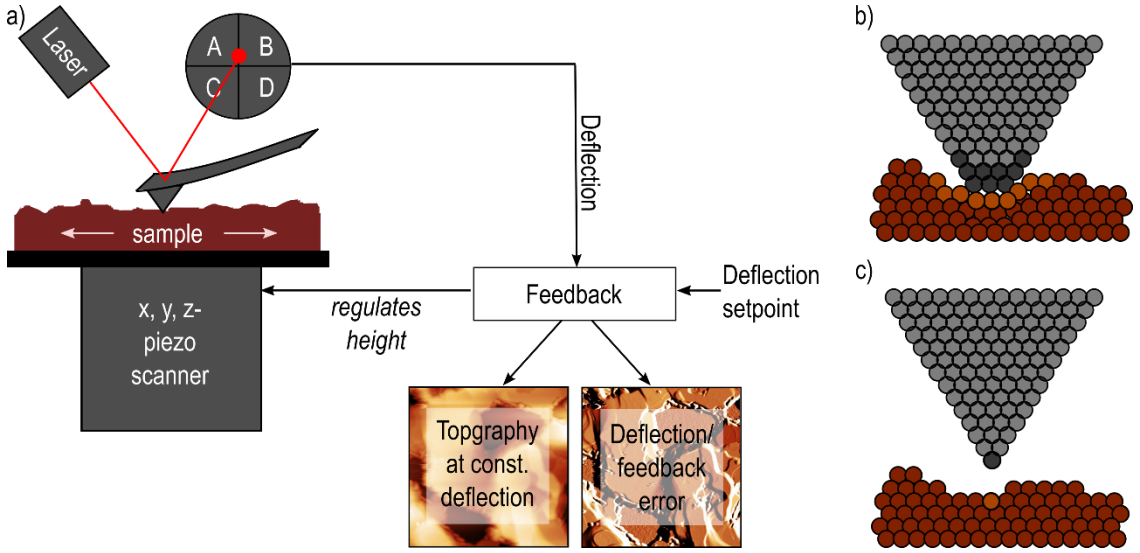

Figure 1.15: a) Scheme of contact mode AFM setup. A tip on a cantilever as force sensor scans the sample surface in x and y, while the cantilever's z-displacement, the deflection, which is caused by surface topography, is detected via optical beam deflection: A laser beam is focused on the cantilever backside and reflected onto a four-quadrant photodiode in an angle depends on the cantilever deflection. The displacement of the reflection is fed to a feedback control that compares the measured deflection to the predefined deflection setpoint and adjusts the tip-sample distance via the z-scanner height accordingly to facilitate a constant tip-sample force. The topography and feedback error channels give information on the surface structure. b) In contact mode AFM the blunt tip indents softer samples and several tip atoms interact with several sample atoms. Interacting tip and sample atoms are highlighted by darker and brighter colors, respectively. c) The ideal tip-sample interaction is limited to the outermost tip atom and only one sample atom.

Since contact mode AFM operates in the repulsive force regime, damage to the tip apex and sample surface is common. Particularly structures of soft samples are prone to alteration during contact mode AFM, where local forces of more than 100 nN can be reached (Chapter 3.1.3.2). At an assumed tip-sample contact radius of 10 nm, a force of 100 nN translates to a pressure of ~300 MPa. Moreover, due to their close proximity several tip atoms interact with several surface atoms during contact mode AFM, which limits the lateral resolution to the dimensions of the blunt tip apex in the range of tens of nanometers (Figure 1.15b).[193,196] In ideal AFM measurements, on the other hand, only the outermost tip atom interacts with the sample to facilitate atomic resolution (Figure 1.15c).[202]

Despite its drawbacks in spatial resolution, contact mode AFM is the foundation of several functional AFM techniques, including piezoresponse force microscopy (PFM) and conductive AFM (CAFM), described in Chapters 1.4.1.4 and 1.4.1.5, respectively. Both modes require physical contact between tip and sample. In PFM, the contact mode facilitates the measurement of the sample's oscillating piezoresponse, with minimized electrostatic crosstalk;[190] In CAFM, the physical tip-sample contact allows mapping the sample's conductivity via the local current flow between tip and sample at applied bias.[191]

1.4.1.3 Amplitude modulation or tapping mode AFM

To overcome the limited resolution and destructive tip-sample interaction in contact mode AFM, dynamic AFM modes operate with intermittent or no contact. Here, the cantilever oscillates above the sample. At the lower turning point of the oscillation, the tip either shortly touches the surface or remains in close proximity to the surface to prevent an alteration of tip or sample. With the tip-sample interaction limited to the lower turning point of the cantilever's sinusoidal motion, dynamic AFM mainly operates in attractive van der Waals force regime, which allows for high-resolution imaging up to atomic resolution. The resonance frequency ω_0, the oscillation amplitude A and the phase shift between excitation and cantilever response φ sensitively react to changes in the force environment and can therefore be used as imaging parameters. [193,196,200]

In amplitude modulation AFM (AM-AFM), which is also called tapping mode, the measurement is conducted with a constant amplitude in the single to double digit nanometer range at a fixed frequency ω at or close to the cantilever's resonance ω_0. A signal generator feeds an AC voltage at the chosen drive frequency $U(\omega)$ to a piezo-actuator connected to the cantilever. The AC voltage induces an oscillation of the piezo-actuator, which excites the cantilever at the same frequency while it scans across the sample. The photodiode detects the oscillating signal as the tip interacts with the surface and passes the signal to a lock-in amplifier (LIA).[193,200] Generally, an LIA allows the detection of particularly small oscillation amplitudes in noisy environments by enhancing the signal with a reference at the same frequency and integrating over several oscillation periods.[203] During AM-AFM, the LIA measures the oscillation amplitude A and phase φ at the drive frequency of the AC voltage ω. Like in contact mode AFM, the PI-feedback compares the oscillation amplitude of the cantilever to a setpoint amplitude and regulates the tip-sample distance via the z-piezo-scanner to maintain a constant amplitude. Images of the topography at constant amplitude, the amplitude as error signal of the feedback and the phase are generated from the feedback output. The phase contrast can give information on variations in the material properties, such as composition, friction, viscoelasticity and adhesion (Figure 1.16a).[193,200]

The cantilever motion in the presence of tip-sample forces $F_{ts}(z)$ follows the laws of a driven harmonic oscillator with damping:

$$m\frac{d^2z}{dt^2} = k[z + A_0\cos(\omega t + \varphi)] - \frac{m\omega_0}{Q}\frac{dz}{dt} + F_{ts}(z)$$

Equation 1.23: Driven and damped harmonic oscillator with tip-sample interaction.[193]

With the cantilever mass m, displacement z, spring constant k, the driving amplitude A_0 at frequency ω with phase φ, resonance frequency ω_0 and quality factor Q, which serves as measure for the damping. In AM-AFM, where the feedback maintains a constant amplitude, we can assume that the drive compensates for the damping term, which leads to a simplified equation of motion:

$$m\frac{d^2z}{dt^2} = kz + F_{ts}(z)$$

Equation 1.24: Cantilever motion in AM-AFM.[193]

Assuming small oscillation amplitudes, the linear expansion of the force results yields a frequency shift $\Delta\omega$ proportional to the force gradient:

$$\Delta\omega \propto \frac{dF_{ts}(z)}{dz}$$

Equation 1.25: Relation between frequency shift Δω and force gradient $dF_{ts}(z)/dz$.[193]

Hence, a change of the force gradient affects the frequency shift of the cantilever resonance, which will move to higher values if repulsive forces govern and to lower values if attractive forces dominate. At constant detection frequency ω, the frequency shift results in a change of the oscillation amplitude and phase (Figure 1.16b).[193,204]

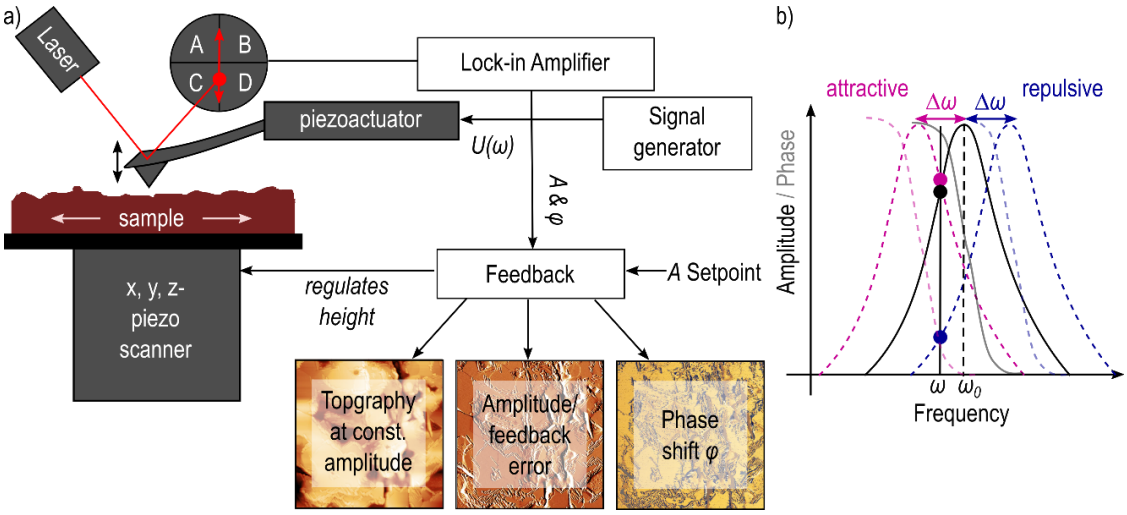

Figure 1.16: a) Scheme of AM-AFM setup: A signal generator excites the piezo-actuator connected to the cantilever with an AC voltage *U(ω)* at a frequency close to the cantilever resonance ω_0. The oscillating cantilever with the tip scans the sample surface in x and y, while the amplitude of the cantilever, changed by a shift in the resonance due to tip-sample interaction, is detected via optical beam deflection method. The amplitude is fed a Lock-in amplifier, which extracts and measures the amplitude from background noise and passes the signal to a feedback control. The feedback compares the measured amplitude to the predefined amplitude setpoint and adjusts the tip-sample distance via the z-scanner height to facilitate a constant amplitude and tip-sample force. The topography, feedback error (amplitude) and phase channels give information on the surface structure and mechanical properties. b) Attractive and repulsive tip-sample forces induce a shift of the cantilever resonance ω_0 to lower and higher values, respectively. The shift $\Delta\omega$ leads to a change of the oscillation amplitude *A* and phase φ.[200]

For the operation of AM-AFM in air, adhesion by capillary forces and long-range attractive forces often result in jump-to-contact instabilities of the cantilever. These instabilities can be overcome if the cantilever's retraction force at the lower turning point of the oscillation exceeds the adhesion. This can be achieved by the use of larger amplitudes, which may limit the resolution, or by stiffer cantilevers.[193,196,200] Furthermore, measurements in controlled humidity environments like gloveboxes with inert gases minimize the influence of capillary forces.[205]

AM-AFM is a foundation of KPFM for surface and photopotential imaging, discussed in Chapter 1.4.1.6. Here, the surface topography and KPFM potential distribution are resolved simultaneously, with topography imaging at the cantilever resonance via AM-AFM.[206]

1.4.1.4 Piezoresponse force microscopy

Piezoresponse force microscopy (PFM), a contact mode AFM technique, can access electromechanical properties of ferroelectric samples (Chapter 1.3.1.1).[190,207] The working principle of PFM is based on the inverse piezoelectric effect. Upon the application of a voltage, a piezoelectric material expands or contracts depending on the orientation of its internal polarization. In PFM, a conductive tip applies an AC voltage to a piezoelectric or ferroelectric sample, while scanning the surface at constant force. Consequently, the AC drive excites the sample to a sinusoidal mechanical oscillation, which is called piezoresponse, that is detected as periodic cantilever deflection via an LIA (Figure 1.17a). The amplitude of the sample oscillation is determined by the excitation amplitude and the piezoelectric coefficient. The piezoelectric coefficient gives the magnitude of the electromechanical coupling and links the directionality of response and excitation.[190] For example, the piezoelectric coefficient d_{33} describes the out-of-plane piezoresponse upon out-of-plane excitation, whereas the in-plane piezoresponse upon out-of-plane excitation is described by the d_{34} and d_{35}, in y and x direction, respectively.[208] Furthermore, the PFM amplitude resolves the position of domain walls as local minima: Whenever the direction of the internal polarization within the sample changes by 180°, the piezoresponse at the interface between the two opposite domains cancels out and the amplitude becomes zero. The phase lag between the AC excitation and the sample's piezoresponse depends on the local orientation of the polarization. When ferroelectric domains feature a polarization oriented perpendicular to the surface, a change their polarization orientation by 180° will show as 180° contrast change in the PFM phase (Figure 1.17b).[190]

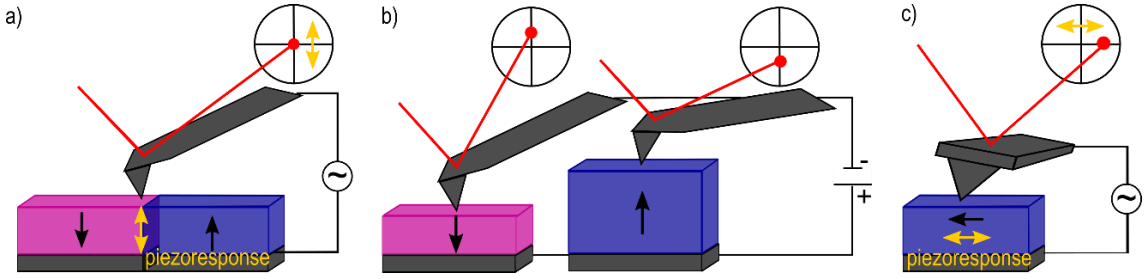

Figure 1.17: a) Scheme of working principle in PFM, where a conductive cantilever scans the surface in contact mode and applies an AC voltage. The AC voltage introduces an oscillation in piezoelectric samples, called piezoresponse, which is detected as periodic cantilever deflection. b) Depending on the direction of the electric field and the orientation of the internal polarization, the ferroelectric domains either expand or contract, leading to a 180° phase difference between oppositely oriented out-of-plane domains. c) Lateral PFM detects the in-plane piezoresponse via periodic cantilever torsion.

The polarization in ferroelectric domains can exist in varying angles with respect to the sample surface, depending on the crystal structure and symmetry groups of the material. Therefore, the vertical piezoresponse of the sample only gives partial information. PFM also operates in a lateral mode, where the in-plane piezoresponse upon the application of an our-of-plane AC field, according to the coefficients d_{34} and d_{35}, leads to an oscillating torsion of the cantilever (Figure 1.17c).[190]

Typical piezoelectric coefficients in ferroelectrics are in the range of a few tens of pm/V, resulting in extremely small piezoresponses. To increase the signal-to-noise ratio, PFM often employs at AC frequencies close to the cantilever's contact resonance $\omega_{0,\,C}$, which is around three to five times the free resonance (Figure 1.18a and b).[190] However, operation close to the contact resonance

introduces inaccuracies: Here, the PFM signals depend on the tip-sample contact mechanics. Particularly on rough samples, where the tip-sample contact area changes during the scan due to step edges, protrusions or indentations, and on mechanically inhomogeneous samples, the contact resonance can vary by several kHz. Thus, Rodriguez *et al.* introduced dual amplitude resonance tracking (DART) PFM, in which two drive frequencies $\omega_{AC,\,1}$ and $\omega_{AC,\,2}$ left and right of the contact resonance are used. An additional feedback loop continuously compares the amplitudes ratio at the two frequencies, readjusts the drive frequencies to maintain a constant ratio and thereby compensates for contact resonance shifts. Thus, DART facilitates resonance-enhanced PFM measurements with reduced topographic and mechanical crosstalk by tracking of the contact resonance (Figure 1.18c).[209] Besides topographic and mechanical crosstalk, PFM is prone to electrostatic background interactions F_{el}. Since PFM applies AC voltages up to several volts to the cantilever, substantial electrostatic interactions between the cantilever beam and the sample can occur. The cantilever oscillation caused by electrostatics superimposes on the oscillating deflection originating from the sample's piezoresponse. To exclude the contribution of the electrostatics on the PFM response, Collins *et al.* have introduced a laser Doppler vibrometer as interferometric displacement sensor for PFM. The interferometric displacement sensor allows positioning the AFM laser directly at the tip position, which reduces the influence of background electrostatics (Figure 1.18d).[210]

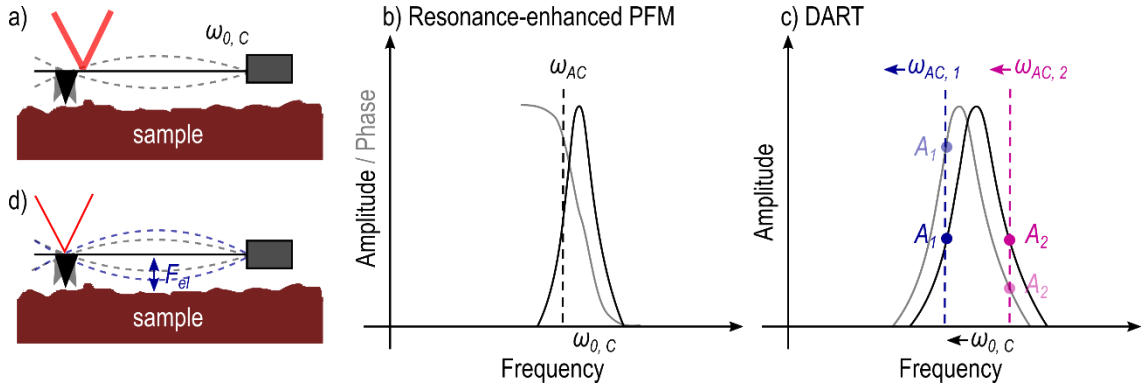

Figure 1.18: a) Schematic of contact resonance $\omega_{0,\,C}$ as grey dashed lines, forming a standing wave motion. b) Contact resonance in frequency spectrum with PFM AC excitation close to the contact resonance $\omega_{0,\,C}$ at ω_{AC}. Detection at the same frequency leads to enhanced signal-to-noise ratio. c) DART working principle using two excitation and detection frequencies $\omega_{AC,1}$ and $\omega_{AC,\,2}$ left and right of the contact resonance. An additional feedback compares the amplitude ratio at both frequencies A_1/A_2 and adjusts the drive frequencies to maintain a constant ratio, thereby compensating for shifts in the contact resonance $\omega_{0,\,C}$.[209] d) Accurate positioning of the interferometric displacement sensor above the tip reduces the influence of electrostatic crosstalk F_{el} on the PFM data.[210]

In addition to ferroelectric domain imaging, PFM can measure local ferroelectric hysteresis loops by ramping a DC sample bias while measuring the sample's piezoresponse. Plotting the PFM phase versus the voltage reveals the coercive voltage required to switch the polarization orientation in the material. Moreover, AFM allows manipulating ferroelectric patterns by permanently switching the polarization direction with the domains. Therefore, a constant DC bias is applied to the sample during a contact mode scan. A subsequent PFM measurement will show a change in the phase contrast, if a DC bias above the coercive voltage was used in the previous step.[190,207]

1.4.1.5 Conductive atomic force microscopy

In conductive atomic force microscopy (CAFM), a conductive tip scans the sample surface in contact mode while applying a DC bias. The conductive tip is connected to a current amplifier, which measures the electric current that flows between tip and conductive areas of the sample. Thereby, CAFM maps local conductivity variations on electrically inhomogeneous, such as composites or polycrystalline thin films. Since the height feedback maintains a constant tip-sample force, CAFM images current distribution and topography of the sample simultaneously. [188,191,192] On photoactive materials, such as solar cell light absorber, CAFM can measure the photoconductive behavior of the sample by resolving the currents distribution upon illumination. For photoconductive measurements, the wavelengths of the AFM laser should lie outside of the material's absorption regime.[211]

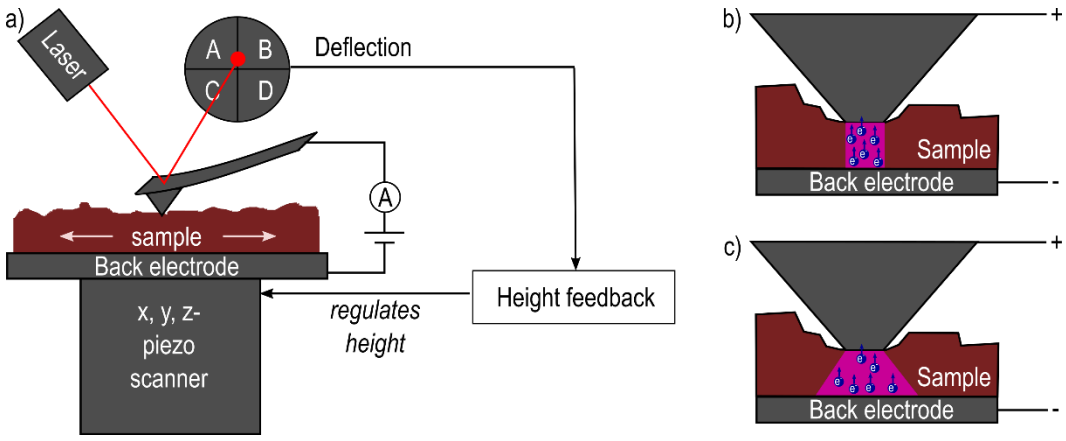

Figure 1.19: a) Schematic working principle of CAFM. A conductive tip scans the surface in contact mode with an active height feedback to maintain a constant force. Simultaneously a DC voltage is applied between tip and sample or back electrode and a voltage amplifier measures the local current flow. b) Underestimated mechanical tip-sample contact area during CAFM. c) Actual probed area during CAFM, caused by current spreading.[213]

When interpreting CAFM data, it is important to consider possible sources of error during the measurement. First, the contact mode scan may alter the conductive tip coating. As described in Chapter 1.4.1.2, contact mode AFM can cause damage to the sample as well as the tip. If the coating of the tip wears off due to a high contact and shear force or the tip is contaminated, the contrast in the conductivity image will change.[212] Here, the repeated measurements with different scan angle can verify the reliability of the data. Second, the thin surface water layer, present in ambient conditions, can reduce the current sensitivity, particularly for soft cantilevers. For low spring constants, the contact force does not suffice to penetrate through the water layer and establish and electrical tip-sample contact. Vacuum or a humidity-controlled environment, like gloveboxes with inert gases, mitigate the influence of surface water on the CAFM results.[212] Third, for quantitative analysis of CAFM data, current spreading should be taken into account. The mechanical tip-sample contact area underestimates the actual probed sample area by up to three orders of magnitude.[213] The electrical conductivity σ_{el} is inversely proportional to the area A via:

$$\sigma_{el} = \frac{I}{A \cdot E_{el}}$$

Equation 1.26: Electrical conductivity σ_{el} in depedence of area A.

with current I and electric field strength E_{el}.[19] Therefore, the underestimation of the probed area implies a vast overestimation of the sample conductivity.[213] Considering these points, a reliable quantitative analysis of CAFM data is difficult.

1.4.1.6 Kelvin probe force microscopy

Electrostatic interactions between tip and sample arise from the difference in their material-specific work functions Φ_{tip} and Φ_{sample}.[188] Kelvin probe force microscopy (KPFM), first introduced in 1991,[214] uses this electrostatic interaction for material characterization by measuring the local contact potential difference V_{CPD} between tip and sample:

$$V_{CPD} = \frac{\phi_{tip} - \phi_{sample}}{-e}$$

Equation 1.27: Contact potential difference V_{CPD} from work function difference between tip Φ_{tip} and sample Φ_{sample}.

A conductive tip and a conductive or semiconductive sample from different materials will feature a difference in their Fermi levels due to their work functions (Figure 1.20a). As tip and sample are electrically connected, electrons flow from the material with the lower work function to the other until the two Fermi levels align, according to the equilibrium requirement. Once the equilibrium state is reached, the misalignment of the vacuum levels E_v introduces a charging of tip and sample and leading to the formation of a contact potential difference V_{CPD} and a corresponding electrostatic force (Figure 1.20b). By applying a bias V_{DC} that nullifies the electrostatic tip-sample force, the V_{CPD} can be determined from the magnitude of V_{DC} (Figure 1.20c). In KPFM, an additional feedback control adjusts the V_{DC} to compensate the electrostatic force at each pixel of the scan, thereby resolving the V_{CPD} distribution. For a known tip work function, the V_{CPD} gives the work function of the sample.[189]

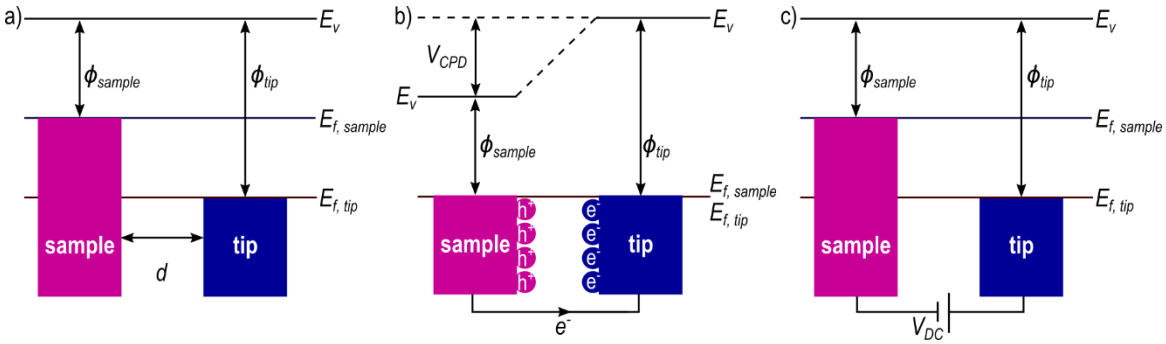

Figure 1.20: a) The Fermi levels of tip $E_{f,tip}$ and sample $E_{f,sample}$ are not aligned without electrical contact. b) Alignment of Fermi levels and charging up of tip and sample due to electron flow. Contact potential difference V_{CPD} results from misalignment of vacuum levels E_v. c) Compensation of V_{CPD} and surface charges by application of bias V_{DC}. The amount of voltage applied to nullify V_{CPD} equals the work function difference of tip and sample.

In order to accurately detect the electrostatic force introduced by the V_{CPD}, KPFM applies an AC voltage V_{AC} to the conductive cantilever. This AC voltage introduces an oscillation of the electrostatic forces, which in turn mechanically excites the cantilever. The periodic electrostatic forces $F_{el}(z, t)$ between tip and sample upon AC excitation are described by:

$$F_{el}(z,t) = -\frac{1}{2}\frac{\partial C(z)}{\partial z}[(V_{DC} \pm V_{CPD}) + V_{AC}\sin(\omega t)]^2$$

Equation 1.28: Periodic electrostatic force $F_{el}(z, t)$ acting between tip and sample during KPFM.

with the gradient of capacitance C between tip and sample $\frac{\partial C(z)}{\partial z}$, frequency ω, distance z and time t. Equation 1.28 can be divided into three separate equations with different frequency components:

$$F_{DC} = -\frac{1}{2}\frac{\partial C(z)}{\partial z}[(V_{DC} \pm V_{CPD})^2]$$

Equation 1.29: DC force F_{DC} introducing static cantilever deflection.

giving the static deflection of the cantilever,

$$F_{\omega} = -\frac{\partial C(z)}{\partial z}(V_{DC} \pm V_{CPD}) + V_{AC}\sin(\omega t)$$

Equation 1.30: AC force F_{ω} at frequency ω with contribution of V_{CPD}.

the force component at frequency ω, which measures V_{CPD}, and finally:

$$F_{2\omega} = \frac{\partial C(z)}{\partial z}\frac{1}{4}V_{AC}^2[\cos(2\omega t) - 1]$$

Equation 1.31: AC force $F_{2\omega}$ at frequency 2ω.

used in capacitance microscopy. By adjusting the bias V_{DC} accordingly during the KPFM scan, the feedback eliminates the oscillation at ω caused by the electrostatic force component F_{ω} and thereby determines V_{CPD} for each pixel.[189]

To detangle the topography signal and the V_{CPD}, KPFM either exploits the different distance dependence of van der Waals and electrostatic forces or uses different frequencies to image topography and V_{CPD} simultaneously. For the former, dual-pass amplitude modulation (AM)-KPFM scans each scan line twice (Figure 1.21a): In the first scan, the sample topography is image in AM-AFM via a mechanical oscillation at the cantilever resonance ω_0. In a second scan, the cantilever lifts by ~50 nm, the mechanical excitation is turned off and an AC voltage at the same frequency is applied. An LIA detects the amplitude at ω_0 and the PFM feedback adjusts the DC bias to nullify this amplitude and measure the V_{CPD}. Since every scan line is measured twice, an AM KPFM scan takes longer than regular topography scans. Moreover, dual pass AM-KPFM detects the V_{CPD} via the long-rage electrostatic force, which leads to background interactions that limit the resolution to around 25 nm.[189,191,206]

On the other hand, frequency modulated (FM) heterodyne KPFM uses different frequencies to image topography and V_{CPD} simultaneously (Figure 1.21b). Here, the application of the AC voltage at $\omega_{AC} \neq \omega_0$ induces a frequency mixing and satellite peaks appear at $\omega_0 \pm \omega_{AC}$ in the frequency response of the cantilever. These peaks directly depend on the electrostatic force gradient $\partial F/\partial z$. By choosing an $\omega_{AC} = \omega_1 - \omega_0$, with ω_1 as second cantilever Eigenmode, one of the satellite peaks coincides with ω_1 and the signal-to-noise ratio increases. An LIA detects the amplitude at ω_1 and the KPFM feedback nullifies the amplitude via DC bias application to measure V_{CPD}. Meanwhile, the

sample topography is measured at the resonance ω_0, allowing simultaneous topography and potential imaging. The dependence on the force gradient in FM heterodyne KPFM limits the tip-sample interaction to the tip apex resulting in higher resolutions than in dual pass AM-KPFM. The separation of the mechanical and electrical detection by more than 100 kHz in FM heterodyne KPFM additionally lowers the crosstalk between topography and V_{CPD} and decreases the time resolution to ~0.2 ms. This time resolution enables fast scan rates, while maintaining a high resolution and potential sensitivity.[206,215,216]

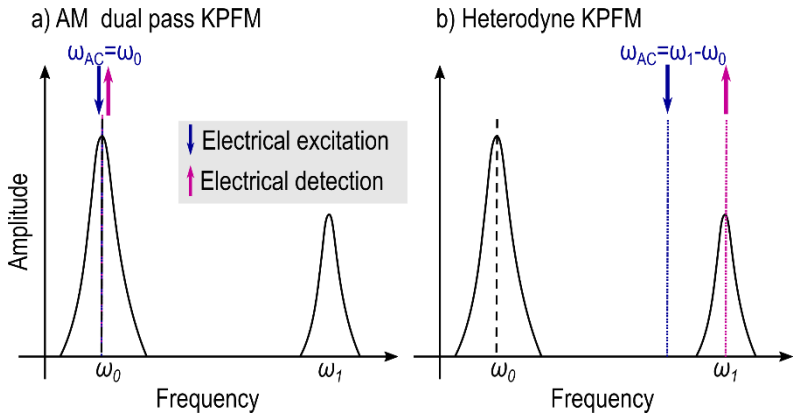

Figure 1.21: KPFM detection schemes in dual pass AM KPFM and FM heterodyne KPFM. a) Dual pass AM KPFM with electrical excitation and detection at the cantilever resonance ω_0. To detangle topography and KPFM signal, each scan line is measured twice: The first pass in direct surface proximity and the second pass in a few tens of nm from the surface. The topography is measured via short-ranged van der Waals interaction during the first pass, the electric excitation and detection is done at the same frequency via long-ranged electrostatic forces during the second pass. b) Heterodyne KPFM as a single pass mode, measures topography and KPFM simultaneously at different frequencies. Topography is measured at ω_0, whereas the electric excitation occurs at $\omega_0 - \omega_1$ and the detection at second Eigenmode ω_1.

KPFM is commonly used to distinguish materials with different work functions in polymer blends, colloid samples or cross-sections of multilayer devices, like solar cells.[191] However, due to the surface potential sensitivity, the technique is also suitable to resolve bias- or light-induced charge distributions in the active layers of solar cells: The difference of the V_{CPD} measured on a solar cell absorber with and without illumination gives the photopotential.[188]

1.4.2 Complementary Methods

1.4.2.1 X-ray diffraction

With AFM-based characterization limited to surface structures, bulk characterization requires complementary investigations methods. X-ray diffraction (XRD) is an established technique to resolve the bulk structure in crystalline materials. Generally, diffraction occurs when electromagnetic waves interact with an object in their beam path. The interaction induces a characteristic diffraction pattern of varying intensity distributions due to interference. To employ diffraction for structural analysis, the wavelength of the electromagnetic wave must be smaller than the features investigated. Max von Laue found that x-rays are suited to study the arrangement of atoms in bulk crystalline structures as the wavelength of certain x-rays are in the order of atom spacings in a crystal lattice.[18,19]

X-rays are generated when high-energy electron beams radiate metal surfaces. As incoming electrons collide with inner-shell metal electrons, they transfer parts of their kinetic energy. With the additional energy, inner-shell electrons can overcome the vacuum level and escape the metal surface. Higher shell electrons relax into the vacancies created by the escaped electrons by emitting electromagnetic radiation with characteristic wavelengths between 10 pm to 10 nm, which are X-rays. The wavelength of these x-rays depends on the metal as well as the involved energy levels. If an electron relaxes into the first energy level K (n=1), it will emit K-radiation; if an electron relaxes into the L (n=2) or M (n=3) energy level, it will emit L- or M- radiation, respectively. Typically used for structural analysis via XRD is the K-radiation of copper, molybdenum and tungsten, which feature wavelengths between 20 and 150 pm.[18,217]

Crystals consist of periodical 3D-arrangements of atoms, ions or molecules with typical spacings in the single-digit Å-regime, thus, hundreds of pm. The arrangements can be divided into unit cells as smallest possible entity that contains all symmetry operations of the full crystal structure. Via translation, these unit cells build up the entire crystal.[50] Possible symmetry elements, inversion centers, mirror planes and or/ rotation axis, define the placement of atoms, ions or molecules with respect to each other within the unit cells.[19] Based on the symmetry elements present, all crystal structures can be categorized into more than 200 space groups, which belong to seven crystal systems. These crystal systems differ in their angles α, β, and γ between lattice vectors $\vec{a}$, $\vec{b}$ and $\vec{c}$ as well as their magnitudes $|\vec{a}|$, $|\vec{b}|$ and $|\vec{c}|$. For example, in a tetragonal system is $|\vec{a}| = |\vec{b}| \neq |\vec{c}|$ and $\alpha = \beta = \gamma = 90°$, while in a cubic system is $|\vec{a}| = |\vec{b}| = |\vec{c}|$ and $\alpha = \beta = \gamma = 90°$.[19] The resulting crystal lattices can also be subdivided into crystal planes. The intersections of crystal planes with the crystal axis, given by the lattice vectors $\vec{a}$, $\vec{b}$ and $\vec{c}$, define the Miller indices (hkl), used to describe a pool of parallel crystal planes.[19]

In XRD, these crystal planes reflect the incoming x-rays. Reflections on parallel crystal planes lead to constructive interference following Bragg's law:

$$n\lambda = 2d\sin\theta$$

Equation 1.32: Bragg's law to describe the occurance of contructive interference.

where λ is the wavelength of the x-rays, d is the distance of the reflecting lattice planes, n is the order parameter of the reflection and θ is the angle between incident beam and crystal plane (Figure 1.22a). Since constructive interference of the x-ray reflections on different lattice planes appears at different angles, the detected intensity is plotted against 2θ in XRD patterns. The peaks from constructive interference, also called reflections, can thus be assigned to the according planes. The arrangement of the reflections in the XRD pattern is characteristic of the investigated structure and corresponds to the structure's reciprocal lattice.[18]

XRD analyzes the structure of single crystals, powders or polycrystalline thin films. Powder XRD was developed by Debye and Scherrer. They irradiated crystalline powder sample with monochromatic x-rays and found that due to the different orientations of the microscopic crystals, the crystal planes reflect x-rays in the according angles in a cone-like beam path. Here, reflections

from different crystal planes appear as continuous rings in a 2D XRD pattern, called Debye-Scherrer rings (Figure 1.22b). If the crystallites in powder or polycrystalline thin film XRD have a preferential out-of-plane orientation, the rings will exhibit local intensity maxima instead of a continuous intensity. Thus, 2D XRD can be employed to investigate whether crystallites in polycrystalline thin-films have a texture (Figure 1.22c).[18]

In 1D powder XRD, a detector rotates around the sample out-of-plane with the incident beam to give 1D diffraction patterns as a cross section through the Debye rings. However, for textured samples this method can be inaccurate, since 1D XRD only resolves reflections in specular condition and neglects reflections with intensity maxima at differing positions (Figure 1.22d).[18]

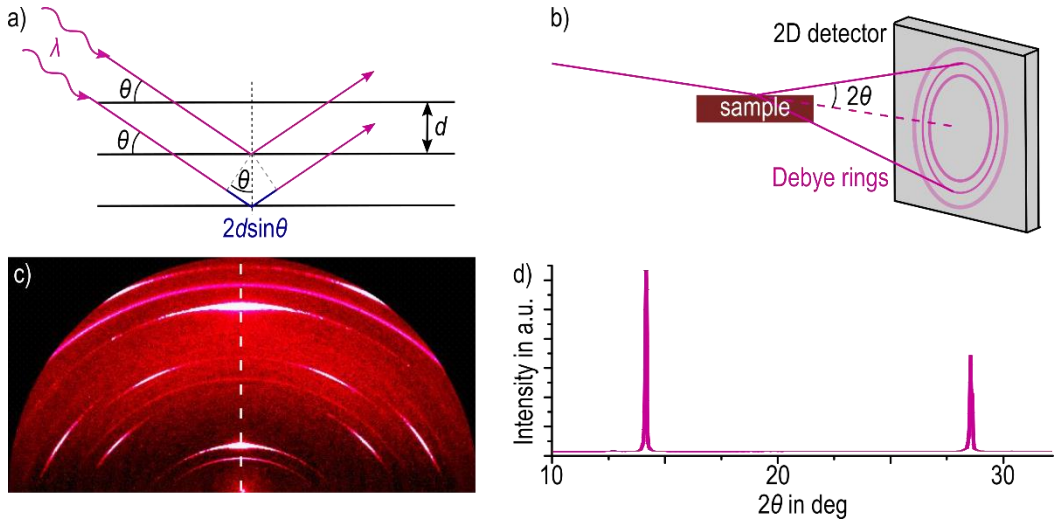

Figure 1.22: a) Derivation of Bragg's law (Equation 1.32) for x-ray beam with wavelength λ and incident angle θ, shown in pink, diffracted on parallel lattice planes of crystal (black lines) with distance d. Reflected Beams on neighboring planes exhibit a difference in pathlength of $2d\sin\theta$, highlighted in blue. Constructive interference, visible as peaks also called reflections in the XRD spectrum, will occur, if $2d\sin\theta$ is an integer multiple n of the wavelength λ.[18] b) Schematic of experimental setup for 2D XRD measurement on polycrystalline thin film. 2D detector allows resolving continuous Debye rings for films with random crystal orientations or localized reflections on textured films.[19] c) Exemplary 2D XRD measurement on polycrystalline $MAPbI_3$ thin film showing Debye-Scherrer rings with localized maxima indicative of preferential out-of-plane orientation, also called texture. d) Cross section through the Debye-Scherrer rings along the dashed white line in c at specular condition.

1.4.2.2 Photoluminescence microscopy

Evaluation of the quality and suitability of candidates for solar cell light absorption requires characterization of the material's optoelectronic properties, including band gap, recombination rates and lifetimes as well as photocarrier dynamics. PL, which is emitted during radiative recombination of photocarriers, provides information on these properties via spectroscopy, microscopy and/or time-resolved measurements.[3]

As described in Chapter 1.2.3.3, in the absence of extraction, all photocarriers in the solar cell absorber will recombine. The governing recombination mechanism depends on the charge carrier density as well as the defect density in the absorber material. Monomolecular recombination involves only one free photocarrier, while the other is trapped in defect states, at crystal inhomogeneities, surfaces or grain boundaries.[8] Radiative recombination, on the other hand, is a bimolecular process, where free electrons and holes have to occupy the same position in the

absorber to recombine under emission of PL with an energy given by the band gap of the absorber (Figure 1.23a). Therefore, PL spectroscopy can measure the electronic structure of the material, including the band gap, presence of impurity states or luminescence quantum efficiency.[218] Static PL microscopy on polycrystalline thin films resolves heterogeneities in defect densities, since trap-mediated recombination quenches the PL. Therefore, grains with higher defect density appear dimmer in the microscopy image than grains with lower defect density.[186] Time-resolved PL detection upon picosecond excitation pulses resolve recombination rates and the lifetimes of photocarriers.[219] Furthermore, spatially decoupled PL excitation and static or time-resolved detection resolves charge carrier diffusion lengths L_D and times τ_{Diff} (Figure 1.23b).[34,35,177,220,221]

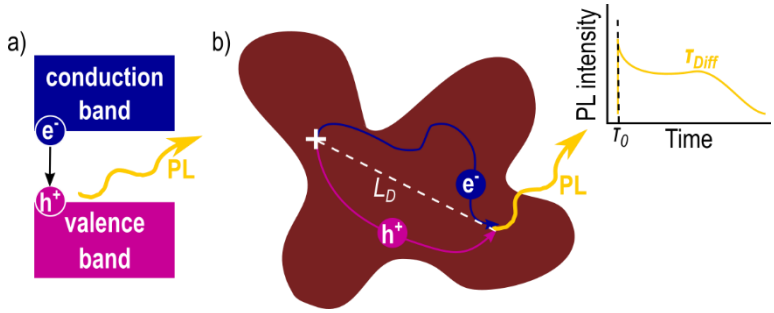

Figure 1.23: a) Energetic view on the PL emission upon radiative recombination, caused by a single step relaxation of an electron in the conduction band with a hole in the valance band via emission of a photon with energy $E = E_g$ (Chapter 1.2.3.3). b) Spatially resolved recombination event, where a photogenerated electron and hole pair diffuses separately from the excitation position, marked by the white cross, until they collide and recombine radiatively. The effective distance between excitation and detection is the diffusion length L_D (Equation 1.10); the time between excitation and detection is the diffusion time τ_{Diff}.

Spatially decoupled PL excitation and detection allows visualizing the photocarrier distribution in the absorber. In the absence of extraction layers and electric fields, this distribution originates from charge carrier diffusion.[8] Thus, the static distribution in PL microscopy with local excitation and widefield detection can resolve diffusion lengths L_D and identify barriers that may restrict the diffusion as anisotropy in the distribution (Figure 1.24a).[160] Moreover, confocal and time-resolved PL detection, as depicted in Figure 1.24b, measures diffusion times τ_{Diff} of photocarriers, allowing to calculate diffusion constants via Equation 1.9. [34,35,177,220,221] To evaluate the influence of structural features in the absorber, such as grain boundaries or domain walls, on the carrier dynamics, spatial and time-resolved PL microscopy can be correlated to AFM and XRD data.[35]

For interpretation of the resulting PL data, influence of light trapping and photon recycling has to be considered: Large differences in diffraction indices between substrate, absorber and environment, like $MAPbI_3$ on glass in air, lead to a confinement of emitted PL within the absorber layer. This trapped PL, most commonly originating from the excitation position, superimposes onto local PL from diffusive charges as shown schematically in the time trace in Figure 1.23b. To detangle the contribution of charge carrier diffusion and trapped PL on the detected signal, the time-resolved PL response can be fitted with an initial mono-exponential decay describing the trapped PL and a delayed peak function describing the diffusion signal (Equation 3.1).[34,35,37,177,220–222] In materials with sharp absorption onset and broad PL emission, trapped PL can be reabsorbed in a process called photon recycling. In PL measurements, photon recycling artificially increases observed charge carrier diffusion lengths.[164] However, according to our Simulation 8.17 in the Appendix 8.2

the influence of photon recycling on the detected diffusion signal is minimal at excitation energy densities below 1 μJ/cm², which translates to carrier densities below $1.5 \cdot 10^{16}$ cm^{-3}.

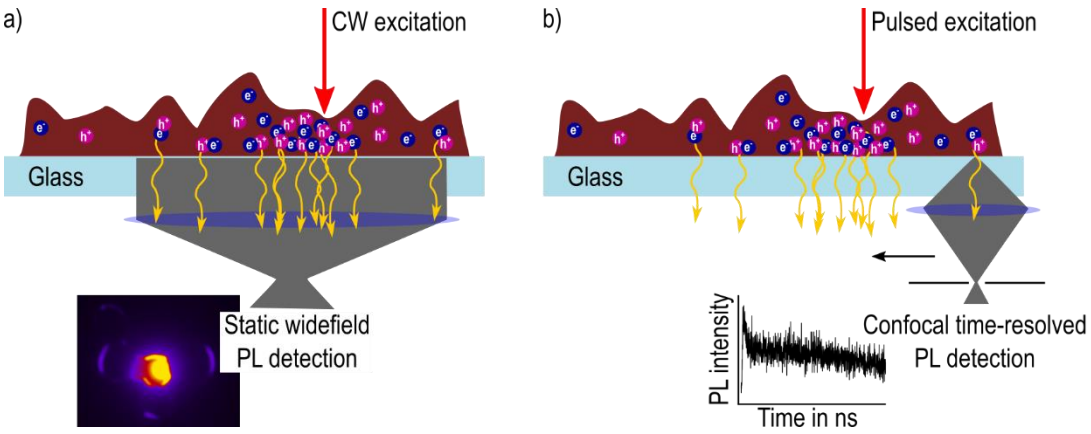

Figure 1.24: PL microscopy detection schemes to characterize charge carrier diffusion in solar cell light absorbers without carrier extraction upon local excitation, simplified to only show uniaxial PL emission through the glass substrate. a) Local excitation via continuous wave laser (CW) generates a high density of photocarriers at the excitation position, most of which recombine at this position, while others diffuse through the absorber before radiatively recombining. A widefield camera captures the PL emission from all recombination events simultaneously to resolve the distribution and diffusion lengths L_D of photocarriers, as shown in the static PL image in the lower left on a $MAPbI_3$ grain cluster. b) Excitation with a pulsed laser, while a confocal PL detection with a time-correlated single photon counting (TCSPC) unit scans the absorber to detect the time-resolved PL decays after each excitation pulse in varying distances from the excitation position. Peak functions in the PL decays, as shown in the lower left corner, originate from diffusive photocarriers and give diffusion times τ_D and, thus, constants D (Equation 1.9).

1.4.2.3 UV-vis spectroscopy

Solar cells work most efficiently the more photons are absorbed to create charge carriers within the photoactive material. A strong optical absorption in the ultraviolet (UV) and visible (vis) range is essential for a high PCE. To investigate the absorption range and the wavelength-dependent absorbance a monochromatic light source radiates the sample with a given intensity I_0 at varying wavelengths λ between around 200 and 800 nm, while a photodiode detects the intensity I of the light after it passed through the sample (Figure 1.25a).[18] To reduce the influence of scattering present in polycrystalline thin films, detection via integrating sphere can be used (Figure 1.25a).[223] The ratio between the two intensity values I_0 and I at a given wavelength defines the transmission $T = \frac{I}{I_0}$. According to the empirical law of Beer-Lambert, the intensity decreases exponentially within the sample to give $I = I_0 e^{-\alpha l}$ with the absorption coefficient α and the layer thickness l (Equation 1.5). To simplify, the parameter of the absorbance A was introduced, which summarizes the absorption coefficient α as well as the sample geometry and is described as:[18]

$$A = \log \frac{I_0}{I}$$

Equation 1.33: Absorbance A from ration of intensities I and I_0.

Figure 1.25 shows a typical absorbance spectrum of $MAPbI_3$ in the UV-vis regime compared to the solar spectrum.[23] A strong overlap of the spectra is required to achieve optimal solar cell operation.[8]

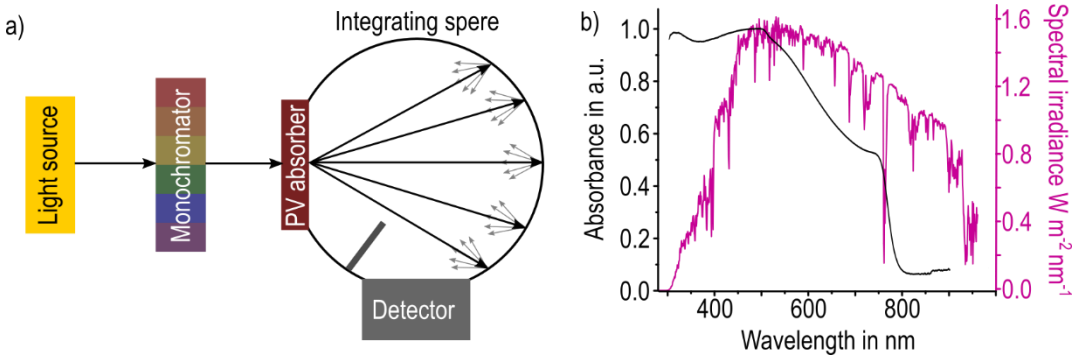

Figure 1.25: a) Experimental setup for UV-vis spectroscopy on polycrystalline PV absorber with integrating sphere detection to minimize the influence of scattering.[223] b) Absorbance spectrum of $MAPbI_3$ solar cell absorber versus the solar radiation spectrum at sea level at an absolute air mass of 1.5 depicted pink.[23]

1.4.2.4 Focused ion beam

In conventional microscopy methods, the diffraction limit - the minimal distance d between two points that can be resolved - is given by:

$$d = \frac{\lambda}{2NA}$$

Equation 1.34: Diffraction limit d in dependence of numerical aperture NA and wavelength λ.

NA is the numerical aperture of the objective and λ is the wavelength of the radiation. For optical microscopy operated in the visible light regime, the wavelength dependence implies a minimal resolution in the range of hundreds of nm.[18] Since electrons have a smaller de Broglie wavelength than photons due to their higher mass, electron microscopy overcomes the resolution limitation of optical microscopes. In scanning electron microscopy (SEM), an electron gun, such as a tungsten filament, generates an electron beam e.g., by thermal emission, that is focused by electromagnetic lenses. When the electrons hit the surface, they interact with the sample atoms to produce various signals, including secondary, backscattered and Auger electrons, as well as x-rays. Different detectors collect each signal as the electron beam scans over the surface. Secondary electrons, which are generated as incoming electrons transfer their kinetic energy to sample electrons, mainly carry the topography information used in SEM imaging. An electron beam with energies between 2 and 1000 keV, translating to wavelengths between 1 and 600 pm, can achieve resolutions below 1 nm.[224]

For focused ion beam (FIB) microscopy, an ion beam instead of an electron beam scans the surface. Here, the ions pass through electromagnetic lenses, which focus the ions into a beam and onto the sample. Via field emission, a coated tungsten needle emits the ions. Usually, FIB employs Gallium (Ga) due to the element's low evaporation temperature and high vapor pressure. The beam-sample interactions are analog to SEM: Reflected and backscattered ions, secondary electrons and electromagnetic radiation. The detection of secondary electrons yields topography images with resolutions of around 10 nm, limited by the signal-to-noise ratio. Measurements with FIB are more invasive than SEM measurements due to the higher masses of ions and a possible implementation of Ga ions in the sample structure. Modern FIB microscopes combine SEM and FIB capabilities for high flexibility via dual beam technology.[225]

Both, electron and ion beam, cannot only image surfaces, but also manipulate samples either via material deposition or ablation (Figure 1.26). For the former, a needle introduces a gaseous precursor of the deposition material, which absorbs on the sample surface in a process comparable to a local chemical vapor deposition induced via electron or ion beam.[226] For an electron beam, the impact with the incoming electrons allows a controlled non-destructive deposition of the layer.[225] Analogously, the FIB can also deposit material on the sample surface to facilitate faster deposition rates. However, FIB deposition but suffers from a possible implementation of ions into the sample.[226] To avoid the potentially adverse implementation to Ga^+ ions in a sensitive sample such as solar cell cross sections, it is feasible to first apply thin deposition layer via the electron beam to protect the sample and then continue with a faster deposition using the ion beam.[227] In our KPFM cross section study in Chapter 5, we first deposited a 100 nm thick Pt layer using the electron beam and then a 2 µm thick layer using the ion beam, to protect the cross section in the subsequent micro-milling step.[228]

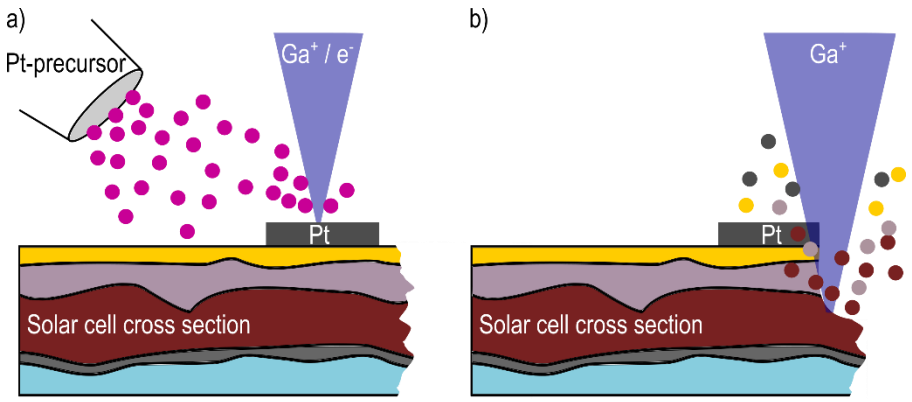

Figure 1.26: a) Pt deposition onto the gold electrode of a solar cell cross section, which acts as protection layer, via electron (e^-) or Ga^+ ion beam in dual beam microscope. Pt is introduced by a needle in form of a gaseous organometallic precursor.[226] b) Material ablation via micro-milling using an ion beam to polish a rough surface for subsequent AFM characterization. To avoid contamination the beam is applied parallelly to the cross section and the previously deposited protective Pt layer prevents ion implementation in the upper sample layers.

For material ablation, the more destructive nature of the ion beam is advantageous to achieve high rates for sputtering or micro-milling. FIB allows removing sample material locally with a precision of 10 nm to create special structures, cut filaments from large samples and polish rough surfaces.[225] By choosing a low beam energy, a suitable angle and depositing protective metal layers onto the sample an incorporation of ions becomes minimal (Figure 1.26b).[227] For polishing of PSC cross sections that allow KPFM across the active layers (Chapter 5), we adjusted the ion beam parallel to the cross section and selected a milling depth far beyond the cross section width to avoid contamination of the active layers.[228]

Bibliography

1 United Nations, Paris Agreement, https://unfccc.int/sites/default/files/english_paris_agreement.pdf, (accessed 7 October 2021).

2 International Energy Agency, Verteilung der weltweiten Energieerzeugung nach Energieträger im Jahr 2019,

https://de.statista.com/statistik/daten/studie/167998/umfrage/weltweiter-energiemix-nach-energietraeger/, (accessed 9 October 2021).

3 P. Würfel and U. Würfel, *Physics of solar cells: from basic principles to advanced concepts*, John Wiley & Sons, 2016.

4 Kraftfahrt Bundesamt, Anzahl der Elektroautos in Deutschland von 2011 bis 2021, https://de.statista.com/statistik/daten/studie/265995/umfrage/anzahl-der-elektroautos-in-deutschland/, (accessed 9 October 2021).

5 Bundesverband der Energie- und Wasserwirtschaft (BDEW), Welche Gründe würden für Sie für den Kauf eines Elektroautos sprechen?, https://de.statista.com/statistik/daten/studie/582695/umfrage/umfrage-zu-positiven-aspekten-von-elektroautos-in-deutschland/, (accessed 9 October 2021).

6 Center for Solar Energy and Hydrogen Research Baden-Württemberg (ZSW), Anzahl von Elektroautos weltweit von 2012 bis 2020, https://de.statista.com/statistik/daten/studie/168350/umfrage/bestandsentwicklung-von-elektrofahrzeugen/, (accessed 9 October 2021).

7 C. J. Chen, *Physics of solar energy*, John Wiley & Sons, 2011.

8 J. A. Nelson, *The physics of solar cells*, World Scientific Publishing Company, 2003.

9 C. Tong, *Introduction to materials for advanced energy systems*, Springer, 2019.

10 H. J. Snaith, *J. Phys. Chem. Lett.*, 2013, **4**, 3623–3630.

11 N. R. E. L. (NREL), Best Research-Cell Efficiency Chart, https://www.nrel.gov/pv/cell-efficiency.html, (accessed 10 October 2021).

12 A. Kojima, K. Teshima, Y. Shirai and T. Miyasaka, *J. Am. Chem. Soc.*, 2009, **131**, 6050–6051.

13 M. M. Lee, J. Teuscher, T. Miyasaka, T. N. Murakami and H. J. Snaith, *Science (80-.).*, 2012, **338**, 643–647.

14 H.-S. Kim, C.-R. Lee, J.-H. Im, K.-B. Lee, T. Moehl, A. Marchioro, S.-J. Moon, R. Humphry-Baker, J.-H. Yum and J. E. Moser, *Sci. Rep.*, 2012, **2**, 591.

15 H. Zhou, Q. Chen, G. Li, S. Luo, T. Song, H.-S. Duan, Z. Hong, J. You, Y. Liu and Y. Yang, *Science (80-.).*, 2014, **345**, 542–546.

16 M. Saliba, T. Matsui, J.-Y. Seo, K. Domanski, J.-P. Correa-Baena, M. K. Nazeeruddin, S. M. Zakeeruddin, W. Tress, A. Abate and A. Hagfeldt, *Energy Environ. Sci.*, 2016, **9**, 1989–1997.

17 W. S. Yang, B.-W. Park, E. H. Jung, N. J. Jeon, Y. C. Kim, D. U. Lee, S. S. Shin, J. Seo, E. K. Kim and J. H. Noh, *Science (80-.).*, 2017, **356**, 1376–1379.

18 P. W. Atkins and J. De Paula, 1998.

19 W. Demtröder, *Experimentalphysik 3: Atome, Moleküle und Festkörper*, Springer-Verlag, 2016.

20 C. Kittel, P. McEuen and P. McEuen, *Introduction to solid state physics*, Wiley New York, 1996, vol. 8.

21 C. Janiak, T. M. Klapotke, H.-J. Meyer and B. Neumuller, *Moderne Anorganische Chemie*, de Gruyter, 1998.

22 W. H. Strehlow and E. L. Cook, *J. Phys. Chem. Ref. Data*, 1973, **2**, 163–200.

23 K. Emery, Reference Solar Spectral Irradiance: Air Mass 1.5, http://rredc.nrel.gov/solar/spectra/am1.5/, (accessed 26 May 2016).

24 W. Shockley and H. J. Queisser, *J. Appl. Phys.*, 1961, **32**, 510–519.

25 Sbyrnes321, Shockley-Queisser Full Curve, https://commons.wikimedia.org/wiki/File:ShockleyQueisserFullCurve_(DE).svg, (accessed 15 January 2019).

26 B. Ehrler, E. M. Hutter and J. J. Berry, *ACS Energy Lett.*, 2021, **6**, 565–567.

27 O. D. Miller, E. Yablonovitch and S. R. Kurtz, *IEEE J. Photovoltaics*, 2012, **2**, 303–311.

28 S. Rühle, *Sol. Energy*, 2016, **130**, 139–147.

29 S. W. Koch, M. Kira, G. Khitrova and H. M. Gibbs, *Nat. Mater.*, 2006, **5**, 523–531.

30 H. Mehrer, *Diffusion in solids: fundamentals, methods, materials, diffusion-controlled processes*, Springer Science & Business Media, 2007, vol. 155.

31 G. Hodes and P. V Kamat, 2015.

32 M. B. Johnston and L. M. Herz, *Acc. Chem. Res.*, 2016, **49**, 146–154.

33 R. G. Hunsperger, in *Integrated Optics*, Springer, 2002, pp. 193–210.

34 R. Ciesielski, F. Schäfer, N. F. Hartmann, N. Giesbrecht, T. Bein, P. Docampo and A. Hartschuh, *ACS Appl. Mater. Interfaces*, 2018, **10**, 7974–7981.

35 I. M. Hermes, A. Best, L. Winkelmann, J. Mars, S. M. Vorpahl, M. Mezger, L. Collins, H.-J. Butt, D. S. Ginger, K. Koynov and S. A. L. Weber, *Energy Environ. Sci.*, 2020, **13**, 4168–4177.

36 T. Kirchartz, 2019.

37 L. M. Pazos-Outón, M. Szumilo, R. Lamboll, J. M. Richter, M. Crespo-Quesada, M. Abdi-Jalebi, H. J. Beeson, M. Vrućinić, M. Alsari and H. J. Snaith, *Science (80-.).*, 2016, **351**, 1430–1433.

38 R. Brenes, M. Laitz, J. Jean, D. W. deQuilettes and V. Bulović, *Phys. Rev. Appl.*, 2019, **12**, 14017.

39 I. Schmitt Menzel, A. Mailwald, J. Marschner, K. von Westerman, H.-G. Kobeck, M. Schmolke and M. Schoof, 2004.

40 T. Dittrich, *Materials concepts for solar cells*, World Scientific, 2015.

41 C. S. Tao, J. Jiang and M. Tao, *Sol. Energy Mater. Sol. Cells*, 2011, **95**, 3176–3180.

42 T. J. Jacobsson, J.-P. Correa-Baena, M. Pazoki, M. Saliba, K. Schenk, M. Grätzel and A. Hagfeldt, *Energy Environ. Sci.*, 2016, **9**, 1706–1724.

43 M. I. H. Ansari, A. Qurashi and M. K. Nazeeruddin, *J. Photochem. Photobiol. C Photochem. Rev.*, 2018, **35**, 1–24.

44 S. De Wolf, J. Holovsky, S.-J. Moon, P. Löper, B. Niesen, M. Ledinsky, F.-J. Haug, J.-H. Yum and C. Ballif, *J. Phys. Chem. Lett.*, 2014, **5**, 1035–1039.

45 S. D. Stranks, G. E. Eperon, G. Grancini, C. Menelaou, M. J. P. Alcocer, T. Leijtens, L. M. Herz, A. Petrozza and H. J. Snaith, *Science (80-.).*, 2013, **342**, 341–344.

46 L. M. Herz, *ACS Energy Lett.*, 2017, **2**, 1539–1548.

47 Z. Yang, C. Chueh, F. Zuo, J. H. Kim, P. Liang and A. K. Jen, *Adv. Energy Mater.*, 2015, **5**, 1500328.

48 M. A. Green, A. Ho-Baillie and H. J. Snaith, *Nat. Photonics*, 2014, **8**, 506–514.

49 S. A. Bretschneider, J. Weickert, J. A. Dorman and L. Schmidt-Mende, *APL Mater.*, 2014, **2**, 155204.

50 E. Riedel and C. Janiak, *Anorganische chemie*, de Gruyter, 2015.

51 C. C. Stoumpos, C. D. Malliakas and M. G. Kanatzidis, *Inorg. Chem.*, 2013, **52**, 9019–9038.

52 T. Baikie, Y. Fang, J. M. Kadro, M. Schreyer, F. Wei, S. G. Mhaisalkar, M. Graetzel and T. J. White, *J. Mater. Chem. A*, 2013, **1**, 5628–5641.

53 Y. Dang, Y. Liu, Y. Sun, D. Yuan, X. Liu, W. Lu, G. Liu, H. Xia and X. Tao, *CrystEngComm*, 2015, **17**, 665–670.

54 M. T. Weller, O. J. Weber, P. F. Henry, A. M. Di Pumpo and T. C. Hansen, *Chem. Commun.*, 2015, **51**, 4180–4183.

55 P. S. Whitfield, N. Herron, W. E. Guise, K. Page, Y. Q. Cheng, I. Milas and M. K. Crawford, *Sci. Rep.*, 2016, **6**, 1–16.

56 Y. Kawamura, H. Mashiyama and K. Hasebe, *J. Phys. Soc. Jpn.*, 2002, **71**, 1694–1697.

57 A. Poglitsch and D. Weber, *J. Chem. Phys.*, 1987, **87**, 6373–6378.

58 F. Hao, C. C. Stoumpos, R. P. H. Chang and M. G. Kanatzidis, *J. Am. Chem. Soc.*, 2014, **136**, 8094–8099.

59 C. Quarti, E. Mosconi and F. De Angelis, *Chem. Mater.*, 2014, **26**, 6557–6569.

60 J. Breternitz, M. Tovar and S. Schorr, *Sci. Rep.*, 2020, **10**, 16613.

61 A. K. Tagantsev, L. E. Cross and J. Fousek, *Domains in ferroic crystals and thin films*, Springer, 2010, vol. 13.

62 J. M. Frost, K. T. Butler, F. Brivio, C. H. Hendon, M. Van Schilfgaarde and A. Walsh, *Nano Lett.*, 2014, **14**, 2584–2590.

63 S. Liu, F. Zheng, N. Z. Koocher, H. Takenaka, F. Wang and A. M. Rappe, *J. Phys. Chem. Lett.*, 2015, **6**, 693–699.

64 D. Rossi, A. Pecchia, M. A. der Maur, T. Leonhard, H. Röhm, M. J. Hoffmann, A. Colsmann and A. Di Carlo, *Nano Energy*, 2018, **48**, 20–26.

65 A. Pecchia, D. Gentilini, D. Rossi, M. Auf der Maur and A. Di Carlo, *Nano Lett.*, 2016, **16**, 988–992.

66 K. T. Butler, J. M. Frost and A. Walsh, *Energy Environ. Sci.*, 2015, **8**, 838–848.

67 J. N. Wilson, J. M. Frost, S. K. Wallace and A. Walsh, *APL Mater.*, 2019, **7**, 10901.

68 A. R. Warwick, J. Íñiguez, P. D. Haynes and N. C. Bristowe, *J. Phys. Chem. Lett.*, 2019, **10**, 1416–1421.

69 M. D. Glinchuk, A. V Ragulya and V. A. Stephanovich, *Nanoferroics*, Springer, 2013.

70 V. K. Wadhawan, *Resonance*, 2002, **7**, 15–24.

71 K. Aizu, *Phys. Rev. B*, 1970, **2**, 754–772.

72 K. M. Rabe, M. Dawber, C. Lichtensteiger, C. H. Ahn and J.-M. Triscone, in *Physics of Ferroelectrics*, Springer, 2007, pp. 1–30.

73 E. K. H. Salje, *Annu. Rev. Mater. Res.*, 2012, **42**, 265–283.

74 P. S. Bednyakov, B. I. Sturman, T. Sluka, A. K. Tagantsev and P. V Yudin, *npj Comput. Mater.*, 2018, **4**, 1–11.

75 P. Bednyakov, T. Sluka, A. Tagantsev, D. Damjanovic and N. Setter, *Adv. Mater.*, 2016, **28**, 9498–9503.

76 T. Sluka, A. K. Tagantsev, P. Bednyakov and N. Setter, *Nat. Commun.*, 2013, **4**, 1808.

77 X.-K. Wei, T. Sluka, B. Fraygola, L. Feigl, H. Du, L. Jin, C.-L. Jia and N. Setter, *ACS Appl. Mater. Interfaces*, 2017, **9**, 6539–6546.

78 V. K. Wadhawan, *Phase Transitions A Multinatl. J.*, 1982, **3**, 3–103.

79 E. K. H. Salje and J. C. Lashley, in *Disorder and Strain-Induced Complexity in Functional Materials*, Springer, 2012, pp. 1–18.

80 R. Shi, Z. Zhang, W. Fang and R. Long, *Nanoscale Horiz.*

81 T. W. Jones, A. Osherov, M. Alsari, M. Sponseller, B. C. Duck, Y.-K. Jung, C. Settens, F. Niroui, R. Brenes and C. V Stan, *Energy Environ. Sci.*, 2019, **12**, 596–606.

82 S. Jariwala, H. Sun, G. W. P. Adhyaksa, A. Lof, L. A. Muscarella, B. Ehrler, E. C. Garnett and D. S. Ginger, *Joule*, 2019, **3**, 3048–3060.

83 Y. Rakita, O. Bar-Elli, E. Meirzadeh, H. Kaslasi, Y. Peleg, G. Hodes, I. Lubomirsky, D. Oron, D. Ehre and D. Cahen, *Proc. Natl. Acad. Sci. U.S.A*, 2017, **114**, E5504–E5512.

84 I. M. Hermes, S. A. Bretschneider, V. W. Bergmann, D. Li, A. Klasen, J. Mars, W. Tremel, F. Laquai, H.-J. Butt, M. Mezger, R. Berger, B. J. Rodriguez and S. A. L. Weber, *J. Phys. Chem. C*.

85 Y. Liu, L. Collins, R. Proksch, S. Kim, B. R. Watson, B. Doughty, T. R. Calhoun, M. Ahmadi, A. V Ievlev and S. Jesse, *Nat. Mater.*, 2018, **17**, 1013–1019.

86 H. Röhm, T. Leonhard, M. J. Hoffmann and A. Colsmann, *Energy Environ. Sci.*, 2017, **10**, 950–955.

87 H. Röhm, T. Leonhard, M. J. Hoffmann and A. Colsmann, *Adv. Funct. Mater.*, 2020, **30**, 1908657.

88 I. Anusca, S. Balčiūnas, P. Gemeiner, Š. Svirskas, M. Sanlialp, G. Lackner, C. Fettkenhauer, J. Belovickis, V. Samulionis and M. Ivanov, *Adv. Energy Mater.*, 2017, **7**, 1700600.

89 B. Huang, G. Kong, E. N. Esfahani, S. Chen, Q. Li, J. Yu, N. Xu, Y. Zhang, S. Xie and H. Wen, *npj Quantum Mater.*, 2018, **3**, 1–8.

90 L. M. Garten, D. T. Moore, S. U. Nanayakkara, S. Dwaraknath, P. Schulz, J. Wands, A. Rockett, B. Newell, K. A. Persson, S. Trolier-McKinstry and D. S. Ginley, *Sci. Adv.*, 2019, **5**, eaas9311.

91 A. Gómez, Q. Wang, A. R. Goñi, M. Campoy-Quiles and A. Abate, *Energy Environ. Sci.*, 2019, **12**, 2537–2547.

92 J. Beilsten-Edmands, G. E. Eperon, R. D. Johnson, H. J. Snaith and P. G. Radaelli, *Appl. Phys. Lett.*, 2015, **106**, 173502.

93 T. S. Sherkar and L. J. A. Koster, *Phys. Chem. Chem. Phys.*, 2016, **18**, 331–338.

94 M. N. F. Hoque, M. Yang, Z. Li, N. Islam, X. Pan, K. Zhu and Z. Fan, *ACS Energy Lett.*, 2016, **1**, 142–149.

95 A. M. A. Leguy, P. Azarhoosh, M. I. Alonso, M. Campoy-Quiles, O. J. Weber, J. Yao, D. Bryant, M. T. Weller, J. Nelson and A. Walsh, *Nanoscale*, 2016, **8**, 6317–6327.

96 M. Coll, A. Gomez, E. Mas-Marza, O. Almora, G. Garcia-Belmonte, M. Campoy-Quiles and J. Bisquert, *J. Phys. Chem. Lett.*, 2015, **6**, 1408–1413.

97 Y. Kutes, L. Ye, Y. Zhou, S. Pang, B. D. Huey and N. P. Padture, *J. Phys. Chem. Lett.*, 2014, **5**, 3335–3339.

98 B. Chen, J. Shi, X. Zheng, Y. Zhou, K. Zhu and S. Priya, *J. Mater. Chem. A*, 2015, **3**, 7699–7705.

99 H.-S. Kim, S. K. Kim, B. J. Kim, K.-S. Shin, M. K. Gupta, H. S. Jung, S.-W. Kim and N.-G. Park, *J. Phys. Chem. Lett.*, 2015, **6**, 1729–1735.

100 Z. Xiao, Y. Yuan, Y. Shao, Q. Wang, Q. Dong, C. Bi, P. Sharma, A. Gruverman and J. Huang, *Nat. Mater.*, 2015, **14**, 193–198.

101 Z. Fan, J. Xiao, K. Sun, L. Chen, Y. Hu, J. Ouyang, K. P. Ong, K. Zeng and J. Wang, *J. Phys. Chem. Lett.*, 2015, **6**, 1155–1161.

102 G. Sharada, P. Mahale, B. P. Kore, S. Mukherjee, M. S. Pavan, C. De, S. Ghara, A. Sundaresan, A. Pandey and T. N. G. Row, *J. Phys. Chem. Lett*, 2016, **7**, 2412–2419.

103 Y. Liu, L. Collins, A. Belianinov, S. M. Neumayer, A. V Ievlev, M. Ahmadi, K. Xiao, S. T. Retterer, S. Jesse and S. V Kalinin, *Appl. Phys. Lett.*, 2018, **113**, 72102.

104 E. Strelcov, Q. Dong, T. Li, J. Chae, Y. Shao, Y. Deng, A. Gruverman, J. Huang and A. Centrone, *Sci. Adv. Adv.*, 2017, **3**, e1602165.

105 R. M. Kennard, C. J. Dahlman, R. A. DeCrescent, J. A. Schuller, K. Mukherjee, R. Seshadri and M. L. Chabinyc, *Chem. Mater.*, 2021, **33**, 298–309.

106 A. A. Medjahed, P. Dally, T. Zhou, N. Lemaitre, D. Djurado, P. Reiss and S. Pouget, *Chem. Mater.*, 2020, **32**, 3346–3357.

107 X. Xiao, W. Li, Y. Fang, Y. Liu, Y. Shao, S. Yang, J. Zhao, X. Dai, R. Zia and J. Huang, *Nat. Commun.*, 2020, **11**, 2215.

108 A. Tkach, O. Okhay, A. Santos, S. Zlotnik, R. Serrazina, P. M. Vilarinho and M. E. Costa, in *Advances in Thin Films, Nanostructured Materials, and Coatings*, Springer, 2019, pp. 331–342.

109 Y. Ivry, J. F. Scott, E. K. H. Salje and C. Durkan, *Phys. Rev. B*, 2012, **86**, 205428.

110 S. Matzen, O. Nesterov, G. Rispens, J. A. Heuver, M. Biegalski, H. M. Christen and B. Noheda, *Nat. commun.*, 2014, **5**, 1–8.

111 M. U. Rothmann, W. Li, Y. Zhu, U. Bach, L. Spiccia, J. Etheridge and Y.-B. Cheng, *Nat. Commun.*, 2017, **8**, 1–8.

112 S. M. Vorpahl, R. Giridharagopal, G. E. Eperon, I. M. Hermes, S. A. L. Weber and D. S. Ginger, *ACS Appl. Energy Mater.*, 2018, **1**, 1534–1539.

113 H. J. Snaith, A. Abate, J. M. Ball, G. E. Eperon, T. Leijtens, N. K. Noel, S. D. Stranks, J. T.-W. Wang, K. Wojciechowski and W. Zhang, *J. Phys. Chem. Lett.*, 2014, **5**, 1511–1515.

114 H.-W. Chen, N. Sakai, M. Ikegami and T. Miyasaka, *J. Phys. Chem. Lett.*, 2015, **6**, 164–169.

115 J. Wei, Y. Zhao, H. Li, G. Li, J. Pan, D. Xu, Q. Zhao and D. Yu, *J. Phys. Chem. Lett.*, 2014, **5**,

3937–3945.

116 A. L. Montero-Alejo, E. Menéndez-Proupin, P. Palacios, P. Wahnón and J. C. Conesa, *J. Phys. Chem. C*, 2017, **121**, 26698–26705.

117 S. N. Rashkeev, F. El-Mellouhi, S. Kais and F. H. Alharbi, *Sci. Rep.*, 2015, **5**, 1–8.

118 L. Chen, C. Paillard, H. J. Zhao, J. Íñiguez, Y. Yang and L. Bellaiche, *npj Comput. Mater.*, 2018, **4**, 1–6.

119 Y. Yuan and J. Huang, *Acc. Chem. Res.*, 2016, **49**, 286–293.

120 P. Calado, A. M. Telford, D. Bryant, X. Li, J. Nelson, B. C. O'Regan and P. R. F. Barnes, *Nat. Commun.*, 2016, **7**, 1–10.

121 J. M. Frost and A. Walsh, *Acc. Chem. Res.*, 2016, **49**, 528–535.

122 F. Brivio, A. B. Walker and A. Walsh, *APL Mater.*, 2013, **1**, 42111.

123 A. M. A. Leguy, J. M. Frost, A. P. McMahon, V. G. Sakai, W. Kockelmann, C. Law, X. Li, F. Foglia, A. Walsh and B. C. O'regan, *Nat. Commun.*, 2015, **6**, 1–11.

124 S. Meloni, T. Moehl, W. Tress, M. Franckevičius, M. Saliba, Y. H. Lee, P. Gao, M. K. Nazeeruddin, S. M. Zakeeruddin and U. Rothlisberger, *Nat. Commun.*, 2016, **7**, 1–9.

125 J. L. Minns, P. Zajdel, D. Chernyshov, W. van Beek and M. A. Green, *Nat. Commun.*, 2017, **8**, 15152.

126 E. Mosconi and F. De Angelis, *ACS Energy Lett.*, 2016, **1**, 182–188.

127 R. A. Belisle, W. H. Nguyen, A. R. Bowring, P. Calado, X. Li, S. J. C. Irvine, M. D. McGehee, P. R. F. Barnes and B. C. O'Regan, *Energy Environ. Sci.*, 2017, **10**, 192–204.

128 J. Liu, M. Hu, Z. Dai, W. Que, N. P. Padture and Y. Zhou, *ACS Energy Lett.*, 2021, **6**, 1003–1014.

129 S. van Reenen, M. Kemerink and H. J. Snaith, *J. Phys. Chem. Lett.*, 2015, **6**, 3808–3814.

130 J. M. Azpiroz, E. Mosconi, J. Bisquert and F. De Angelis, *Energy Environ. Sci.*, 2015, **8**, 2118–2127.

131 P. Delugas, C. Caddeo, A. Filippetti and A. Mattoni, *J. Phys. Chem. Lett.*, 2016, **7**, 2356–2361.

132 C. Eames, J. M. Frost, P. R. F. Barnes, B. C. O'regan, A. Walsh and M. S. Islam, *Nat. Commun.*, 2015, **6**, 1–8.

133 C. Li, A. Guerrero, Y. Zhong and S. Huettner, *J. Phys. Condens. Matter*, 2017, **29**, 193001.

134 C. Li, A. Guerrero, Y. Zhong, A. Gräser, C. A. M. Luna, J. Köhler, J. Bisquert, R. Hildner and S. Huettner, *Small*, 2017, **13**, 1701711.

135 C. Besleaga, L. E. Abramiuc, V. Stancu, A. G. Tomulescu, M. Sima, L. Trinca, N. Plugaru, L.

Pintilie, G. A. Nemnes and M. Iliescu, *J. Phys. Chem. Lett.*, 2016, **7**, 5168–5175.

136 W. Peng, C. Aranda, O. M. Bakr, G. Garcia-Belmonte, J. Bisquert and A. Guerrero, *ACS Energy Lett.*, 2018, **3**, 1477–1481.

137 J. Carrillo, A. Guerrero, S. Rahimnejad, O. Almora, I. Zarazua, E. Mas-Marza, J. Bisquert and G. Garcia-Belmonte, *Adv. Energy Mater.*, 2016, **6**, 1502246.

138 S. Kim, S. Bae, S.-W. Lee, K. Cho, K. D. Lee, H. Kim, S. Park, G. Kwon, S.-W. Ahn and H.-M. Lee, *Sci. Rep.*, 2017, **7**, 1–9.

139 D. Di Girolamo, N. Phung, F. U. Kosasih, F. Di Giacomo, F. Matteocci, J. A. Smith, M. A. Flatken, H. Köbler, S. H. Turren Cruz and A. Mattoni, *Adv. Energy Mater.*, 2020, **10**, 2000310.

140 J. S. Yun, J. Seidel, J. Kim, A. M. Soufiani, S. Huang, J. Lau, N. J. Jeon, S. Il Seok, M. A. Green and A. Ho-Baillie, *Adv. Energy Mater.*, 2016, **6**, 1600330.

141 S. A. L. Weber, I. M. Hermes, S.-H. Turren-Cruz, C. Gort, V. W. Bergmann, L. Gilson, A. Hagfeldt, M. Graetzel, W. Tress and R. Berger, *Energy Environ. Sci.*, , DOI:10.1039/c8ee01447g.

142 M. H. Futscher, J. M. Lee, L. McGovern, L. A. Muscarella, T. Wang, M. I. Haider, A. Fakharuddin, L. Schmidt-Mende and B. Ehrler, *Mater. Horizons*, 2019, **6**, 1497–1503.

143 G. Grancini, S. Marras, M. Prato, C. Giannini, C. Quarti, F. De Angelis, M. De Bastiani, G. E. Eperon, H. J. Snaith and L. Manna, *J. Phys. Chem. Lett.*, 2014, **5**, 3836–3842.

144 H. Yu, F. Wang, F. Xie, W. Li, J. Chen and N. Zhao, *Adv. Funct. Mater.*, 2014, **24**, 7102–7108.

145 Q. Dong, Y. Yuan, Y. Shao, Y. Fang, Q. Wang and J. Huang, *Energy Environ. Sci.*, 2015, **8**, 2464–2470.

146 S. T. Williams, F. Zuo, C.-C. Chueh, C.-Y. Liao, P.-W. Liang and A. K.-Y. Jen, *ACS Nano*, 2014, **8**, 10640–10654.

147 J.-P. Correa-Baena, A. Abate, M. Saliba, W. Tress, T. J. Jacobsson, M. Grätzel and A. Hagfeldt, *Energy Environ. Sci.*, 2017, **10**, 710–727.

148 J. Burschka, N. Pellet, S.-J. Moon, R. Humphry-Baker, P. Gao, M. K. Nazeeruddin and M. Grätzel, *Nature*, 2013, **499**, 316–319.

149 M. Liu, M. B. Johnston and H. J. Snaith, *Nature*, 2013, **501**, 395–398.

150 Z. Xiao, Q. Dong, C. Bi, Y. Shao, Y. Yuan and J. Huang, *Adv. Mater.*, 2014, **26**, 6503–6509.

151 B. Conings, A. Babayigit, T. Vangerven, J. D'Haen, J. Manca and H.-G. Boyen, *J. Mater. Chem. A*, 2015, **3**, 19123–19128.

152 J. You, Y. Yang, Z. Hong, T.-B. Song, L. Meng, Y. Liu, C. Jiang, H. Zhou, W.-H. Chang and

G. Li, *Appl. Phys. Lett.*, 2014, **105**, 183902.

153 D. Shen, X. Yu, X. Cai, M. Peng, Y. Ma, X. Su, L. Xiao and D. Zou, *J. Mater. Chem. A*, 2014, **2**, 20454–20461.

154 S. Xiao, K. Zhang, S. Zheng and S. Yang, *Nanoscale horizons*, 2020, **5**, 1147–1154.

155 G. A. MacDonald, M. Yang, S. Berweger, J. P. Killgore, P. Kabos, J. J. Berry, K. Zhu and F. W. DelRio, *Energy Environ. Sci.*, 2016, **9**, 3642–3649.

156 D. Luo, R. Su, W. Zhang, Q. Gong and R. Zhu, *Nat. Rev. Mater.*, 2020, **5**, 44–60.

157 P. Docampo, F. C. Hanusch, N. Giesbrecht, P. Angloher, A. Ivanova and T. Bein, *Apl Mater.*, 2014, **2**, 81508.

158 S. Y. Leblebici, L. Leppert, Y. Li, S. E. Reyes-Lillo, S. Wickenburg, E. Wong, J. Lee, M. Melli, D. Ziegler and D. K. Angell, *Nat. Energy*, 2016, **1**, 1–7.

159 J.-S. Park, J. Calbo, Y.-K. Jung, L. D. Whalley and A. Walsh, *ACS Energy Lett.*, 2019, **4**, 1321–1327.

160 D. W. DeQuilettes, S. Jariwala, S. Burke, M. E. Ziffer, J. T.-W. Wang, H. J. Snaith and D. S. Ginger, *ACS Nano*, 2017, **11**, 11488–11496.

161 M. Grätzel, *Nat. Mater.*, 2014, **13**, 838–842.

162 M. A. Green, Y. Jiang, A. M. Soufiani and A. Ho-Baillie, *J. Phys. Chem. Lett.*, 2015, **6**, 4774–4785.

163 M. R. Filip, G. E. Eperon, H. J. Snaith and F. Giustino, *Nat. Commun.*, 2014, **5**, 1–9.

164 M. Ansari-Rad and J. Bisquert, *Phys. Rev. Appl.*, 2018, **10**, 34062.

165 T. Kirchartz, F. Staub and U. Rau, *ACS Energy Lett.*, 2016, **1**, 731–739.

166 Q. Lin, A. Armin, R. C. R. Nagiri, P. L. Burn and P. Meredith, *Nat. Photonics*, 2015, **9**, 106–112.

167 J. M. Richter, M. Abdi-Jalebi, A. Sadhanala, M. Tabachnyk, J. P. H. Rivett, L. M. Pazos-Outón, K. C. Gödel, M. Price, F. Deschler and R. H. Friend, *Nat. commun.*, 2016, **7**, 1–8.

168 P. Fassl, V. Lami, F. J. Berger, L. M. Falk, J. Zaumseil, B. S. Richards, I. A. Howard, Y. Vaynzof and U. W. Paetzold, *Matter*, 2021, **4**, 1391–1412.

169 I. L. Braly, D. W. deQuilettes, L. M. Pazos-Outón, S. Burke, M. E. Ziffer, D. S. Ginger and H. W. Hillhouse, *Nat. Photonics*, 2018, **12**, 355–361.

170 G. Giorgi, J.-I. Fujisawa, H. Segawa and K. Yamashita, *J. Phys. Chem. Lett.*, 2013, **4**, 4213–4216.

171 T. M. Brenner, D. A. Egger, A. M. Rappe, L. Kronik, G. Hodes and D. Cahen, 2015.

172 C. Wehrenfennig, G. E. Eperon, M. B. Johnston, H. J. Snaith and L. M. Herz, *Adv. Mater.*,

2014, **26**, 1584–1589.

173 O. G. Reid, M. Yang, N. Kopidakis, K. Zhu and G. Rumbles, *ACS Energy Lett.*, 2016, **1**, 561–565.

174 I. Grill, M. F. Aygüler, T. Bein, P. Docampo, N. F. Hartmann, M. Handloser and A. Hartschuh, *ACS Appl. Mater. Interfaces*, 2017, **9**, 37655–37661.

175 D. Shi, V. Adinolfi, R. Comin, M. Yuan, E. Alarousu, A. Buin, Y. Chen, S. Hoogland, A. Rothenberger and K. Katsiev, *Science (80-.).*, 2015, **347**, 519–522.

176 E. M. Hutter, G. E. Eperon, S. D. Stranks and T. J. Savenije, *J. Phys. Chem. Lett.*, 2015, **6**, 3082–3090.

177 W. Tian, R. Cui, J. Leng, J. Liu, Y. Li, C. Zhao, J. Zhang, W. Deng, T. Lian and S. Jin, *Angew. Chem. Int. Ed.*, 2016, **55**, 13067–13071.

178 A. H. Hill, K. E. Smyser, C. L. Kennedy, E. S. Massaro and E. M. Grumstrup, *J. Phys. Chem. Lett.*, 2017, **8**, 948–953.

179 A. Castro-Méndez, J. Hidalgo and J. Correa-Baena, *Adv. Energy Mater.*, 2019, **9**, 1901489.

180 D. H. Arias, D. T. Moore, J. van de Lagemaat and J. C. Johnson, *J. Phys. Chem. Lett.*, 2018, **9**, 5710–5717.

181 M. Yang, Y. Zeng, Z. Li, D. H. Kim, C.-S. Jiang, J. van de Lagemaat and K. Zhu, *Phys. Chem. Chem. Phys.*, 2017, **19**, 5043–5050.

182 T. S. Sherkar, C. Momblona, L. Gil-Escrig, J. Ávila, M. Sessolo, H. J. Bolink and L. J. A. Koster, *ACS energy Lett.*, 2017, **2**, 1214–1222.

183 J. M. Snaider, Z. Guo, T. Wang, M. Yang, L. Yuan, K. Zhu and L. Huang, *ACS Energy Lett.*, 2018, **3**, 1402–1408.

184 L. M. Herz, *Ann. Rev. Phys. Chem.*, 2016, **67**, 65–89.

185 D. W. de Quilettes, S. M. Vorpahl, S. D. Stranks, H. Nagaoka, G. E. Eperon, M. E. Ziffer, H. J. Snaith and D. S. Ginger, *Science (80-.).*, 2015, **348**, 683–686.

186 C. M. Wolff, P. Caprioglio, M. Stolterfoht and D. Neher, *Adv. Mater.*, 2019, **31**, 1902762.

187 K. Valadi, S. Gharibi, R. Taheri-Ledari, S. Akin, A. Maleki and A. E. Shalan, *Environ. Chem. Lett.*, 2021, **19**, 2185–2207.

188 M. Saliba, J.-P. Correa-Baena, C. M. Wolff, M. Stolterfoht, N. Phung, S. Albrecht, D. Neher and A. Abate, *Chem. Mater.*, 2018, **30**, 4193–4201.

189 K. Miyano, N. Tripathi, M. Yanagida and Y. Shirai, *Acc. Chem. Res.*, 2016, **49**, 303–310.

190 V. M. Le Corre, M. Stolterfoht, L. Perdigon Toro, M. Feuerstein, C. Wolff, L. Gil-Escrig, H. J. Bolink, D. Neher and L. J. A. Koster, *ACS Appl. Energy Mater.*, 2019, **2**, 6280–6287.

191 P. Schulz, E. Edri, S. Kirmayer, G. Hodes, D. Cahen and A. Kahn, *Energy Environ. Sci.*, 2014, **7**, 1377–1381.

192 Y. Hou, S. Scheiner, X. Tang, N. Gasparini, M. Richter, N. Li, P. Schweizer, S. Chen, H. Chen and C. O. R. Quiroz, *Adv. Mater. Interfaces*, 2017, **4**, 1700007.

193 H.-S. Kim, I.-H. Jang, N. Ahn, M. Choi, A. Guerrero, J. Bisquert and N.-G. Park, *J. Phys. Chem. Lett.*, 2015, **6**, 4633–4639.

194 K. Wojciechowski, T. Leijtens, S. Siprova, C. Schlueter, M. T. Hörantner, J. T.-W. Wang, C.-Z. Li, A. K.-Y. Jen, T.-L. Lee and H. J. Snaith, *J. Phys. Chem. Lett.*, 2015, **6**, 2399–2405.

195 S. Ravishankar, S. Gharibzadeh, C. Roldán-Carmona, G. Grancini, Y. Lee, M. Ralaiarisoa, A. M. Asiri, N. Koch, J. Bisquert and M. K. Nazeeruddin, *Joule*, 2018, **2**, 788–798.

196 O. Almora, I. Zarazua, E. Mas-Marza, I. Mora-Sero, J. Bisquert and G. Garcia-Belmonte, *J. Phys. Chem. Lett.*, 2015, **6**, 1645–1652.

197 S. J. Kim, K. Choi, B. Lee, Y. Kim and B. H. Hong, *Annu. Rev. Mater. Res.*, 2015, **45**, 63–84.

198 Y. Fang, C. Bi, D. Wang and J. Huang, *ACS Energy Lett.*, 2017, **2**, 782–794.

199 R. Berger, A. L. Domanski and S. A. L. Weber, *Eur. Polym. J.*, 2013, **49**, 1907–1915.

200 W. Melitz, J. Shen, A. C. Kummel and S. Lee, *Surf. Sci. Rep.*, 2011, **66**, 1–27.

201 E. Soergel, *J. Phys. D Appl. Phys.*, 2011, **44**, 464003.

202 R. Berger, H. Butt, M. B. Retschke and S. A. L. Weber, *Macromol. Rapid Commun.*, 2009, **30**, 1167–1178.

203 S. A. L. Weber, H.-J. Butt and R. Berger, in *Scanning Probe Microscopy in Nanoscience and Nanotechnology 3*, Springer, 2012, pp. 551–573.

204 E. Meyer, H. J. Hug and R. Bennewitz, *Scanning probe microscopy*, Springer, 2003, vol. 4.

205 G. Binnig, H. Rohrer, C. Gerber and E. Weibel, *Phys. Rev. Lett.*, 1982, **49**, 57.

206 G. Binnig, C. F. Quate and C. Gerber, *Phys. Rev. Lett.*, 1986, **56**, 930.

207 S. Morita, *Roadmap of scanning probe microscopy*, Springer Science & Business Media, 2006.

208 G. Meyer and N. M. Amer, *Appl. Phys. Lett.*, 1988, **53**, 1045–1047.

209 F. J. Giessibl, *Rev. Mod. Phys.*, 2003, **75**, 949.

210 J. M. Frost, K. T. Butler and A. Walsh, *APL Mater.*, 2014, **2**, 81506.

211 R. Garcıa and R. Perez, *Surf. Sci. Rep.*, 2002, **47**, 197–301.

212 S. Sadewasser and C. Barth, *Charact. Mater.*, 2002, 1–12.

213 F. J. Giessibl, *Science (80-.).*, 1995, **267**, 68–71.

214 J. H. Scofield, *Am. J. Phys.*, 1994, **62**, 129–133.

215 A. Guerrero, E. J. Juarez-Perez, J. Bisquert, I. Mora-Sero and G. Garcia-Belmonte, *Appl. Phys. Lett.*, 2014, **105**, 133902.

216 H. R. Moutinho, C.-S. Jiang, B. To, C. Perkins, M. Muller, M. M. Al-Jassim and L. Simpson, *Sol. Energy Mater. Sol. Cells*, 2017, **172**, 145–153.

217 A. Axt, I. M. Hermes, V. W. Bergmann, N. Tausendpfund and S. A. L. Weber, *Beilstein J. Nanotechnol.*, 2018, **9**, 1809–1819.

218 S. V Kalinin, B. J. Rodriguez and A. L. Kholkin, *Encycl. Nanotechnol.*, 2012, 2117–2125.

219 S. V Kalinin, B. J. Rodriguez, S. Jesse, J. Shin, A. P. Baddorf, P. Gupta, H. Jain, D. B. Williams and A. Gruverman, *Microsc. Microanal.*, 2006, **12**, 206–220.

220 B. J. Rodriguez, C. Callahan, S. V Kalinin and R. Proksch, *Nanotechnology*, 2007, **18**, 475504.

221 L. Collins, Y. Liu, O. S. Ovchinnikova and R. Proksch, *ACS Nano*, 2019, **13**, 8055–8066.

222 J. R. O'Dea, L. M. Brown, N. Hoepker, J. A. Marohn and S. Sadewasser, *MRS Bull.*, 2012, **37**, 642–650.

223 L. Jiang, J. Weber, F. M. Puglisi, P. Pavan, L. Larcher, W. Frammelsberger, G. Benstetter and M. Lanza, *Materials (Basel).*, 2019, **12**, 459.

224 H. Qiu, X. Dong, J. H. Shim, J. Cho and J. M. Mativetsky, *Appl. Phys. Lett.*, 2018, **112**, 263102.

225 M. Nonnenmacher, M. P. o'Boyle and H. K. Wickramasinghe, *Appl. Phys. Lett.*, 1991, **58**, 2921–2923.

226 J. L. Garrett and J. N. Munday, *Nanotechnology*, 2016, **27**, 245705.

227 U. Zerweck, C. Loppacher, T. Otto, S. Grafström and L. M. Eng, *Phys. Rev. B*, 2005, **71**, 125424.

228 R. D. Deslattes, E. G. Kessler Jr., P. Indelicato, L. de Billy, E. Lindroth, J. Anton, J. S. Coursey, D. J. Schwab, R. Sukumar, K. Olsen and R. A. Dragoset, X-ray transition database, https://www.nist.gov/pml/x-ray-transition-energies-database, (accessed 16 October 2021).

229 J. Hidalgo, A. Castro-Méndez and J. Correa-Baena, *Adv. Energy Mater.*, 2019, **9**, 1900444.

230 T. Kirchartz, J. A. Márquez, M. Stolterfoht and T. Unold, *Adv. energy Mater.*, 2020, **10**, 1904134.

231 K. Handloser, N. Giesbrecht, T. Bein, P. Docampo, M. Handloser and A. Hartschuh, *ACS Photonics*, 2016, **3**, 255–261.

232 W. Tian, C. Zhao, J. Leng, R. Cui and S. Jin, *J. Am. Chem. Soc.*, 2015, **137**, 12458–12461.

233 T. W. Crothers, R. L. Milot, J. B. Patel, E. S. Parrott, J. Schlipf, P. Müller-Buschbaum, M. B. Johnston and L. M. Herz, *Nano Lett.*, 2017, **17**, 5782–5789.

234 A. K. Gaigalas and L. Wang, *J. Res. Natl. Inst. Stand. Technol.*, 2008, **113**, 17.

235 K. D. Vernon-Parry, *III-Vs Rev.*, 2000, **13**, 40–44.

236 C. A. Volkert and A. M. Minor, *MRS Bull.*, 2007, **32**, 389–399.

237 J. Wiedemair, J.-S. Moon, D. E. Eaton, B. Mizaikoff and C. Kranz, eds. O. Dössel and W. C. Schlegel, Springer Berlin Heidelberg, Berlin, Heidelberg, 2010, pp. 372–375.

238 V. W. Bergmann, S. A. L. Weber, F. J. Ramos, M. K. Nazeeruddin, M. Grätzel, D. Li, A. L. Domanski, I. Lieberwirth, S. Ahmad and R. Berger, *Nat. Commun.*, 2014, **5**, 1–9.

239 I. M. Hermes, Y. Hou, V. W. Bergmann, C. J. Brabec and S. A. L. Weber, *J. Phys. Chem. Lett.*, , DOI:10.1021/acs.jpclett.8b02824.

2 Scope and aim

$MAPbI_3$ is a perovskite material that has been successfully used as light absorber in PSCs[1–4] and is studied for application in light-emitting diodes[5] as well as photodetectors.[6] To push the performance of $MAPbI_3$-based optoelectronic devices, the transport of electronic charges within single grains, across polycrystalline thin films and full PSCs has to be optimized for efficient charge extraction. In this work, my primary aim was to explore the influence of boundary structures on different lengths scales on the charge carrier transport to identify preferential pathways or bottlenecks, which should be eliminated in future devices. The boundary structures that I studied in the scope of this work span from subcrystalline domain walls, over grain boundaries, to heterointerfaces to the extraction layers in full PSCs (Figure 2.1). All these interfaces are thought impact the charge carrier dynamics in different ways.[7–12]

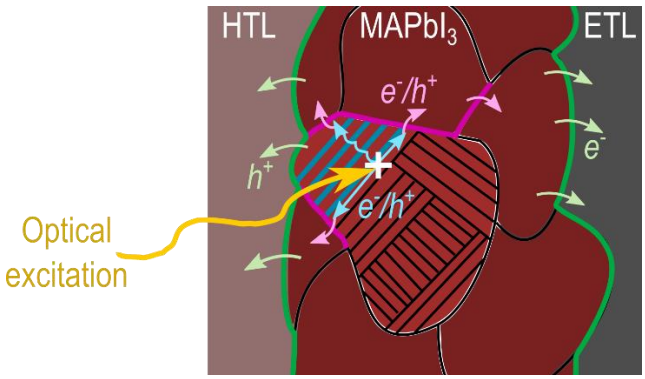

Figure 2.1: Schematic drawing of the charge carrier transport in a PSC following the charge carrier generation via illumination marked by the white cross. The boundary structures I investigated in the scope of this work are subcrystalline domain walls highlighted in blue, grain boundaries highlighted in pink and heterointerfaces to the extraction layers highlighted in green. To identify bottlenecks or preferential pathways, I studied the influence of these interfaces on the charge carrier transport, indicated by the bright blue, pink and green arrows, respectively.

In Chapter 3, I focused on boundary structures that could affect charge carrier dynamics within single $MAPbI_3$ grains. With tetragonal perovskite materials being prone to feature ferroic properties,[13] researchers have long suspected room temperature $MAPbI_3$ to be ferroelectric.[7,14,15] But while unambiguous proof for ferroelectricity remains elusive, studies by us and other research groups instead showed the presence ferro*elasticity* in room temperature $MAPbI_3$.[16–18] In our 2016 publication on subcrystalline ferroelastic domains in subchapter 3.1.1, we visualized the periodic arrangement of the domains and assigned a possible orientation via vertical and lateral PFM as well as 2D XRD.[16] Subsequently, I investigated the bulk orientation of the domains with respect to a (110) surface plane in subchapter 3.1.2, as well as the domains' response to external stimuli including heat, mechanical stress and electric field application by in-situ PFM in subchapter 3.1.3. Knowledge on the bulk arrangement of the domains and their response to stress and heat can aid to tailor domain patterns in the future for the most efficient charge transport.

Since ferroelastic domain walls disrupt the crystalline order as subcrystalline boundaries, they can display electronic anomalies by posing as local potential barriers or featuring a flexoelectric polarization, which could delay or accelerate the charge carrier transport, respectively.[8,19] In

subchapter 3.2.1, I explored the effect of domain walls on the drift current via vertical and lateral conductivity measurements using CAFM. Moreover, in our 2020 study on the influence of domain walls on the charge carrier diffusion via spatial and time-resolved PL microscopy in subchapter 3.2.2, we were able to resolve an anisotropy in the photocarrier diffusion that directly correlates to the domain arrangement.[20] The diffusion anisotropy shows that ferroelastic domain walls bear the potential to control the directionality of charge carrier dynamics within single $MAPbI_3$ grains.

In Chapter 4, I investigated the influence of grain boundaries in polycrystalline $MAPbI_3$ thin films on charge carrier drift and diffusion as well as light propagation. Generally, polycrystalline PV devices allow for a cheaper and easier production than monocrystalline solar cells. However, grain boundaries in polycrystalline films can introduce non-radiative recombination centers, impede with the charge carrier transport in the polycrystalline absorber and thereby lower the charge extraction[21] or increase the light outcoupling via scattering.[22,23] For PSCs, researchers have found that grain boundaries are largely benign for non-radiative recombination. On the other hand, grain boundaries are believed to impose significant barriers to the inter-grain carrier transport.[10,24–29] In the scope of this chapter, I focused on correlating the individual grain boundary morphology with its electronic transport properties. The knowledge on how the grain boundary morphology affects the charge carrier transport can further add to the improvement of the polycrystalline thin films, via passivation treatments as well as increases in crystallinity and grain size. Furthermore, the importance of efficient photon management in PSCs is on the rise to push the *PCE* towards the radiative efficiency limit. Therefore, I also studied the impact of grain boundaries as possible scattering centers on light propagation, which is required for photon recycling.[30,31]

Finally in Chapter 5, I explored the impact of heterointerfaces to the transport layers on the carrier extraction in full PSC devices. PSCs are *pin*-junctions, where the $MAPbI_3$ perovskite absorber is sandwiched between hole- and electron- selective extraction layers, which are called HTL and ETL, respectively. Here, suitable offsets in the conduction and valence band between HTL/ETL and $MAPbI_3$ ensure a high charge selectivity and efficient extraction. In PSCs, previous studies indicate that not only the band alignment and intrinsic conductivity of the extraction layers is decisive for efficient performance, but also their stability with respect to mobile ions in the perovskite absorber layer.[12,32] Particularly, the organic HTL can react with iodide ions, which lowers the material's doping concentration and thereby increases the series resistance. For our 2018 study on the influence of heterointerfaces on the charge extraction in PSCs in Chapter 5, we compared the charge distributions in two cells with apparently different concentrations of mobile ions via cross section KPFM.[33] Indeed, a penetration of negative charges into the HTL appeared to increase the series resistance of the full device, which suggests negative iodide ions reacted with the HTL. Thus, this study highlights the importance of chemically stable heterointerfaces to enable an efficient charge carrier extraction from PSCs.

Bibliography

1. Kojima, A., Teshima, K., Shirai, Y. & Miyasaka, T. Organometal halide perovskites as visible-light sensitizers for photovoltaic cells. *J. Am. Chem. Soc.* **131**, 6050–6051 (2009).

2. Lee, M. M., Teuscher, J., Miyasaka, T., Murakami, T. N. & Snaith, H. J. Efficient hybrid solar cells based on meso-superstructured organometal halide perovskites. *Science (80-.).* **338**,

643–647 (2012).

3. Kim, H.-S. *et al.* Lead iodide perovskite sensitized all-solid-state submicron thin film mesoscopic solar cell with efficiency exceeding 9%. *Sci. Rep.* **2**, 591 (2012).

4. Yoo, J. J. *et al.* An interface stabilized perovskite solar cell with high stabilized efficiency and low voltage loss. *Energy Environ. Sci.* **12**, 2192–2199 (2019).

5. Jaramillo-Quintero, O. A., Sanchez, R. S., Rincon, M. & Mora-Sero, I. Bright visible-infrared light emitting diodes based on hybrid halide perovskite with Spiro-OMeTAD as a hole-injecting layer. *J. Phys. Chem. Lett.* **6**, 1883–1890 (2015).

6. Ashar, A. Z., Ganesh, N. & Narayan, K. S. Hybrid Perovskite-Based Position-Sensitive Detectors. *Adv. Electron. Mater.* **4**, 1700362 (2018).

7. Frost, J. M. *et al.* Atomistic origins of high-performance in hybrid halide perovskite solar cells. *Nano Lett.* **14**, 2584–2590 (2014).

8. Warwick, A. R., Íñiguez, J., Haynes, P. D. & Bristowe, N. C. First-principles study of ferroelastic twins in halide perovskites. *J. Phys. Chem. Lett.* **10**, 1416–1421 (2019).

9. DeQuilettes, D. W. *et al.* Tracking photoexcited carriers in hybrid perovskite semiconductors: trap-dominated spatial heterogeneity and diffusion. *ACS Nano* **11**, 11488–11496 (2017).

10. Ciesielski, R. *et al.* Grain boundaries act as solid walls for charge carrier diffusion in large crystal MAPI thin films. *ACS Appl. Mater. Interfaces* **10**, 7974–7981 (2018).

11. Bergmann, V. W. *et al.* Real-space observation of unbalanced charge distribution inside a perovskite-sensitized solar cell. *Nat. Commun.* **5**, 1–9 (2014).

12. Kim, H.-S., Seo, J.-Y. & Park, N.-G. Impact of selective contacts on long-term stability of CH3NH3PbI3 perovskite solar cells. *J. Phys. Chem. C* **120**, 27840–27848 (2016).

13. Tagantsev, A. K., Cross, L. E. & Fousek, J. *Domains in ferroic crystals and thin films*. **13**, (Springer, 2010).

14. Stoumpos, C. C., Malliakas, C. D. & Kanatzidis, M. G. Semiconducting tin and lead iodide perovskites with organic cations: phase transitions, high mobilities, and near-infrared photoluminescent properties. *Inorg. Chem.* **52**, 9019–9038 (2013).

15. Snaith, H. J. *et al.* Anomalous hysteresis in perovskite solar cells. *J. Phys. Chem. Lett.* **5**, 1511–1515 (2014).

16. Hermes, I. M. *et al.* Ferroelastic Fingerprints in Methylammonium Lead Iodide Perovskite. *J. Phys. Chem. C* **120**, (2016).

17. Strelcov, E. *et al.* CH3NH3PbI3 perovskites: Ferroelasticity revealed. *Sci. Adv. Adv.* **3**, e1602165 (2017).

18. Kennard, R. M. *et al.* Ferroelastic Hysteresis in Thin Films of Methylammonium Lead

Iodide. *Chem. Mater.* **33**, 298–309 (2021).

19. Salje, E. K. H. Ferroelastic materials. *Annu. Rev. Mater. Res.* **42**, 265–283 (2012).

20. Hermes, I. M. *et al.* Anisotropic carrier diffusion in single MAPbI3 grains correlates to their twin domains. *Energy Environ. Sci.* **13**, 4168–4177 (2020).

21. Nelson, J. A. *The physics of solar cells*. (World Scientific Publishing Company, 2003).

22. Agarwal, A. M. *et al.* Low-loss polycrystalline silicon waveguides for silicon photonics. *J. Appl. Phys.* **80**, 6120–6123 (1996).

23. Liao, L. *et al.* Optical transmission losses in polycrystalline silicon strip waveguides: effects of waveguide dimensions, thermal treatment, hydrogen passivation, and wavelength. *J. Electron. Mater.* **29**, 1380–1386 (2000).

24. Castro-Méndez, A., Hidalgo, J. & Correa-Baena, J. The Role of Grain Boundaries in Perovskite Solar Cells. *Adv. Energy Mater.* **9**, 1901489 (2019).

25. Arias, D. H., Moore, D. T., van de Lagemaat, J. & Johnson, J. C. Direct measurements of carrier transport in polycrystalline methylammonium lead iodide perovskite films with transient grating spectroscopy. *J. Phys. Chem. Lett.* **9**, 5710–5717 (2018).

26. Yang, M. *et al.* Do grain boundaries dominate non-radiative recombination in CH 3 NH 3 PbI 3 perovskite thin films? *Phys. Chem. Chem. Phys.* **19**, 5043–5050 (2017).

27. Sherkar, T. S. *et al.* Recombination in perovskite solar cells: significance of grain boundaries, interface traps, and defect ions. *ACS energy Lett.* **2**, 1214–1222 (2017).

28. Snaider, J. M. *et al.* Ultrafast imaging of carrier transport across grain boundaries in hybrid perovskite thin films. *ACS Energy Lett.* **3**, 1402–1408 (2018).

29. Reid, O. G., Yang, M., Kopidakis, N., Zhu, K. & Rumbles, G. Grain-size-limited mobility in methylammonium lead iodide perovskite thin films. *ACS Energy Lett.* **1**, 561–565 (2016).

30. Pazos-Outón, L. M. *et al.* Photon recycling in lead iodide perovskite solar cells. *Science (80-.).* **351**, 1430–1433 (2016).

31. Crothers, T. W. *et al.* Photon reabsorption masks intrinsic bimolecular charge-carrier recombination in CH3NH3PbI3 perovskite. *Nano Lett.* **17**, 5782–5789 (2017).

32. Carrillo, J. *et al.* Ionic reactivity at contacts and aging of methylammonium lead triiodide perovskite solar cells. *Adv. Energy Mater.* **6**, 1502246 (2016).

33. Hermes, I. M., Hou, Y., Bergmann, V. W., Brabec, C. J. & Weber, S. A. L. The Interplay of Contact Layers: How the Electron Transport Layer Influences Interfacial Recombination and Hole Extraction in Perovskite Solar Cells. *J. Phys. Chem. Lett.* **9**, (2018).

3 Ferroelastic twins: Their properties and effect on photocarriers

Compounds with a perovskite crystal structure often display a variety of ferroic properties, including ferroelectricity and ferroelasticity (Chapter 1.3.1.1).[1,2] $MAPbI_3$ not only crystallizes in a perovskite structure, but additionally has a center ion with an electric dipole of 2.3 D, and could therefore exhibit a permanent ferroelectric polarization.[3] An early XRD study of $MAPbI_3$ by Stoumpos *et al.* suggested ferroelectricity as well as orientational crystal twins that were introduced by crystalline distortion, which is indicative of ferroelasticity.[4] Shortly after, Kutes *et al.* reported on the first experimental observation of ferroelectricity in $MAPbI_3$ via PFM.[5] However, their data interpretation was disputed by subsequent PFM studies,[6–8] which demonstrated instable polarization switching[6] and irreversible topography changes upon the application of a switching bias above 2.5 V.[7] Instead of ferroelectricity, these studies suggested capacitive effects, ionic motion or topography and mechanical crosstalk as origin of the PFM contrast.[7,9]

In our 2016 PFM study on polycrystalline $MAPbI_3$ thin films, we resolved a subcrystalline periodic pattern on micrometer-sized grains with a (110) crystal orientation (Figure 3.1). We attributed the periodic pattern to ferroelastic twin domains, which could form during the cubic-tetragonal phase transition to release internal strain, in agreement with Stoumpos *et al.*.[4] Bias switching experiments indicated the absence of an out-of-plane ferroelectric polarization in the domains (Chapter 3.1.1).[10] Subsequently, several research groups reproduced the same domain pattern via various characterization techniques, including PFM,[11–14] polarized light,[15] scanning microwave,[16] and transmission electron microscopy,[17] as well as x-ray[18,19] and neutron diffraction.[20] The diffraction and transmission experiments confirm that the observed pattern is not limited to the surface but is also present in bulk. I investigated the bulk orientation of the domains by resolving twin domains on the sidewalls of an isolated $MAPbI_3$ grain (Chapter 3.1.2). Furthermore, I was able to support our hypothesis on the ferroelastic nature of the domain pattern using PFM measurements above the cubic-tetragonal phase transition as well as mechanical switching (Chapter 3.1.3).[13,15,17,21]

Despite the discussions and uncertainty surrounding $MAPbI_3$'s ferroic properties, researchers began to explore implications of a possible ferroelectricity on electronic processes in perovskite-based optoelectronics early on. Some theoretical studies modelled the effect of ferroelectric domains on charge carrier transport. Among those, Frost *et al.* and Liu *et al.* proposed that charged ferroelectric domain walls attract photocarriers and facilitate the long diffusion lengths observed for PSCs.[22,23] The influence of ferroelastic domains on carrier dynamics only recently gained more attention, when two theoretical studies suggested a beneficial effect of ferroelastic domain walls on the charge carrier separation and transport.[24,25]

We have investigated the effect of subcrystalline ferroelastic domains on the charge carrier dynamics experimentally via CAFM (Chapter 3.2.1) and a correlated spatial- and time-resolved PL microscopy and PFM study (Chapter 3.2.2).[21] CAFM experiments and static PL experiments did not show an influence of the domains on the lateral conductivity and charge carrier distribution in agreement with a recent study by Xiao *et al.*.[26] However, using spatial- and time-resolved PL

microscopy, we were able to resolve an anisotropic diffusion behavior of photocharges: Carriers moving parallel to the ferroelastic domain walls exhibited higher diffusion constants than for carriers travelling perpendicular to the domain walls.[21]

3.1 Subcrystalline domains in $MAPbI_3$: Properties and nature

As demonstrated over the past five years, various microscopy and diffraction techniques are able to detect the twin domains in $MAPbI_3$.[10,11,20,12–19] Among these techniques, PFM is particularly suitable for an in-depth characterization, as it resolves domains with a nanometer resolution by probing the material's out-of-plane and in-plane electromechanical response (Figure 3.1). The real-space, high resolution visualization of the domain arrangement in $MAPbI_3$ facilitates the study of the possible domain influence on charge transport in PSCs when correlated with conductivity or photoluminescence measurements. Furthermore, PFM can directly capture changes in the domain structure upon heating across the ferroic cubic-tetragonal phase transition or switching events and thereby elucidate the nature of the domains.[13,15,27]

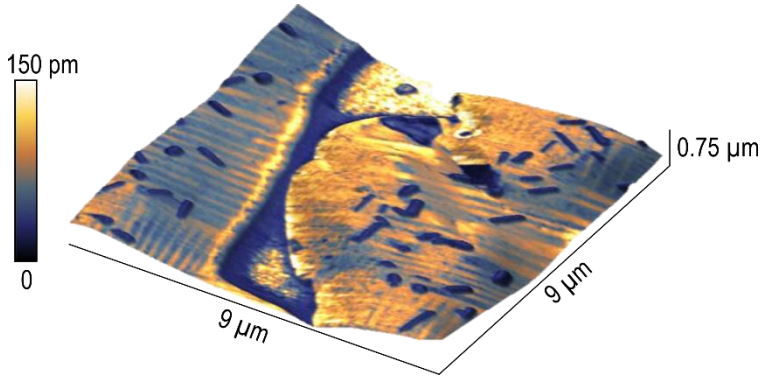

Figure 3.1: 3D overlay of AFM height of $MAPbI_3$ grains with vertical PFM amplitude. The PFM amplitude shows the distinct periodic domain pattern, which is indicative of ferroelastic twin domains. Protruding rods with low PFM amplitude likely are PbI_2 as degradation product of $MAPbI_3$ (V_{AC}=2.56 V, f_{AC}=260 kHz close to vertical contact resonance).

The following subchapters 3.1.1–3.1.3 focus on the structure and nature of the periodic twin domains in $MAPbI_3$. In our 2016 PFM study in Chapter 3.1.1, we imaged and characterized domain arrangements on micrometer-sized $MAPbI_3$ grains, which strongly resemble the characteristic fingerprints of ferroelasticity known from ferroic perovskite compounds such as PZT or PST.[10,28,29] With Chapter 3.1.2, I continued the study of the domain arrangement by imaging the piezoresponse on grain sidewalls to gain insights on the domain orientation in a bulk grain with respect to the interfaces. Since the domains can affect charge carrier dynamics in PSCs,[21] knowledge on their bulk orientation with respect to the extraction layer interfaces is important for device optimization. Lastly, the data presented in Chapter 3.1.3 aims at investigating the underlying nature of the domains. An unambiguous assignment of a ferroic character to $MAPbI_3$, requires an in-depth study of the domain behavior across the ferroic cubic-tetragonal phase transition and the material's switching behavior.[1] Here, I performed PFM measurements during heat treatments as well as mechanical and electrical switching experiments. My findings not only confirm the ferroelastic nature of the domains, but also demonstrate routes for targeted domain manipulation, which allow for further device optimization in PSCs.

3.1.1 Ferroelastic fingerprints in methylammonium lead iodide perovskite

Ilka M. Hermes,[†] Simon A. Bretschneider,[†] Victor W. Bergmann,[†] Dan Li,[†] Alexander Klasen,[†,‡] Julian Mars,[†,∥] Wolfgang Tremel,[‡] Frédéric Laquai,[†,§] Hans-Jürgen Butt,[†] Markus Mezger,[†,∥] Rüdiger Berger,[†] Brian J. Rodriguez,[⊥] and Stefan A. L. Weber[†,∥]

[†] *Max Planck Institute for Polymer Research, Ackermannweg 10, 55128 Mainz, Germany*

[‡] *Institute of Inorganic Chemistry and Analytical Chemistry, Johannes Gutenberg University Mainz, Duesbergweg 10-14, 55128 Mainz, Germany*

[§] *Solar and Photovoltaics Engineering Research Center (SPERC), King Abdullah University of Science and Technology (KAUST), Thuwal, Kingdom of Saudi Arabia*

[∥] *Institute of Physics, Johannes Gutenberg University Mainz, Staudingerweg 10, 55128 Mainz, Germany*

[⊥] *School of Physics and Conway Institute of Biomolecular and Biomedical Research, University College Dublin, Belfield, Dublin 4, Ireland*

-Published in the Journal of Physical Chemistry C (J. Phys. Chem. C) 2016, 120, 5724−5731, https://doi.org/10.1021/acs.jpcc.5b11469 -

Abstract

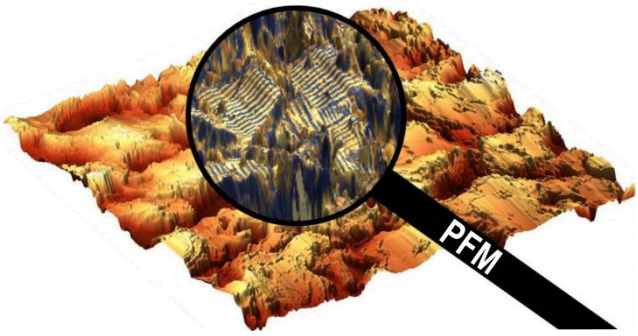

Methylammonium lead iodide ($MAPbI_3$) perovskite shows an outstanding performance in photovoltaic devices. However, certain material properties, especially the possible ferroic behavior, remain unclear. We observed distinct nanoscale periodic domains in the piezoresponse of $MAPbI_3(Cl)$ grains. The structure and the orientation of these striped domains indicate ferroelasticity as their origin. By correlating vertical and lateral piezoresponse force microscopy experiments performed at different sample orientations with X-ray diffraction, the preferred domain orientation is suggested to be the a_1-a_2-phase. The observation of these ferroelastic fingerprints appears to strongly depend on the film texture and thus the preparation route. The ferroelastic twin domains could form due to the introduction of strain during the cubic-tetragonal phase transition.

Introduction

The development of solar cells based on methylammonium lead iodide ($MAPbI_3$) perovskite has seen impressive dynamics over the past few years.[30−32] Intensive research has pushed the power conversion efficiency (PCE) of perovskite solar cells to a certified value of over 20%.[33] Besides their inexpensive production, the success of perovskite solar cells originates from the unique properties of the perovskite: A strong optical absorption and charge carrier diffusion lengths of up to 1 μm that lead to internal quantum efficiencies of more than 90%.[34−40] However, the physical origin of these properties and their dependence on the device architecture and on the preparation route are not fully understood.

A fundamental material property that has been suggested in the context of the unique solar cell performance is ferroelectricity.[22] Frost *et al.* suggested that charged ferroelectric domain walls could act as charge carrier-specific pathways through the perovskite grains.[22] It has also been proposed that ferroelectricity of the perovskite material causes the hysteretic anomaly that has been observed in the photocurrent-voltage (*j-V*) curves of perovskite solar cells.[22,41–45] This hysteresis can lead to an overestimation of the PCE and its origin is heavily discussed. It has been suggested that time-dependent processes, such as migrating ions, electronic traps, or the alignment of the spontaneous polarization upon applying an electric field, contribute to the hysteresis.[8,34,35,41,46–51] However, more recent publications indicate that ferroelectricity does not contribute to the hysteresis at all or only in a minor way, as opposed to ion migration and electronic traps.[46,47,50,52]

$MAPbI_3$, like other perovskite materials, fulfills the structural requirements for a ferroic material: The lead and the halide ions form a three-dimensional network of corner-sharing PbI_6 octahedra. The organic methylammonium cations (MA^+) occupy the cuboctahedral gap. At temperatures above 327 K, $MAPbI_3$ crystallizes in a cubic structure, between 165 and 327 K in a tetragonal structure and below 165 K in an orthorhombic structure.[4,53–55] The tetragonal structure at room temperature was found to crystallize either in the nonpolar, centrosymmetric space group $I4/mcm$[54,56,57] or the polar space group $I4cm$.[4,53] The symmetry lowering phase transition from the cubic $Pm\bar{3}m$[58] to the noncentrosymmetric tetragonal $I4cm$ structure in $MAPbI_3$ classifies as ferroelectric as well as ferroelastic.[1]

A ferroelastic phase transition leads to a distortion of the crystal lattice causing a spontaneous strain in the material – analogous to the spontaneous polarization / magnetization in ferroelectric / ferromagnetic materials. The internal strain can be compensated by the formation of twin domains oriented along different crystallographic axes. A tetragonal structure allows crystalline orientations along the a_1-, a_2-, and *c*-axes. Upon application of an external stress, the strain can be switched.[59] Like ferroelectricity, ferroelasticity is a nonlinear property and commonly observed in materials with a perovskite crystal structure.[1,60]

To shed light on the microscopic origin of these effects, atomic force microscopy (AFM) can correlate the topography of a sample to other local material properties, such as electrical potential, piezoelectricity, or conductivity.[49,61–63] In particular, piezoresponse force microscopy (PFM) can locally probe the electromechanical properties of piezoelectric samples. It is an AFM method based on the inverse piezoelectric effect. As ferroelectricity is always coupled to piezoelectricity, PFM can also visualize ferroic domains.[62,63] By scanning a surface in contact mode and simultaneously applying an ac voltage via a conductive cantilever, a piezoelectric material deforms periodically. The amplitude of the piezoresponse gives the magnitude of the electromechanical coupling and thus the positions of domain walls, where the material's piezoresponse is minimal. The phase between excitation and piezoresponse contains information about the orientation of the polarization within the domains. Two measurement modes are possible: (a) Vertical PFM uses the vertical cantilever deflection signal to detect the out-of-plane piezoresponse, and (b) lateral PFM uses the lateral deflection signal caused by torsion of the cantilever to detect the in-plane piezoresponse. The polarization direction of ferroelectric domains can be permanently switched by applying a dc bias

during a scan in contact mode.[62,63] Furthermore, PFM can locally measure ferroelectric hysteresis loops.

Several groups have performed vertical PFM measurements on $MAPbI_3$ perovskite films. Yet, the findings of these studies were contradictory. Kutes *et al.* observed switchable ferroelectric domains in their $MAPbI_3$ films,[5] which was confirmed by subsequent PFM studies.[43,64–66] However, Xiao *et al.* reported that they did not find any evidence of ferroelectricity using PFM.[8] Recently, two publications claimed that the $MAPbI_3$ perovskite does not exhibit ferroelectricity at room temperature based on PFM measurements and macroscopic polarization methods.[6,7] The previous PFM studies prepared the perovskite films by various preparation routines and obtained dense perovskite films with grain sizes up to 1 µm.

Here, we prepared $MAPbI_3$(Cl) films via solvent annealing, yielding in less dense films with grains up to 10 µm that exhibited a high crystalline orientation and a distinct morphology of multiple terraces. On top of these grains, we performed vertical and lateral PFM and locally resolved a striped domain structure with spacing between 100 and 350 nm in the PFM signal that could not be observed in their topography. The structure and the orientation of the domains suggest that $MAPbI_3$ is ferroelastic, causing the twin domain pattern when prepared as described. By correlating vertical and lateral PFM with X-ray diffraction experiments, we propose that the a_1-a_2-phase is the preferred orientation of polarization within these ferroelastic twin domains.

Results and Discussion

The topography of the solvent-annealed $MAPbI_3$ film showed grains in varying shapes and sizes that ranged between 1 and 10 µm in diameter (Figure 3.2a). The surface of these grains exhibited a distinct terrace structure, suggesting a high crystallinity of the $MAPbI_3$ compound. While on top of the terraces no extraordinary topographic features were observed, the vertical PFM phase (Figure 3.2b) and amplitude (Figure 3.2c) revealed a striped structure with a spacing of 100 nm up to 350 nm. In the PFM phase (Figure 3.2b), only a weak contrast between adjacent stripes was observed. For adjacent out-of-plane ferroelectric domains, a phase difference of 180° would be expected. However, the phase difference of only a few degrees in Figure 3.2b indicates that the polarization in these domains might be oriented partially in-plane. The piezoresponse amplitude (Figure 3.2c) showed the same structure as the PFM phase with a strong contrast e.g. in the magnified areas 1 and 2.

Materials with a center of inversion do not exhibit piezoelectricity.[67] Therefore, the presence of a piezoresponse on the perovskite grains suggests that the material does not crystallize in the centrosymmetric space group $I4/mcm$[54,56,57] but more likely in the polar space group $I4cm$. The piezoresponse increased linearly with the applied electric potential up to V_{ac} = 2.5 V (SI in Appendix 8.1, Figure 8.1).

Within single grains, distances between adjacent stripes are largely uniform. On different grains, however, the spacing varies between 100 and 350 nm. The amplitude profiles in Figure 3.2d were extracted along the red and the blue line in area 1 and area 2 in Figure 3.2c, respectively. While stripes of the same contrast on the grain in the magnified area 1 were on average 230 nm apart, stripes of the same contrast on the grain in area 2 had distances of only 120 nm. It appeared that

the spacing between the grains was correlated with the grain size.[68] However, due to the complex morphology of the perovskite grains, single grains could not be readily distinguished. A statistical analysis of this correlation was therefore not possible. Furthermore, both magnified areas showed that the stripes change their direction by 90° within a single grain. The 90° angle between the domains is in good agreement with the tetragonal crystal structure of $MAPbI_3$ at room temperature.[4,53–55] In area 1 the dark stripes became narrower toward stripes with a perpendicular orientation like needles. The periodic structure, the 90° direction change, and the correlation between domain size and grain size are reminiscent of the periodic ferroelastic twin domains in thin films of the ferroelectric and ferroelastic ceramics $Pb_{0.7}Zr_{0.3}TiO_3$ (PZT) and $Pb_xSr_{1-x}TiO_3$ (PST), observed by Ivry *et al.* as well as Matzen *et al.*, respectively.[28,29]

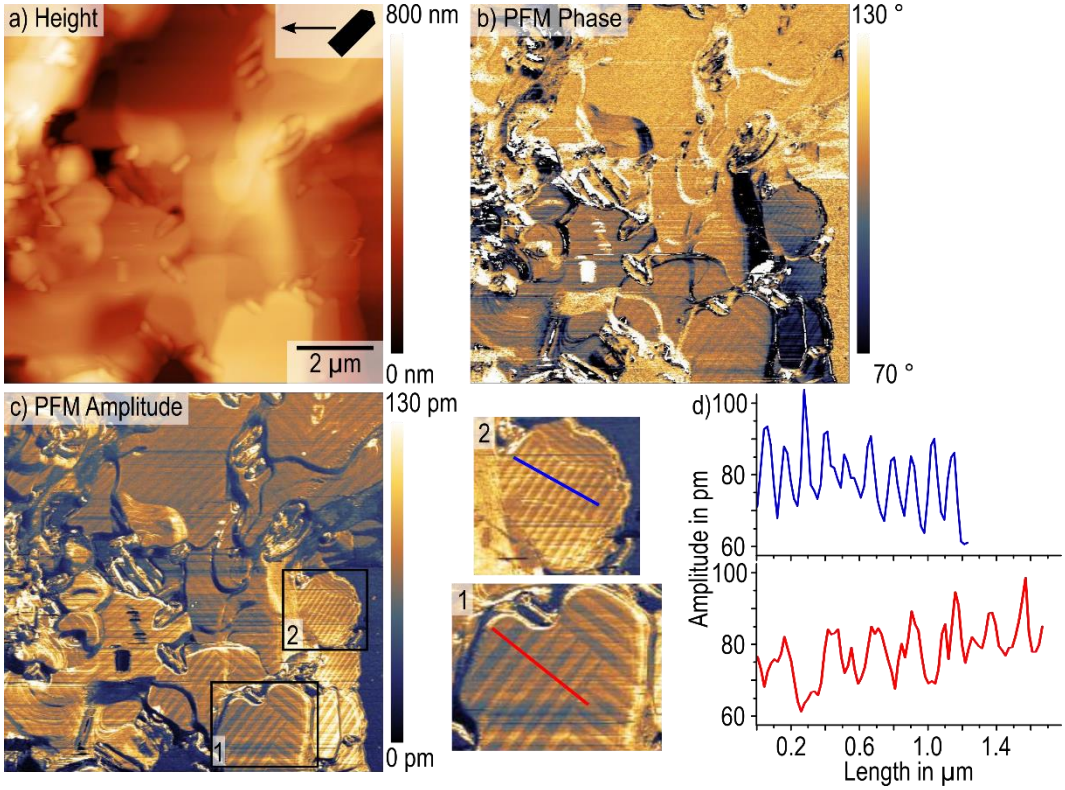

Figure 3.2: Vertical PFM measurement on $MAPbI_3$ film: a) Topography; b) PFM phase; c) PFM amplitude with magnified areas 1 and 2; d) amplitude profiles extracted along the red line in area 1 (red) and the blue line in area 2 (blue). V_{ac} = 2.5 V, f_{Drive} = 300 kHz, and scan angle = 45°; cantilever orientation and fast scan direction are indicated in the insets in the upper right corner of (a). Reprinted with permission from J. Phys. Chem. C 2016, 120, 10, 5724–5731. Copyright 2016 American Chemical Society.

Ferroelastic materials that grow under external stress can reduce this stress by forming twin domains. The external stress can be caused, for example, by epitaxial growth on a substrate that forces the compound into a structure it usually does not crystallize in. As the substrate in our perovskite samples is PEDOT:PSS, an amorphous polymer mixture, epitaxial strain seems unlikely. To exclude a further influence of the substrate, we additionally prepared perovskite films directly on ITO glass and observed the same periodic pattern as on PEDOT:PSS (SI in Appendix 8.1, Figure 8.2).

The preparation of the $MAPbI_3$ films was performed at 100 °C, where the compound crystallizes in a cubic structure. During cooling of the sample, a possibly ferroic phase transition to the tetragonal crystal structure occurs at around 54 °C.[4,53–55] We propose that this phase transition induces an internal strain that is compensated by the formation of twin domains due to ferroelasticity of the compound.

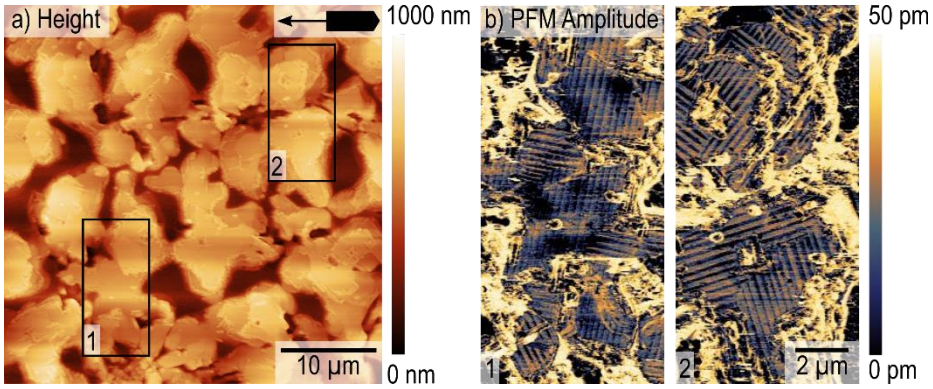

Figure 3.3: Vertical PFM measurement on $MAPbI_3$ film: a) Topography; b) PFM amplitude of magnified areas indicated by the black boxes in (a). V_{ac} = 1.5 V, f_{Drive} = 290 kHz, and scan angle = 0°; cantilever orientation and fast scan direction are indicated in the inset in the upper right corner of (a). Reprinted with permission from J. Phys. Chem. C 2016, 120, 10, 5724–5731. Copyright 2016 American Chemical Society.

While it may seem from Figure 3.2 that the direction of the stripes of adjacent grains is correlated, a closer analysis revealed that the twin domains in areas 1 and 2 in Figure 3.2c have an angle of 4.5° with respect to each other. A complementary measurement on a larger area of 40 × 40 µm² further confirmed that there is no correlation of the pattern across grain boundaries (Figure 3.3). Indicated by the black boxes in the topography (Figure 3.3a) are the areas that were magnified in Figure 3.3b to image the PFM amplitude on adjacent perovskite grains. Here, it is apparent that the stripe direction on adjacent grains is not correlated.

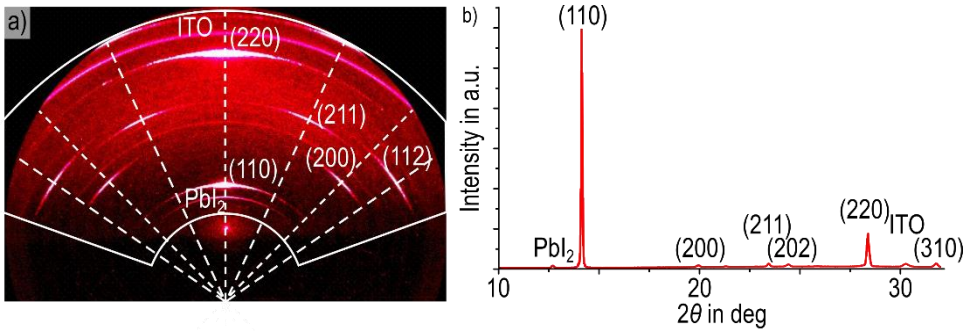

Figure 3.4: a) 2D X-ray diffraction pattern of $MAPbI_3$. Dashed lines indicate the azimuthal angle where maxima in the perovskite Bragg reflections were observed. b) Radially integrated intensity in the sector indicated in a by solid white lines. Reprinted with permission from J. Phys. Chem. C 2016, 120, 10, 5724–5731. Copyright 2016 American Chemical Society.

To further characterize the texture of the polycrystalline $MAPbI_3$ film, we used X-ray diffraction (XRD) (Figure 3.4a). The peak positions at 14.11°, 19.95°, 23.42°, 24.42°, 28.38°, and 31.76° extracted from the radially averaged XRD pattern correspond to the (110), (200), (211), (202), (220), and (310) Bragg reflections of the tetragonal $MAPbI_3$ structure, respectively (Figure 3.4b).[58,69–72] The weak reflection at 12.67° indicates the presence of crystalline PbI_2 in the

sample.[70,72,73] Likely, this is caused by partial degradation of $MAPbI_3$ during the annealing at temperatures of 100 °C.[74] Consistent with previous studies, no reflections related to $MAPbCl_3$ were observed. Furthermore, the absence of split peaks excludes a phase separation into iodide- and chloride-rich phases as origin of the domain pattern.[75]

The pronounced radial intensity variations observed in the 2D data sets indicate a strong preferential grain orientation within the polycrystalline perovskite film (Figure 3.4a). For the (110) and the (220) reflections, intensity maxima were observed close to the specular condition. In contrast, for the (200) reflection two off-specular maxima at $\chi = 45°$ and $\chi = 135°$ were observed (dashed lines in Figure 3.4a and SI in Appendix 8.1, Figure 8.3). This suggests that the (110) crystal plane of the perovskite grains is predominantly orientated parallel to the film surface. No preferred in-plane orientation of the grains was observed in the XRD measurements.

As the weak phase contrast in Figure 3.2b suggested, the observation of a vertical PFM signal could be caused by purely or partially in-plane oriented domains. In-plane components of the domain orientation can induce a vertical PFM signal via cantilever buckling (Figure 3.5a). Cantilever buckling can be distinguished from deflection of the cantilever by rotating the sample by 90°.[62] Signals from cantilever buckling are strongly dependent on the angle between cantilever and the domain orientation, whereas true out-of-plane sample deformations do not show such dependence. Upon rotating the sample by 90° with respect to the cantilever, we indeed observed a contrast inversion in the vertical PFM amplitude and phase (Figure 3.5b–e). This indicates that the orientation of the domains has an in-plane component and the vertical signal is at least partially caused by cantilever buckling.

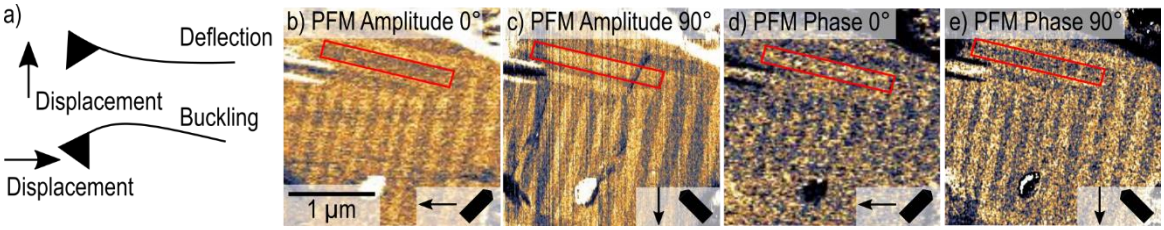

Figure 3.5 a) Illustration of difference between vertical deflection and cantilever buckling. (b–e) Vertical PFM measurement on $MAPbI_3$ film (V_{ac} = 2.5 V, f_{Drive} = 300 kHz, and scan angle = 45°; cantilever orientation and fast scan direction are indicated in the insets in the lower right corners. b) PFM amplitude at 0° sample rotation and c) at 90° sample rotation, d) PFM phase at 0° sample rotation, and e) at 90° sample rotation. The red box marks the same domain in (b–e). Reprinted with permission from J. Phys. Chem. C 2016, 120, 10, 5724–5731. Copyright 2016 American Chemical Society.

Considering the in-plane component of the polarization in the twin domains and the texture of the perovskite grains, there are three possible domain structures within the (110) crystal plane. The *a*-*c*-phase (Figure 3.6) consists of an in-plane oriented polarization along the *c*-axis of the unit cell that alternates with domains, in which the polarization is oriented along the *a*-axis in a 45° angle with respect to the surface. However, if only one of the domains is oriented out-of-plane (*a*-domain) while the other domain is oriented in-plane (*c*-domain), the domain pattern will most likely be visible in the topography of the sample. The differences in the lattice parameters *a* and *c* cause a roof-like structure in the topography. The latter is the case for the ferroelectric and ferroelastic $PbTiO_3$ and $BaTiO_3$ domains oriented along the *c*-axis (out-of-plane) and the *a*-axis (in-plane) of the

tetragonal unit cell.[29,76] Since the striped pattern in the $MAPbI_3$ grains could not be observed in the topography, we conclude that both twinning domains are either oriented in the same non-90° angle out-of-plane or purely in-plane.

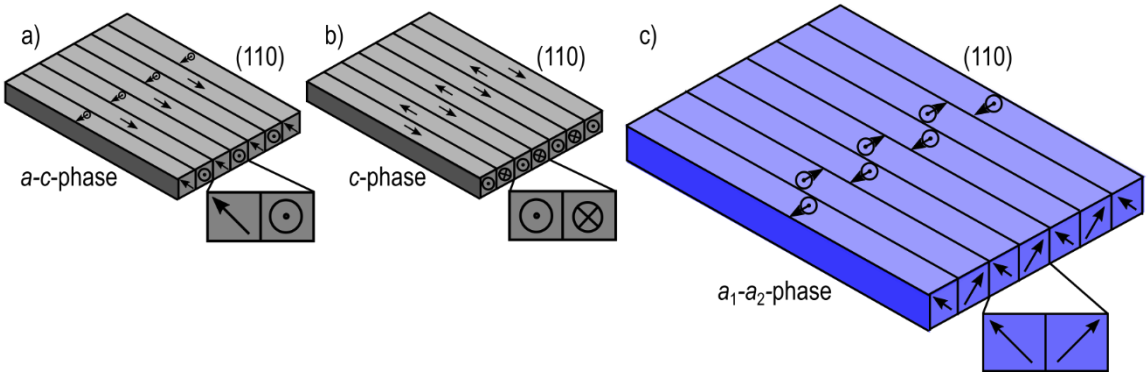

Figure 3.6: Possible orientations of the polarization (indicated by the arrows) in the ferroelastic twin domains within the (110) crystal plane of $MAPbI_3$: a) *a*-*c*-phase with alternating out-of-plane domains along the *a*-axis and in-plane domains along the *c*-axis, b) purely in-plane *c*-phase with antiparallel domains, and c) proposed a_1-a_2-phase in a 45° angle out-of-plane and 90° with respect to each other. Reprinted with permission from J. Phys. Chem. C 2016, 120, 10, 5724–5731. Copyright 2016 American Chemical Society.

A purely in-plane structure consists of neighboring domains in an antiparallel polarization orientation along the *c*-axis (*c*-phase, Figure 3.6b). Assuming such a domain structure and that the vertical PFM signal is only caused by cantilever buckling, we would expect the PFM amplitudes on all the stripes that are oriented parallel to the cantilever to be of the same value. However, in Figure 3.2c, the PFM amplitude shows the same alternating contrast on different stripe orientations and even for stripes parallel to the cantilever (e.g., in magnified area 1).

Based on the results presented so far, we propose a domain structure, in which the polarization of adjacent twin domains is oriented in a 45° angle to the surface and a 90° angle with respect to each other (a_1-a_2-phase, Figure 3.6c). The vertical PFM signal would be caused by a combination of cantilever deflection and buckling. Thereby, the observed inversion in the vertical PFM contrast upon sample rotation can be explained.

To further support the suggested a_1-a_2 domain structure within the $MAPbI_3$ grains, we performed lateral PFM measurements on the film. The perovskite film showed a lateral piezoresponse (Figure 3.7a and b), which resembled the periodic pattern observed in the vertical PFM measurements (Figure 3.2). The presence of a lateral PFM signal confirms that the orientation of the domain structures has an in-plane component. By measuring at 0° and 90° sample rotation, it is possible to determine the domain orientation from the change of the phase contrast (Figure 3.7a).[62] Upon rotating the sample by 90° from Figure 3.7a to b, the PFM phase contrast was inverted, while the contrast in the PFM amplitude remained largely unchanged (insets in Figure 3.7a and b). In the area highlighted by the red oval, this inversion is very distinct.

Both twin domains in the a_1-a_2-phase (Figure 3.6c) have the same angle with respect to the cantilever. Therefore, the contrast inversion in the PFM phase and the unchanged PFM amplitude upon sample rotation are in agreement with this domain structure assignment (Figure 3.6c).

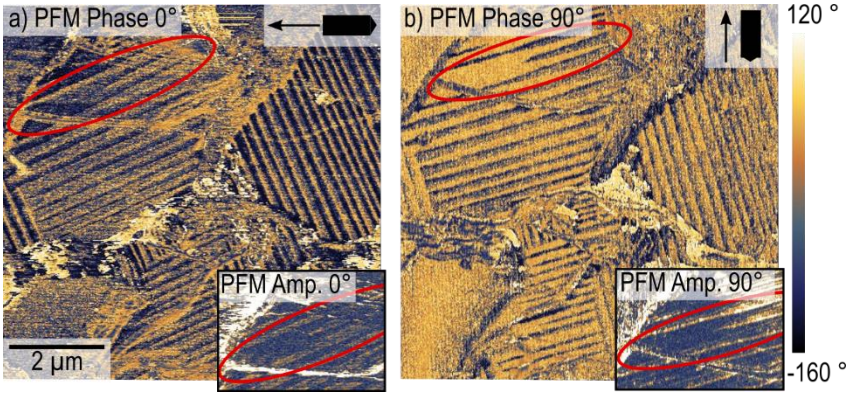

Figure 3.7: Lateral PFM on $MAPbI_3$ film: a) PFM phase at 0° and b) at 90° sample rotation. The insets in the lower right corners show the PFM amplitude both with the same data scale. The red oval marks the same domain (V_{ac} = 2.5 V, f_{Drive} = 600 kHz, and scan angle = 0°; cantilever orientation and scan direction are indicated in the insets in the upper right corners). Reprinted with permission from J. Phys. Chem. C 2016, 120, 10, 5724–5731. Copyright 2016 American Chemical Society.

Subsequently, we performed ferroelectric switching experiments to examine whether the ferroelastic stripes contribute to a possible ferroelectricity of the perovskite. During an AFM scan in contact mode, we applied dc voltages between +4 and −4 V to the tip with scan rates between 0.3 and 1 Hz. We did not use higher voltages to avoid damage to the sample. In the case of ferroelectric switching, the contrast of the phase of the piezoresponse should be inverted in a subsequent PFM scan. However, the contrast of the PFM signals and the arrangement of the stripes remained unchanged after applying a dc bias in agreement with Xiao *et al.*.[8] We locally measured ferroelectric hysteresis loops, which did not show a switching event (SI in Appendix 8.1, Figure 8.4).

The absence of polarization switching in the above experiments, however, does not generally exclude ferroelectricity. Wei *et al.* observed switching in the orientation of ferroelectric domains on the time scales of several seconds.[45] We performed the dc scans with velocities between 3 and 12 µm/s, which might be too fast to switch the domain orientation. In context of the *j-V* hysteresis, several studies have reported on slow processes within the perovskite layer and connected them to migrating ions or trapped charges.[8,34,35,41,47–49] The resulting internal electric field could also screen the applied dc voltage and interfere with the ferroelectric switching. As the perovskite is electrically conductive, it is also possible that the conductivity induces a breakdown of the tip voltage, which is then insufficient to switch the orientation of the polarization within the domains. Finally, if the ferroelectric polarization has in-plane components, these domains cannot easily be switched via AFM methods. The field that is applied to the film by an AFM tip is mainly perpendicular to the surface, which makes the switching of in-plane domains unlikely, but not impossible.[29]

To exclude topographic crosstalk as the origin of the periodic pattern in the PFM signals, we additionally probed the sample topography with the less invasive tapping mode AFM (Figure 3.8). Neither the height (Figure 3.8a) nor the amplitude error signal (Figure 3.8b) correlated to the striped pattern observed in the PFM amplitude signal of the same area, as shown in the upper right corner of Figure 3.8b. The striped pattern appeared in the PFM signals, only. However, we observed terraces and steps on the grains, indicating a layered crystallite growth.

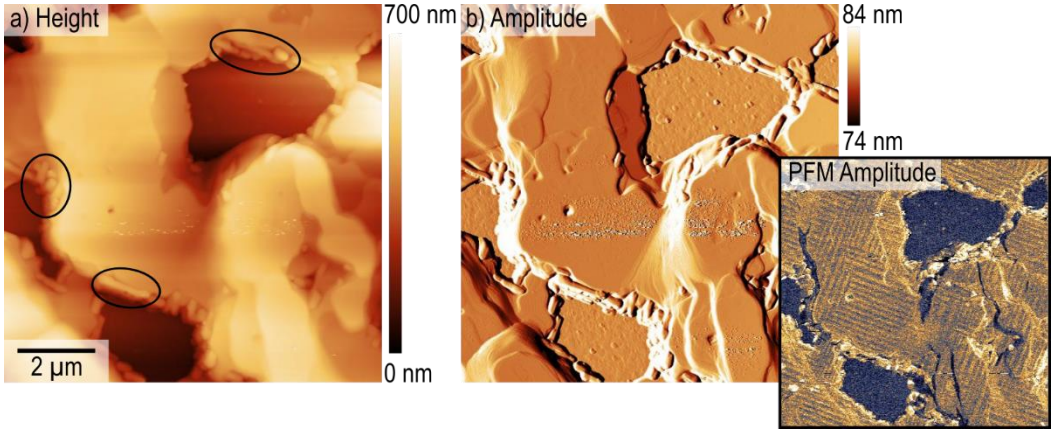

Figure 3.8: Tapping mode measurement on $MAPbI_3$ film. a) Topography and b) amplitude error signal. The PFM amplitude of the same area is shown in the upper right corner of b) for comparison. Reprinted with permission from J. Phys. Chem. C 2016, 120, 10, 5724–5731. Copyright 2016 American Chemical Society.

The perovskite layer was up to 1 µm thick but did not completely cover the substrate. Holes reaching down to the PEDOT:PSS, corresponding to the dark areas in the height channel (Figure 3.8a), showed no PFM response (Figure 3.8b). We can therefore exclude that the observed piezoresponse was caused by the substrate. At the edges of the grains, we observed small rods, highlighted by the black ovals in Figure 3.8a, which are between 150 and 700 nm long and 100 to 200 nm wide. We assigned these rods to the perovskite degradation product PbI_2. This assignment is in agreement with the XRD results discussed above (Figure 3.4) and UV–vis spectroscopy results (SI in Appendix 8.1, Figure 8.5).

Summary

We examined the electromechanical response of micrometer-sized $MAPbI_3$ grains by PFM. Distinct periodic domains were observed with distances between 100 and 350 nm. These striped domains in the piezoresponse were oriented either parallel or perpendicular with respect to each other - a characteristic fingerprint of ferroelasticity.[59] Previous PFM studies on polycrystalline perovskite films did not observe such a domain pattern. These studies used different preparation routes, such as the successive spin coating/annealing routine[5] or a two-step thermal/solvent annealing routine,[8] and yielded dense films of $MAPbI_3$ grains with sizes up to 1 µm. None of the studies obtained grains with a similar terrace structure as the samples presented in this study. However, independent from the observation of the domain pattern, ferroelasticity is a property that would be present in $MAPbI_3$, even when prepared otherwise. The XRD results revealed that the (110) crystal plane is oriented parallel to the sample surface. By performing vertical and lateral PFM experiments at 0° and 90° sample rotation, we propose that a polarization within the ferroelastic domains is oriented in the a_1-a_2-phase with a 45° angle with respect to the sample surface. These domains might also be ferroelectric, but so far, ferroelectric switching experiments did not show a switchable out-of-plane polarization in the perovskite films. Based on our results, we propose that $MAPbI_3$ is ferroelastic and that periodic twin domains form to compensate internal strain introduced by the cubic-tetragonal phase transition following sample annealing.

To finally prove ferroelasticity in $MAPbI_3$ perovskite, further measurements will be necessary such as mechanic hysteresis experiments. Conducting ferroelastic domain walls that can be caused

by head-to-head and tail-to-tail orientation could be an explanation of the increased charge carrier diffusion lengths in large $MAPbI_3$ grains, as suggested by Frost *et al.*.[22] They could also contribute to the *j-V* hysteresis by trapping free charge carriers in defects. To further investigate the properties of the possibly ferroic domain walls in $MAPbI_3$, local conductivity measurements e.g., via conductive AFM with and without illumination, will be required.

Experimental

Sample Preparation. Methylammonium iodide (CH_3NH_3I) was synthesized as described by Lee *et al.*.[32] Lead chloride ($PbCl_2$, Sigma-Aldrich, 99.999%) was dehydrated under high-vacuum conditions and in nitrogen atmosphere at 60 °C. The perovskite solution was prepared in a 3:1 molar ratio of the precursors CH_3NH_3I and $PbCl_2$ with a concentration of 40wt% in anhydrous dimethylformamide (DMF, Sigma). Indium tin oxide (ITO) substrates (PGO, $R_{\square} \leq 20\ \Omega/\square$) were cleaned with 2% Hellmanex II, acetone, and isopropanol and treated with an argon plasma for 20 min prior to the deposition of filtered (450 nm) poly(3,4-ethylenedioxythiophene) polystyrene-sulfonate (PEDOT:PSS, Heraeus Clevios P VPAI 4083) in water. The PEDOT:PSS/water mixture was deposited on the substrate by spin-coating at 2500 rpm for 5 s, followed by 5000 rpm for 25 s and subsequently annealed at 140 °C for 20 min. The samples were transferred into a nitrogen-filled glovebox with less than 1 ppm of H_2O. The perovskite solution was kept at 60 °C prior deposition. For a 1 by 1 in. sample, around 100 μL of solution was used and spin-coated for 45 s at 2000 rpm. The samples then rested at least 30 min in the glovebox. For the solvent annealing, the samples were placed on the hot plate, and 10 μL of DMF was dropped on the hot plate, similar to Xiao *et al.*.[9] The substrates and the DMF were covered with a watch glass in a way that the DMF could dissipate during the solvent annealing. The substrates were annealed for 1 h at 100 °C in the presence of DMF and in a second annealing step in nitrogen atmosphere for another hour at 100 °C. The cells were kept at least 12 h in the glovebox prior to measurements.

Piezoresponse Force Microscopy. Piezoresponse characterization of the perovskite films was performed on an MFP3D atomic force microscope from Asylum Research (Oxford Instruments) and an HF2 lock-in amplifier by Zürich Instruments. To avoid degradation of the hygroscopic perovskite material by humidity, the MFP-3D was operated in a glovebox in nitrogen atmosphere. Following the preparation, the samples were quickly transferred from the preparation glovebox into the MFP-3D glovebox. The PFM measurements were performed at room temperature with PPP-EFM cantilevers from Nanosensors with free resonance frequencies of 70 kHz and spring constants of $k \sim 2$ N/m. AC voltages with peak amplitudes between 1 and 2.5 V were applied to the conductive cantilevers to excite the material. We chose ac frequencies of around 300 kHz, just below the contact resonance to make use of the resonance enhancement. No additional back electrode was used, a small area of the perovskite was removed by scratching, and PEDOT:PSS was connected to ground. For switching experiments, the sample was scanned in contact mode at scan speeds below 0.5 Hz, while simultaneously applying a dc voltage of up to 4 V via the conductive cantilever. Lateral PFM was performed at a drive frequency of 600 kHz. We used an AC amplitude of 2.5 V.

X-ray Diffraction. X-ray diffraction of the perovskite film was measured using Cu Kα radiation (Rigaku MicroMax 007 X-ray generator, Osmic Confocal Max-Flux curved multilayer optics). The sample was mounted in reflection geometry at an incident angle of 4.5° on a six-circle

diffractometer. 2D diffraction patterns were recorded by an image plate detector (Mar345, 150 µm pixel size) at a sample–detector distance of 356.83 mm.

UV–Vis Absorption. The absorption spectrum of the $MAPbI_3$ film was measured with a PerkinElmer Lambda 900 spectrometer with integrated sphere.

Author Contributions

I.M.H. performed the PFM measurements and interpreted the PFM data with B.R. and S.A.L.W., who supervised this work; I.M.H. and S.A.B. prepared the $MAPbI_3$ samples; I.M.H., J.M and M.M. performed and interpreted the XRD measurements; I.M.H. and A.K. performed the UV-vis experiments and I.M.H. interpreted the respective data; H.-J.B., and R.B., contributed to the data interpretation. I.M.H. wrote the manuscript under supervision of S.A.L.W. with help of B.R., H.-J.B., R.B. and M.M.; All authors contributed to the scientific discussion and revision of the manuscript.

Associated Content

The Supporting Information can be found in the Appendix 8.1 and contains:

PFM amplitude in dependence of V_{ac} voltage, PFM measurement of $MAPbI_3$ on ITO, intensity distributions of the (110) and the (200) Bragg reflections, ferroelectric switching experiment, UV–vis absorption spectra of $MAPbI_3$.

Acknowledgements

The authors thank Doru C. Lupascu and Florian Johann (Asylum Research) for vivid discussions. R.B. and V.W.B. thank the IRTG 1404 for funding, F.L. thanks the Max Planck Society for funding the Max Planck Research Group, and D.L. thanks China Scholarship Council (CSC) for funding. J.M. and M.M. acknowledge the MAINZ Graduate School of Excellence, funded through the Excellence Initiative (DFG/GSC 266).

-Publication end-

3.1.2 Domain orientation in bulk $MAPbI_3$

- Unpublished-

Introduction

To investigate the nature of the subcrystalline domain pattern resolved via PFM, several research groups reproduced the domain pattern with a variety of characterization techniques.[11–20] While many of these subsequent studies used surface-sensitive AFM techniques, diffraction experiments by Rothmann *et al.*, Kennnard *et al.*, and Medjahed *et al.*, among others, offered vital insights on the presence of domains and their orientation in the bulk material.[17–20] The domain arrangement in bulk $MAPbI_3$ is significant when we consider that domains and/or domain walls affect charge carrier dynamics in $MAPbI_3$-based optoelectronic devices, as suggested by our 2020 study and several theoretical studies (Chapter 3.2.2).[21–24,77] Since several researchers reported on a preferential (110) crystal orientation in $MAPbI_3$ thin films,[78–81] the relative orientation of domain walls in bulk with respect to the (110) plane is of particular interest: For the domain walls oriented

perpendicular to the interfaces of absorber and extraction layers, the charge extraction could be faster than for angles below 90°.[21]

Rothmann *et al.* were first to propose domain walls along the (112) crystal plane, which serves as mirror plane between *a*- and *c*- twin domains.[17] Here, *a*-domain refers to a domain with an in-plane *c*-axis, while in *c*-domains the *c*-axis is orientated perpendicular to the surface. Later publications corroborated (112) domain walls,[18,19] which translates to an angle of 58° between the (110) plane and the (112) plane.[82] Typically, *a*-*c*-domains result in height differences visible in the AFM topography. However, the twin domains observed in our PFM study (Chapter 3.1.1) appeared to be purely in-plane a_1-a_2-domains. Using diffraction methods, a_1-a_2-domains are more difficult to distinguish and characterize.[18] Kennard *et al.* suggested domain walls between a_1 and a_2 domains are also oriented along the (112) crystal plane, while Strelkov *et al.* proposed domain walls with 70° or 110° angle with respect to (110), based on polarized light microscopy.[15,18]

Results and discussion

To gain insights on the domains wall orientation with respect to the predominant (110) surface plane for a_1-a_2-domains, I imaged domains on the sidewalls of $MAPbI_3$ crystals via lateral PFM. In order to access the sidewalls, I changed the preparation routine by performing the solvent annealing step in ambient conditions instead of N_2. Researchers have shown that the presence of humidity during the annealing step can increase the crystallinity as well as the crystal size without degradation.[83–86] The resulting $MAPbI_3$ films contained large isolated crystallites and one of them featured sufficiently flat sidewall slopes to access with the cantilever during the PFM scan. 2D XRD on a comparable sample using the same preparation routine showed a purely tetragonal $MAPbI_3$ phase with a preferential (110) crystal orientation, in agreement with our previous findings (Figure 3.4, SI in Appendix 8.2, Figure 8.11).[10,21]

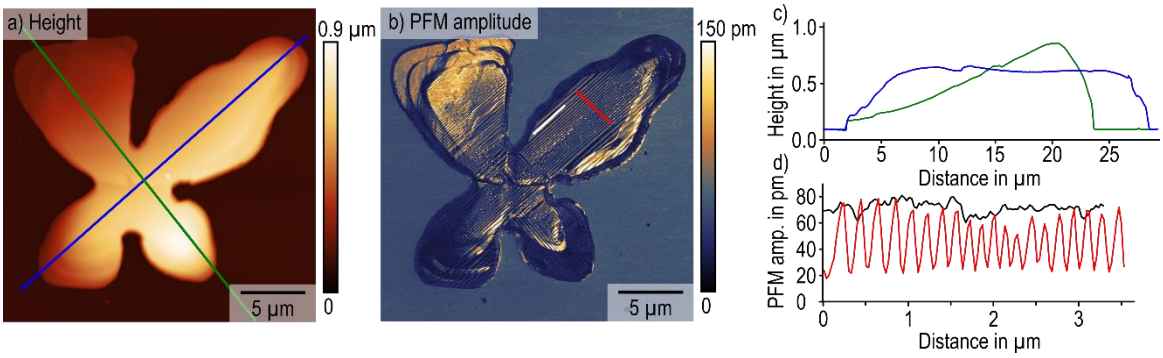

Figure 3.9: Lateral PFM measurement on a large, isolated $MAPbI_3$ grain on fused silica. a) The height channel shows a four-armed crystallite with a maximum thickness of 0.8 µm. b) The PFM amplitude displays the characteristic striped domain pattern assigned to ferroelasticity. c) Height profiles extracted along green and blue line in a). d) PFM amplitude profiles extracted along the red and white line in b), showing an average domain spacing of 130 nm in the red profile. Lateral PFM performed with 2V AC excitation close to lateral contact resonance at 718 kHz.

A lateral PFM measurement on the $MAPbI_3$ grain with accessible sidewalls captured the periodic fingerprint of ferroelastic twin domains with a particularly sharp contrast (Figure 3.9). This grain featured four arms that stretched over a maximum diameter of ~26.5 µm. From the line profile of the height in Figure 3.9c, I found a thickness gradient along the green profile and a maximum thickness of 0.8 µm. The lateral PFM amplitude in Figure 3.9b and the red line profile in d) feature

periodic domains with spacings between 70 and 190 nm, while the black line profile illustrates the absence of a PFM contrast along a single domain. Most importantly, I not only resolved the domain pattern on top, but also on the sidewalls of the grain. Overlaying the lateral PFM amplitude onto the 3D topography visualizes the domain wall orientation on the sidewalls of the $MAPbI_3$ grain, which allowed determining the domain wall orientation with respect to the surface plane (Figure 3.10).

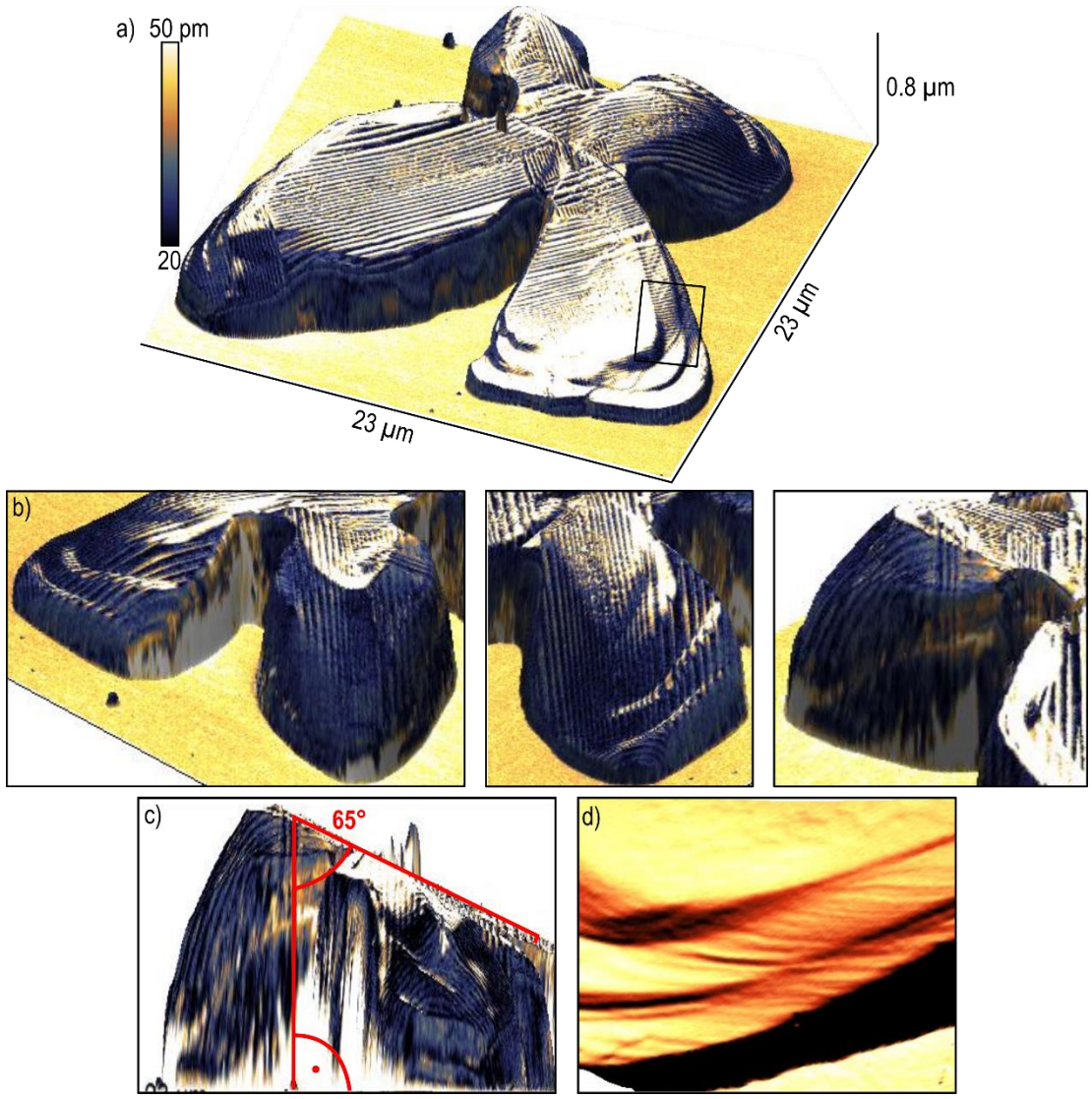

Figure 3.10: a) Three-dimensional overlay of AFM height and lateral PFM amplitude from Figure 3.9 to visualize the domain pattern on the sidewalls of the $MAPbI_3$ grain. b) Enlarged image details show the sidewall domain arrangement from different perspectives, c) Image detail showing the 90° angle of the domain with respect to the substrate interface and the 65° angle with respect to the tilted grain surface. d) Deflection image detail showing terraces and steps, indicative of the (110) surface plane, extracted at the position of the black box in a).

Based on the contrast-enhanced PFM signal on the grain sidewalls, I found that domains resolved on the grain surface continue on the sidewalls without directional change (Figure 3.10a). The angle of the domains on the sidewalls with respect to the substrate interface is ~90°, as displayed in the enlarged image details from different perspectives in Figure 3.10b. The absence of a directional change between the domains imaged on the grain surface and sidewalls as well as the

90° angle from the sidewall domain pattern to the substrate suggest a perpendicular alignment of domains within the bulk material.

Analyzing the sidewall domain pattern with respect to the grain surface instead of the substrate interface, I measured a 65° angle, since the grain featured a considerable height gradient (Figure 3.10c). However, the deflection image detail of the same scan (Figure 3.10d) showed a distinct terrace structure with several steps, observed previously on the (110) surface plane of $MAPbI_3$ (Figure 3.8). Hence, I assume that the height gradient is a result of a stepwise increase of the layer thickness instead of a tilt in the (110) surface plane.

Summary

Lateral PFM measurements on the accessible sidewalls of a large $MAPbI_3$ grain revealed that domains imaged on the sidewalls are likely aligned in a 90° angle with respect to the substrate. The orientation of the domains on the grain sidewalls suggests an according bulk arrangement: Perpendicular to the (110) surface plane. Practical implications of this result arise from our subsequent study in Chapter 3.2.2. Here, we observed that twin domains facilitate a faster charge carrier transport parallel to domain walls.[21–24,77] Therefore, a perpendicular bulk domain alignment with respect to the interfaces between $MAPbI_3$ and the extraction layers is the ideal condition for fast and efficient charge extraction in a PV device. This finding is in direct agreement with previous investigations that reported on a facet dependence of the photocurrent and an increase in the PSC performance for (110) surface planes in the $MAPbI_3$ layer.[87,88]

Experimental

Sample preparation:

See Chapter 3.1.1 for the preparation of the precursor solution and cleaning procedure of the fused silica substrate.

Spin-coating was performed at 1750 rpm for 60 s with an acceleration of 250 rpm/s in a N_2-Glovebox. After spin-coating, the samples were first annealed at room temperature for 30 minutes inside the glovebox, then transferred out of the glovebox for a solvent annealing step at 100 °C for 60 min in air on a preheated hot plate.[9] Immediately after the solvent annealing, the samples were moved into another nitrogen glovebox for storage and PFM characterization.

Piezoresponse force microscopy (PFM):

See Chapter 3.1.1 for the resonance-enhanced lateral PFM measurement.

Here, I used a conductive platinum-iridium coated SCM PIT-V2 cantilever from Bruker with a free resonance frequency of around 70 kHz and spring constant of k ~ 2.7 nN/nm. A metal plate served as back electrode of the sample.

3.1.3 Probing the nature of $MAPbI_3$'s twin domains

- Unpublished-

Depending in the influence of the twin domain in $MAPbI_3$ on charge carriers and the device performance in PSCs,[21–24,26,77] researchers have to investigate ways to either eliminate, introduce or

tailor domain arrangements. A detrimental effect of the domains on the device stability, as suggested by Xiao *et al.* and Kennard *et al.,* would entail an elimination of the domains or minimization of the domain density.[18,26] On the other hand, a positive effect of the domain walls on the charge carrier diffusion and recombination, as proposed by several theoretical studies, would call for a purposeful introduction of domains and control over the domain arrangement.[21–24] A targeted manipulation of the domains requires a detailed understanding of the origin, nature and properties of the periodic domain pattern.

The mechanistic origin of $MAPbI_3$'s subcrystalline domains has sparked discussion in the recent years. Particularly the interpretation of the PFM contrast was subject to vivid debates on whether or not ferroelectricity/-elasticity causes the observed periodic signal.[11–14,16,21,27,89,90] Several groups assigned the PFM contrast to ferroelectricity based on the contrast formation in stereotypical ferroelectrics.[11,13,14] Here, the inverse piezoelectric effect, present in all ferroelectrics, leads to a characteristic sample deformation upon voltage application, classified as true electromechanical sample response.[62,91,92] However, subsequent reports on PFM contrast formation in $MAPbI_3$ found indications that the sample response may not be truly electromechanical, but instead a combination of electrostatic and mechanical crosstalk.[12,89,90] In fact, all PFM studies on $MAPbI_3$ resolved the periodic domain pattern via resonance-enhanced PFM – a technique, which is notoriously prone to topography and mechanical crosstalk.[91,92] Resonance-enhanced PFM amplifies the inherent piezoresponse of the sample by using an AC excitation frequency close to the contact resonance of the cantilever (Figure 1.18).[62] Yet, the contact resonance reacts highly sensitive towards changes in the tip-sample contact mechanics. A local change in the nanomechanical sample properties as anticipated for ferroelastic crystal twins could therefore introduce a shift of the contact resonance and lead to mechanical crosstalk in the PFM measurement.[91,92] Combined with an electrostatic crosstalk caused by electronic and ionic capacitive effects, the PFM contrast could have been wrongfully assigned to a true electromechanical behavior and, thus, ferroelectricity.[12,89,90]

Macroscopic ferroelectric switching experiments further support this hypothesis. Among others, Beilsten-Edmands *et al.* and Xiao *et al.* have not found indications for the presence of ferroelectricity on $MAPbI_3$ perovskite.[7,8,47,93–95] On the other hand, most materials characterized via ferroelectric switching experiments are insulating ceramics with large band gaps.[1,96,97] $MAPbI_3$ is a semiconductor with a high ion mobility, which complicates traditional ferroelectric switching experiments: The low band gap of 1.5-1.6 eV[4,58,98,99] leads to significant leakage currents during macro- or microscopic ferroelectric characterization and, therefore, impairs the reliability of switching experiments.[1,7,94,100–102] Additionally, mobile ions present in $MAPbI_3$ can screen the ferroelectric switching field,[3,48,95,103–105] or, on the contrary, cause a false polarization switching signal by redistributing.[1,3,47,94] Therefore, an unambiguous verdict on ferroelectricity in $MAPbI_3$ is particularly challenging.

Because of the limited reliability of switching experiments for certain materials, Tagantsev advocates for classifying ferroics based on their crystal symmetry: Ferroic materials exhibit symmetry-breaking crystallographic phase transition from a symmetric high temperature phase to the ferroic phase.[1] For $MAPbI_3$, the symmetry relation between the cubic and room temperature

tetragonal phase remains unclear, since different studies report on either a polar[4,53,102] or a non-polar[20,54,56,57] symmetry for the material's tetragonal phase (Chapter 1.3.1).

Here, I investigated the possible nature of the domain pattern in $MAPbI_3$ by probing the domain behavior across the phase transition temperature. Furthermore, I explored the mechanical and electrical switching behavior by applying mechanical pressure via the AFM tip and a lateral electric field, respectively. The change of the domain arrangement upon heat treatment and mechanical pressure application not only supports our initial classification of $MAPbI_3$ as ferroelastic (Chapter 3.1.1) but also offers routes for targeted domain engineering.

3.1.3.1 Domain behavior across the cubic-tetragonal phase transition

Introduction

Ferroic domain formation during a crystallographic phase transition originates from a loss of point symmetry from the high temperature phase to the low temperature phase.[1,106] The symmetry relation between the space groups of high and low temperature phase dictate whether the resulting domains have ferroelectric and/or ferroelastic properties.[1,107] A ferroelastic phase transition requires a change in the crystal class, while a ferroelectric phase transition requires the loss of inversion symmetry during the phase transition.[1,107,108]

$MAPbI_3$ crystallizes in a cubic $Pm\bar{3}m$ at high temperatures and undergoes a phase transition to its room temperature tetragonal structure at 54-59 °C.[4,20,54,56,58] For $MAPbI_3$'s tetragonal structure, researchers suggest two different space groups: Either the centrosymmetric $I4/mcm$[54,56,58] or $I4cm$[4,53] – a polar subgroup of $I4/mcm$. $I4cm$ differs from $I4/mcm$ in its lack of a mirror plane, allowing an ionic displacement in the unit cell that leads to a permanent polarization and thus ferroelectricity.[109] Both space groups are difficult to differentiate in powder XRD, since they feature the same translation symmetry, as well as in single crystal diffraction due to heavy twinning.[20] Independent of the exact tetragonal space group, $MAPbI_3$'s phase transition 54-59 °C [4,20,54,56,58] includes a change of the crystal class – from cubic to tetragonal – as required for ferroelasticity (Chapter 1.3.1).

To investigate the phase transition as possible origin of the domain pattern resolved via PFM, I performed two temperature-dependent PFM experiments crossing the phase transition temperature. In both experiments, I conducted the first scan at room temperature in the tetragonal phase, the second at elevated temperatures of 70-75 °C in the cubic $MAPbI_3$ phase and the third at room temperature in tetragonal phase. The domain pattern disappeared during the heating step and reappeared after cooling the sample back down to room temperature, indicating the cubic-tetragonal phase transition is indeed the origin of the domain formation.[4,13,14,17] The change of the domain arrangement in the second experiment suggests that heat treatment could be used for targeted domain manipulation.

Results and discussion

For the heating experiment, I prepared a $MAPbI_3$ thin film on an ITO substrate using solvent annealing and $PbCl_2$ as precursor to achieve large and highly oriented grains.[9,69,110,111] Prior to the heating experiment using a Peltier element, I imaged a recognizable sample area in lateral PFM at room temperatures in Figure 3.11a and focused on two grains on the top right and the bottom left.

Both grains featured the characteristic periodic domain pattern,[10–17] which was particularly distinct in the PFM amplitude. The height and deflection signals showed flat terraces and steps in the grain structure as well as some rod-shaped particles on the grain edges, which likely are PbI_2 crystallites as the predominant degradation product of $MAPbI_3$ (Chapter 3.1.1).

Upon reaching a stage temperature of 75 °C, I waited until a thermal equilibrium was established to avoid thermal drift and repeated the lateral PFM measurement on the same measurement area (Figure 3.11b). I observed that height and deflection signal only slightly changed on the upper right grain, possibly due to an advancing sample degradation and potential damage caused by the AFM tip. In the PFM amplitude, on the other hand, the periodic domain pattern entirely disappeared, which implies that the cubic phase of $MAPbI_3$ was reached. The absence of the domain structure in the cubic phase indicates that the cubic-tetragonal phase transition is the origin of the twin domain formation.

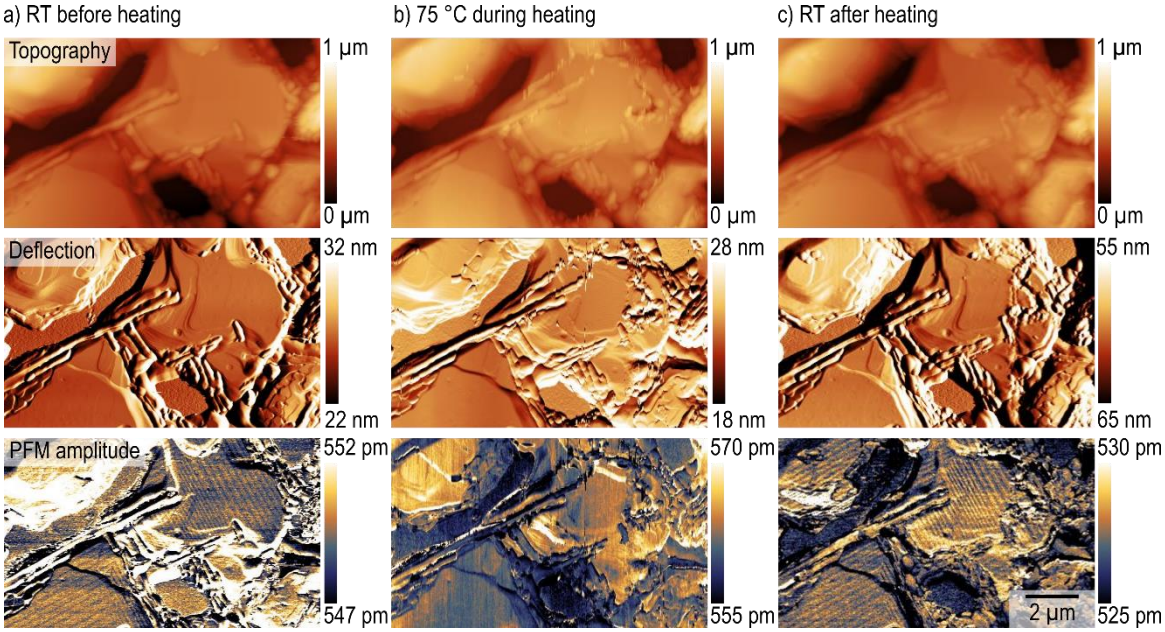

Figure 3.11: Lateral PFM measurements on large $MAPbI_3$ grains on an ITO substrate conducted on a Peltier element at three different temperatures. a) Height, deflection and PFM amplitude before heating at room temperature (RT). b) Height, deflection and PFM amplitude on the same area at a stage temperature of 75 °C. c) Height, deflection and PFM amplitude on the same area after heating at room temperature (RT). Lateral PFM performed with 2.5 V AC excitation close to lateral contact resonance at 653 kHz, 659 kHz and 661 kHz, respectively.

To exclude that the disappearance of the domains at elevated temperatures arise from an irreversible material change, I performed a third lateral PFM measurement after the heating step at room temperature shown in Figure 3.11c. The domain pattern in the PFM amplitude reappeared in the same arrangement as in the first measurement, whereas height and deflection signal remained largely unchanged compared to the scan at 75° C stage temperature in Figure 3.11b.

These results agree with the literature, where Stoumpos *et al.* reported on the reversible domain formation upon crossing $MAPbI_3$'s cubic-tetragonal phase transition and assigned this phenomenon to twinning releasing strain caused by lattice distortion due to symmetry loss.[4] Subsequently, other researchers confirmed the reversible twin formation using heating experiments while imaging with transmission electron microscopy (TEM), PFM, XRD and neutron

diffraction.[13,14,17,19,20] In particular, Medjahed *et al.* investigated the temperature- and precursor-dependence of the domain formation. They found that domain formation in $MAPbI_3$ becomes more likely when using chloride-containing precursors in the synthesis due to an increase of the internal strain: While the initial film crystallization still contains chloride, the subsequent anion exchange with the larger iodide during annealing amplifies internal strain in the tetragonal phase and thus leads to domain formation.[19] This study strongly supports the initial hypothesis by Stoumpos *et al.* that domains form to release internal strain in $MAPbI_3$ crystals upon the cubic-tetragonal phase transition, which classifies as ferroelastic.[1,18–20]

Nevertheless, a strain-induced domain formation does not exclude additional ferroelectricity, particularly since the exact space group of the $MAPbI_3$'s tetragonal phase remains unclear.[20] A temperature-dependent PFM spectroscopy study attempted to resolve whether the phase transition is ferroelectric by measuring local ferroelectric hysteresis curves in the tetragonal and in the cubic $MAPbI_3$ phase. Indeed, they observed a disappearance of the hysteresis, when the material was in its cubic phase.[13] However, PFM spectroscopy on $MAPbI_3$ in particular have been shown to be unreliable, thereby impairing the validity of these findings.[6,91]

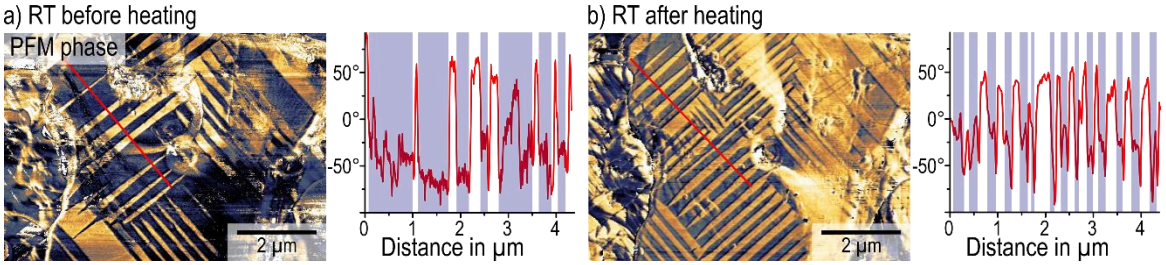

Figure 3.12: Lateral PFM phase on a large $MAPbI_3$ grain on a glass substrate conducted before a) and after b) heating the sample above the cubic-tetragonal phase transition to 70°C. The line profiles extracted at the same sample positions show the change in the domain regularity following the heating step. Lateral PFM performed with 1.5 V AC excitation close to lateral contact resonance at 675 kHz. Reprinted with permission from Energy Environ. Sci., 2020, Advance Article. - Published by The Royal Society of Chemistry.

Interestingly, my first experiment in Figure 3.11 as well as other temperature-dependent microscopy studies showed domains reappearing after cooling in the same positions as before the heating step. This behavior is common for ferroelastic twin domain, which are often pinned to crystalline defect sites.[1,18] However, in an additional temperature-dependent PFM experiment on an initially more irregular domain structure, I observed not only orientational domain changes but also an increase in density and regularity in Figure 3.12. Comparing room temperature scans before and after heating, the domain orientation changed by 90° in several areas of the grain e.g., in the bottom center of the scan area. Moreover, the domain density and the regularity of the domain width increased almost everywhere on the grain. Upon analyzing the line profiles extracted at the same position before and after heating above the phase transition, I found an average domain width of 0.46 µm with a standard deviation of 0.29 µm before heating. After heating the average domain width decreased to 0.15 µm with a significant decrease in the standard deviation to 0.03 µm. The total amount of the domains doubled after the heating step.

I assume that the change of the domain structure in this particular sample was caused by an energetically instable initial domain structure. The annealing process during the sample

preparation ended more abruptly than usual due to a power outage of the heating plate. Meanwhile, the cooling during the temperature-dependent PFM experiment had a defined cooling rate of 1 °C/min. The change of the domain pattern in dependence of the cooling rates after heating suggests that a targeted domain manipulation via gentle heat treatments to 70 °C is possible to tune domains as required: Fast cooling could reduce the domain density and slow cooling could increase the domain regularity.

Summary

Temperature-dependent PFM experiments showed the disappearance of the twin domain pattern in the cubic $MAPbI_3$ phase, which confirms the material's cubic-tetragonal phase transition as origin of the twin domain formation. Since the transition from a cubic to a tetragonal structure introduces internal strain, twin domains can release this strain by adopting an alternating crystal orientation. Moreover, I found that the domain pattern can change within a heating and cooling cycle, likely in dependence of the cooling rates. The response of the domain pattern to the cooling rates offers possibilities to control the domain pattern in the future: Fast cooling rates could decrease the domain density if required. A more targeted domain manipulation via certain external stimuli (stress, electric field) depending on the nature of the domains is focus of the following subchapter.

3.1.3.2 Targeted domain manipulation

Introduction

Besides their phase transition, ferroelectric and –elastics are classified by their switching behavior upon the application of external stimuli. Per definition, ferroelectrics exist in two or more degenerate polarization states, which an external electric field can switch, if it exceeds the material-specific coercive field. Corresponding, ferroelastic materials feature two or more strain states, which are controllable by external mechanical stress (Chapter 1.3.1.1).[1,107,108] Hence, for the ferroelastic and perhaps ferroelectric $MAPbI_3$, it is most promising to explore mechanical and electrical switching as routes for domain tailoring.

The study of $MAPbI_3$'s domain response upon external electric and mechanical stimuli not only offers device optimization via domain manipulation, but also advances the understanding of the material behavior under device operation. A possible domain change in the build-in field of the working solar cell may have implications for the charge carrier transport.[11,14,22,23,27] Likewise, insights on the domain response upon external stress is vital for the material's implementation in flexible PV devices.[15,18,21,24,26] Here, I resolved the domain pattern in $MAPbI_3$ crystallites in thin films via PFM upon application of external stress and an electric field. I found a small but distinct change of the domain arrangement, when I applied high tip-sample contact forces during an AFM contact scan, while the lateral electric field appeared to have no influence on the domain pattern.

Results and discussion – mechanical switching

To investigate the domain behavior upon external stress application, I prepared a $MAPbI_3$ thin film with large crystallites on an ITO substrate with a PEDOT:PSS interlayer via the solvent annealing routine with precursors containing iodide and chloride.[9,69,108,10] The particular grain chosen for the experiment in Figure 3.13 featured a large flat surface area with some rod-shaped

particles in the grain center and the outer edges, which are likely PbI_2 as governing $MAPbI_3$ degradation product.[10,69,112]

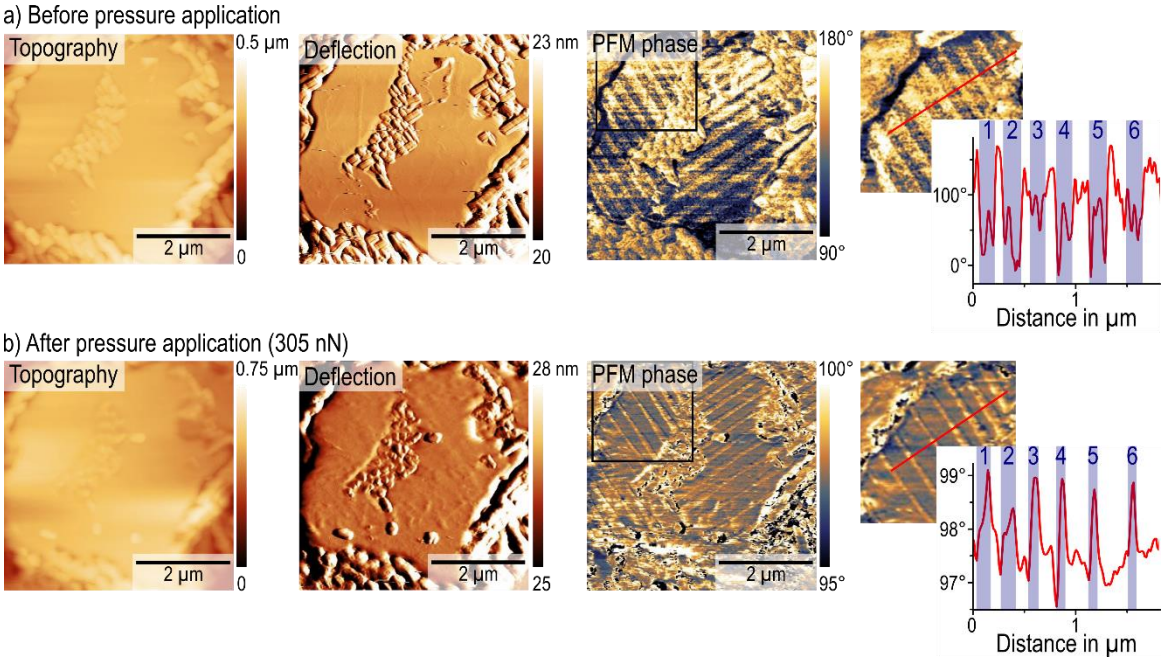

Figure 3.13: Vertical PFM measurements on a large $MAPbI_3$ grain on an ITO substrate with a PEDOT:PSS interlayer before and after pressure application of 305 nN via the AFM cantilever during a contact mode scan. a) Topography, deflection and PFM phase before pressure application featuring domains with uniform widths in the line profile of the PFM phase extracted along the red line (Table 3.1). b) Topography, deflection and PFM phase after pressure application featuring a decrease in widths for the blue-shaded domains in the line profile of the PFM phase extracted along the red line (Table 3.1). Vertical PFM performed with 2.0 V AC excitation close to vertical contact resonance at 290 kHz in a) and performed with 1.5 V AC excitation close to vertical contact resonance at 300 kHz in b).

Prior to the force application, the PFM phase on the flat grain surface showed the familiar periodic domain pattern with a regular spacing between the alternating dark and bright domains (Figure 3.13a). Analysis of the phase line profile along the red line gave a largely uniform width of the dark domains between 0.15 and 0.19 µm (Table 3.1). After the initial PFM scan performed with a force setpoint of 45 nN, I did a regular contact mode scan with a normal tip-sample force of 305 nN. Following this scan at a high contact force, I exchanged the AFM cantilever to avoid measurement artefacts caused by a blunt tip and remeasured the same area with a new tip (Figure 3.13b). I observed only slight changes in the sample topography and the deflection due to particles deposition on the flat $MAPbI_3$ surface. The domain pattern in the PFM phase on the other hand differed from the initial measurement. Here, I found a contrast inversion, but more importantly, the widths of the previously dark, now bright domains decreased to 0.8 – 0.15 µm (Table 3.1). By analyzing the line profile of the PFM phase extracted at the same position as before pressure application, I found that all but one of these domains shrunk in width by up to 0.11 µm.

The change of the domain width upon the application of mechanical stress via the AFM tip, agrees with observations of Strelcov *et al.*, who resolved the ferroelastic response of $MAPbI_3$ via polarized light microscopy by systematically deforming a thin film on a flexible substrate.[15] More recently, Kennard *et al.* investigated the mechanical domain behavior via grazing incidence wide-

angle x-ray scattering (GIWAXS) on a flexible polyimide substrate to characterize the ferroelastic hysteresis and showed a minimum domain density at maximum stress.[18]

Table 3.1: Domain width measured in the PFM phase line profiles extracted at the same position along the red line in Figure 3.13a and b before and after pressure application of 305 nN via the AFM cantilever.

DOMAIN NO.	WIDTH BEFORE PRESSURE	WIDTH AFTER PRESSURE
1	0.15 µm	0.15 µm
2	0.19 µm	0.15 µm
3	0.15 µm	0.09 µm
4	0.17 µm	0.08 µm
5	0.19 µm	0.08 µm
6	0.15 µm	0.09 µm

Ferroelastic switching via normal tip-sample forces during AFM has been performed successfully on materials with an *a*-*c* domain orientation, where the long *c*-axis alternates in out-of-plane and in-plane orientation.[113] In $MAPbI_3$, the absence the periodic domains in the sample topography indicates that the domain orientation is a purely in-plane a_1-a_2 arrangement (Chapter 3.1.1). Therefore, the change of the domain width likely originates from the shear forces between tip and sample instead of normal forces. These shear forces, applied in 45° with respect to the domain walls, could reduce or increase the width of every other domain depending on the orientation of the *c*-axis. Hence, it is feasible that an AFM tip facilitates a mechanical manipulation of in-plane ferroelastic domains.

Results and discussion – electrical switching

To investigate the domain response upon an electric field application, I chose a $MAPbI_3$ thin film with large crystallites that was prepared via solvent annealing with iodide and chloride containing precursors. Here, instead of a conductive substrate, I used a glass substrate. Since our previous vertical PFM switching spectroscopy data suggested the absence of an out-of-plane ferroelectric polarization (Chapter 3.1.1; SI in Appendix 8.1, Figure 8.4), I prepared a lateral device structure to study the behavior of the domains in a lateral electric field. Assuming the presence of an in-plane ferroelectric polarization in the domains, I would expect a change in the domain orientation in a lateral electric field. Therefore, I deposited gold electrodes on top of the $MAPbI_3$ thin film separated by a gap of 14 µm (Figure 3.14a). I tested for the absence of leakage currents or electrical shorts across the gap prior to the experiment using a multimeter.

Via the optical camera in the AFM, I identified a suitable measurements area with a single $MAPbI_3$ grain positioned in the gap between the two electrodes in Figure 3.14b. In this particular grain, the upper right corner is partially coated with Gold while the rest of the grain remained uncoated. Therefore, this grain was ideally suited for the lateral switching experiment. In the lateral PFM amplitude prior to the voltage application, I resolved the periodic domain pattern, with several 90° direction changes. Some of the domains were aligned almost parallel to the gold electrodes. After the initial scan, I applied a voltage of 35 V between the two electrodes for 10 min. In the

approximation of a homogeneous electric field between the two electrodes, the voltage of 35 V corresponds to an electric field of 2.5×10^6 V/m. In comparison, typical experimental values for the coercive field of BTO and PZT are 0.2×10^6 V/m and 10×10^6 V/m, respectively.[114] However, the domain pattern resolved in the PFM amplitude after the voltage application remained unchanged.

My findings on the absence of an in-plane electrical switchability are in direct contrast to the results of a recent study by Röhm *et al.*. They found a change in the domain structure upon applying an electric field of 4.5×10^6 V/m for 11 min in an interdigitated electrode array.[27] Hence, it is feasible that the applied field of 2.5×10^6 V/m was not sufficient to switch the domain orientation in $MAPbI_3$, since I did not exceed the material's coercive field. On the other hand, the domain switching observed of Röhm *et al.* could also be strain-related, considering that the experimental architecture of interdigitated electrodes is commonly used to generate surface acoustic waves.[115] Since my experimental setup only used two opposing electrodes without an array structure, surface acoustic wave generation is not anticipated.

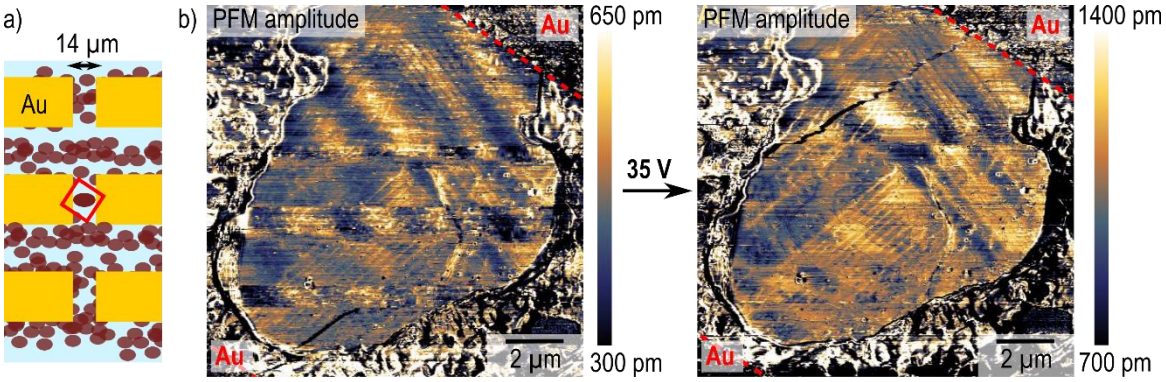

Figure 3.14: a) Schematic depiction of sample layout with gold electrodes (Au) deposited on $MAPbI_3$ film with 14 µm gap. An exemplary scan area with an isolated grain within the gap is highlighted by the red box. b) Lateral PFM amplitude on a large $MAPbI_3$ grain on a glass substrate in the 14 µm gap between two gold electrodes before and after the application of a lateral electric field of 2.5×10^6 V/m for 10 min. The domain arrangement remained unchanged after the bias application. Lateral PFM performed with 2.0 V AC excitation close to lateral contact resonance at 600 kHz.

Summary

My investigation of the domain behavior in $MAPbI_3$ upon external mechanical stress and a lateral electric field showed a change of the domain width after stress application, while the domain pattern remained unchanged in a lateral electric field. The mechanical response of the domain pattern further confirms the ferroelastic character of $MAPbI_3$ offering new possibilities for strain engineering. For example, the application of external stress prior to device operation may reduce the domain density if required, or a combination of external stress and heat treatments may facilitate a more regular domain periodicity. A targeted generation of different domain patterns could also aid to investigate the domain influence on the device performance more systematically.

The absence of a response of the domain pattern upon electric field application suggests that no ferroelectric polarization is present in $MAPbI_3$. On the other hand, an electrical switching may have required higher voltages as demonstrated by Röhm *et al.*.[27] Moreover, the semiconductive nature of $MAPbI_3$ as well as the material's high ion mobility exacerbates a reliable ferroelastic characterization, due to leakage currents and ionic screening. Unlike other insulating ferroelectrics,

these properties can interfere with ferroelectric switching experiments and thus prevent a final verdict on $MAPbI_3$'s possible ferroelectricity.

Experimental

Sample preparation:

See Chapter 3.1.1 for preparation of precursor solution, substrate cleaning, $MAPbI_3$ deposition and annealing and PEDOT:PSS deposition.

For the preparation of the lateral $MAPbI_3$ device in Figure 3.14, a 12 µm thick tungsten wire was glued to the center of an electrode evaporation mask. Subsequently, the evaporation mask was placed on top of the sample and gold electrodes with thicknesses of ~100 nm were evaporated on top of the $MAPbI_3$ film. After the evaporation, the gold electrode on one side of the gap was connected to a metal puck with silver paste and put on ground via the AFM sample bias. The other side was contacted via a wire glued to the electrode with silver paste. This electrode was the connected to an external power source for bias application.

Piezoresponse force microscopy (PFM):

See Chapter 3.1.1 for lateral and vertical PFM measurements in Figure 3.11 and Figure 3.13.

For the first heating experiment in Figure 3.11, the sample was positioned on a Peltier element with a temperature range of ~5 to 85 °C. To facilitate an optimal heat transfer we applied thermal paste between the stage and the sample. The Peltier element was turned off during the first and the third scan and heated to 75 °C during the second scan. In between each measurement, I waited over night to achieve thermal equilibrium.

Lateral PFM measurements in Figure 3.12 and Figure 3.14 were performed on a Cypher ES AFM (Oxford Instruments) in nitrogen atmosphere with a platinum-iridium coated PPP-EFM cantilever with a free resonance frequency of 75 kHz and spring constants of $k \sim 2.8$ nN nm^{-1}. For the heating experiment in Figure 3.12, the initial sample temperature was 26 °C. The sample was then heated at 1 °C min^{-1} to 70 °C and subsequently cooled to 27 °C. After reaching 27 °C, I waited around 30 min for the sample temperature to equilibrate before measuring PFM. For the electric switching experiment with the lateral device in Figure 3.14 one side of the electrodes was grounded and the other was connected to an external power source for bias application.

3.1.4 Conclusion and outlook

In this subchapter, we explored the structure and nature of subcrystalline periodic domains in the (110) crystal plane of $MAPbI_3$ via PFM. Their arrangement and response to heat as well as mechanical stress confirmed the ferroelastic nature of the domains. These ferroelastic domains likely form to compensate internal strain from the cubic-tetragonal phase transition. They appear to align in an in-plane a_1-a_2 structure, where the long c-axis lies parallel to the surface. Additional sidewall measurements suggest that domain walls in the bulk material are oriented perpendicular to the (110) surface plane. Since domain walls can affect the charge carrier diffusion (Chapter 3.2.2), knowledge on the domain wall orientation throughout bulk grains allows further optimization of the charge carrier extraction in PSCs. Here, the tailoring the grain texture to a (110)

surface plane should enable a fast charge extraction along domains – a finding that is in direct agreement with a previous study by Docampo *et al.*, who detected an improvement of short circuit currents for a (110) surface orientation o $MAPbI_3$.[88] Moreover, the ferroelastic nature of the domains offers the possibility for strain engineering via external application of mechanical stress or heat treatments with defined cooling rates. Both routes allow changing the density or regularity of domains as required to improve the charge carrier transport.

Future investigations on the structure and switchability of $MAPbI_3$'s ferroelastic twin domains could include cross sectional PFM measurements to confirm the perpendicular domain orientation within bulk grains, a more systematic study on the influence of cooling rates on the domain arrangement as well the effect of combined heat and stress application. For the latter, the additional application of heat might lower the activation energy for mechanical domain switching using AFM or substrate bending and thus, facilitate easy domain tailoring. Furthermore, Medjahed *et al.* have recently suggested that the choice of $MAPbI_3$ precursors increases or lowers internal strain.[19] Hence, variations of the MAI to $PbCl_2$ ratio could lead to changes in the internal strain and domain pattern. Moreover, a successful application of $MAPbI_3$ in flexible PV devices requires a systematic correlation of the domain pattern with the substrate bending. Finally, high resolution TEM could provide insights on the domain walls structure to identify the possible presence of a local polarization.

3.2 Subcrystalline domains in $MAPbI_3$: Effect on charge carriers

Classic ferroelectrics and -elastics like bismuth ferrite ($BiFeO_3$, BFO),[116–118] BTO[119,120] and PZT[121,122] display electronic anomalies at their domain walls that can introduce an electrical conductivity in otherwise insulating bulk materials (Chapter 1.3.1.1). In their 2009 study, Seidel *et al.* used CAFM to image a current along certain domain walls in BFO, which they attributed to polarization components oriented perpendicular to the domain walls.[118,123] Even slight deviations of the polarization orientation from neutral head-to-tail domain wall arrangements result in a bound charge, which needs to be screened by free charge carriers to lower the domain wall energy.[1,123] Furthermore, Seidel *et al.* proposed a reduction of the band gap at the position of domain walls based on simulations. Thus, the accumulation of charge carriers and the local reduction of the band gap lead to the observed domain wall conductivity in BFO.[118] On a comparable BFO thin film, I captured the domain wall conductivity by imaging a ferroelectric domain that was oriented opposite to the bulk via PFM. Simultaneously, I resolved a current signal using CAFM that directly correlates to the domain wall positions (Figure 3.15).

Some ferroelectric and ferroelastic domain walls can also act as sites of increased doping concentrations, when mobile ions or ion vacancies instead of electronic carriers counteract the bound domain wall charge.[60,124] In WO_{3-x}, this domain wall doping even leads to 2D superconductivity at low temperatures.[125] Moreover, purely ferroelastic domain walls in non-polar materials can carry a polarization as a result of flexoelectricity: A strain gradient, which is present at ferroelastic domain walls, breaks the centrosymmetry of the non-polar material locally and thereby introduces an electrical polarization.[126–128]

Considering the astonishing domain wall properties in classic insulating ferroelectrics and ferroelastics, I studied whether the subcrystalline twin domains in the semiconductive $MAPbI_3$ possess similar electric attributes and if so, how they affect the charge carrier transport in PSCs. Correlative CAFM and PFM in Chapter 3.2.1 and time- and spatially resolved PL microscopy in Chapter 3.2.2. allowed investigating a possible domain wall conductivity as well as the domain influence on charge carrier diffusion. While the domain walls did not show an enhanced conductivity in CAFM measurements, we found that the domains introduce anisotropic charge carrier diffusion times.[21] The domain influence on the charge carrier diffusion may originate from a possible domain wall polarization due to flexoelectricity[24,127,128] and/or an increased concentration of shallow trap states that delay the charge transport across domain walls.[129,130]

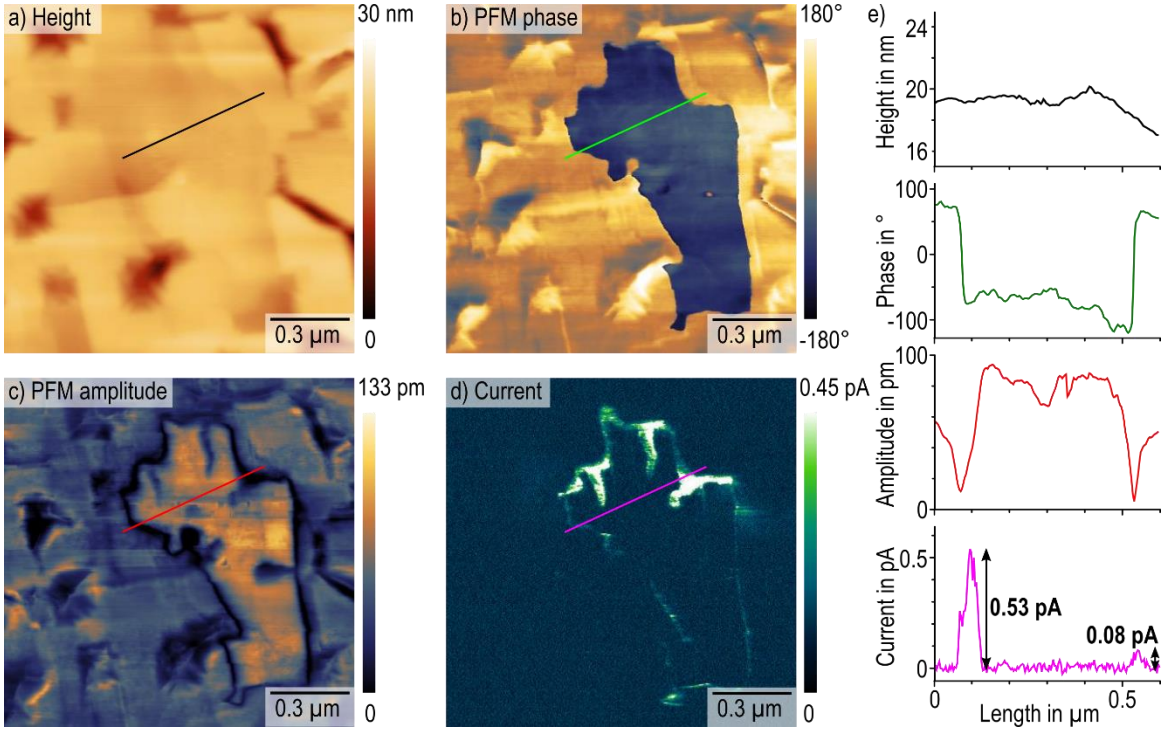

Figure 3.15: Simultaneous vertical PFM and CAFM measurement on a bismuth ferrite thin film (provided by Dr. Akash Bhatnagar at Centre for Innovation Competence SiLi-nano, Halle, Germany). The sample topography is shown in a). A ferroelectric domain with opposite polarization than the surrounding area is imaged in PFM phase b) with a ~180° contrast and PFM amplitude c) with amplitude minima at the position of the domain walls. The current image d) captured the conductivity of the domain walls at 2 V DC sample bias. Line profiles across the domain in e) highlight the correlation of PFM and CAFM signals and display currents of up to 0.53 pA at the domain walls. Vertical PFM and CAFM were performed on an NX10 AFM (Park Systems GmbH, Suwon, Korea) with an ElectriMulti75-G cantilever, 2 V AC excitation close to vertical contact resonance at 375 kHz and a DC bias of 2 V, applied simultaneously to the sample stage using an AC/DC coupler. Current detection via an Ultra-Low Noise Current Amplifier Series LCA (FEMTO Messtechnik GmbH, Berlin, Germany).

3.2.1 Domain influence on conductivity

- Unpublished-

Introduction

Early in the perovskite research, theoreticians proposed the presence of conduction paths in $MAPbI_3$ along ferroelectric domain walls, similar to BFO or PZT.[22,23,77,131] By forming alternating

domain walls with negative and positive bound charge as suggested by the scientists, the conductive domain walls would then facilitate charge selective carrier transport and therefore explain the material's astonishing diffusion length of up to the micrometer scale (Figure 1.10c).[22,23,38,77,131,132] However, conductive ferroelectric domain walls in $MAPbI_3$ have yet to be observed experimentally and the lack of unambiguous evidence for ferroelectricity in general,[12,47,90] makes this early hypothesis appear unlikely.[12,47,90]

Instead of domain wall conductivity, two PFM/ CAFM studies resolved a photocurrent contrast that directly correlates to the bulk domain arrangement of the twin domains.[11,14] The authors of one of the studies linked the domain contrast in the photocurrent to an alternating polar behavior of the domains. Based on lateral resonance tracking PFM, they suggested that only every other domain carries polarization, which lowers the photocurrent in these domains.[14] On the other hand, the authors of the second study proposed alternating polarization orientations behind the contrast: On those domains with a higher photocurrent, they suspected a more favorable polarization orientation, carrying a normal component with respect to the surface.[11] However, in a 2019 report, investigators propose that the correlation of photocurrent and bulk domain pattern is not caused by ferroelectric polarization but instead originates from photoinduced strain in the ferroelastic domains. This strain introduces chemical inhomogeneities, which influence the directionality of the photocharge extraction.[133]

Meanwhile, a possible flexoelectric polarization formation at $MAPbI_3$'s ferroelastic domain walls like in $SrTiO_3$ or in WO_3[126–128] and its effect on charge carriers only recently garnered some attention, when Warwick *et al.* proposed an in-plane polarization of 6 μC/cm² along the twin domain walls. They modelled that this in-plane domain wall polarization could enhance the photocarrier mobility, which potentially affects the material's in-plane conductivity.[24]

Here, I explored whether the twin domains resolved via PFM affect the normal conductivity in crystalline $MAPbI_3$ thin films by correlating PFM measurements with CAFM measurements with and without illumination. Additionally, I studied the in-plane conductivity in dependence of the domain wall arrangement by detecting a current on single isolated $MAPbI_3$ grain partially covered with a gold electrode on a glass substrate.

Results and discussion

To correlate the normal current to the twin domain pattern in $MAPbI_3$, I prepared a thin film featuring micrometer-sized grains on a conductive ITO substrate with PEDOT:PSS coating using a solvent annealing step.[9] The grain topography in Figure 3.16a showed a 2-4 μm wide and 5 μm long grain with a flat surface area in the center and an accumulation of rod-shaped PbI_2 particles, which is a common $MAPbI_3$ degradation product, at the outer edges.[10] On the flat area, the vertical PFM phase (Figure 3.16b) resolved the familiar periodic pattern of the twin domains that displayed a 90° orientation change on the left side, as described in Chapter 3.1.1.[10] The current image on the same grain in Figure 3.16c was captured subsequently without illumination at 1 V sample bias. I observed a current on the flat area, while step edges with the PbI_2 particles were non-conductive. The median current on the conductive grain regions was 33 pA. The current image featured some tip-related measurement artefacts, where some scan lines exhibited a higher current than others, visible also in the line profiles in Figure 3.16d, extracted along the pink and blue line in c). This artefact is

typically caused by a change of the conductive tip coating due to shear forces or an accumulation of contaminants on the tip apex.

Regarding a possible presence of conductive domain walls like in BFO (Figure 3.15) or a regulation of the current via the bulk domains polarzation,[11,14] I found no correlation between current signal and domain pattern. Neither the current image in Figure 3.16c nor the line profiles in d) featured a periodic signal resembling the periodicity bulk domains or the domain walls. The absence of a domain-related current signal generally suggests a negligible influence of domain walls or bulk domains on the conductivity. On the other hand, previous reports observed the correlation of normal current in $MAPbI_3$'s photoresponse.[11,14] Therefore, I illuminated the sample through the transparent bottom electrode with a white light source during the current detection in a subsequent measurement.

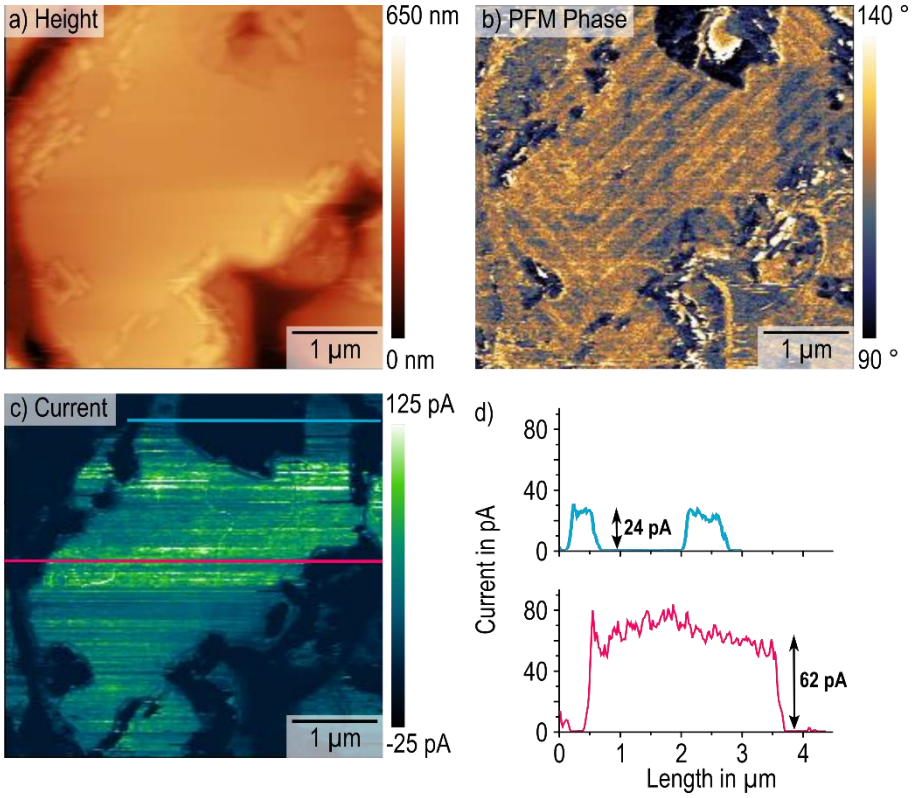

Figure 3.16: Vertical PFM and CAFM measurement of a large $MAPbI_3$ grain on a conductive ITO substrate with PEDOT:PSS coating. a) Sample topography, b) vertical PFM phase showing the periodic twin domains, c) current signal on the same grain, measured without external illumination at 1 V sample bias. No periodic modulations corelated to domains were observed in the current image and line profiles in d). Vertical PFM performed with 1.0 V AC excitation close to vertical contact resonance at 300 kHz.

In Figure 3.17, I directly compared the dark current in a) with the subsequently recorded photocurrent in b) on the same grain. I observed an increase of the median current on the conductive regions to 41 pA at 1 V sample bias. Like for the dark current, I did not observe a correlation of the photocurrent and the domain pattern. This discrepancy with literature results could originate from an insufficient current sensitivity or a flooding of the surface with free electronic charge carriers or ions that superimpose onto any domain regulation of the conductivity. In fact, Huang *et al.* avoided the use any sample bias, when they resolved the domain pattern in the

photocurrent, and Röhm *et al.* used a bias below 1 V in their experiment.[11,14] Thus, the additional charge injection and field may have impeded with the domain-related current detection. Moreover, I observed the fine substructure in the photocurrent of the grain could be an indication of surface degradation. The irregular pattern of the substructure may relate to the terraces observed on the (110) surface plane of $MAPbI_3$: As the amplitude image in Figure 3.8a shows the trace edges are often rounded as less regular than the domains, similar to current pattern in Figure 3.17b. Due to local defects like dangling bonds or adsorbates terraces edges could be particularly prone to local degradation. Indeed, the deflection image of the same scan area in Figure 3.17c shows that the substructure in the photocurrent corresponds to the terrace structure on the grain as well as several protrusions, which formed upon illumination. These protrusions are indicative of a surface degradation that interferes with the current detection.

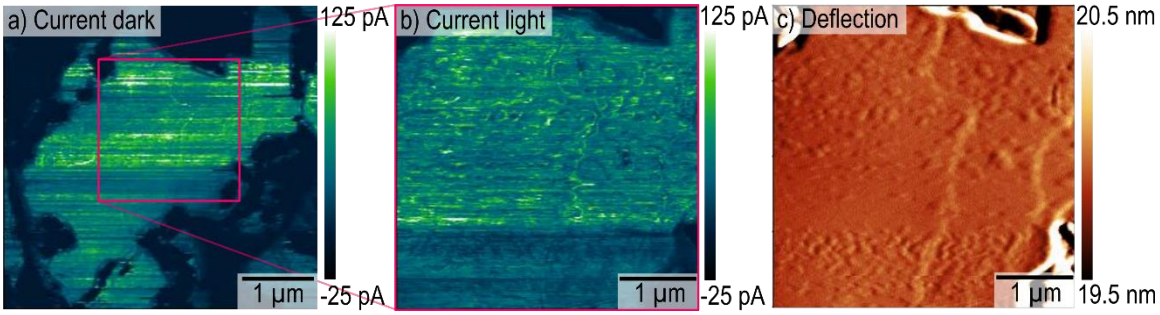

Figure 3.17: CAFM measurement of same large $MAPbI_3$ grain on a conductive ITO substrate with PEDOT:PSS coating. as in Figure 3.16 with 1 V sample bias and additional white light illumination with a large area scan in a) and an enlarged view on the photocurrent distribution in b). c) Deflection showing the surface structure of the same scan area in b) in detail as topography error.

To probe the possible influence of ferroelectric domain walls on the lateral conduction as suggested in the theory studies of Warwick *et al.* and Shi *et al.*,[24,25] I sputtered a 60 nm thick gold electrode onto a solvent-annealed $MAPbI_3$ thin film with micrometer-sized grains, which was prepared on an insulating glass substrate. With the gold electrode just covering parts of the film, I was able to locate an isolated grain, where the gold electrode contacted the two lower corners of the grain. Yet, the gold contact was sufficient to allow a current flow from the gold electrode across the grain to the conductive AFM tip after bias application of -800 mV to the electrode (Figure 3.18a). Prior to the CAFM measurement, I imaged the domain pattern of the same grain using lateral PFM to facilitate a possible correlation of domains and lateral conductivity (Figure 3.18b).

The median current on the grain was 25 pA with a maximum current of 45 pA in the upper left corner in Figure 3.18a. Comparing the heterogeneous current distribution to the PFM amplitude in Figure 3.18b, I found a correlation of the area with a higher current and the position where the domain alignment changes by 90°. This position is highlighted by the red dashed line, whereas the area of a current above 26 pA is shaded red (Figure 3.18c). The corresponding current signal and domain pattern could be due to a domain wall influence on the lateral conduction caused by localized flexoelectric polarization.[24]

However, in the lower left corner of the grain, which displays the same domain arrangement as the upper left corner, the current is well below 26 pA with a magnitude comparable to the rest of the grain, which would directly contradict the previous hypothesis. Recently, Xiao *et al.* have

investigated the charge carrier drift across twin domains in a comparable experimental setup and concluded that the domain walls have a negligible influence on the carrier transport in an electric field based on their results.[26] This study and the decreased current in the lower left corner of the grain cast some doubts on an domain wall effect on the lateral conductivity. Instead of a domain wall influence the higher conductivity in the upper left corner may also be caused by the increase step density at this position. The terrace steps that are recognizable in the PFM amplitude in Figure 3.18b, can increase the tip-sample contact area and therefore the detected current.

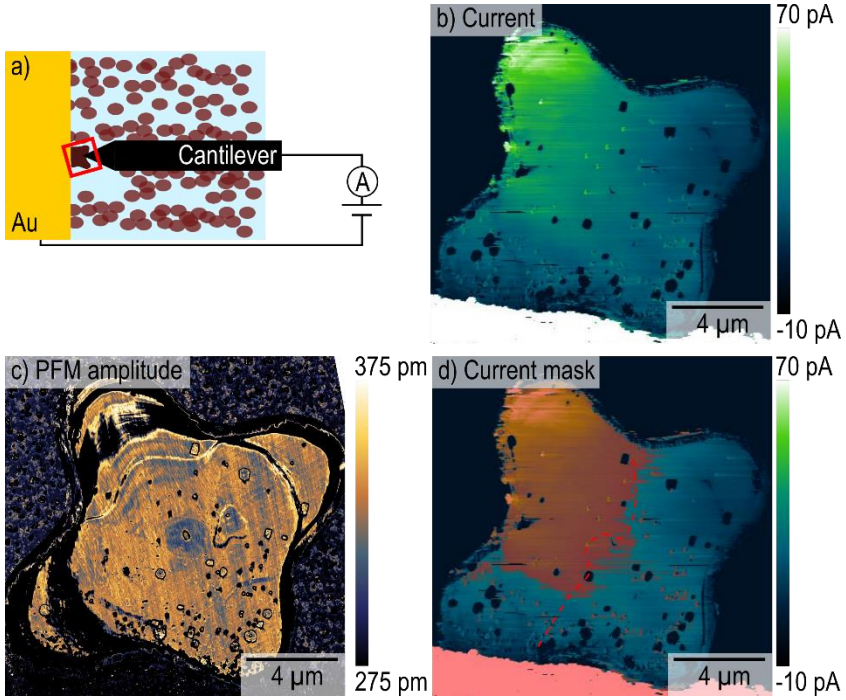

Figure 3.18: a) Schematic depiction of experimental layout with gold electrode deposited on $MAPbI_3$ film and lateral CAFM measurement. Exemplary scan area with isolated grain partially covered by the electrode is highlighted in red. b) CAFM on $MAPbI_3$ grain partially covered with a gold electrode (bottom left corner) performed with a sample bias connected to the gold electrode of -800 mV without external illumination. c) Lateral PFM was performed with 1.5 V AC excitation close to the lateral contact resonance at 711 kHz. d) Areas with a conductivity above 26 pA are masked in red, the red dashed line indicated the position of a 90° orientation change of the twin domains in the PFM amplitude.

Summary

In this subchapter, I investigated the impact of the subcrystalline ferroelastic domains on the vertical and lateral drift current in $MAPbI_3$ grains. However, normal and lateral CAFM measurements yielded ambiguous results. Normal CAFM data did not show a domain-related contrast in the current and photocurrent, which suggests an absence of conductive ferroelectric domain walls, unlike originally proposed models (Chapter 1.3.1.1, Figure 1.10c).[22,23,77,131] On the other hand, local photocurrent variations that correspond to the change of the surface structure indicate a degradation of the $MAPbI_3$ grain upon illumination and bias application. This degradation likely impeded an accurate current detection. To avoid surface degradation during photo-CAFM in the future, the sample system could be changed to more stable single crystals. Furthermore, a reiteration of the measurements with an ultra-low-noise current amplifier with a pico-Ampère current resolution could aid to resolve features in the conductivity at lower bias and light intensities. Besides the surface degradation, a rearrangement of mobile ions in the electric

field of CAFM is likely to interfere with the current detection. Here, ions or ion vacancies could move to the surface and thereby counteract the electric field required for charge collection. This flooding of the surface with ionic charge carriers and the degradation or the surface could also be prevented reducing the tip-sample contact time, as demonstrated by Leblebici *et al.*.[87]

As for the effect of ferroelastic domain walls on the lateral drift current due to a possible flexoelectric polarization,[24] I observed a faint current contrast between domains with a 90° orientation change, which may indicate a preferential conduction parallel to domain walls. However, to confirm this hypothesis, further measurements are required, particularly to exclude topography crosstalk via terrace steps in the current. Moreover, a repetition of the experiments under illumination could aid to resolve a domain effect on the photocarriers.

Following the investigation on the domain influence on charge carrier drift in an electric field using CAFM, we next studied whether subcrystalline domains or domain walls affect the charge carrier diffusion using a correlated PFM and time- and specially resolved PL microscopy.

Experimental

Sample preparation:

See Chapter 3.1.1

For the preparation of the lateral $MAPbI_3$ device, I placed a shadow mask onto the $MAPbI_3$ film and evaporated the gold with 45 mA.

Conductive atomic force microscopy

I conducted all CAFM measurements in nitrogen atmosphere on an Asylum Research (Oxford Instruments) MFP3D atomic force microscope positioned in a glovebox using an ORCA high sensitivity current amplifier and PtIr-coated PPP-EFM cantilevers. For the white light illumination (UVICO-VIS) I used an illumination intensity of ~1000 W/m^2, filtered through a Schott KG 3 band-pass filter (transmission >50%, from 350 to 750 nm).

Piezoresponse force microscopy (PFM):

See Chapter 3.1.1

3.2.2 Anisotropic charge carrier diffusion in single $MAPbI_3$ grains correlates to their twin domains

Ilka M. Hermes,[a, *] Andreas Best,[a] Leonard Winkelmann,[a,c] Julian Mars,[a] Sarah M. Vorpahl,[b] Markus Mezger,[a, c] Liam Collins,[d] Hans-Jürgen Butt,[a] David S. Ginger,[b] Kaloian Koynov[a] and Stefan A. L. Weber[a, c, *]

[a] *Max Planck Institute for Polymer Research, Ackermannweg 10, 55128 Mainz, Germany.*

[b] *Department of Chemistry, University of Washington, Seattle, Washington 98105, United States.*

[c] *Institute of Physics, Johannes Gutenberg University Mainz, Duesbergweg 10-14, 55128 Mainz, Germany*

[d] *Center for Nanophase Materials Sciences, Oak Ridge National Laboratory, 1 Bethel Valley Rd., Oak Ridge, Tennessee 37830, USA*

-Published in Energy & Environmental Science (Energy Environ. Sci.) 2020, 13, 4168-4177 https://doi.org/10.1039/D0EE01016B -

Reprinted with permission from Energy Environ. Sci., 2020, Advance Article. - Published by The Royal Society of Chemistry.

Abstract

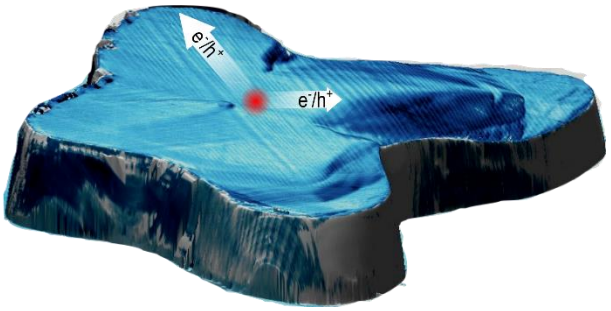

Polycrystalline thin films and single crystals of hybrid perovskites – a material group successfully used for photovoltaic and optoelectronic applications – reportedly display heterogeneous charge carrier dynamics often attributed to grain boundaries or crystalline strain. Here, we locally resolved the carrier diffusion in large, isolated methylammonium lead iodide ($MAPbI_3$) grains via spatial- and time-resolved photoluminescence microscopy. We found that the anisotropic carrier dynamics directly correlate with the arrangement of ferroelastic twin domains. Comparing diffusion constants parallel and perpendicular to the domains showed carriers diffuse around 50 – 60% faster along the parallel direction. Extensive piezoresponse force microscopy experiments on the nature of the domain pattern suggest that the diffusion anisotropy most likely originates from structural and electrical anomalies at ferroelastic domain walls. We believe that the domain walls act as shallow energetic barriers, which delay the transversal diffusion of carriers. Furthermore, we demonstrate a rearrangement of the domains via heat treatment above the cubic-tetragonal phase transition. Together with the previously reported strain engineering via external stress, our findings promise additional routes to tailor the directionality of the charge carrier diffusion in $MAPbI_3$-based photovoltaics and optoelectronics as well as other ferroelastic materials for optoelectronic applications.

Broader context

Many perovskite compounds exhibit ferroic properties, such as ferromagnetism or ferroelectricity. Among these properties, the lesser known ferroelasticity originates from a change of the crystal structure below a critical temperature, which introduces an internal strain in the material. To compensate for the internal strain, the crystal forms domains with alternating crystal orientation, often arranged as periodic needle twins that display 90° direction changes. With the integration of the room-temperature ferroelastic perovskite $MAPbI_3$ in photovoltaic and optoelectronic devices, knowing if and how ferroelastic domains affect the electronic charge carrier transport is crucial for device optimization. In this study, we were able to directly correlate an anisotropic charge carrier diffusion with the orientation of ferroelastic twin domains in isolated $MAPbI_3$ grains. Due to the ferroelastic nature of the domains it is possible to modify the domain orientation via external stress and controlled heat treatments above the ferroelastic cubic-tetragonal phase transition of the material. The influence of ferroelastic domains on carrier dynamics offers unique opportunities to customize the directionality of charge carrier transport in the $MAPbI_3$ and other ferroelastic materials studied for optoelectronic applications.

Introduction

Organic-inorganic hybrid perovskites display astonishing optoelectronic properties making them suitable materials for the active layer in photovoltaics (PV),[30–32,134] light-emitting diodes[135] and detectors.[136] Among others, direct band gaps,[4,99] the high defect tolerance[137] and long charge carrier diffusion lengths[38,132,138] qualify hybrid perovskites for planar heterojunction devices. As such, the diffusion length in methylammonium lead iodide ($MAPbI_3$) can exceed the usual film thickness of 300 – 500 nm in perovskite PV devices by up to an order of magnitude.[38,132,138] The diffusion length L_D is the average distance photoexcited carriers diffuse before recombining. L_D depends on the diffusion constant D via $L_D = \sqrt{D\tau}$, with the charge carrier lifetime τ.[139] While the carrier lifetimes, given by the recombination rates, depend on the trap and carrier density, the diffusion constant is a material property.

However, values reported for the diffusion constant in $MAPbI_3$ vary strongly with significant differences between single crystals and polycrystalline thin films, and even grain-to-grain variations within the same films.[140–147] Furthermore, several investigations of charge carrier dynamics in polycrystalline thin films found an anisotropy in the diffusion correlated to limited carrier transport across grain boundaries. The limited inter-grain carrier transport could stem from poor inter-grain connectivity or a mismatch in crystalline orientation.[140,148–151] In their study on grain boundary restrictions of the carrier diffusion, Ciesielski *et al.* resolved an apparent asymmetrical spatial distribution of diffusion constants within one single grain.[152] This observation raises two questions: Do individual $MAPbI_3$ grains display an anisotropic charge carrier diffusion? If so, which mechanism introduces this diffusion anisotropy?

Indeed, Stavrakas *et al.* recently visualized anisotropic carrier diffusion in $MAPbBr_3$ single crystals. They proposed buried crystal boundaries in the bulk material lead to the diffusion anisotropy.[147] Evidence for buried boundaries was delivered by Jariwala *et al.*, who imaged sub-grain boundaries in single $MAPbI_3$ grains via electron backscatter diffraction. These sub-grain boundaries could originate from crystal strain introduced via the cubic – tetragonal phase transition.[148]

To investigate the diffusion anisotropy in $MAPbI_3$ and the underlying mechanism, we employed spatial- and time-resolved photoluminescence (PL) microscopy[149,152–154] as well as piezoresponse force microscopy (PFM). PL microscopy detects photons released during the bimolecular recombination of photoexcited charge carriers. In a sample layout without charge extraction, we could use PL microscopy to map the spatial distribution of diffusive charges upon local excitation. By applying a pulsed excitation, we furthermore detected time-resolved PL decays, which carry information on the carrier dynamics. To probe the carrier diffusion times we scanned the detection of the time-resolved PL over isolated $MAPbI_3$ grains at varying distances from the excitation position. The time-resolved PL decays featured a delayed, distance-dependent diffusion signal, which revealed a distinct diffusion anisotropy. We found that this diffusion anisotropy directly correlated to the arrangement of ferroelastic twin domains, visualized by PFM on the same grains.

Results

Spatial- and time-resolved photoluminescence microscopy

To resolve the lateral distribution of carrier diffusion times in single $MAPbI_3$ grains, we used spatial- and time-resolved PL microscopy: We measured time-resolved PL decays following picosecond excitation pulses in varying distances from the excitation, by moving the detection volume independently from the fixed excitation position over the grain (SI in Appendix 8.2, Figure 8.6). Previous studies employed similar experimental setups to determine local diffusion constants or evaluate the diffusion across grain boundaries in hybrid perovskites thin films.[149,152–154] Here, we focused on investigating diffusion properties of single, isolated $MAPbI_3$ grains; first, to achieve an adequate range of distances between excitation and detection position without resolution limitations, and second, to exclude quenching effects from inter-grain carrier diffusion.

The investigated $MAPbI_3$ grain (Figure 3.19a) featured 4 arms. At its widest, the grain had a diameter of more than 20 µm, with an overall area of ~230 μm^2. According to Johnston *et al.* the diffusion length expected for our initial charge carrier density of 10^{16} cm^{-3} (SI in Appendix 8.2, Calculation 8.7), is in the order of 10 – 20 µm[138] and, thus, comparable to the dimensions of the grain.

We positioned the pulsed laser excitation in the center of the grain and proceeded to move the detection volume of the time-resolved PL away from the excitation in different directions along the arms. Four exemplary PL decays detected at comparable distances d_1, d_2, d_3 and d_4 between 6.5 ± 0.8 and 6.9 ± 0.8 µm from the excitation are shown in Figure 3.19b–e.

The detected PL decays were of superposition of two signals. In agreement with previous studies,[149,152–154] we assigned the fast, initial peak and its associated exponential decay to wave-guided PL emission from the position of the excitation spot. Due to the large mismatch of the refractive indices of air, $MAPbI_3$ and glass, the emission from the excitation position can be trapped in the grain.[155–158] The second signal, a delayed peak function, represents PL emitted at the position of the detection volume via bimolecular recombination of diffusive, non-excitonic charge carriers.[149,152–154] For quantitative analysis we fitted all time-resolved PL decays with an overlay of an exponential decay and a peak function, given by:

$$y = A_{wg} \times \mathrm{e}^{-(t-t_0)/\tau_{wg}} + \frac{A_{Diff}}{t-t_0} \times \mathrm{e}^{-\tau_0/(t-t_0)} + y_0$$

Equation 3.1: Fit function of PL decay.

With the amplitude A_{wg} and decay time τ_{wg} of the wave-guided PL, the amplitude A_{Diff} and diffusion time τ_{Diff} of the diffusive carriers and the offsets in t and y t_0 and y_0, respectively. For the diffusion peak function, we used a two-dimensional diffusion equation, under the assumption that the excitation occurs along a vertical line through the grain, from which the carriers diffuse radially.[152]

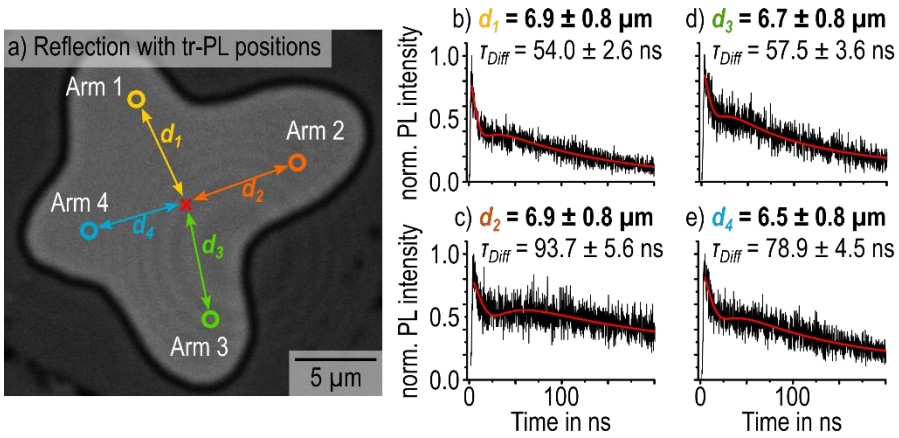

Figure 3.19: (a) Optical reflection image of the investigated isolated $MAPbI_3$ grain. The detection positions of four exemplary time-resolved PL decays along different grain directions in comparable distances d_1, d_2, d_3 and d_4 (6.5 – 6.9 µm) from the excitation position (red cross) are marked by the yellow, orange, green and blue circle, respectively. (b–e) The four corresponding PL decays detected in distances d_1, d_2, d_3 and d_4. The red lines in (b–e) represent the data fits according to Equation 3.1. Excitation with 633 nm wavelength, a fluence of 0.77 µJ cm^{-2}, a repetition rate of 2 MHz and 0.81 µm beam diameter (SI in Appendix 8.2, Figure 8.8). Reprinted with permission from Energy Environ. Sci., 2020, Advance Article. - Published by The Royal Society of Chemistry.

Comparing the diffusion times τ_{Diff} obtained from the data-fits for the four detection positions in Figure 3.19b–e, we observed a considerable shift to longer diffusion times for arms 2 (93.7 ± 5.6 ns) and 4 (78.9 ± 4.5 ns), compared to 1 (54.0 ± 2.6 ns) and 3 (57.5 ± 3.6 ns; more PL traces in SI in Appendix 8.2, Figure 8.9). Previous reports attributed such anisotropic charge carrier diffusion in hybrid perovskites to crystallographic anomalies such as buried grain boundaries.[146–148,159] As such, multiple groups observed a sharp drop of the static PL distribution at the position of visible as well as buried grain boundaries, which can inhibit the charge carrier transport.[140,148,152,159]

Static PL distribution

To investigate whether the anisotropy of the diffusion times was caused by buried grain boundaries, we mapped the static PL distribution upon local excitation at the same position as in Figure 3.19. The PL distribution was largely homogeneous without sharp intensity drop, which would have indicated the presence of buried grain boundaries (Figure 3.20a). Instead, the PL distribution displayed a diffuse maximum in the PL emission at the position of the excitation spot and local maxima at the positions of the grain boundaries, which originated from the enhanced out-coupling of wave-guided PL (Figure 3.20a–c).[149] Analyzing the line-profiles of PL distribution along the green and black profiles in 2a, we observed an anisotropic distribution with an elongated intensity-tail in arm 2. While the PL intensity in arms 1, 3 and 4 dropped by 50% in distances of 3.5, 3.0 and 3.7 µm from the excitation, respectively, in arm 2 the 50%-mark was reached at a distance of 5.7 µm. In light of the long diffusion times observed in arm 2 in the time-resolved PL data, the result from the static PL is surprising. It seems that longer diffusion times correspond neither to a decrease of the carrier density along the same grain direction nor to an increase of non-radiative recombination. We suggest two possible explanations for the time-resolved and static PL microscopy results: Either an acceleration of the diffusion along arms 1 and 3 or a deceleration of the diffusion along arms 2 and 4.

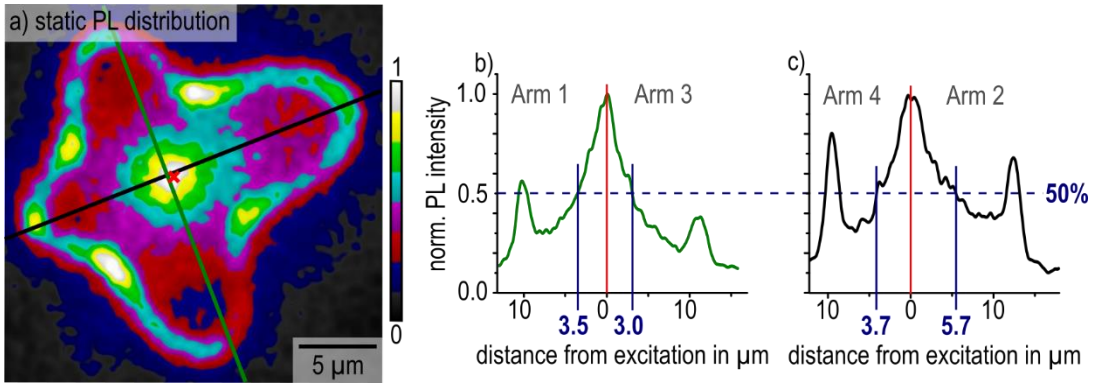

Figure 3.20: (a) Static PL distribution of the $MAPbI_3$ grain. The position of the excitation laser spot is marked with the red cross. An increased PL is detected at the grain boundaries, most likely due to enhanced outcoupling of wave-guided PL. (b) and (c) show the intensity distributions corresponding to the green and black line-profiles in (a), with local maxima at the position of the excitation as well as the grain boundaries. Reprinted with permission from Energy Environ. Sci., 2020, Advance Article. - Published by The Royal Society of Chemistry.

For the first scenario, several computational studies proposed a mechanism that would lower the bimolecular recombination and lead to an accelerated diffusion: These calculations showed that charged ferroelectric domain walls as well as polarized ferroelastic domain walls could act as charge-selective carrier pathways, which allow for charge carrier transport with minimized scattering.[22–25,77,131] The perovskite PV community largely accepted the existence of ferroelasticity in $MAPbI_3$ based on the observation of ferroelastic twin domains with a variety of imaging techniques, including PFM, transmission electron microscopy and polarized light optical microscopy.[10–13,15,17] Unambiguous evidence for the material's ferroelectricity however remains elusive.[6,12,90] In one of the following sections, we investigated ferroelectricity in $MAPbI_3$ by means of advanced PFM measurements.

In the second possible scenario, the grain could have a higher concentration of shallow traps along arm 2 and, to lower extend, along arm 4. Shallow traps can delay the carrier diffusion without acting as non-radiative recombination centers.[160,161] The anisotropy in the trap distribution may again relate to ferroelasticity in $MAPbI_3$, with structural and electronic anomalies at the position of domain walls delaying the transversal motion of charge carriers.

Piezoresponse force microscopy

Ferroelectric and -elastic domain patterns can be resolved by PFM – a contact mode scanning probe microscopy method, which applies an AC voltage between a conductive tip and the sample. Since ferroelectric materials are piezoelectric, the AC voltage drives an oscillating piezoresponse. In PFM, the amplitude and phase response of the sample- cantilever system is detected by a lock in amplifier and recorded while scanning the tip across the surface. Thereby, PFM maps ferroelectric domain patterns.[62,162,163] PFM can image both out-of-plane and in-plane piezoresponses by detecting the vertical or torsional cantilever displacements, respectively.

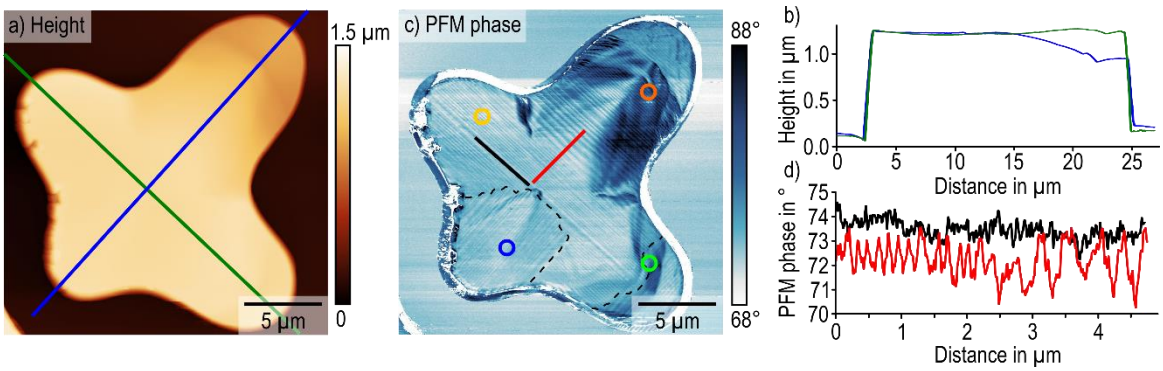

Figure 3.21: Lateral PFM measurement (1.5 V AC excitation, 735 kHz, 49 nN) on the isolated $MAPbI_3$ grain on glass. (a) Height signal with positions of profiles (green and blue line) shown in (b). (b) Height profiles, extracted at the position of the blue and green line in (a). (c) Lateral PFM phase images periodic twin domains with position of the profiles shown in (d) (solid red and black line). Dashed black lines outline areas with a 90° direction change. The detection positions of the time-resolved PL decays in Figure 3.19(b–e) are indicated by the circles. (d) PFM phase line-profiles, extracted at the positions of the solid red and black line in (c), showed the absence of periodicity in the profile parallel to the domains (black) and varying periodicities between 0.13 and 0.50 µm in the profile perpendicular to the domains (red). Reprinted with permission from Energy Environ. Sci., 2020, Advance Article. - Published by The Royal Society of Chemistry.

We collected lateral PFM data on the same isolate $MAPbI_3$ grain (Figure 3.21). The height signal and the deflection signal as height error showed an overall smooth surface with some terrace-like step edges (Figure 3.21a and b, SI in Appendix 8.2, Figure 8.10). Defined step edges and the flat surface suggested a high crystallinity as well as preferential crystal orientation, confirmed by 2D XRD (SI in Appendix 8.2, Figure 8.11). In agreement with our previous study, 2D XRD revealed that the majority of the grains on our sample had a (110) orientation parallel to the surface.[10] Simultaneously to the height signal, we measured the PFM phase signal (Figure 3.21c). In this image, we clearly distinguished a periodic domain pattern, that displayed no correlation to the height signal. Some of the domains spanned over almost the entire width of the grain from arm 1 to arm 3. The direction of the stripes changed by 90° for arm 4 and for the last 3 µm of arm 3 as indicated by the dashed lines in Figure 3.21c. The PFM phase profile in Figure 3.21d extracted along the red line perpendicular to the domains in Figure 3.21c shows that the domain widths varied between 0.13 and 0.50 µm.

When correlating the time-resolved PL decays (Figure 3.19b–e) to the periodic domain pattern (Figure 3.21c), we observed that shorter diffusion times coincided with a carrier diffusion parallel to the domains, while longer diffusion times coincided with a carrier diffusion perpendicular to the domains. Along arm 1, the carriers exclusively travelled parallel to domains towards the detection position, resulting in the shortest diffusion time (Figure 3.19b). Along arm 2, the carriers exclusively diffused perpendicular to the domains, which led to the longest detected diffusion time (Figure 3.19c). Along arms 3 and 4 (Figure 3.19d and e), the domain orientation changed by 90° between excitation and detection positions. Thus, the diffusion times detected here were combinations of parallel and perpendicular diffusion times. In arm 3, the domain orientation changed from parallel to perpendicular in close proximity to the detection position, giving rise to the shorter diffusion time compared to arm 4.

To evaluate the consistency of the correlation of the diffusion anisotropy and domain arrangement, we compared several PL decays at additional distances parallel and perpendicular to

the domains (SI in Appendix 8.2, Figures 8.12 and 8.13), inverted the excitation and detection positions (SI in Appendix 8.2, Figure 8.14) and repeated the PL and PFM measurements on another large, isolated $MAPbI_3$ grain (SI in Appendix 8.2, Figures 8.15 and 8.16). In agreement with the initial results, we consistently detected longer diffusion times for diffusion paths perpendicular than for those parallel to the domains. These results suggest that the origin for anisotropic charge carrier diffusion in $MAPbI_3$ perovskite is directly related to the domain pattern resolved via PFM.

Diffusion anisotropy

To quantify the diffusion along both directions of the domain pattern, we plotted the distance d versus the diffusion times τ_{Diff} and fitted the diffusion constants D via:

$$y = \sqrt{4\tau_{Diff} \times D}$$

Equation 3.2: Fit function to determine diffusion constant D.

We derived Equation 3.2 from the diffusion constants in two dimensions given by $D = d^2/4\tau_{Diff}$.[152] For the diffusion parallel to the domains, we obtained a diffusion constant of $D_{\parallel} = 1.9 \pm 0.1\ cm^2/s$ and for the perpendicular diffusion a constant of $D_{\perp} = 1.2 \pm 0.1\ cm^2/s$ (Figure 3.22a and b). These values agreed with diffusion constants from the literature measured within single grains of polycrystalline $MAPbI_3$ thin films; reported values range between 0.8 and 3.3 cm^2/s.[144,149,152] Calculating the carrier mobilities from the diffusion constants via the Einstein relation, $D = \mu \times kT/q$, with the Boltzmann constant k, the temperature T and the charge of the carrier q,[139] yielded $\mu_{\parallel} = 72 \pm 6\ cm^2/Vs$ in parallel and $\mu_{\perp} = 48 \pm 4\ cm^2/Vs$ in perpendicular direction. These mobility values were in the range of mobilities reported for polycrystalline and single crystal $MAPbI_3$.[145] Overall, we found that both the diffusion constant as well as the mobility of the charge carriers in the parallel direction were 50 – 60% higher than perpendicular to the domains, allowing us to quantify the diffusion anisotropy.

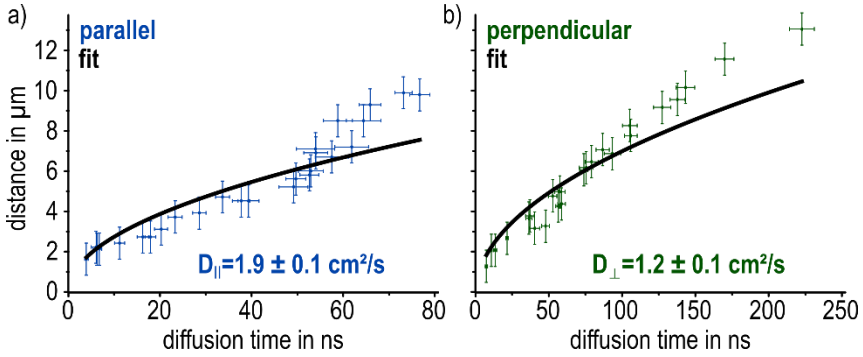

Figure 3.22: (a) Diffusion times parallel to the domains derived from fits of time-resolved PL decays plotted versus the distance between detection and excitation with the data fit according to Equation 3.2 and the parallel diffusion constant $D_{\parallel}$. (b) Diffusion times perpendicular to the domains derived from fits of time-resolved PL decays plotted versus the distance between detection and excitation with the data fit according to Equation 3.2 and the perpendicular diffusion constant $D_{\perp}$. Reprinted with permission from Energy Environ. Sci., 2020, Advance Article. - Published by The Royal Society of Chemistry.

While the fit of the diffusion constants coincided well with the data points at low diffusion times, we observed deviations from the fit for distances of more than 8 µm in both directions. This

deviation from the fitted random-walk diffusion model suggests that an additional mechanism affects the carrier diffusion especially at larger distances from the excitation. We exclude a macroscopic drift effect originating from grain boundaries, since diffusion times from the grain center and diffusion times with inverted excitation and detection locations coincide (SI in Appendix 8.2, Figure 8.14).

A possible candidate for this additional mechanism is photon recycling: A photon emitted via bimolecular recombination can be re-absorbed to create another free carrier pair at some distance from the source. In $MAPbI_3$, the low escape cone and high photoluminescence quantum yield of radiative recombination facilitates photon recycling, since light is kept in the crystal for longer distances, which increases the reabsorption probability.[155,156,158,164,165] Photon recycling is a diffusive process, but with higher velocities than pure carrier diffusion.[157] Thus, an overlay of pure diffusion and photon recycling would lead to an apparent acceleration of diffusion with increasing distance from the excitation. On the other hand, due to the squared dependence of the radiative recombination on the carrier density, we expect the decrease of the local carrier concentration further from the excitation to result in a lower probability for radiative recombination.[138] Therefore, the effect of photon recycling becomes weaker with increasing distances from the excitation (SI in Appendix 8.2, Simulation 8.17).

Mechanistic origin of domain influence on the carrier diffusion

The distinct correlation of the diffusion anisotropy and the domain arrangement suggests that the underlying nature of the domains directly affects the carrier transport. By now, several researchers resolved periodic twin domains in $MAPbI_3$ thin films and single crystals, independent of the substrate or the preparation procedure.[10–13,15,17] A requirement for the observation of the domains is a high crystallinity and, for surface sensitive methods like PFM, a uniform crystal orientation. Previous PFM studies on $MAPbI_3$ delivered contradictory interpretations of the periodic twins.[10–14,16,81,89] While some groups claim the PFM signal originates from ferroelectricity,[11,13,14,16,81] others assigned the PFM signal to competing mechanisms.[12,89,90] As such, Liu *et al.* suggested that the periodic PFM contrast originates from mechanical differences between the domains due to ion redistribution and ferroelasticity instead of ferroelectricity.[12,89]

While the ferroelectric nature of the periodic domains remains under discussion, their ferroelastic nature is widely accepted.[10,12,15,17,89,95] Ferroelastic domains naturally arise from changes of the crystal system to release internal strain.[1,60] In $MAPbI_3$, strain is introduced via the cubic-tetragonal phase transition at 54 °C, which occurs during preparation upon cooling to room temperature following the annealing step.[4,10,17,53,54] Consequently, periodic ferroelastic twin domains of alternating crystal orientation form.[1,60] Ferroelastic domain walls locally disrupt the crystalline order and therefore form energetic barriers. These barriers can act as shallow trap states or scattering centers, which delay the carrier diffusion perpendicular to domains.[130] Additionally, Warwick *et al.* proposed that the structural anomalies in ferroelastic domain walls (~1 nm in width) in the absence of bulk ferroelectricity introduce a localized in-plane electrical polarization of up to 6 $\mu C/cm^2$, potentially driving the carrier separation.[24] A charge-selective accumulation of electrons or holes in domain walls can introduce an electrostatic repulsion between carriers of the same species within domain walls, thus accelerating the apparent diffusion. This additional local drift

effect could explain the observed deviations from the random-walk diffusion in Figure 3.22. Likewise, Shi *et al.* found a suppression of non-radiative recombination in their calculations due to an effective charge carrier separation facilitated by ferroelastic domains, which reduce the electron-phonon coupling.[25]

On the other hand, theoretical studies on charge separation and transport based on ferroelectricity proposed charged domain walls with 90° head-to-head or tail-to-tail polarization orientation.[22,23,77,131] However, head-to-head and tail-to-tail orientation states give rise to energetically instable domain walls due to large depolarization fields and rarely occur naturally.[1,123] Instead, a weak charging of head-to-tail domain walls due to slight deviations from the 90° angle induced by internal strain and lattice mismatch is more likely.[1,123]

To determine the presence or absence of a ferroelectric polarization in $MAPbI_3$ and therefore the decisive driving mechanism behind the diffusion anisotropy, we performed additional PFM experiments on comparable $MAPbI_3$ samples. In particular, we aimed at investigating whether the PFM contrast originates from a true electromechanical (i.e., ferroelectric) response or simply from a contrast in the contact mechanics (i.e., ferroelastic). Changes in tip-sample contact mechanics e.g. introduced by variations of the contact stiffness, can strongly alter the detected motion of the electrostatically actuated cantilever, even in the absence of piezo- or ferroelectricity.[91]

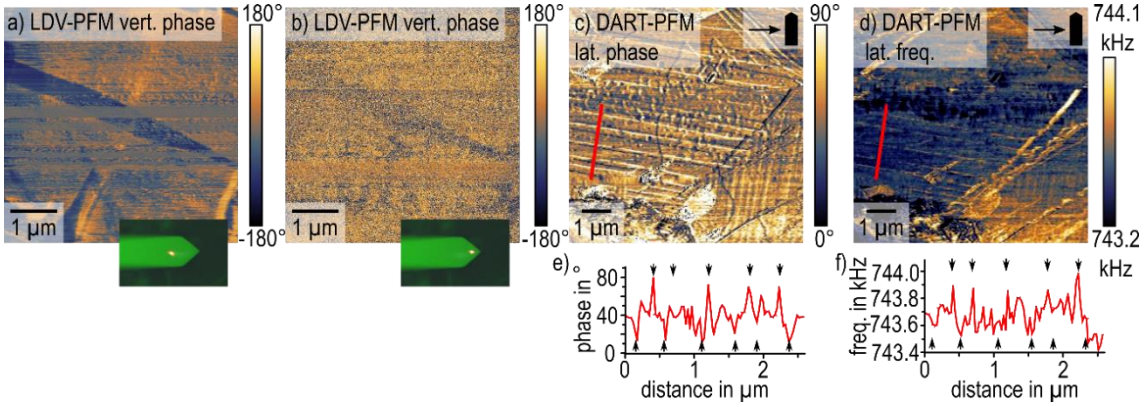

Figure 3.23: Complimentary PFM measurements to investigate the nature of the domain pattern. (a) and (b) show the vertical (vert.) PFM phase measured with a laser Doppler vibrometer (LDV) positioned far away from the tip (a) and on top of the tip (b). (c) lateral (lat.) PFM phase measured via dual amplitude resonance tracking (DART) and the corresponding DART frequency in (d). The cantilever alignment (scan angle 90°) and the scan direction are indicated in the box in the upper right corner. (e) Line profile extracted along the red line in (c). Domain wall positions indicated by the black arrows. (f) Line profile extracted along the red line in d. Domain wall positions indicated by the black arrows. Reprinted with permission from Energy Environ. Sci., 2020, Advance Article. - Published by The Royal Society of Chemistry.

First, we investigated the vertical PFM signal with a laser Doppler vibrometer (LDV), as demonstrated previously (Figure 3.23a and b).[12,91] Here, we observed a strong dependence of the PFM contrast on the laser position of the LDV: When we positioned the laser spot far from the tip on the cantilever, a distinct PFM phase contrast showed a needle shape domain with more than 100° phase difference to the rest of the imaged area (Figure 3.23a). However, when the position of the laser coincided with the position of the AFM tip,[166] the domain contrast in the PFM phase vanished (Figure 3.23b). The dependence of the vertical PFM signal on the laser position suggests that instead of a true electromechanical response, the vertical PFM contrast was caused by changes

in the tip-sample contact mechanics or by cantilever buckling. A lateral electromechanical response can introduce a false contrast in the vertical PFM signal due to a buckling motion of the cantilever.[10] Overall, we exclude a true out-of-plane electromechanical response as source of the vertical PFM signal.

Since LDV exclusively measures the vertical electromechanical response, we investigated the nature of the lateral PFM signal via dual amplitude resonance tracking (DART) PFM. DART PFM tracks changes in the contact resonance via a feedback system that controls the excitation frequency.[92] The DART frequency provides information on the nature of the PFM contrast, since variations in the tip-sample contact stiffness, either due to mechanical or topographic cross-talk cause changes in the contact resonance.[92]

By comparing the lateral DART PFM phase and the DART frequency output, we found a coinciding periodic domain pattern in the frequency and in the phase (Figure 3.23c–f). For the domains on the left side of the image, where the stripes aligned almost perpendicular to the cantilever, both channels displayed a contrast only at the position of domain walls. In the PFM phase, the domain walls featured an alternating contrast: A domain wall with a lower phase than the bulk followed a domain wall with a larger phase and vice versa. The DART frequency on the other hand, only imaged domain walls with a larger PFM phase as local frequency maxima, while the low phase domain walls were not resolved.

The alternating domain wall contrast in the PFM phase indicates an alternating parallel and antiparallel polarization along the domain walls, as suggested by Warwick *et al.*.[24] The reduced domain wall contrast on the vertically aligned domains on the right-hand side of the image supports this hypothesis: Here, the cantilever is oriented parallel to the domains and therefore not sensitive to the lateral electromechanical signal along the domain walls. For the bulk domains, on the other hand, we observed a largely uniform PFM phase signal suggesting the absence of a bulk ferroelectricity in $MAPbI_3$.

Meanwhile, the domain walls contrast in the DART frequency originates from local changes in the tip-sample contact mechanics, which shift the contact resonance frequency. Local strain gradients and structural anomalies at ferroelastic domain walls naturally affect the sample's nanomechanical properties and therefore the contact mechanics. As to why only every other domain wall changes the tip-sample contact mechanics, we suggest an impact of the orientation of the local strain gradient, which alternates between adjacent domain walls.[24]

Based on this in-depth investigation on the origin of the PFM response on $MAPbI_3$, we conclude that the structural and electrical deviations at ferroelastic domain walls from the bulk are the main contribution to the anisotropic carrier diffusion in $MAPbI_3$. In context of the previously proposed mechanisms – an acceleration of the diffusion parallel to the domains or a deceleration of the diffusion perpendicular to the domains – the latter seems to be the governing mechanism. The local disruption of the crystalline order and the strain gradients at the domain walls introduce shallow energy barriers, which delay the transversal motion of charge carriers. However, the apparent presence of a local polarization at the ferroelastic domain walls may lead to an additional

acceleration effect of the charge carriers.[24] Lastly, we did not observe indications for charged ferroelectric domain walls as charge-specific carrier pathways as previously proposed.[22,23,77,131]

In applied perovskite devices, the effect of the anisotropic carrier diffusion on the vertical carrier transport depends on the texture of the polycrystalline $MAPbI_3$ thin films: Rothmann *et al.* proposed a 45° angle of the domain walls with respect to the (110) crystal plane.[17] For highly oriented thin films, we expect the influence on the diffusion anisotropy to be minor along the 45° domain walls. However, in thin films with random crystal orientations of the constituent grains the impact of the diffusion anisotropy could introduce heterogeneities in the inter-grain carrier diffusion as previously reported.[140,148–151]

Manipulation of the domain arrangement

The relation between ferroelastic domain pattern and carrier diffusion offers new paths of device improvement for PSCs or perovskite-based optoelectronics by customizing the directionality of the carrier diffusion. Similar to other ferroic properties, the crystal orientation in ferroelastic domains can be switched upon application of an external stress.[1] Strelcov *et al.* demonstrated this stress-induced ferroelastic domain switching already in 2017.[15]

Here, we focused on the effect of heat treatments on the domain alignment. As such, we found that heating a freshly annealed $MAPbI_3$ sample with a predominantly irregular domain pattern over the ferroelastic cubic-tetragonal phase transition temperature of 54 °C[4,53,54] led to a complete disappearance of the domain pattern, further confirming the ferroelastic nature of the domains (Figure 3.24a and b). Upon cooling the sample back to room temperature with a well-defined cooling rate of 1 °C per minute, the domain pattern reappeared with a changed arrangement: An increase of the domain density and more regular spacings between the domains (Figure 3.24c). We suggest that the abrupt cooling after the annealing step introduced the disorder and the lower domain density in the initial state of the sample, while the well-defined cooling rates resulted in an ordered, high density domain arrangement.

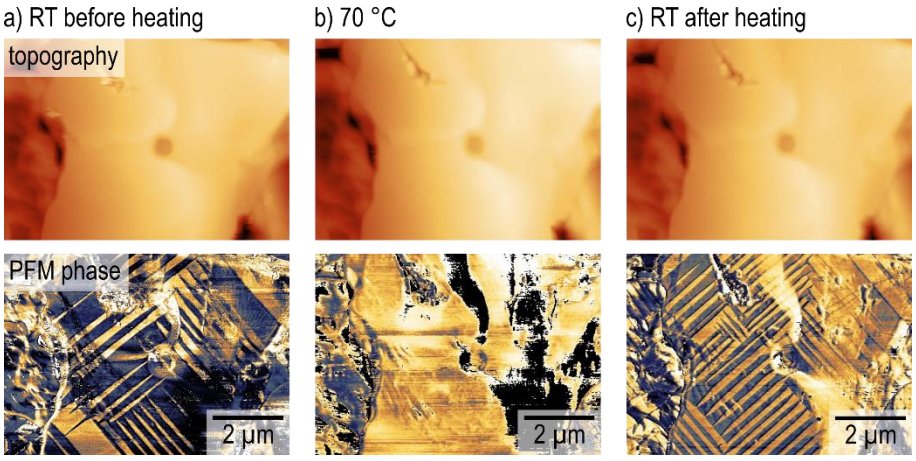

Figure 3.24: AFM topography (top row) and corresponding lateral PFM phase (a) before (at 26 °C), (b) during (at 70 °C) and (c) after (at 27 °C) the heating experiment over the cubic-tetragonal phase transition at 54 °C, visualizing a change

in the domain pattern following the heating cycle. Reprinted with permission from Energy Environ. Sci., 2020, Advance Article. - Published by The Royal Society of Chemistry.

Therefore, targeted heat treatment as well as stress-induced domain switching should be explored as future pathways to either reduce the anisotropy in the carrier diffusion by lowering the domain density or to introduce a preferential directionality in the carrier diffusion, by parallel domain alignment.

Summary

Via spatial- and time-resolved PL microscopy we resolved an anisotropic distribution of carrier diffusion times on isolated $MAPbI_3$ grains. This anisotropic charge carrier diffusion directly correlates to the arrangement of ferroelastic twin domains, which form to reduce crystalline strain due to the cubic-tetragonal phase transition. Quantitative analysis of the diffusion dependence on the domain arrangement gave a 50 – 60% higher diffusion constant parallel ($D_{\parallel} = 1.9 \pm 0.1$ cm^2/s) than perpendicular to the domains ($D_{\perp} = 1.2 \pm 0.1$ cm^2/s). Extensive PFM investigations on the underlying nature of the domains indicated the presence of local strain gradients and crystallographic inhomogeneities, as well as an electrical polarization at ferroelastic domain walls. We propose that these structural and electrical anomalies at the domain walls act as energetic barriers, which delay the carrier diffusion perpendicular to the domains introducing the diffusion anisotropy. Finally, we showed the possibility to manipulate the domain pattern via heat treatment above the phase transition temperature, opening new routes for optimizing optoelectronic devices based on $MAPbI_3$ and other ferroelastic materials.

Experimental

Sample preparation:

For the preparation of the $MAPbI_3$ thin films, we dissolved the precursors methylammonium iodide CH_3NH_3I (Methylammonium iodide was synthesized as described by Lee *et al.*)[32] and $PbCl_2$ (Sigma-Aldrich, 99.999%) in a 3:1 ratio with a concentration of 40wt% in anhydrous dimethylformamide (Sigma-Aldrich). We cleaned glass coverslips with thickness of 150 µm in an ultrasound bath for 15 minutes each in 2% Hellmanex solution, deionized water, acetone and isopropanol, in this order. The ultrasound cleaning was followed by a 5-minute treatment in oxygen plasma. The spin-coating of the solution onto the coverslips was performed in a nitrogen glovebox at 1750 rpm for 60 s with an acceleration of 250 rpm/s. Afterwards the samples annealed at room temperature for 30 minutes in the glovebox, followed by a solvent annealing[9] step at 100 °C for 60 min in air on a preheated hot plate. Immediately after the solvent annealing, we transferred the samples into another nitrogen glovebox, equipped with an atomic force microscope (AFM).

Spatial- and time-resolved photoluminescence (PL):

For the excitation, we used a picosecond laser (Hamamatsu Picosecond Light Pulser PLP-10) with a pulse width of 95 ± 5 ps at 635 nm wavelength, repetition rates of 2 MHz (for time-resolved PL) and 20 MHz (for static PL) and fluences between 0.77 and 0.89 µJ/cm^2 (SI in Appendix 8.2, Figure 8.6). Due to the large bandwidth of the excitation laser, the beam was guided through a 633 nm clean-up filter (Semrock, 632.8 nm MaxLine) with a bandwidth of 2.4 nm FWHM, changing the center wavelength to 633 nm. The excitation light was focused via a 20x objective (Olympus LMPLFL20, numerical aperture NA= 0.4) onto the sample surface with a spot diameter

of 0.81 µm at FWHM and 1.4 µm $1/e^2$ width (SI in Appendix 8.2, Figure 8.8). The sample was placed onto the stage of an inverted microscope (Olympus IX70) equipped with a 50x objective (Olympus MPLAPO50, NA= 0.95) and coupled to an Olympus FluoView FV300 confocal laser scanning unit. For the static PL measurements, the collected PL was detected with a photomultiplier, after passing a dichroic mirror, the pinhole (300 µm) and a 660 nm longpass filter (Chroma HQ660LP). For the time-resolved PL, after passing the pinhole (60 µm), the collected PL emission was guided through an optical fiber to a PicoQuant detection unit equipped with two single photon avalanche diodes (τ-SPAD) connected to a TCSPC board (TimeHarp 200). In front the diodes, a 635 nm long pass filter (Semrock, 635 nm Edge Basic) and a 633 nm notch filter (Semrock, 633 nm StopLine Single-notch) with a bandwidth of 25 nm were placed. For a pinhole of 60 µm and the 50x objective, the detection spot had a radius of 0.18 µm for a wavelength of 765 nm. The instrument response function was ~1.4 ns at FWHM. During the scan, nitrogen was continuously flowing over the sample to avoid degradation (SI in Appendix 8.2, Figure 8.18).

Piezoresponse force microscopy (PFM):

Lateral PFM was measured on an MFP-3D atomic force microscope from Asylum Research (Oxford Instruments) and a Zurich Instruments HF2 lock-in amplifier in a nitrogen glovebox. The measurements were performed at room temperature with conductive platinum-iridium coated SCM PIT-V2 cantilevers from Bruker with free resonance frequencies of 70 kHz and spring constants of k ~ 2.5 nN/nm. We measured lateral PFM at AC excitation voltages with peak amplitudes of 1.5 V close to the lateral contact resonance at 735 kHz to utilize the resonance enhancement. As back electrodes, we used aluminum. To mark the PFM-characterized sample areas for the PL microscopy we scratched a pattern into the $MAPbI_3$ film and measured close to a scratch.

The LDV-PFM measurements were performed using a commercial Cypher ES AFM (Asylum Research, Santa Barbara, CA) with an integrated quantitative Laser Doppler Vibrometer (LDV) system (Polytec GmbH, Waldbronn, Germany) to achieve highly sensitive electromechanical imaging and spectroscopy. Measurements were performed using Pt/Ir-coated cantilevers (ElectriMulti 75G from Budget Sensors) with a nominal spring constant of ~3 N/m and resonance frequency of ~75 kHz were used. All measurements were captured at room temperature under nitrogen flow. We measured the LDV-PFM signal at AC excitation voltages with peak amplitudes of 2 V at 265 kHz.

For the lateral dual amplitude resonance tracking (DART) experiments, we again used the MFP-3D atomic force microscope from Asylum Research (Oxford Instruments) in a nitrogen glovebox with SCM PIT-V2 cantilevers with free resonance frequencies of 70 kHz and spring constants of k ~ 2.5 nN/nm at room temperature. The lateral contact resonance was at 746 kHz and the two sidebands for the frequency tracking were generated at 1.5 kHz from the resonance. The AC drive was 1.5 V.

The heating experiment was performed on a Cypher ES AFM (Oxford Instruments) in nitrogen atmosphere. For the lateral PFM measurements, we used a platinum-iridium coated PPP-EFM cantilever with a free resonance frequency of 75 kHz and spring constants of k ~ 2.8 nN/nm. The AC drive was 1.5 V at 675 kHz. The sample temperature before the heating step was 26 °C.

Afterwards the sample was heated at 1 °C/min to 70 °C. We waited around 30 min for the sample temperature to equilibrate before measuring. Afterwards the sample was cooled to 27 °C and we waited around 30 min for the sample temperature to equilibrate before measuring the PFM signal.

X-ray diffraction (XRD):

X-ray diffraction on the $MAPbI_3$ film was measured on a 6-circle diffractometer using Cu Kα radiation (Rigaku MicroMax 007 Xray generator, Osmic Confocal Max-Flux curved multilayer optics). The sample was mounted in reflection geometry at an incident angle of 4.5°. 2D scattering patterns were collected on an image plate detector (Mar345, 150 μm pixel size) at a sample-detector distance of 356.83 mm.

Author Contributions

I.M.H. and L.W. prepared the $MAPbI_3$ samples. I.M.H. and A.B. performed the spatial- and time-resolved PL microscopy measurements under supervision of K.K., S.A.L.W and H.-J.B.. I.M.H. performed lateral and DART PFM measurements under supervision of S.A.L.W and H.-J.B., as well as the heating PFM measurements with S.V. under supervision of D.S.G.. L.W. and L.C. performed the LDV-PFM measurements. I.M.H., J.M. and M.M. performed the 2D XRD measurements. I.M.H. interpreted the PL, PFM and XRD data with contributions of S.A.L.W. and L.C. S.A.L.W. modelled the contribution of photon recycling. I.M.H. wrote the manuscript with help of S.A.L.W., D.S.G. and L.C.. All authors contributed to the scientific discussion and revision of the manuscript.

Associated Content

The Supporting Information can be found in Appendix 8.2, and contains:

A schematic of the spatial- and time-resolved PL microscopy setup, the diameter of the laser spot, the calculation of the charge carrier density at the given laser fluence, additional time-resolved PL decays to Figure 3.19, deflection image of the PFM measurement in Figure 3.21, 2D XRD measurement, overlays of PFM phase and additional time-resolved PL decays, time-resolved PL decays with inverted excitation and detection setup, PFM measurement of second $MAPbI_3$ grain, time-resolved PL decays on second $MAPbI_3$ grain, simulation of contribution of photon recycling to diffusion process, PFM measurement after PL measurements.

Acknowledgements

I.M.H. acknowledges ERC Grant No. 340391 SuPro for funding. D.S.G. and S.M.H. acknowledge support from the DOE (DE-SC0013957). LDV-PFM was conducted at the Center for Nanophase Materials Sciences, which is a DOE Office of Science User Facility. PFM during heat treatment was conducted at the Molecular Analysis Facility, a National Nanotechnology Coordinated Infrastructure site at the University of Washington, which is supported in part by the National Science Foundation (Grant ECC-1542101), the University of Washington, the Molecular Engineering & Sciences Institute, the Clean Energy Institute, and the National Institutes of Health. We thank Rüdiger Berger and Denis Andrienko for helpful discussions.

-Publication end-

3.2.3 Conclusion and outlook

In this subchapter, we explored the influence of ferroelastic domain walls as subcrystalline boundary structures on the charge carrier transport with and without an external electric field. While the domain influence on the vertical and lateral (photo-) conductivity was inconclusive, we found that ferroelastic domain walls cause an anisotropy in the carrier diffusion. Whether the domain walls facilitate a faster diffusion along the domain walls due to a flexoelectric polarization, delay the perpendicular transport by acting as shallow carrier traps or both, needs to be investigated in the future. Particularly, a faster charge transport along ferroelastic domain walls promises new electronic applications and performance enhancements not only in $MAPbI_3$ but also in other nonpolar ferroelastic materials. Domain walls as nanometer-sized switchable 2D topological structures bear a significant potential for electronics and optoelectronics.

For future studies on the interaction of charge carriers and ferroelastic domain walls, a spectral analysis of the PL signals in Chapter 3.2.2 would be useful. PL spectra could detangle signals of photon recycling and diffusive charges and thereby allow a detailed differentiation of the domain wall effect on trapped light and charge carriers. Furthermore, since PL microscopy can only capture diffusive carriers that recombine bimolecularly (Chapter 1.4.2.2), it is not possible to distinguish between hole and electron diffusion. Time-resolved pump-probe KPFM with a nanosecond time resolution could visualize and differentiate charge carriers before recombination. Thereby, we could resolve preferable hole and electron diffusion pathways. Moreover, the nanometer spatial resolution of KPFM may allow resolving differences in the diffusion times on bulk domains and domain walls.

My CAFM studies on the domain influence on the carrier drift in an electric field were inconclusive. The high ionic mobility in $MAPbI_3$ may have resulted in ionic surface flooding, which screened local variations in electronic conductivity. Likewise, a degradation of the grain surface could have interfered with current detection in CAFM. Here, lower sample biases or illumination intensities combined with a high sensitivity current detection could provide remedy in the future. Furthermore, a point-by-point current detection as demonstrated by Leblebici *et al.*[87] could increase the tip and sample lifetime. High quality single crystals may also lead to a higher sample imaging stability. CAFM aside, time- and spatially resolved PL or pump-probe KPFM measurements on a lateral device in an electric field application may facilitate a more controlled drift characterization. These less invasive characterization methods allow for an improved accuracy due to reduced crosstalk, while imaging the impact of domain walls on charge carriers in the build-in field of solar cells.

Beyond the effect of subcrystalline domains on electronic charges, this study could be expanded to the domain impact on ionic charges in the future. With ferroelastic domain walls prone to act as preferential doping sites (Chapter 1.3.1.1), a local accumulation of ionic charges is possible. Here, chemical mapping techniques with high spatial resolution such as nano-IR, tip-enhanced Raman spectroscopy or energy-dispersive x-ray spectroscopy (EDX) could aid to detect local variations in ion concentration and detangle electronic and ionic contributions on the KPFM signal, if required.

3.3 Ferroelastic twins – concluding remarks

In this chapter, I presented our in-depth investigations on the structure, nature and effect on charge carriers of subcrystalline twin domains in $MAPbI_3$. The domain pattern, its mechanical response and behavior across $MAPbI_3$'s cubic-tetragonal phase transition suggest a ferroelastic nature, whereas ferroelectricity appears unlikely. These ferroelastic domains affect photocarriers by introducing an anisotropy in the diffusion constants measured parallel or perpendicular to the domain walls: The parallel diffusion gave a diffusion constant of $D_{\parallel} = 1.9 \pm 0.1\,\mathrm{cm^2/s}$ and the perpendicular diffusion a diffusion constant of $D_{\perp} = 1.2 \pm 0.1\,\mathrm{cm^2/s}$. Ferroelastic domain walls as subcrystalline boundaries can disrupt the local crystal structure significantly (Chapter 1.3.1.1). Hence, we suggest that the anisotropy originates either from domain walls acting as shallow potential barriers, which delay the perpendicular carrier diffusion, or from domain walls featuring a flexoelectric polarization, which accelerates the parallel carrier diffusion.

In the future, the domain influence on the charge carrier diffusion could be exploited for PSC optimization. With the 90° domain alignment with respect to the (110) surface plane throughout bulk crystals, a faster carrier transport parallel to the domains promises a more efficient charge extraction for (110) film texture than for other crystal orientations. This finding directly agrees with a previous study by Docampo *et al.*, who observed maximum short circuit currents for a (110) texture,[88] and could explain the facet-dependent PCE imaged on non-textured $MAPbI_3$ thin films.[87]

Moreover, due to the ferroelastic nature of the domains, heat treatments and application of mechanical stress offer routes to tailor domain patterns as required via targeted strain engineering. For example, fast cooling rates and torsional stress can reduce the overall domain density to allow for an isotropic carrier diffusion.

With their response to external stimuli and apparent effect on electronic charges, ferroelastic domain walls can be viewed as flexible and functional subcrystalline boundary structures with applications beyond PSCs. Here, future studies could explore the optoelectronic impact of ferroelastic domain walls in perovskite-based photodiodes and photodetectors and expand to other functional ferroelastics.

Bibliography:

1. Tagantsev, A. K., Cross, L. E. & Fousek, J. *Domains in ferroic crystals and thin films*. **13**, (Springer, 2010).
2. Cohen, R. E. Origin of ferroelectricity in perovskite oxides. *Nature* **358**, 136–138 (1992).
3. Wilson, J. N., Frost, J. M., Wallace, S. K. & Walsh, A. Dielectric and ferroic properties of metal halide perovskites. *APL Mater.* **7**, 10901 (2019).
4. Stoumpos, C. C., Malliakas, C. D. & Kanatzidis, M. G. Semiconducting tin and lead iodide perovskites with organic cations: phase transitions, high mobilities, and near-infrared photoluminescent properties. *Inorg. Chem.* **52**, 9019–9038 (2013).
5. Kutes, Y. *et al.* Direct observation of ferroelectric domains in solution-processed

CH3NH3PbI3 perovskite thin films. *J. Phys. Chem. Lett.* **5**, 3335–3339 (2014).

6. Coll, M. *et al.* Polarization switching and light-enhanced piezoelectricity in lead halide perovskites. *J. Phys. Chem. Lett.* **6**, 1408–1413 (2015).

7. Fan, Z. *et al.* Ferroelectricity of CH3NH3PbI3 perovskite. *J. Phys. Chem. Lett.* **6**, 1155–1161 (2015).

8. Xiao, Z. *et al.* Giant switchable photovoltaic effect in organometal trihalide perovskite devices. *Nat. Mater.* **14**, 193–198 (2015).

9. Xiao, Z. *et al.* Solvent annealing of perovskite-induced crystal growth for photovoltaic-device efficiency enhancement. *Adv. Mater.* **26**, 6503–6509 (2014).

10. Hermes, I. M. *et al.* Ferroelastic Fingerprints in Methylammonium Lead Iodide Perovskite. *J. Phys. Chem. C* **120**, (2016).

11. Röhm, H., Leonhard, T., Hoffmann, M. J. & Colsmann, A. Ferroelectric domains in methylammonium lead iodide perovskite thin-films. *Energy Environ. Sci.* **10**, 950–955 (2017).

12. Liu, Y. *et al.* Chemical nature of ferroelastic twin domains in CH3NH3PbI3 perovskite. *Nat. Mater.* **17**, 1013–1019 (2018).

13. Vorpahl, S. M. *et al.* Orientation of Ferroelectric Domains and Disappearance upon Heating Methylammonium Lead Triiodide Perovskite from Tetragonal to Cubic Phase. *ACS Appl. Energy Mater.* **1**, 1534–1539 (2018).

14. Huang, B. *et al.* Ferroic domains regulate photocurrent in single-crystalline CH3NH3PbI3 films self-grown on FTO/TiO2 substrate. *npj Quantum Mater.* **3**, 1–8 (2018).

15. Strelcov, E. *et al.* CH3NH3PbI3 perovskites: Ferroelasticity revealed. *Sci. Adv. Adv.* **3**, e1602165 (2017).

16. Garten, L. M. *et al.* The existence and impact of persistent ferroelectric domains in MAPbI3. *Sci. Adv.* **5**, eaas9311 (2019).

17. Rothmann, M. U. *et al.* Direct observation of intrinsic twin domains in tetragonal CH3NH3PbI3. *Nat. Commun.* **8**, 1–8 (2017).

18. Kennard, R. M. *et al.* Ferroelastic Hysteresis in Thin Films of Methylammonium Lead Iodide. *Chem. Mater.* **33**, 298–309 (2021).

19. Medjahed, A. A. *et al.* Unraveling the Formation Mechanism and Ferroelastic Behavior of MAPbI3 Perovskite Thin Films Prepared in the Presence of Chloride. *Chem. Mater.* **32**, 3346–3357 (2020).

20. Breternitz, J., Tovar, M. & Schorr, S. Twinning in MAPbI3 at room temperature uncovered through Laue neutron diffraction. *Sci. Rep.* **10**, 16613 (2020).

21. Hermes, I. M. *et al.* Anisotropic carrier diffusion in single MAPbI3 grains correlates to their

twin domains. *Energy Environ. Sci.* **13**, 4168–4177 (2020).

22. Frost, J. M. *et al.* Atomistic origins of high-performance in hybrid halide perovskite solar cells. *Nano Lett.* **14**, 2584–2590 (2014).

23. Liu, S. *et al.* Ferroelectric domain wall induced band gap reduction and charge separation in organometal halide perovskites. *J. Phys. Chem. Lett.* **6**, 693–699 (2015).

24. Warwick, A. R., Íñiguez, J., Haynes, P. D. & Bristowe, N. C. First-principles study of ferroelastic twins in halide perovskites. *J. Phys. Chem. Lett.* **10**, 1416–1421 (2019).

25. Shi, R., Zhang, Z., Fang, W. & Long, R. Ferroelastic Domains Drive Charge Separation and Suppress Electron– Hole Recombination in All– Inorganic Halide Perovskites: Time–Domain Ab Initio Analysis. *Nanoscale Horiz.* (2020).

26. Xiao, X. *et al.* Benign ferroelastic twin boundaries in halide perovskites for charge carrier transport and recombination. *Nat. Commun.* **11**, 2215 (2020).

27. Röhm, H., Leonhard, T., Hoffmann, M. J. & Colsmann, A. Ferroelectric Poling of Methylammonium Lead Iodide Thin Films. *Adv. Funct. Mater.* **30**, 1908657 (2020).

28. Ivry, Y., Scott, J. F., Salje, E. K. H. & Durkan, C. Nucleation, growth, and control of ferroelectric-ferroelastic domains in thin polycrystalline films. *Phys. Rev. B* **86**, 205428 (2012).

29. Matzen, S. *et al.* Super switching and control of in-plane ferroelectric nanodomains in strained thin films. *Nat. commun.* **5**, 1–8 (2014).

30. Kojima, A., Teshima, K., Shirai, Y. & Miyasaka, T. Organometal halide perovskites as visible-light sensitizers for photovoltaic cells. *J. Am. Chem. Soc.* **131**, 6050–6051 (2009).

31. Kim, H.-S. *et al.* Lead iodide perovskite sensitized all-solid-state submicron thin film mesoscopic solar cell with efficiency exceeding 9%. *Sci. Rep.* **2**, 591 (2012).

32. Lee, M. M., Teuscher, J., Miyasaka, T., Murakami, T. N. & Snaith, H. J. Efficient hybrid solar cells based on meso-superstructured organometal halide perovskites. *Science (80-.).* **338**, 643–647 (2012).

33. Yang, W. S. *et al.* High-performance photovoltaic perovskite layers fabricated through intramolecular exchange. *Science (80-.).* **348**, 1234–1237 (2015).

34. Grätzel, M. The light and shade of perovskite solar cells. *Nat. Mater.* **13**, 838–842 (2014).

35. McGehee, M. D. Perovskite solar cells: continuing to soar. *Nat. Mater.* **13**, 845–846 (2014).

36. Snaith, H. J. Perovskites: the emergence of a new era for low-cost, high-efficiency solar cells. *J. Phys. Chem. Lett.* **4**, 3623–3630 (2013).

37. Kazim, S., Nazeeruddin, M. K., Grätzel, M. & Ahmad, S. Perovskite as light harvester: a game changer in photovoltaics. *Angew. Chem. Int. Ed.* **53**, 2812–2824 (2014).

38. Stranks, S. D. *et al.* Electron-hole diffusion lengths exceeding 1 micrometer in an organometal trihalide perovskite absorber. *Science (80-.).* **342**, 341–344 (2013).

39. Wehrenfennig, C., Eperon, G. E., Johnston, M. B., Snaith, H. J. & Herz, L. M. High charge carrier mobilities and lifetimes in organolead trihalide perovskites. *Adv. Mater.* **26**, 1584–1589 (2014).

40. Nazeeruddin, M. K. & Snaith, H. Methylammonium lead triiodide perovskite solar cells: A new paradigm in photovoltaics. *Mrs Bull.* **40**, 641–645 (2015).

41. Snaith, H. J. *et al.* Anomalous hysteresis in perovskite solar cells. *J. Phys. Chem. Lett.* **5**, 1511–1515 (2014).

42. Frost, J. M., Butler, K. T. & Walsh, A. Molecular ferroelectric contributions to anomalous hysteresis in hybrid perovskite solar cells. *APL Mater.* **2**, 81506 (2014).

43. Chen, B. *et al.* Interface band structure engineering by ferroelectric polarization in perovskite solar cells. *Nano Energy* **13**, 582–591 (2015).

44. Chen, H.-W., Sakai, N., Ikegami, M. & Miyasaka, T. Emergence of hysteresis and transient ferroelectric response in organo-lead halide perovskite solar cells. *J. Phys. Chem. Lett.* **6**, 164–169 (2015).

45. Wei, J. *et al.* Hysteresis analysis based on the ferroelectric effect in hybrid perovskite solar cells. *J. Phys. Chem. Lett.* **5**, 3937–3945 (2014).

46. O'Regan, B. C. *et al.* Optoelectronic studies of methylammonium lead iodide perovskite solar cells with mesoporous TiO2: separation of electronic and chemical charge storage, understanding two recombination lifetimes, and the evolution of band offsets during J–V hysteresis. *J. Am. Chem. Soc.* **137**, 5087–5099 (2015).

47. Beilsten-Edmands, J., Eperon, G. E., Johnson, R. D., Snaith, H. J. & Radaelli, P. G. Non-ferroelectric nature of the conductance hysteresis in CH3NH3PbI3 perovskite-based photovoltaic devices. *Appl. Phys. Lett.* **106**, 173502 (2015).

48. Zhang, Y. *et al.* Charge selective contacts, mobile ions and anomalous hysteresis in organic–inorganic perovskite solar cells. *Mater. Horiz.* **2**, 315–322 (2015).

49. Bergmann, V. W. *et al.* Real-space observation of unbalanced charge distribution inside a perovskite-sensitized solar cell. *Nat. Commun.* **5**, 1–9 (2014).

50. Tress, W. *et al.* Understanding the rate-dependent J–V hysteresis, slow time component, and aging in CH 3 NH 3 PbI 3 perovskite solar cells: the role of a compensated electric field. *Energy Environ. Sci.* **8**, 995–1004 (2015).

51. Unger, E. L. *et al.* Hysteresis and transient behavior in current–voltage measurements of hybrid-perovskite absorber solar cells. *Energy Environ. Sci.* **7**, 3690–3698 (2014).

52. van Reenen, S., Kemerink, M. & Snaith, H. J. Modeling anomalous hysteresis in perovskite solar cells. *J. Phys. Chem. Lett.* **6**, 3808–3814 (2015).

53. Dang, Y. *et al.* Bulk crystal growth of hybrid perovskite material CH3NH3PbI3. *CrystEngComm* **17**, 665–670 (2015).

54. Weller, M. T., Weber, O. J., Henry, P. F., Di Pumpo, A. M. & Hansen, T. C. Complete structure and cation orientation in the perovskite photovoltaic methylammonium lead iodide between 100 and 352 K. *Chem. Commun.* **51**, 4180–4183 (2015).

55. Bretschneider, S. A., Weickert, J., Dorman, J. A. & Schmidt-Mende, L. Research update: physical and electrical characteristics of lead halide perovskites for solar cell applications. *APL Mater.* **2**, 155204 (2014).

56. Poglitsch, A. & Weber, D. Dynamic disorder in methylammoniumtrihalogenoplumbates (II) observed by millimeter-wave spectroscopy. *J. Chem. Phys.* **87**, 6373–6378 (1987).

57. Kawamura, Y., Mashiyama, H. & Hasebe, K. Structural study on cubic-tetragonal transition of CH 3 NH 3 PbI 3. *J. Phys. Soc. Jpn.* **71**, 1694–1697 (2002).

58. Baikie, T. *et al.* Synthesis and crystal chemistry of the hybrid perovskite (CH3NH3) PbI3 for solid-state sensitised solar cell applications. *J. Mater. Chem. A* **1**, 5628–5641 (2013).

59. Salje, E. Phase transitions in ferroelastic and co-elastic crystals. *Ferroelectrics* **104**, 111–120 (1990).

60. Salje, E. K. H. Ferroelastic materials. *Annu. Rev. Mater. Res.* **42**, 265–283 (2012).

61. Berger, R., Domanski, A. L. & Weber, S. A. L. Electrical characterization of organic solar cell materials based on scanning force microscopy. *Eur. Polym. J.* **49**, 1907–1915 (2013).

62. Soergel, E. Piezoresponse force microscopy (PFM). *J. Phys. D Appl. Phys.* **44**, 464003 (2011).

63. Kalinin, S. V, Rodriguez, B. J. & Kholkin, A. L. Piezoresponse force microscopy and spectroscopy. *Encyclopedia of Nanotechnology* 2117–2125 (2012).

64. Chen, B. *et al.* Ferroelectric solar cells based on inorganic–organic hybrid perovskites. *J. Mater. Chem. A* **3**, 7699–7705 (2015).

65. Kim, H.-S. *et al.* Ferroelectric polarization in CH3NH3PbI3 perovskite. *J. Phys. Chem. Lett.* **6**, 1729–1735 (2015).

66. Zhao, P. *et al.* Spontaneous polarization behaviors in hybrid halide perovskite film. *Scr. Mater.* **102**, 51–54 (2015).

67. Kholkin, A. L., Pertsev, N. A. & Goltsev, A. V. Piezoelectricity and Crystal Symmetry. in *Piezoelectric and Acoustic Materials for Transducer Applications.* (eds. Safari, A. & Akdoğan, E. K.) (Springer, 2008).

68. Cao, W. & Randall, C. A. Grain size and domain size relations in bulk ceramic ferroelectric materials. *J. Phys. Chem. Solids* **57**, 1499–1505 (1996).

69. Song, Z. *et al.* Impact of processing temperature and composition on the formation of

methylammonium lead iodide perovskites. *Chem. Mater.* **27**, 4612–4619 (2015).

70. Christians, J. A., Miranda Herrera, P. A. & Kamat, P. V. Transformation of the excited state and photovoltaic efficiency of CH3NH3PbI3 perovskite upon controlled exposure to humidified air. *J. Am. Chem. Soc.* **137**, 1530–1538 (2015).

71. Park, N.-G. Perovskite solar cells: an emerging photovoltaic technology. *Mater. today* **18**, 65–72 (2015).

72. Zhao, Y. & Zhu, K. Charge transport and recombination in perovskite (CH3NH3) PbI3 sensitized TiO2 solar cells. *J. Phys. Chem. Lett.* **4**, 2880–2884 (2013).

73. Lee, Y. H. *et al.* Unraveling the reasons for efficiency loss in perovskite solar cells. *Adv. Funct. Mater.* **25**, 3925–3933 (2015).

74. Supasai, T., Rujisamphan, N., Ullrich, K., Chemseddine, A. & Dittrich, T. Formation of a passivating CH3NH3PbI3/PbI2 interface during moderate heating of CH3NH3PbI3 layers. *Appl. Phys. Lett.* **103**, 183906 (2013).

75. Yu, H. *et al.* The role of chlorine in the formation process of "CH3NH3PbI3-xClx" perovskite. *Adv. Funct. Mater.* **24**, 7102–7108 (2014).

76. Rubio-Marcos, F., Del Campo, A., Marchet, P. & Fernández, J. F. Ferroelectric domain wall motion induced by polarized light. *Nat. commun.* **6**, 1–9 (2015).

77. Rossi, D. *et al.* On the importance of ferroelectric domains for the performance of perovskite solar cells. *Nano Energy* **48**, 20–26 (2018).

78. Mosconi, E., Ronca, E. & De Angelis, F. First-Principles Investigation of the TiO2/Organohalide Perovskites Interface: The Role of Interfacial Chlorine. *J. Phys. Chem. Lett.* **5**, 2619–2625 (2014).

79. Starr, D. E. *et al.* Direct observation of an inhomogeneous chlorine distribution in CH3NH3PbI3−xClx layers: surface depletion and interface enrichment. *Energy Environ. Sci.* **8**, 1609–1615 (2015).

80. Miyadera, T. *et al.* Crystallization Dynamics of Organolead Halide Perovskite by Real-Time X-ray Diffraction. *Nano Lett.* **15**, 5630–5634 (2015).

81. Leonhard, T. *et al.* Probing the Microstructure of Methylammonium Lead Iodide Perovskite Solar Cells. *Energy Technol.* **7**, 1800989 (2019).

82. Han, W.-S., Kang, S.-O. & Suh, I.-H. An Easier Way to Calculate the Crystallographic Interplanar Angles. *Korean J. Crystallogr.* **18**, 7–9 (2007).

83. Conings, B. *et al.* The impact of precursor water content on solution-processed organometal halide perovskite films and solar cells. *J. Mater. Chem. A* **3**, 19123–19128 (2015).

84. Eperon, G. E. *et al.* The importance of moisture in hybrid lead halide perovskite thin film fabrication. *ACS Nano* **9**, 9380–9393 (2015).

85. You, J. *et al.* Moisture assisted perovskite film growth for high performance solar cells. *Appl. Phys. Lett.* **105**, 183902 (2014).

86. Zhou, Q., Jin, Z., Li, H. & Wang, J. Enhancing performance and uniformity of CH 3 NH 3 PbI 3− x Cl x perovskite solar cells by air-heated-oven assisted annealing under various humidities. *Sci. Rep.* **6**, 1–8 (2016).

87. Leblebici, S. Y. *et al.* Facet-dependent photovoltaic efficiency variations in single grains of hybrid halide perovskite. *Nat. Energy* **1**, 1–7 (2016).

88. Docampo, P. *et al.* Influence of the orientation of methylammonium lead iodide perovskite crystals on solar cell performance. *Apl Mater.* **2**, 81508 (2014).

89. Liu, Y. *et al.* Dynamic behavior of CH3NH3PbI3 perovskite twin domains. *Appl. Phys. Lett.* **113**, 72102 (2018).

90. Gómez, A., Wang, Q., Goñi, A. R., Campoy-Quiles, M. & Abate, A. Ferroelectricity-free lead halide perovskites. *Energy Environ. Sci.* **12**, 2537–2547 (2019).

91. Collins, L., Liu, Y., Ovchinnikova, O. S. & Proksch, R. Quantitative electromechanical atomic force microscopy. *ACS Nano* **13**, 8055–8066 (2019).

92. Rodriguez, B. J., Callahan, C., Kalinin, S. V & Proksch, R. Dual-frequency resonance-tracking atomic force microscopy. *Nanotechnology* **18**, 475504 (2007).

93. Sharada, G. *et al.* Is CH3NH3PbI3 Polar. *J. Phys. Chem. Lett* **7**, 2412–2419 (2016).

94. Hoque, M. N. F. *et al.* Polarization and dielectric study of methylammonium lead iodide thin film to reveal its nonferroelectric nature under solar cell operating conditions. *ACS Energy Lett.* **1**, 142–149 (2016).

95. Anusca, I. *et al.* Dielectric response: Answer to many questions in the methylammonium lead halide solar cell absorbers. *Adv. Energy Mater.* **7**, 1700600 (2017).

96. Wang, F., Grinberg, I. & Rappe, A. M. Band gap engineering strategy via polarization rotation in perovskite ferroelectrics. *Appl. Phys. Lett.* **104**, 152903 (2014).

97. Butler, K. T., Frost, J. M. & Walsh, A. Ferroelectric materials for solar energy conversion: photoferroics revisited. *Energy Environ. Sci.* **8**, 838–848 (2015).

98. Leguy, A. M. A. *et al.* Experimental and theoretical optical properties of methylammonium lead halide perovskites. *Nanoscale* **8**, 6317–6327 (2016).

99. Jacobsson, T. J. *et al.* Exploration of the compositional space for mixed lead halogen perovskites for high efficiency solar cells. *Energy Environ. Sci.* **9**, 1706–1724 (2016).

100. Grinberg, I. *et al.* Perovskite oxides for visible-light-absorbing ferroelectric and photovoltaic materials. *Nature* **503**, 509–512 (2013).

101. Rabe, K. M., Dawber, M., Lichtensteiger, C., Ahn, C. H. & Triscone, J.-M. Modern physics of ferroelectrics: Essential background. in *Physics of Ferroelectrics* 1–30 (Springer, 2007).

102. Rakita, Y. *et al.* Tetragonal CH3NH3PbI3 is ferroelectric. *Proc. Natl. Acad. Sci. U.S.A* **114**, E5504–E5512 (2017).

103. Weber, S. A. L. *et al.* How the formation of interfacial charge causes hysteresis in perovskite solar cells. *Energy Environ. Sci.* **11**, (2018).

104. Hermes, I. M., Hou, Y., Bergmann, V. W., Brabec, C. J. & Weber, S. A. L. The Interplay of Contact Layers: How the Electron Transport Layer Influences Interfacial Recombination and Hole Extraction in Perovskite Solar Cells. *J. Phys. Chem. Lett.* **9**, (2018).

105. Bergmann, V. W. *et al.* Local Time-Dependent Charging in a Perovskite Solar Cell. *ACS Appl. Mater. Interfaces* **8**, (2016).

106. Aizu, K. Possible Species of Ferromagnetic, Ferroelectric, and Ferroelastic Crystals. *Phys. Rev. B* **2**, 754–772 (1970).

107. Wadhawan, V. *Introduction to ferroic materials*. (CRC press, 2000).

108. Glinchuk, M. D., Ragulya, A. V & Stephanovich, V. A. *Nanoferroics*. (Springer, 2013).

109. Breternitz, J., Lehmann, F., Barnett, S. A., Nowell, H. & Schorr, S. Role of the iodide–methylammonium interaction in the ferroelectricity of CH3NH3PbI3. *Angew. Chemie Int. Ed.* **59**, 424–428 (2020).

110. Grancini, G. *et al.* The impact of the crystallization processes on the structural and optical properties of hybrid perovskite films for photovoltaics. *J. Phys. Chem. Lett.* **5**, 3836–3842 (2014).

111. Dong, Q. *et al.* Abnormal crystal growth in CH 3 NH 3 PbI 3– x Cl x using a multi-cycle solution coating process. *Energy Environ. Sci.* **8**, 2464–2470 (2015).

112. Li, D. *et al.* Humidity-Induced Grain Boundaries in MAPbI<inf>3</inf> Perovskite Films. *J. Phys. Chem. C* **120**, (2016).

113. Yuan, G. *et al.* Ferroelastic-Domain-Assisted Mechanical Switching of Ferroelectric Domains in Pb (Zr, Ti) O3 Thin Films. *Adv. Electron. Mater.* **6**, 2000300 (2020).

114. Fridkin, V. M. & Ducharme, S. General features of the intrinsic ferroelectric coercive field. *Phys. Solid State* **43**, 1320–1324 (2001).

115. Milsom, R. F., Reilly, N. H. C. & Redwood, M. Analysis of generation and detection of surface and bulk acoustic waves by interdigital transducers. *IEEE Trans. Sonics Ultrason.* **24**, 147–166 (1977).

116. Yang, M.-M., Bhatnagar, A., Luo, Z.-D. & Alexe, M. Enhancement of local photovoltaic current at ferroelectric domain walls in BiFeO 3. *Sci. Rep.* **7**, 1–8 (2017).

117. Makarovic, M., Bayir, M. Ç., Ursic, H., Bradesko, A. & Rojac, T. Domain wall conductivity as the origin of enhanced domain wall dynamics in polycrystalline BiFeO3. *J. Appl. Phys.* **128**, 64104 (2020).

118. Seidel, J. *et al.* Conduction at domain walls in oxide multiferroics. *Nat. Mater.* **8**, 229–234 (2009).

119. Sluka, T., Tagantsev, A. K., Bednyakov, P. & Setter, N. Free-electron gas at charged domain walls in insulating BaTiO3. *Nat. Commun.* **4**, 1808 (2013).

120. Bednyakov, P., Sluka, T., Tagantsev, A., Damjanovic, D. & Setter, N. Free-Carrier-Compensated Charged Domain Walls Produced with Super-Bandgap Illumination in Insulating Ferroelectrics. *Adv. Mater.* **28**, 9498–9503 (2016).

121. Guyonnet, J., Gaponenko, I., Gariglio, S. & Paruch, P. Conduction at domain walls in insulating Pb (Zr0. 2Ti0. 8) O3 thin films. *Adv. Mater.* **23**, 5377–5382 (2011).

122. Maksymovych, P. *et al.* Tunable metallic conductance in ferroelectric nanodomains. *Nano Lett.* **12**, 209–213 (2012).

123. Bednyakov, P. S., Sturman, B. I., Sluka, T., Tagantsev, A. K. & Yudin, P. V. Physics and applications of charged domain walls. *npj Comput. Mater.* **4**, 1–11 (2018).

124. Salje, E. K. H. & Lashley, J. C. Domain boundary engineering in ferroic and multiferroic materials: a simple introduction. in *Disorder and Strain-Induced Complexity in Functional Materials* 1–18 (Springer, 2012).

125. Aird, A. & Salje, E. K. H. Sheet superconductivity in twin walls: experimental evidence of. *J. Phys. Condens. Matter* **10**, L377 (1998).

126. Zubko, P., Catalan, G., Buckley, A., Welche, P. R. L. & Scott, J. F. Strain-gradient-induced polarization in SrTiO 3 single crystals. *Phys. Rev. Lett.* **99**, 167601 (2007).

127. Zubko, P., Catalan, G. & Tagantsev, A. K. Flexoelectric effect in solids. *Annu. Rev. Mater. Res.* **43**, 387–421 (2013).

128. Yun, S. *et al.* Flexopiezoelectricity at ferroelastic domain walls in WO 3 films. *Nat. Commun.* **11**, 1–10 (2020).

129. Ojha, S. K. *et al.* Electron Trapping and Detrapping in an Oxide Two-Dimensional Electron Gas: The Role of Ferroelastic Twin Walls. *Phys. Rev. Appl.* **15**, 54008 (2021).

130. Mao, J. *et al.* High thermoelectric power factor in Cu–Ni alloy originate from potential barrier scattering of twin boundaries. *Nano Energy* **17**, 279–289 (2015).

131. Pecchia, A., Gentilini, D., Rossi, D., Auf der Maur, M. & Di Carlo, A. Role of ferroelectric nanodomains in the transport properties of perovskite solar cells. *Nano Lett.* **16**, 988–992 (2016).

132. Shi, D. *et al.* Low trap-state density and long carrier diffusion in organolead trihalide perovskite single crystals. *Science (80-.).* **347**, 519–522 (2015).

133. Liu, Y. *et al.* Light-Ferroic Interaction in Hybrid Organic–Inorganic Perovskites. *Adv. Opt. Mater.* **7**, 1901451 (2019).

134. Yoo, J. J. *et al.* An interface stabilized perovskite solar cell with high stabilized efficiency and low voltage loss. *Energy Environ. Sci.* **12**, 2192–2199 (2019).

135. Jaramillo-Quintero, O. A., Sanchez, R. S., Rincon, M. & Mora-Sero, I. Bright visible-infrared light emitting diodes based on hybrid halide perovskite with Spiro-OMeTAD as a hole-injecting layer. *J. Phys. Chem. Lett.* **6**, 1883–1890 (2015).

136. Ashar, A. Z., Ganesh, N. & Narayan, K. S. Hybrid Perovskite-Based Position-Sensitive Detectors. *Adv. Electron. Mater.* **4**, 1700362 (2018).

137. Steirer, K. X. *et al.* Defect tolerance in methylammonium lead triiodide perovskite. *ACS Energy Lett.* **1**, 360–366 (2016).

138. Johnston, M. B. & Herz, L. M. Hybrid perovskites for photovoltaics: charge-carrier recombination, diffusion, and radiative efficiencies. *Acc. Chem. Res.* **49**, 146–154 (2016).

139. Hodes, G. & Kamat, P. V. Understanding the implication of carrier diffusion length in photovoltaic cells. (2015).

140. DeQuilettes, D. W. *et al.* Tracking photoexcited carriers in hybrid perovskite semiconductors: trap-dominated spatial heterogeneity and diffusion. *ACS Nano* **11**, 11488–11496 (2017).

141. Vrućinić, M. *et al.* Local Versus Long-Range Diffusion Effects of Photoexcited States on Radiative Recombination in Organic–Inorganic Lead Halide Perovskites. *Adv. Sci.* **2**, 1500136 (2015).

142. Guo, Z., Manser, J. S., Wan, Y., Kamat, P. V & Huang, L. Spatial and temporal imaging of long-range charge transport in perovskite thin films by ultrafast microscopy. *Nat. Commun.* **6**, 7471 (2015).

143. Chen, Y. *et al.* Extended carrier lifetimes and diffusion in hybrid perovskites revealed by Hall effect and photoconductivity measurements. *Nat. Commun.* **7**, 1–9 (2016).

144. Hill, A. H., Smyser, K. E., Kennedy, C. L., Massaro, E. S. & Grumstrup, E. M. Screened charge carrier transport in methylammonium lead iodide perovskite thin films. *J. Phys. Chem. Lett.* **8**, 948–953 (2017).

145. Herz, L. M. Charge-carrier dynamics in organic-inorganic metal halide perovskites. *Ann. Rev. Phys. Chem.* **67**, 65–89 (2016).

146. Delport, G., Macpherson, S. & Stranks, S. D. Imaging carrier transport properties in halide perovskites using time-resolved optical microscopy. *arXiv Prepr. arXiv1911.10615* (2019).

147. Stavrakas, C. *et al.* Visualizing buried local carrier diffusion in halide perovskite crystals via two-photon microscopy. *ACS Energy Lett.* **5**, 117–123 (2019).

148. Jariwala, S. *et al.* Local Crystal Misorientation Influences Non-radiative Recombination in Halide Perovskites. *Joule* **3**, 3048–3060 (2019).

149. Tian, W. *et al.* Limiting perovskite solar cell performance by heterogeneous carrier extraction. *Angew. Chem. Int. Ed.* **55**, 13067–13071 (2016).

150. Reid, O. G., Yang, M., Kopidakis, N., Zhu, K. & Rumbles, G. Grain-size-limited mobility in methylammonium lead iodide perovskite thin films. *ACS Energy Lett.* **1**, 561–565 (2016).

151. Cho, N. *et al.* Pure crystal orientation and anisotropic charge transport in large-area hybrid perovskite films. *Nat. Commun.* **7**, 1–11 (2016).

152. Ciesielski, R. *et al.* Grain boundaries act as solid walls for charge carrier diffusion in large crystal MAPI thin films. *ACS Appl. Mater. Interfaces* **10**, 7974–7981 (2018).

153. Tian, W., Zhao, C., Leng, J., Cui, R. & Jin, S. Visualizing carrier diffusion in individual single-crystal organolead halide perovskite nanowires and nanoplates. *J. Am. Chem. Soc.* **137**, 12458–12461 (2015).

154. Handloser, K. *et al.* Contactless visualization of fast charge carrier diffusion in hybrid halide perovskite thin films. *ACS Photonics* **3**, 255–261 (2016).

155. Yamada, Y. *et al.* Dynamic optical properties of CH3NH3PbI3 single crystals as revealed by one-and two-photon excited photoluminescence measurements. *J. Am. Chem. Soc.* **137**, 10456–10459 (2015).

156. Pazos-Outón, L. M. *et al.* Photon recycling in lead iodide perovskite solar cells. *Science (80-.).* **351**, 1430–1433 (2016).

157. Crothers, T. W. *et al.* Photon reabsorption masks intrinsic bimolecular charge-carrier recombination in CH3NH3PbI3 perovskite. *Nano Lett.* **17**, 5782–5789 (2017).

158. Richter, J. M. *et al.* Enhancing photoluminescence yields in lead halide perovskites by photon recycling and light out-coupling. *Nat. commun.* **7**, 1–8 (2016).

159. Li, W. *et al.* Subgrain special boundaries in halide perovskite thin films restrict carrier diffusion. *ACS Energy Lett.* **3**, 2669–2670 (2018).

160. Castro-Méndez, A., Hidalgo, J. & Correa-Baena, J. The Role of Grain Boundaries in Perovskite Solar Cells. *Adv. Energy Mater.* **9**, 1901489 (2019).

161. Shao, Y., Xiao, Z., Bi, C., Yuan, Y. & Huang, J. Origin and elimination of photocurrent hysteresis by fullerene passivation in CH3NH3PbI3 planar heterojunction solar cells. *Nat. Commun.* **5**, 1–7 (2014).

162. Kalinin, S. V & Gruverman, A. *Scanning probe microscopy: electrical and electromechanical phenomena at the nanoscale*. **1**, (Springer, 2007).

163. Gruverman, A. & Kalinin, S. V. Piezoresponse force microscopy and recent advances in nanoscale studies of ferroelectrics. *J. Mater. Sci.* **41**, 107–116 (2006).

164. Kirchartz, T., Staub, F. & Rau, U. Impact of photon recycling on the open-circuit voltage of metal halide perovskite solar cells. *ACS Energy Lett.* **1**, 731–739 (2016).

165. Ansari-Rad, M. & Bisquert, J. Insight into photon recycling in perovskite semiconductors from the concept of photon diffusion. *Phys. Rev. Appl.* **10**, 34062 (2018).

166. Labuda, A. & Proksch, R. Quantitative measurements of electromechanical response with a combined optical beam and interferometric atomic force microscope. *Appl. Phys. Lett.* **106**, 253103 (2015).

4 Charge and photon transport across grain boundaries

Polycrystalline thin film solar cells like PSCs are typically cheaper and easier to produce than monocrystalline PV.[1,2] Particularly the possibility of fully printable solar cells for simple, large-scale production promises a widespread commercialization of the technology.[3–5] However, grain boundaries in polycrystalline thin film solar cells can affect the charge carrier transport by acting as nonradiative recombination centers, which lower the V_{OC}, or as electrostatic barriers, which decrease the I_{SC}.[1] Furthermore, they can cause scattering losses in propagating light,[6,7] which impedes with light management – a technique used to approach the efficiency limit in solar cells e.g., by facilitating the reabsorption of PL from bimolecular recombination.[1,8]

In perovskite PV, previous studies found a largely benign contribution of grain boundaries to the nonradiative recombination, whereas the charge extraction appears to be significantly affected by the grain boundaries that act as electrostatic barriers.[9–15] The impact of grain boundaries in polycrystalline $MAPbI_3$ on the inter-grain charge carrier transport with and without external electric field was studied in Chapter 4.1. In subchapter 4.1.1, I resolved the lateral charge carrier drift in dependence of the amount of grain boundaries via CAFM and was able to calculate the resistance of single grain boundaries. The grain boundary resistance showed with a significant dependence on the grain boundary morphology, particularly on the spacing between two adjacent grains. Subsequent time-and spatially resolved PL microscopy correlated to AFM topography measurements of an isolated $MAPbI_3$ grain cluster revealed that the inter-grain carrier diffusion features a similar dependence on the grain boundary morphology. Like for the carrier drift, a small spacing between grains appeared to facilitate a faster carrier transport.

Moreover, with the material and interface optimization reaching its limit, the importance of efficient photon management in PSCs rises to approach predicted *PCE*s.[16–19] In order to increase the amount of photon recycling events in $MAPbI_3$ thin films (Chapter 1.3.2.1),[20–22] the effect of grain boundaries on light propagation needs to be explored to avoid energy losses in confined photons.[21,23,24] In Chapter 4.2, I investigated the light propagation in dependence of the grain boundary morphology across a finite $MAPbI_3$ grain cluster via the static as well as spatial and time-resolved PL microscopy after local excitation on one of the constituent grains with a pulsed laser. By correlating the detected PL signal to the AFM topography of the grain cluster, I was able to connect intensity losses to certain grain boundary structures: Small contact areas and gaps between the grains appear to introduce bottlenecks for light propagation. Moreover, I detected confined PL from the initial emission in distances up to 20 µm from the excitation, which indicates a reduced reabsorption probability caused by energy losses in inelastic scattering events. Surprisingly, trapped PL appeared to maintain its directionality, indicating reduced phonon scattering in bulk grains.

4.1 Carrier transport across grain boundaries

-Unpublished-

Introduction

Comparing polycrystalline silicon solar cells to their monocrystalline counterparts, polycrystalline devices typically yield lower overall performances. Among others, the loss in efficiency originates from adverse effects at grain boundaries: Dangling bonds, chemical inhomogeneities and/or ionic displacements grain boundaries can pose as nonradiative recombination centers or electrostatic barriers that decrease the V_{OC} or hinder the charge carrier transport, respectively.[9,12,25] On the other hand, Yan *et al.* reported on an advantageous influence of grain boundaries in doped polycrystalline CdTe solar cells for the carrier extraction and thus performance. Here, Cl ions from a $CdCl_2$ treatment accumulate at grain boundaries, which consequently act as local *pnp*-junctions.[9,25]

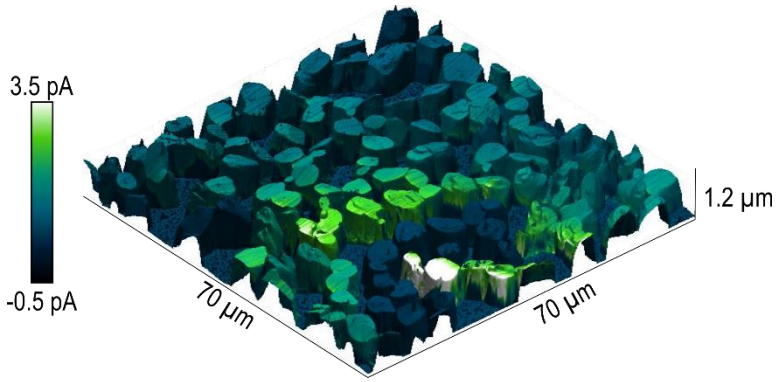

Figure 4.1: 3D overlay of current signal on topography of a lateral CAFM measurement on a polycrystalline $MAPbI_3$ thin film on top of a glass substrate without full coverage. Parts of the film (outside of the scan area) were coated by a gold electrode, to which a sample voltage of 1 V was applied. Only those grains indirectly connected to the gold electrode via other grains showed a measurable current response.

In PSCs, previous studies suggested that grain boundaries are mostly benign for nonradiative recombination and therefore the V_{OC}. They form no deep traps and electronic charge carriers can neutralize charged boundary defects caused by ion vacancies under illumination.[9–15] For the I_{SC} on the other hand, researchers found strong indications that grain boundaries act either as entirely impervious or semitransparent barriers to the charge carrier transport, which was observed via several measurement techniques, including light induced transient grating spectroscopy,[10] fluorescence lifetime imaging microscopy,[11] transient absorption microscopy,[13] time-resolved microwave conductivity,[14] PL microscopy[15,26] and CAFM.[27,28]

The majority of previous inter-grain charge transport investigations were performed on perovskite thin films with full coverage, where each grain shares several grain boundaries with adjacent grains. These multiple grain boundaries make it difficult to quantify and correlate structural boundary properties to the conductivity. Furthermore, small grain sizes in conventional $MAPbI_3$ thin films exacerbate the grain boundary characterization due to resolution limitations. Hence, by increasing the grain sizes and lowering the overall film coverage an in-depth analysis of

the influence of single grain boundaries and their morphological features on inter-grain carrier drift (with electric field) and diffusion (without electric field) becomes possible.

Here, I investigated the impact of grain boundaries on charge carrier drift and diffusion in a polycrystalline $MAPbI_3$ film on glass via CAFM as well as time- and spatially resolved PL microscopy, respectively. In subchapter 4.1.1, I used a conductive AFM tip to detect the inter-grain current flow in varying distances from a thin, biased gold electrode on top of the $MAPbI_3$ film (Figure 4.1). In an applied field, charges passed up to ten grain boundaries and travelled distances of more than 40 µm from the electrode. From the conduction path across a grain cluster, I found that the grain boundaries behave like a series resistance and was able to calculate individual boundary resistances. Upon correlating the resistance to topographic grain boundary features, my results indicate that the resistance primarily depends on the density and crystal quality of the grain boundaries rather than the total contact area between grains. In subchapter 4.1.2, I studied the charge carrier diffusion across grain boundaries via spatial and time-resolved PL microscopy, with decoupled excitation and detection volumes.[15,29–32] Contrary to previous studies,[11,15] I observed that diffusive charges can overcome the grain boundary to an adjacent grain and achieve inter-grain diffusion constants of 1.15 - 1.22 cm^2/s. Like for the inter-grain carrier drift, the grain boundary morphology appears to determine the transparency for charge carrier diffusion.[26,27]

4.1.1 Inter-grain carrier drift

Introduction

To selectively extract charge carriers and generate an electric current, solar cells exhibit an asymmetry in their electrostatic potential, which leads to a built-in electric field. This field drives the separation of electrons and holes as well as their extraction on opposite sides of the absorber layer. Together with diffusion, the drift of charge carriers in the built-in electric field of a solar cell is a main driving force for charge carrier transport (Chapter 1.2.4.1).[33] Detailed knowledge on the influence of grain boundaries on the drift current could provide a road map for performance optimization of polycrystalline PV devices: Understanding the relation between conductivity and grain boundary quantity and morphology offers valuable insights to tune the device preparation for improved carrier extraction. Here, I explored the influence of grain boundaries on the inter-grain carrier transport in polycrystalline $MAPbI_3$ in an electric field without illumination via CAFM as well as possible effects that define the individual grain boundary resistance.

Results and discussion

To characterize the carrier drift in polycrystalline $MAPbI_3$, I prepared a lateral device structure for distance- and grain boundary-dependent CAFM measurements: I evaporated a thin gold electrode onto a polycrystalline $MAPbI_3$ thin film deposited on an insulating glass substrate via solvent annealing to achieve high crystallinity and large grains (Chapter 3.2.1, Figure 3.17a).[29,34,35] The resulting film consisted of multiple interconnected grain clusters with limited number of shared grain boundaries and no full substrate coverage. Thus, the film was ideally suited to study the inter-grain charge transfer (Figure 4.2a). Most grains had a diameter between 4 and 7 µm with some smaller and larger grains ranging between 2 and 12 µm. The gold electrode on the right side of the scan area had a higher roughness on flat grain terraces: A bare $MAPbI_3$ grain displayed a terrace

RMS of <3 nm, while a gold coated grain had a terrace RMS of >7 nm. A line profile determined an electrode thickness of 74 nm (Figure 4.2c).

By applying a sample voltage of 1.5 V to the electrode while performing a large area CAFM scan over 70 × 70 µm², I was able to capture a distance- and grain boundary-dependent current flow across the interconnected grains and clusters (Figure 4.2b). Since a change in the conductive tip coating is a common source of error in CAFM measurements, I chose a scan angle, where the fast scan axis was perpendicular to the electrode interface.[36] Thereby, the unaltered current detection on the electrode in each scan line served as confirmation that the conductive tip coating remained intact over the entire scan. The current on the electrode saturated at 2 nA (Figure 4.2c), which was given by the upper detection limit of the current amplifier.

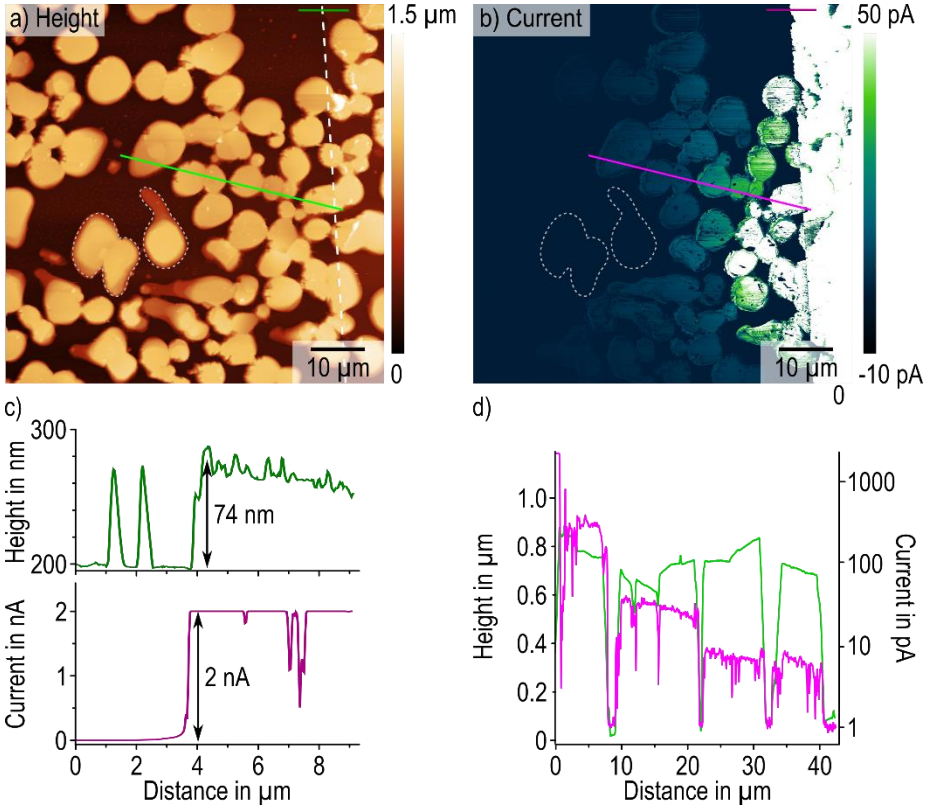

Figure 4.2: Overview of CAFM measurement on polycrystalline $MAPbI_3$ film on glass, partially covered with a biased gold electrode with 1.5 V. a) Topography shows partial surface coverage and interconnected grain clusters. The dashed white line highlights the interface of the gold electrode. b) Current image visualizing distance-and grain boundary-dependence of inter-grain current. Isolated grains and grain clusters, indicated by grey dashed outlines, did not feature a current response. c) Topography and current line profiles extracted at along the dark green and violet line in the upper right corner of a) and b), respectively, showing the height and current response of the biased electrode with a current saturation at 2 nA as upper limit of the current amplifier. d) Topography and current line profiles extracted at along the light green and pink line in a) and b), respectively, showing correlation of current signal and grain position as well as the current decay with increasing electrode distance.

Bare $MAPbI_3$ grains only featured a current response when they were connected to the biased electrode directly or indirectly via other grains. These grains displayed largely uniform currents with typical losses below 10% over the full width of the grain. Isolated grains or clusters, as highlighted by the dashed grey outlines in Figure 4.2b, displayed no detectable current signal. Meanwhile, the current response of the grains in contact with the electrode declined with increasing

distance from the electrode as well as the amount of grain boundaries. This decline is distinctly visible in the line profiles in Figure 4.2d, which not only highlight the correlation of grain position and detected current, but moreover show the current evolution over four different grains and clusters with increasing electrode distance. Displayed in a logarithmic scale, we measured an average current of 236 ± 86.4 pA on the first grain in direct contact with the electrode, 25.5 ± 5.49 pA on the second grain cluster, 6.41 ± 1.16 pA on the third grain cluster and 5.02 ± 1.44 pA on the last grain more than 30 µm from the electrode. Between the first grain, the second grain cluster and the third grain cluster, the current dropped by 89% and 75%, respectively, while the current between the third cluster and the last grain decreased by 22%.

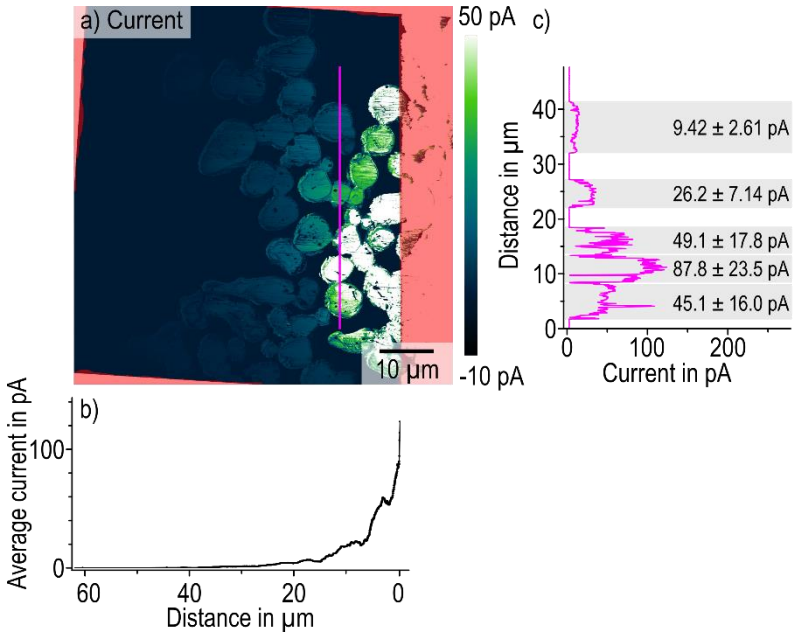

Figure 4.3: a) Current image of CAFM measurement in Figure 4.2 rotated by -3.6° to align the electrode position parallel to the image edge to allow averaging the current signal of each scan line in b). Masked areas shaded red in a) were excluded from the average to consider only the current response of bare $MAPbI_3$ grains. c) Line profile of the current extracted along the pink line in a) at the same distance from the electrode showing the vast deviation of the average current on each grain along the line profile. Each gray shaded box represents a different grain.

I first analyzed the distance dependence by averaging the current signal of each scan line. For this purpose, I rotated the current image from Figure 4.2b by -3.6° to align the electrode interface parallel to the image edge and ensure a consistent electrode position in x for each scan line (Figure 4.3a). After masking all areas except the bare $MAPbI_3$ film and thereby excluding these areas from the following analysis, I averaged the current response over all scan lines and displayed the average current in dependence of the electrode distance (Figure 4.3b). The average current showed a sharp decay from ~120 pA in direct proximity to the electrode to 20 pA at a distance of ~10 µm. 40 µm from the electrode the current converges towards 0. However, the line profile in Figure 4.3c, which was extracted in a distance of 11.5 µm parallel to the electrode interface, revealed that grains with the same distance from the electrode feature vastly different current responses. The average currents on these grains ranged between 9.4 and 87.8 pA. Thus, it appears that the amount of grain boundaries between grain and electrode as well as the inter-grain connectivity i.e., grain boundary quality and/or contact area, are governing influences on the current response rather than the total electrode distance.

To determine the influence of grain boundaries on the inter-grain carrier drift, I analyzed a probable current path across a grain cluster. The median current on each grain along the path excluding grain edges and non-conductive surface particles from the analysis continuously decayed with each grain boundary (Figure 4.4a). I plotted the current with standard deviation against the total number of boundaries n between the respective grain and the electrode in Figure 4.4b. The resulting current evolution in dependence of the amount of grain boundaries follows a $1/n$ trend, as expected for a series resistance. In fact, I was able to fit the current decay using the following equation based on the electrical circuit model in Figure 4.4c:

$$I = I_0 + \frac{U}{nR_{GB} + R_{syst}}$$

Equation 4.1: Current decay.

Here, the dependence of the current I on the amount of grain boundaries n is described by the current offset I_0, the applied bias U, and the total series resistance, which is the sum of all constituent grain boundary resistances $nR_{GB,n}$ plus the system resistance R_{syst} that includes the gold and $MAPbI_3$ interface as well as the tip resistance (Figure 4.4c). Under the assumption that all R_{GB} are similar, the fit gave R_{syst}=16.9 ± 1.6 GΩ.

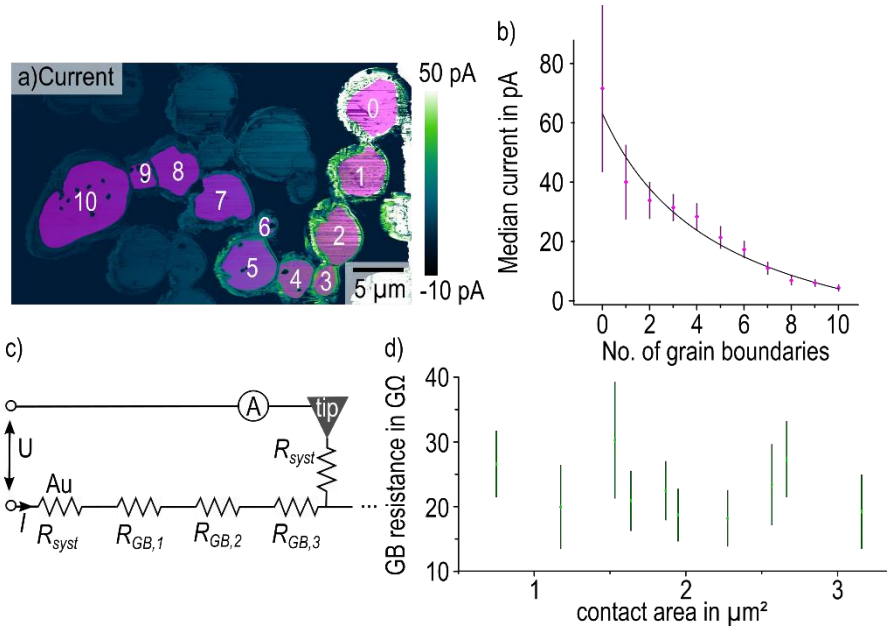

Figure 4.4: a) Enlarged image detail of an interconnected $MAPbI_3$ grain cluster extracted from current image in Figure 4.2b. Pink shaded areas represent the areas used to determine the average current of each grain excluding nonconductive dirt particles and grain edges. Numbers visualize the amount of grain boundaries the charge carriers have to pass from the electrode to the respective grain, starting with 0 for the grain in direct contact with the electrode. b) The median current I versus the amount of grain boundaries n with the standard deviation as error bars. The current decay was fitted via Equation 4.1. d) Schematic of electric circuit model used for Equation 4.1.c) Grain boundary resistance R_{GB}, calculated via Equation 4.2, vs. contact area, determined via topography cross sections across each grain boundary.

Using R_{syst}, allowed calculating each individual $R_{GB,n}$ via:

$$R_{GB,n} = \frac{I_{n-1}}{I_n} R_{n-1}$$

Equation 4.2: Grain boundary resistance.

For the first grain boundary R_{n-1} equals R_{syst}, for all following grain boundaries R_{n-1} is $R_{GB,n-1}$. The calculation according to Equation 4.2 yielded individual grain boundary resistances in the range of tens of giga-Ohm, which is astonishingly high.

To evaluate the influence of the contact area between two adjacent grains on the resistance, I extracted line profiles from the AFM topography along each grain boundary. By integrating the area below the grain boundary, the contact area of each grain boundary could be measured. The plot of the resistance versus the contact area (Figure 4.4d) showed an absence of a clear trend, which suggests that the contact area is not the governing influence on the grain boundary resistance. Instead, another effect must cause local variations in the inter-grain carrier transfer.

Thus, I focused on morphological features that have been proposed to cause differences in inter-grain resistance. MacDonald *et al.* and deQuilettes *et al.* previously reported on local variations in the inter-grain carrier drift and diffusion, respectively. While MacDonald *et al.* connected the grain boundary resistance to the boundary structure throughout the bulk film,[27] deQuilettes *et al.* assigned local changes in grain boundary transparency to a possible facet-dependence,[26] as proposed in earlier studies by Leblebici *et al.* and Docampo *et al.*.[37,38] To explore the influence of crystal facets on the grain boundary resistance, I analyzed the angle between the two grain boundaries that connecting each grain to the rest of the cluster. Therefore, I determined the normal of each boundary and continued to measure the angles between the normals. Angles of 0°, 72° and 92°-93° showed decreases or only slight increases (<2 GΩ) in R_{GB}, while the angles of 17° and 126° displayed significant increases of 8-10 GΩ in R_{GB} (Table 4.1).

Table 4.1: Resistance changes in dependence of angle between grain boundary normals. Increases resistances are marked in red, decreased resistance are marked in blue.

GRAIN BOUNDARIES	ANGLE	RESISTANCE CHANGE
1→2	17°	+10.3 GΩ
2→3	0°	+1.75 GΩ
3→4	92°	-0.510 GΩ
4→5	0°	-3.75 GΩ
5→6	93°	+1.57 GΩ
6→7	72°	-5.66 GΩ
7→8	0°	-0.759 GΩ
8→9	126°	+8.07 GΩ
9→10	0°	-4.13 GΩ

However, while we know that principal crystal planes on the (100), (010) and (001) intersect each other at 0° or 90° and a (112) intersection with a (100) or (010) plane would lead to ~70° angle in $MAPbI_3$[39], a definite statement on a facet dependence of the inter-grain carrier transfer cannot be made. This is because the in-plane orientations of the grains in the cluster and therefore their

shared facets are unknown. Our previous 2D XRD experiments on comparable $MAPbI_3$ film showed a preferential out-of-plane orientation, but no preferential in-plane orientation of the crystallites (Chapter 3.1.1).[35] To investigate a possible facet-dependence in the future, an in-plane texture could be introduced using a substrate template[40] or a film cross section could be studied using CAFM and electron backscattered diffraction (EBSD), which allows resolving local crystal orientations.[41]

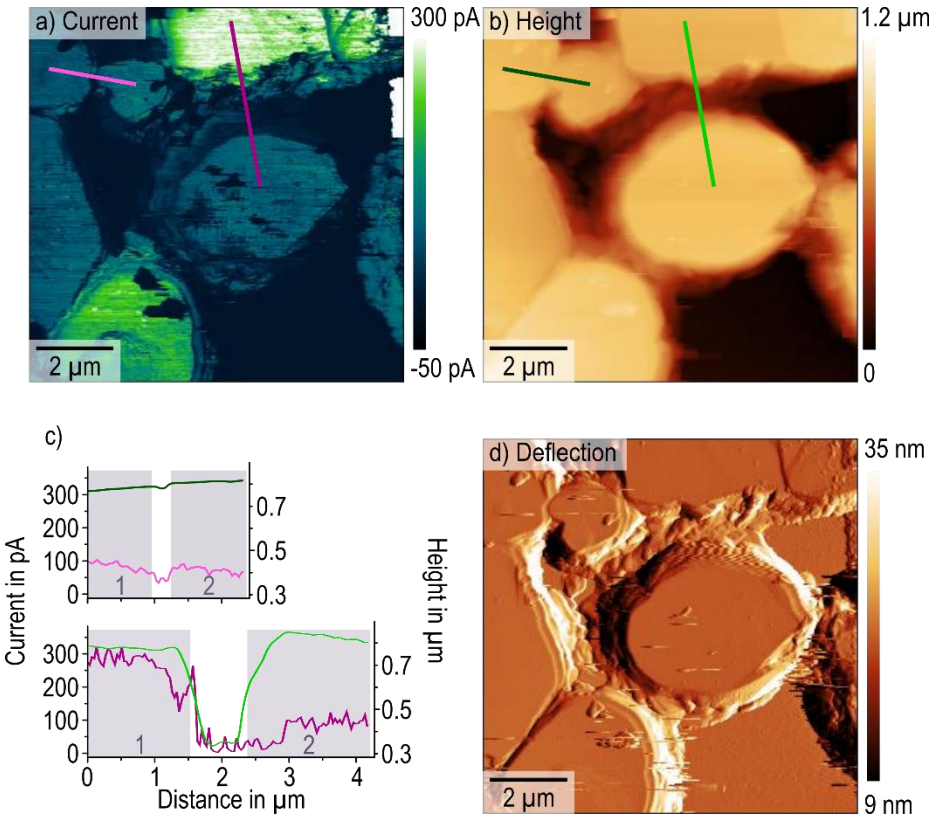

Figure 4.5: Enlarged image details of $MAPbI_3$ grain cluster extracted from CAFM measurement in Figure 4.2c to analyze the influence of the inter-grain connectivity on the charge carrier transport across grain boundaries. a) Current image and b) topography image with the position of the two line profiles in c). d) Deflection signal of the same area visualizing the morphological difference between grain boundaries.

With the analysis of a possible facet-dependence of the resistance remaining inconclusive, I explored the influence of the grain boundary structure by comparing the current drop between two morphologically different grain boundaries. Figure 4.5a and b show a section of the current and topography image of Figure 4.2, respectively. The bright pink and dark green line mark the extraction position of the line profile across an electrically well-conducting grain boundary, while the purple and light green line mark the position of the profile across a poorly conductive grain boundary. Upon analyzing the line profiles in Figure 4.5c, I found that the average current across the conductive grain boundary on top decreases from 88.4 ± 10.3 pA on the first grain to 73.5 ± 9.4 pA on the second grain, which translates into a 16% current drop. The line profile across the poorly conductive grain boundary on the bottom revealed a decrease of the average current from 285.0 ± 16.2 pA on the first grain to 93.1 ± 13.0 pA on the second grain marking a 67% drop in current. Correlating the current to the topography signal showed that the conductive grain boundary was only 0.2 µm wide and ~20 nm deep, whereas the less-conductive grain boundary featured a width of 0.9 µm and a depth of 500 nm. Furthermore, the deflection signal in Figure 4.5d

illustrates that the structure within the gap of the less-conductive boundary did not feature the distinct crystal terraces that we previously observed for the upper layers of $MAPbI_3$ grains (Figure 3.8). The absence of the terrace structure could indicate a local decline in crystal quality, maybe even the presence of amorphous material, which increases the resistance and impedes the inter-grain charge carrier drift.

Summary

To summarize, I studied the inter-grain carrier drift in a low-coverage polycrystalline $MAPbI_3$ film by measuring the lateral current flow from a positively biased gold electrode via the $MAPbI_3$ grain clusters to a conductive AFM tip. I detected currents in distances of up to 40 µm and 10 grain boundaries from the electrode, which highlights the extensive drift lengths in polycrystalline $MAPbI_3$. The current signal displayed a distinct $1/n$ dependence from the number of grain boundaries, corresponding to a series resistance. By fitting the current decay, I was able to determine single grain boundary resistances in a range of tens of giga-Ohm. These astonishingly high grain boundary resistances could originate from the overall low film coverage, which reduced the overall density between the grains. Nevertheless, the high resistances also indicate that grain boundaries can introduce significant current losses in polycrystalline PSCs.

The governing influence on the individual grain boundary resistance appeared to be the morphology rather than the shared contact area between two grains. Here, the density as well as the crystalline quality between the adjacent grains seemed decisive for the inter-grain charge carrier transport. By locally resolving the amorphous content between grain boundaries via high resolution TEM, the crystallinity could be directly connected to the grain boundary resistance. Moreover, a systematic study on the impact of grain boundary passivation could aid to quantitatively evaluate routes for thin film improvement. A possible facet-dependence of the grain-boundary resistance remains unclear, since the in-plane orientation of individual grains in the cluster was unknown.

4.1.2 Inter-grain carrier diffusion

Introduction

In addition to the carrier drift in an electric field, the diffusion of photogenerated charges drives the charge carrier transport in the active layer of a solar cell. The diffusion current describes the carrier motion in a uniform electrostatic potential, where the current is determined by a concentration gradient.[33,42] In photovoltaic materials like $MAPbI_3$, we can study the charge carrier diffusion via PL microscopy, where photons with above band gap energy excite charge carriers and photodiodes detect the PL emission from the bimolecular recombination of the excited charges (Chapter 1.4.2.2).[33] Mapping the distribution of this PL emission upon a local excitation visualizes diffusion lengths and local barriers that may hinder the carrier motion.[26] Additionally, a decoupled pulsed excitation source and time-resolved photodetection can resolve charge carrier dynamics, which allows calculating the diffusion constant from diffusion time and length. These diffusion constants offer insights on the impact of different grain boundaries on the inter-grain carrier transfer: By comparing the diffusion constants of neighboring grains and correlating them to grain boundary density and contact area, we can evaluate which structural grain boundary properties inhibit the inter-grain carrier diffusion. This knowledge enables the targeted improvement of PSC preparation

routes for increased carrier extraction. Here, I used a combination of AFM and via time- and spatially resolved PL microscopy[15,29–32] to investigate the influence of grain boundaries and their morphology on the charge carrier diffusion in an isolated $MAPbI_3$ cluster.

Results and discussion

To study the inter-grain charge carrier diffusion in the absence of an electric field via PL microscopy, I prepared a $MAPbI_3$ thin film on a glass substrate using the solvent annealing routine to achieve large isolated grains and grain clusters.[29,34,35] Figure 4.6a shows the topography of an isolated cluster, which is well suitable for the investigation since each grain has not more than two shared grain boundaries. The cluster consists of four grains sized 5 to 10 µm in diameter with thicknesses ranging between 550 and 720 nm. The corresponding deflection signal in Figure 4.6b was used in the following result section as overlay to the PL data to aid the correlation of PL and morphology. I identified constituent grains and corresponding boundaries from the relative orientation of their ferroelastic twins imaged in the PFM amplitude signal in Figure 4.6c. Since our previous studies exclusively showed orientation changes of 90° for twin domains within single grains on the (110) crystal plane (Figure 3.4),[29,35] deviating angles strongly suggest the transition to another discrete grain. I numbered the grains accordingly and marked isolated grain edges to the uncovered glass substrate by white and black dashed lines in Figure 4.6a,b and c, respectively. Semitransparent green lines highlight the positions of the three shared grain boundaries, which separate adjacent grains in the cluster.

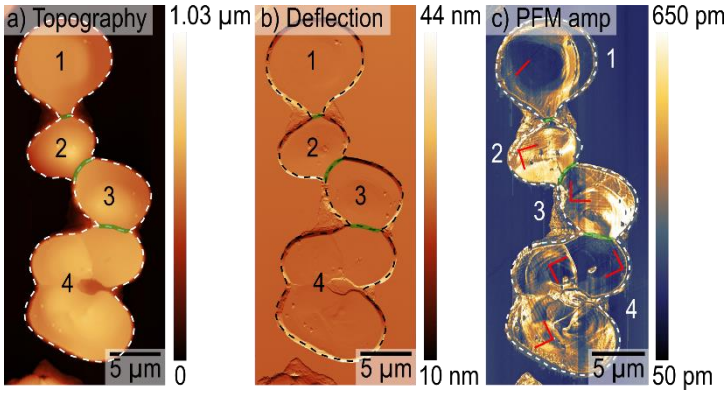

Figure 4.6: Lateral PFM measurement of an isolated $MAPbI_3$ grain cluster on a glass substrate (1.5 V AC excitation, 729 kHz, 55 nN). a) Topography and b) deflection signal with white and black dashed lines, respectively, highlighting isolated grain boundaries, semitransparent green lines highlighting the three shared grain boundaries and the numbering of the grains as used in the result section. c) PFM amplitude resolving the materials ferroelastic twin domains. The domain orientation, as indicated by the red lines, was used to identify grain boundaries.

To resolve the inter-grain carrier diffusion on the cluster, I continued the investigation with spatial and time-resolved resolved PL microscopy approach via a decoupled excitation and detection scheme, as described previously (Chapter 3.2.2).[29] Spatial and time-resolved PL microscopy allows differentiating signals caused by the outcoupling of confined photons and diffusive carriers. I measured three PL transients in increasing distances from the excitation position on grain one: The first detection position was within grain one, close to the grain boundary at 3.6 µm distance from the excitation, the second and third detection positions were placed in the adjacent grain two in distances of 6.8 µm and 8.9 µm from the excitation, respectively (Figure 4.7). Like in Chapter 3.2.2., the PL transients were fitted with a combination of a mono-exponential

decay for waveguided PL emission from the initial recombination at the excitation spot[20–22,43] and a peak function for the PL emission from the bimolecular recombination of photocarriers that diffused to the detection spot: [15,30–32]

$$y = A_{wg} \times \mathrm{e}^{-(t-t_0)/\tau_{wg}} + \frac{A_{Diff}}{t-t_0} \times \mathrm{e}^{-\tau_0/(t-t_0)} + y_0$$

Equation 4.3: Fit function for PL decays.

The first exponential term of the equation contains the decay amplitude A_{wg} and the decay time τ_{wg} of the waveguided PL (Chapter 4.2). The second term, describing the charge carrier diffusion, includes the amplitude of the diffusion peak A_{Diff} and the diffusion time τ_{Diff}. Upon analyzing the PL transients detected within the excited grain one and the adjacent grain two, I found a distinct diffusion signal in all of the transients. Therefore, the data shows that the grain boundaries in my experiment were not acting as hard barriers for the charge carrier diffusion, which is contrary to previous observations.[11,15] Using Equation 4.3, the diffusion times τ_{Diff} for detection positions one, two and three were 51.2 ± 1.2 ns, 101.2 ± 5.1 ns and 172.9 ± 7.4 ns, respectively.

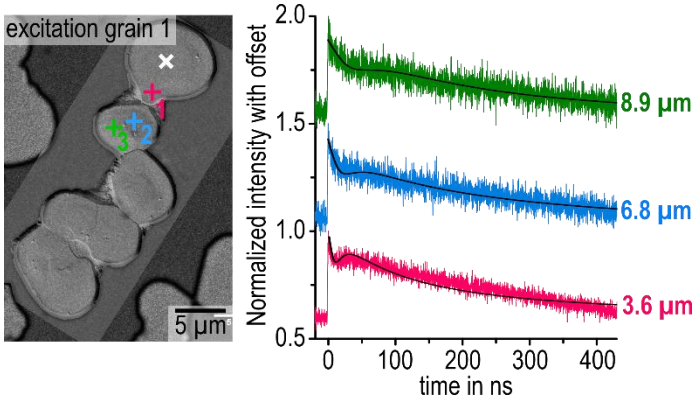

Figure 4.7: Optical reflection image and PL transients upon excitation on grain one of $MAPbI_3$ cluster. Optical reflection image overlaid with the AFM deflection signal from Figure 4.6. The white cross marks the excitation position, detection positions of PL transients on the right indicated by the magenta, blue and green crosses. Fit according to Equation 4.3 shown in black.

Furthermore, I measured three PL transients with excitation on grain four in similar excitation-detection distances of 3.2, 6.1 and 8.9 µm (Figure 4.8). Like previously on grain one, the grain boundary between grain three and four was transparent to diffusive charge carriers as evident by the clear diffusion signal in all three transients. Here, the diffusion times τ_{Diff} detected for positions one, two and three were 44.0 ± 0.9 ns, 77.4 ± 5.3 ns and 161.6 ± 4.9 ns, respectively. To directly compare the influence of the two different grain boundaries on the inter-grain diffusion, I calculated the diffusion constants D of position two and three, after the grain boundary, for both measurements via:

$$D = \frac{R^2}{4\tau_{Diff}}$$

Equation 4.4: Diffusion coefficient.

with the excitation-detection distance *R*. For the excitation on grain one, the diffusion constants on position two and three matched well with 1.14 ± 0.17 cm²/s and 1.15 ± 0.13 cm²/s, respectively. Likewise, for the excitation on grain four, the diffusion constants on position two and three coincided with 1.20 ± 0.20 cm²/s and 1.23 ± 0.13 cm²/s, respectively. The higher diffusion constants for the grain boundary between grain three and four indicate a higher transparency than the grain boundary between grain one and two. Correlating this behavior to topographic structure of the grain boundaries (Figure 4.6a), I found that the contact area between grain one and two with 1.2 µm² was significantly lower than the contact area between grain three and four with 2.8 µm². Moreover, grain boundary one-two featured a depth of 190 nm and a width of 200 nm, whereas grain boundary three-four was only 50 nm deep with a width of less than 20 nm. The apparent influence of the grain boundary morphology on the inter-grain carrier diffusion support my findings in the previous subchapter, where particularly the boundary depth, width and possibly crystallinity affected the inter-grain charge carrier drift (Chapter 4.1.1).

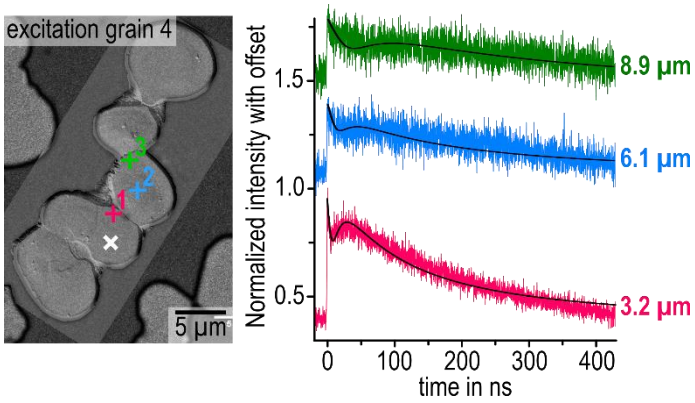

Figure 4.8: Optical reflection image and PL transients upon excitation on grain four of $MAPbI_3$ cluster. Optical reflection image overlaid with the AFM deflection signal from Figure 4.6. The white cross marks the excitation position, detection positions of PL transients on the right indicated by the magenta, blue and green crosses. Fit according to Equation 4.3 shown in black.

Summary

My investigation of the inter-grain carrier diffusion in $MAPbI_3$ via PL microscopy on an isolated grain cluster revealed that grain boundaries act as semitransparent barriers to diffusive charges rather than as hard walls. Using spatial and time-resolved PL detection, I was able to capture a distinct diffusion signal behind grain boundaries. A fit of the diffusion PL signal gave diffusion constants on adjacent grains of 1.15 and 1.22 cm²/s with an apparent dependence on the grain boundary morphology. A large contact area and dense grain boundary, without gaps, seem to facilitate faster inter-grain diffusion. To quantify the amount of diffusive charge carriers that overcome the grain boundaries a spectral analysis of the PL signal could be useful. Since trapped PL superimposes on the diffusion signal a quantification via the amplitude of the diffusion signal is not sufficiently reliable.

4.1.3 Conclusion and outlook

My investigations of the inter-grain carrier transport with and without electric field revealed drift pathways of up to 40 µm and effective diffusion lengths of 9 µm. The lateral conductivity measurement for the inter-grain carrier drift allowed quantifying individual grain boundary resistances within the studied grain cluster. Resistances in the giga-Ohm regime highlight that grain boundaries can pose as significant barriers for the charge extraction. Moreover, I observed a distinct dependence of both inter-grain drift and diffusion from the grain boundary morphology: Particularly dense grain boundaries without significant gaps allow charge transfer with limited current losses as well as faster diffusion. Additionally, the crystallinity of material within the boundary appeared affect the observed current losses in the drift experiment. For PSC application, my findings suggest that the overall current extraction benefits from limiting the amount of grain boundaries that charge carriers have to pass: Even though grain boundaries seem to be semitransparent for carrier drift and diffusion they still introduce current losses and slow down the carrier diffusion by posing as barriers. Hence, grain sizes comparable to the typical absorber layer thicknesses of 300-500 nm,[44–46] should improve the charge carrier extraction from the active $MAPbI_3$ layers and therefore the I_{SC}. Indeed, previous studies have shown an increase in I_{SC} with increasing grain sizes.[47–49] Moreover, dense grain boundaries with a high crystalline quality and minimal amorphous content could reduce losses on polycrystalline films.

In the future, the possible presence of amorphous material between two adjacent grains could be detected via high resolution TEM. Moreover, the impact of grain boundary passivation e.g., with n-trioctylphosphine oxide as demonstrated by deQuilettes *et al.*,[26] on the individual resistances could be studied systematically on a comparable cluster structure. For the inter-grain carrier diffusion, a spectral analysis of the PL could aid to detangle the diffusion signal and trapped PL. Thereby, a quantification of the number of diffusive carriers that pass the grain boundaries might be possible. The spectral analysis of the PL could also aid to determine the influence of photon recycling on the efficient diffusion length. Furthermore, pump-probe KPFM with local excitation could capture differences in the inter-grain hole or electron transport by resolving a positive or a negative surface charging, respectively. Finally, a possible facet-dependence of the inter-grain carrier transport could be explored by introducing an in-plane texture using a substrate template[40] or by studying cross sections of $MAPbI_3$ films with a combination of CAFM and EBSD. Cross-sectional CAFM and EBDS could allow correlating the current response to certain crystal planes.[41]

4.2 Photon transport across grain boundaries

-Unpublished-

Introduction

Research on material and interface optimization in perovskite solar cells based on $MAPbI_3$ and related hybrid perovskites resulted in a certified PCE of more than 25% by 2021.[50–56] To further push the PCE towards the achievable limit of ~31%, as predicted by the radiative efficiency limit,[16–19] photon management becomes essential.[57–59] In GaAs solar cells, the PCE further increased after researchers exploited the material's ability for photon recycling. Since the absorption and emission

spectra in GaAs largely overlap and the non-radiative recombination is low, photons emitted during bimolecular charge recombination, can be reabsorbed to generate another charge carrier couple. By confining photons within the absorber material i.e., minimizing the photon out-coupling via improvement of the back reflectance, the PCE of GaAs cells reached around 29%.[8,50,60–63]

For $MAPbI_3$ perovskites, in which the absorption and emission also overlap significantly, Pazos-Outón *et al.* have first reported on the material's intrinsic ability for photon recycling in 2016. The authors detected PL emission as well as photocurrents from repeated photon absorption and emission in distances of 50 µm from the excitation position in a polycrystalline film.[21] Later, several research groups probed and modelled the implications of photon reabsorption and photon confinement on perovskite solar cell parameters cells.[20,22,57,64–66] Among those, Crothers *et al.* developed a model for recombination kinetics in polycrystalline $MAPbI_3$ that accounted for photon reabsorption to correct the bimolecular recombination rate. They also visualized how photon confinement, which is caused by a mismatch of the refractive indices of vacuum (n=1), $MAPbI_3$ (n=2.5) and quartz (n=1.55), exaggerates the effect of the photon reabsorption. Thereby, photon confinement further increases the spatial and transient charge carrier density distribution as compared to fully index matched interface materials. By specifically designing interface textures to enhance the photon confinement, the open circuit voltage could be pushed further towards the radiative efficiency limit (Chapter 1.3.2.1).[22] A publication by Ciesielski *et al.* used transient PL with spatially decoupled excitation and detection[15,29–32] primarily to visualize the effects of grain boundaries on carrier diffusion. They focused on a single grain boundary in a closed polycrystalline film and found that grain boundaries confine diffusive charge carriers within the excited grain, while trapped PL freely travelled from the excited grain to the adjacent grains.[15] However, since previous studies concentrated on closed perovskite films, where grains share multiple grain boundaries, a detailed and correlative study on how different grain boundary morphologies affect light propagation is still missing.

Here, I aimed at correlating the light propagation to individual grain boundary properties on an isolated $MAPbI_3$ grain cluster on glass substrate, which was previously used to investigate the inter-grain carrier diffusion (Chapter 4.1.2). The chain-like array of the cluster, in which each grain features no more than two shared grain boundaries, allows isolating the impact of each individual grain boundary on the light propagation and subsequent correlation to the morphology. With a decoupled excitation and detection PL, [15,29–32] I mapped the distribution and the dynamics of the PL emission on the grain cluster after local excitation on one of the grains. I detected local PL intensity maxima in distances of up to 20 µm and three grain boundaries away from the excitation. Time-resolved PL measurements revealed that the local PL maxima at isolated grain edges were caused by outcoupling of the initial PL emission from the excitation spot. By comparing the PL data to AFM topography measurements, I was able to link the inter-grain photon propagation to the grain boundary morphology and found that, like for the charge carrier transfer (Chapter 4.1), the density and contact area of the grain boundary appears to govern the light-outcoupling in $MAPbI_3$. Moreover, I found that trapped PL largely maintains its directionality within single grains, suggesting a limited influence of phonon scattering on the photons.

To investigate the relation between light propagation and grain boundaries, I chose the same $MAPbI_3$ grain cluster previously used in my inter-grain carrier diffusion study in Chapter 4.1.2. Since the cluster only consists of four grains with three shared grain boundaries in a chain-like arrangement, the cluster was ideally suited to pinpoint the effect of single grain boundaries on light propagation. The AFM topography of the cluster is shown in Figure 4.6a and discussed in Chapter 4.1.2.

Following the AFM characterization, I imaged the static PL distribution of the cluster upon local excitation on each of the four constituent grains (Figure 4.9a-d): I focused the excitation laser with a wavelength of 633 nm onto one of the grains and mapped the PL distribution of the full grain cluster. The resulting PL images displayed a strong response of the excited grains with a particularly high intensity at isolated grain edges, whereas the intensity at shared grain boundaries dropped. This behavior is indicative of PL photons confined in the film due to a mismatch of the refractive indices of the glass substrate and $MAPbI_3$. The confinement leads to an increased light outcoupling at isolated grain edges, while shared grain boundaries facilitate light propagation to the neighboring grains.[20–22,43]

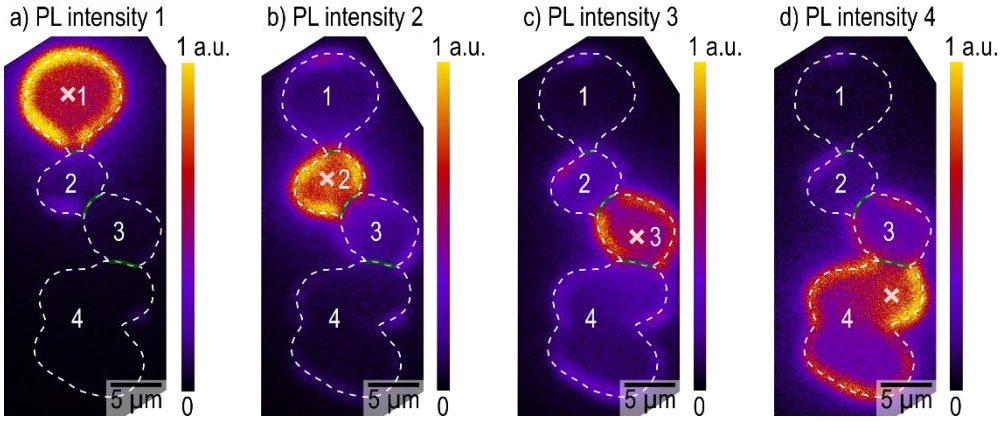

Figure 4.9: Static PL distribution of the $MAPbI_3$ grain cluster upon local optical excitation. The focus position of the excitation laser is marked by the white cross, the dashed lines indicate the grain edges of the grain cluster, derived from the PFM measurement in Figure 4.6. a) Excitation on grain one, b) excitation on grain two, c) excitation on grain three and d) excitation on grain four. Excitation with 633 nm wavelength, a fluence of 0.77 µJ cm^{-2}, a repetition rate of 20 MHz and 0.81 µm beam diameter (SI in Appendix 8.2, Figure 8.8).

For all excitation positions, I detected a PL signal not only on the excited grain but also on the adjacent grains in distances of up to 20 µm. Like for the excited grain, the PL intensity detected in the adjacent grains reached a maximum at the position of isolated grain edges, likely caused by enhanced outcoupling of confined photons at these positions. The highest intensities were typically observed on those isolated grain opposite to the shared grain boundary, which suggests that propagated light maintains a certain directionality. This maintained directionality of the propagated light indicates a reduced phonon scattering within bulk grains.

Comparing the PL distributions for different excitation positions revealed variations in the grain boundary transparency: For excitation on the first grain, the intensity dropped sharply at the first grain boundary between grain one and two. On the other hand, excitation on the other three grains visualized seemingly more transparent grain boundaries between grains two and three as well as

three and four. To quantify this effect, I averaged the intensity on each individual grain and calculated the relative PL intensity losses between the excited grain and the rest of the grains (Table 4.2). Indeed, the intensity drop at the grain boundary between grain one and two was more significant than for any other grain boundary with ~75% for excitation in one of the adjacent grains. Meanwhile, the grain boundary between grain three and four appeared to be particularly transparent with an intensity drop of only 30% from grain four to grain three.

Table 4.2: Relative losses of average PL intensity between excited grain and adjacent grains in the $MAPbI_3$ cluster extracted from Figure 4.9.

EXCITATION POSITION	DETECTION POSITION			
	GRAIN 1	**GRAIN 2**	**GRAIN 3**	**GRAIN 4**
GRAIN 1	-	76%	92%	97%
GRAIN 2	74%	-	65%	89%
GRAIN 3	85%	50%	-	65%
GRAIN4	87%	65%	30%	-

For further analysis of the apparent transparency differences of grain boundaries one-two and three-four, I extracted line profiles from PL distribution spanning over the full grain cluster (Figure 4.10). I particularly focused on local PL maxima at isolated grain edges. With the excitation placed on grain one (Figure 4.10a and b), the PL intensity featured a sharp drop after passing the first grain boundary one-two, as anticipated from previous observations in Figure 4.9 and Table 4.2. Grain two displayed a local PL maximum at the isolated grain edge opposite of the shared grain boundary one-two 8.8 µm from the excitation. The intensity of the local PL maximum was 30% of the intensity detected on isolated grain edges in grain one. In grain three and four, I resolved two weak local intensity maxima in distances of 14.4 and 18.2 µm from the excitation, respectively. Both maxima exhibited only 8% of the grain edge intensity measured on grain one. For the excitation positioned on grain four, in Figure 4.10c and d, I found a more gradual intensity decrease from the excitation grain across the cluster. A local intensity maximum on grain three, 7.8 µm from the excitation on the isolated grain edge opposite to the shared grain boundary three-four, featured 54% of the grain edge intensity on grain four. The local maximum on grain two, detected 11.7 µm from the excitation, displayed 37% of the PL intensity measured on an isolated grain edge in grain four. In grain one, I resolved a local intensity maximum on the grain edges with 17% of the grain edge intensity of grain four, 19.6 µm from the excitation position.

To determine whether the detected intensity maxima in Figure 4.10 were mainly caused by the outcoupling of confined PL from the excitation site, carrier diffusion or a combination of both, I performed spatial and time-resolved PL microscopy measurements as described previously (Chapter 3.2.2). A spatial decoupling the time-resolved detection and pulsed excitation allows resolving the time lag between excitation and detection in dependence of their distance (SI in Appendix 8.2, Figure 8.6). Since the charge carrier diffusion occurs on much longer time scales than light propagation, even when we consider an effective acceleration by photon recycling (SI in

Appendix 8.2, Simulation 8.17),[67], spatial and time-resolved resolved PL microscopy facilitates a reliable differentiation of the two mechanisms.[15,31,32]

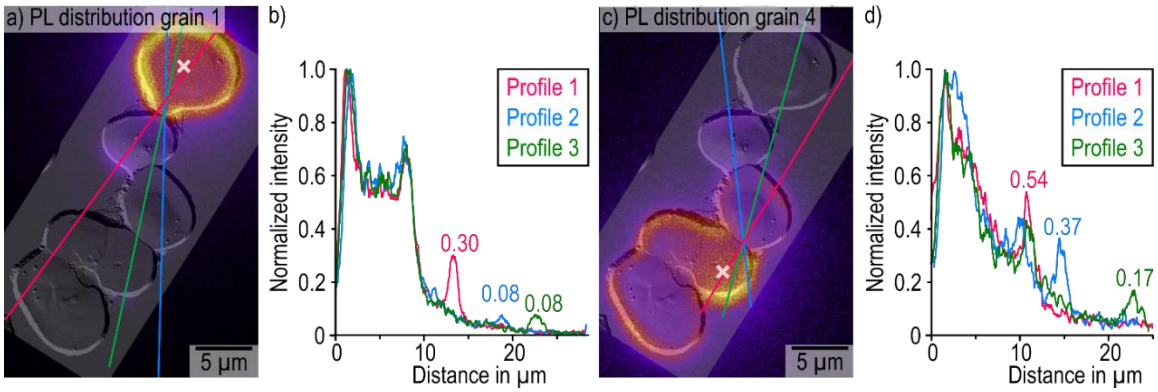

Figure 4.10: a) Static PL distribution of $MAPbI_3$ grain cluster upon local optical excitation in grain one overlayed with a semitransparent image of the AFM deflection from Figure 4.6. The excitation position is marked by the white cross, extraction positions of the three line profiles in b) shown by the magenta (Profile 1), blue (Profile 2) and green line (Profile 3). c) Static PL distribution of $MAPbI_3$ grain cluster upon local optical excitation in grain four overlayed with a semitransparent image of the AFM deflection from Figure 4.6. The excitation position is marked by the white cross, extraction positions of the three line profiles in d) shown by the magenta (Profile 1), blue (Profile 2) and green line (Profile 3). All line profiles were smoothed with a 7-point moving average. Excitation with 633 nm wavelength, a fluence of 0.77 µJ cm^{-2}, a repetition rate of 20 MHz and 0.82 µm beam diameter (SI in Appendix 8.2, Figure 8.8).

Therefore, I placed the time-resolved PL detection on the excitation spot on grain one (Position 0) as well as on each of the three local intensity maxima on grain two in 8.8 µm (Position 1), grain three in 14.4 µm (Position 2) and grain four in 18.2 µm distance from the excitation (Position 3) (Figure 4.11a). The PL transients measured at these four positions are given in Figure 4.11b. Comparing the PL emission onsets of the four transients, I found that the onsets occur simultaneously on all four detection positions, independent of the distance and amount of grain boundaries between excitation and detection. Together with the absence of the characteristic diffusion feature in the time traces (Figure 4.7 and Figure 4.8), the simultaneous emission onsets indicate that the PL signal resolved at isolated grain edges is mainly caused by the outcoupling of confined PL emission from initial radiative recombination at the excitation site. Contributions from diffusive charge carriers appear to be negligible at these positions. I repeated the measurement with the excitation on grain four and time-resolved PL detection at the excitation position and the local maxima on grains one, two and three in 7.8, 11.7 and 19.6 µm distance from the excitation, respectively (Figure 4.11c and d). All detection positions displayed simultaneous emission onsets, thereby confirming my finding that the PL emission at isolated grain edges is governed by outcoupling of confined photons.

With outcoupling of trapped PL dominating the signal at local intensity maxima, I evaluated the influence of grain boundaries on light propagation in $MAPbI_3$ by directly comparing the relative intensity decay across grain boundary one-two and three-four (Figure 4.10). The apparent lower optical transparency of grain boundary one-two, suggested by the intensity drop to 30% on the edge of grain two and to 8% on grain three and four, could be linked to the relatively smaller contact area of 1.2 µm² posing as a bottleneck for confined photons. Grain boundary three-four, on the other hand, featured a contact area of 2.8 µm². Moreover, the distinct gap between grain one and two of

190 nm in depth and 200 nm in width, which is well below the wavelength of the confined PL, may act as Rayleigh scattering center. For example, in polycrystalline silicon waveguides the structure and quality of grain boundaries relates to scattering losses.[6,7] The likely influence of the grain boundary morphology on the light propagation in polycrystalline $MAPbI_3$ suggests that an overall reduction in the grain boundary density by an increase of the grains size aids the photon confinement and thereby enhances the photon recycling probability.[59]

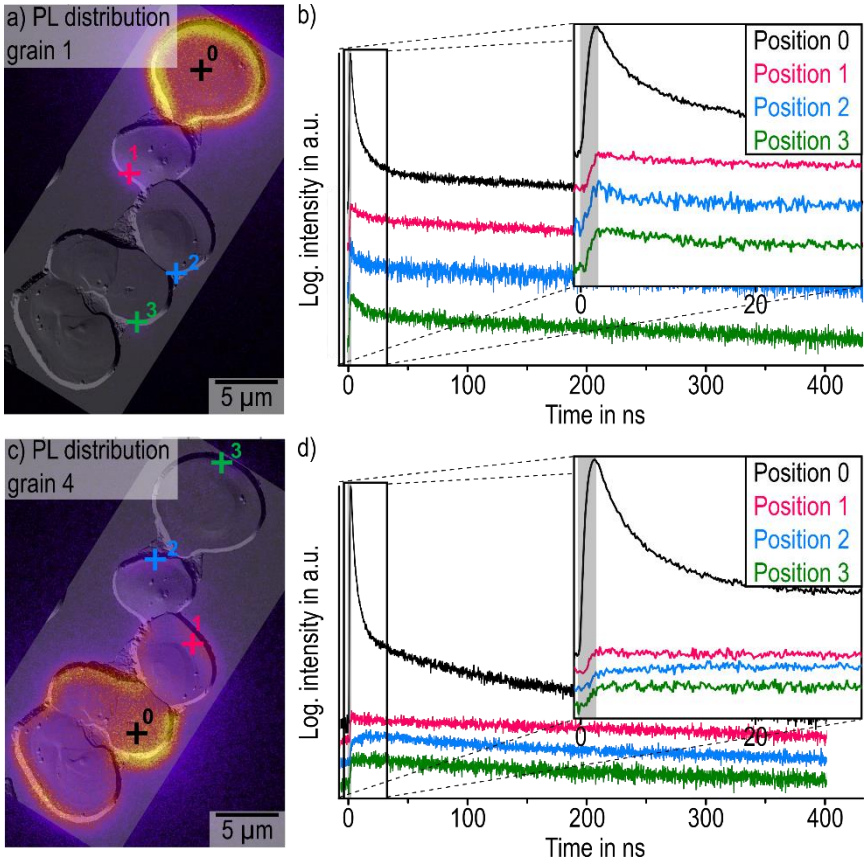

Figure 4.11: a) Static PL distribution of $MAPbI_3$ grain cluster upon local optical excitation on grain one overlayed with a semitransparent image of the AFM deflection from Figure 4.6. The excitation position is marked by the black cross, coinciding with detection position 0 for the time-resolved PL decay. Detection positions on grains two, three and four are marked by the magenta, blue and green crosses 1, 2 and 3, respectively. b) Time-resolved PL decays measured at positions 0, 1, 2 and 3 in a). The grey shaded area marks the instrument response function of 1.4 ns. The enlarged decay displayed the simultaneous emission onset on all four detection positions. c) Static PL distribution for excitation on grain four with AFM deflection from Figure 4.6. The excitation position is marked by the black cross, coinciding with time-resolved PL detection position 0. Detection positions on grains three, two and one are marked by the magenta, blue and green crosses 1, 2 and 3, respectively. d) Time-resolved PL decays measured at positions 0, 1, 2 and 3 in c) with the instrument response function in grey and zoom-in to highlight the simultaneous emission onset on all four detection positions. Excitation with 633 nm wavelength, a fluence of 0.77 µJ cm^{-2}, 0.82 µm beam diameter and a repetition rate of 20 MHz for the static and 2MHz for the time-resolved PL (SI in Appendix 8.2,Figure 8.8).

Aside from the apparent grain boundary influence on the light propagation, the distance travelled by PL from the initial radiative recombination was surprising, considering reports on photon recycling in $MAPbI_3$ and its absorption length at the emission wavelength.[21,22,67,68] At the typical $MAPbI_3$ emission wavelength of 765 nm[21], the absorption coefficient α is 1-3*10^4 cm^{-1},[68] leading to an expected absorption length $L_a = 1/\alpha$ of 0.3 – 1 µm. Hence, several re-absorption events can be expected for the initial PL as it propagates through the grain cluster, which would

delay the emission onset significantly. Pazos-Outon *et al.* modelled the number of recycling steps per photon at 765 nm in dependency of the travel distance. From their model 15 – 20 recycling steps are possible for photons passing ~20 µm through the full cluster.[21] However, as the confined photons travel across the perovskite film, they can lose energy due to inelastic scattering events, previously observed as red-shift by more than 30 nm in the PL signal.[21,23,24,66] The re-absorption probability of these red-shifted photons decreases substantially with respect to 765 nm photons. Pazos-Outon *et al.* calculated expected 5-6 recycling events at 800 nm over a distance of 20 µm, while a shift to 820 nm results in zero recycling events over 20 µm.[21] On the other hand, I observed that the confined PL on grains that are adjacent to the excited grain maintain their directionality. The occurrence of inelastic phonon scattering however would change not only the photon energy but also their directionality. Here, one explanation to the maintained directionality is that the majority of inelastic phonon scattering takes place in the excited grains and those lower energy photons travel through adjacent grains without substantial scattering events. Overall, a reliable determination of the nature of the photons detected on the opposite end of the grain cluster requires a spectral analysis of the signal in the future.

Summary

In this subchapter, I investigated the influence of grain boundaries on the light propagation in an isolated $MAPbI_3$ grain cluster consisting of four grains and three shared grain boundaries. By using spatial and time-resolved PL microscopy, I confirmed that local PL maxima at isolated grain edges across the cluster originate from outcoupling of trapped photons, which are emitted during the initial radiative recombination at the excitation site. The confined photons largely maintained their directionality on those grain adjacent to the excited grain, which resulted in local PL maxima at those grain edges opposite to the shared grain boundary. Astonishingly, some confined photons exceeded the expected absorption length by more than an order of magnitude. For these photons the re-absorption probability likely decreased due to energy losses during inelastic scattering events in the excited grain. Moreover, static PL imaging indicated that certain grain boundaries can pose as significant bottleneck to confined photons depending on their morphology. The correlation of the PL signal with AFM topography suggested that a small contact area between adjacent grains and the presence of a sub-wavelengths gap, which may act as Rayleigh-scattering center, impede a loss-free light propagation.

4.2.1 Conclusion and outlook

With the optimization of material composition and interfaces in PSCs, photon management becomes increasingly important to reach the theoretical efficiency limit. For future device improvements with a focus on photon management via photon recycling, perovskite layers need to allow light propagation with minimal scattering losses and parasitic absorption by contact alyers.[20,59] Here, I investigated light propagation in polycrystalline $MAPbI_3$. Overall, my results showed that confined photons in a $MAPbI_3$ cluster can travel up to 20 µm across several grain boundaries, while maintaining their directionality in bulk grain adjacent to the excited grain. The reduced reabsorption probability of these grains could originate from a shift to lower wavelengths via inelastic scattering in the excited grain. Moreover, grain boundaries can increase the outcoupling probability of the confined PL, if they feature sub-wavelengths gaps. For PSCs, my

findings suggest that an increase in grain size and improvement of grain boundary quality i.e., a reduction of possible scattering scenters, such as gaps, could enhance the light propagation and reabsorption probability.

In the future, a more quantitative characterization of the re-absorption probability of confined photons in the $MAPbI_3$ requires a spectral analysis of the outcoupled PL signal. Spectral analysis allows estimating energy losses of the confined photon introduced by scattering events and will provide insights on how to minimize these energy losses. Furthermore, a change of the sample architecture to a more applied PV layer structure may add insights on parasitic absorption losses caused by extraction layers and change the escape probability of the confined photons.

4.3 Grain boundaries – concluding remarks

Applied PSCs as thin film solar cells contain a polycrystalline perovskite absorber layer, sandwiched between charge selective extraction layers and electrodes. With typical layers thicknesses of 300-500 nm and grain sizes between 100 and 500 nm,[44–46] charge carriers and confined photons are likely to encounter grain boundaries prior to extraction or re-absorption, respectively. In this chapter, I studied the influence of grain boundaries on the inter-grain charge carrier drift and diffusion as well as the light propagation on interconnected $MAPbI_3$ grain clusters. Large grains and a low number of shared grain boundaries helped to correlate electronic and optical properties to the grain boundary morphology. I found that, while grain boundaries are semitransparent, they act as substantial barriers for the inter-grain carrier transport as well as light propagation. The transparency displays a strong dependence on their morphology: Dense grain boundaries without gaps appeared to facilitate faster diffusion, reduced resistance and lower PL intensity losses.

For the optimization of applied perovskite PV and other optoelectronic applications including photodetectors, my findings suggest that a reduction of the grain boundary density by increasing the overall grain size could improve the charge carrier extraction as well as photon reabsorption probability. Here, a high crystalline quality with low amorphic material content and a uniform out-of-plane texture could reduce electrostatic barriers and optical scattering centers. Particularly, the possible role of grain boundaries as scattering centers that impede light propagation should be considered for future *PCE* optimization via photon management. Moreover, energetic losses of confined photons due to inelastic phonon scattering in the perovskite layer lower their re-absorption probability and therefore the V_{OC} of the PSCs.[20,22]

Subsequent studies on the impact of grain boundaries on inter-grain charge transfer could be performed in cross sections of the perovskite layer to simulate the out-of-plane carrier extraction present in PSCs. Moreover, this would allow a correlation of the carrier transport with an EBSD analysis on dominant crystal facets, based on previous studies suggesting a facet dependence in carrier extraction.[26,37,38] For future studies on the light propagation, a spectral analysis in addition to the time- and spatially resolved PL microscopy is essential. Resolving the wavelength of the confined photons allows evaluating energy losses within the absorption layer and developing of strategies on how to avoid these losses.

Experimental

Sample preparation:

See Chapter 3.2.1 for gold evaporation.

See Chapter 3.2.2 for $MAPbI_3$ preparation and deposition.

Conductive atomic force microscopy

See Chapter 3.2.1, for CAFM measurements.

Spatial and time-resolved photoluminescence (PL):

See Chapter 3.2.2 for spatial and time-resolved PL microscopy.

Piezoresponse force microscopy (PFM):

See Chapter 3.1.1 for lateral PFM measurements.

Bibliography

1. Nelson, J. A. *The physics of solar cells*. (World Scientific Publishing Company, 2003).
2. Green, M. A. Thin-film solar cells: review of materials, technologies and commercial status. *J. Mater. Sci. Mater. Electron.* **18**, 15–19 (2007).
3. Hu, Y. *et al.* Improved performance of printable perovskite solar cells with bifunctional conjugated organic molecule. *Adv. Mater.* **30**, 1705786 (2018).
4. Jiang, P. *et al.* Fully printable perovskite solar cells with highly-conductive, low-temperature, perovskite-compatible carbon electrode. *Carbon N. Y.* **129**, 830–836 (2018).
5. Yang, Z. *et al.* High-performance fully printable perovskite solar cells via blade-coating technique under the ambient condition. *Adv. Energy Mater.* **5**, 1500328 (2015).
6. Agarwal, A. M. *et al.* Low-loss polycrystalline silicon waveguides for silicon photonics. *J. Appl. Phys.* **80**, 6120–6123 (1996).
7. Liao, L. *et al.* Optical transmission losses in polycrystalline silicon strip waveguides: effects of waveguide dimensions, thermal treatment, hydrogen passivation, and wavelength. *J. Electron. Mater.* **29**, 1380–1386 (2000).
8. Kosten, E. D., Atwater, J. H., Parsons, J., Polman, A. & Atwater, H. A. Highly efficient GaAs solar cells by limiting light emission angle. *Light Sci. Appl.* **2**, e45–e45 (2013).
9. Castro-Méndez, A., Hidalgo, J. & Correa-Baena, J. The Role of Grain Boundaries in Perovskite Solar Cells. *Adv. Energy Mater.* **9**, 1901489 (2019).
10. Arias, D. H., Moore, D. T., van de Lagemaat, J. & Johnson, J. C. Direct measurements of carrier transport in polycrystalline methylammonium lead iodide perovskite films with transient grating spectroscopy. *J. Phys. Chem. Lett.* **9**, 5710–5717 (2018).
11. Yang, M. *et al.* Do grain boundaries dominate non-radiative recombination in CH 3 NH 3 PbI 3 perovskite thin films? *Phys. Chem. Chem. Phys.* **19**, 5043–5050 (2017).

12. Sherkar, T. S. *et al.* Recombination in perovskite solar cells: significance of grain boundaries, interface traps, and defect ions. *ACS energy Lett.* **2**, 1214–1222 (2017).

13. Snaider, J. M. *et al.* Ultrafast imaging of carrier transport across grain boundaries in hybrid perovskite thin films. *ACS Energy Lett.* **3**, 1402–1408 (2018).

14. Reid, O. G., Yang, M., Kopidakis, N., Zhu, K. & Rumbles, G. Grain-size-limited mobility in methylammonium lead iodide perovskite thin films. *ACS Energy Lett.* **1**, 561–565 (2016).

15. Ciesielski, R. *et al.* Grain boundaries act as solid walls for charge carrier diffusion in large crystal MAPI thin films. *ACS Appl. Mater. Interfaces* **10**, 7974–7981 (2018).

16. Pazos-Outón, L. M., Xiao, T. P. & Yablonovitch, E. Fundamental Efficiency Limit of Lead Iodide Perovskite Solar Cells. *J. Phys. Chem. Lett.* **9**, 1703–1711 (2018).

17. Sha, W. E. I., Ren, X., Chen, L. & Choy, W. C. H. The efficiency limit of CH3NH3PbI3 perovskite solar cells. *Appl. Phys. Lett.* **106**, 221104 (2015).

18. Braly, I. L. *et al.* Hybrid perovskite films approaching the radiative limit with over 90% photoluminescence quantum efficiency. *Nat. Photonics* **12**, 355–361 (2018).

19. Shockley, W. & Queisser, H. J. Detailed balance limit of efficiency of p-n junction solar cells. *J. Appl. Phys.* **32**, 510–519 (1961).

20. Richter, J. M. *et al.* Enhancing photoluminescence yields in lead halide perovskites by photon recycling and light out-coupling. *Nat. commun.* **7**, 1–8 (2016).

21. Pazos-Outón, L. M. *et al.* Photon recycling in lead iodide perovskite solar cells. *Science (80-.).* **351**, 1430–1433 (2016).

22. Crothers, T. W. *et al.* Photon reabsorption masks intrinsic bimolecular charge-carrier recombination in CH3NH3PbI3 perovskite. *Nano Lett.* **17**, 5782–5789 (2017).

23. Gan, Z. *et al.* The dominant energy transport pathway in halide perovskites: photon recycling or carrier diffusion? *Adv. Energy Mater.* **9**, 1900185 (2019).

24. Fassl, P. *et al.* Revealing the internal luminescence quantum efficiency of perovskite films via accurate quantification of photon recycling. *Matter* **4**, 1391–1412 (2021).

25. Yan, Y. *et al.* Physics of grain boundaries in polycrystalline photovoltaic semiconductors. *J. Appl. Phys.* **117**, 112807 (2015).

26. DeQuilettes, D. W. *et al.* Tracking photoexcited carriers in hybrid perovskite semiconductors: trap-dominated spatial heterogeneity and diffusion. *ACS Nano* **11**, 11488–11496 (2017).

27. MacDonald, G. A. *et al.* Methylammonium lead iodide grain boundaries exhibit depth-dependent electrical properties. *Energy Environ. Sci.* **9**, 3642–3649 (2016).

28. Kutes, Y. *et al.* Mapping the photoresponse of CH3NH3PbI3 hybrid perovskite thin films at the nanoscale. *Nano Lett.* **16**, 3434–3441 (2016).

29. Hermes, I. M. *et al.* Anisotropic carrier diffusion in single MAPbI3 grains correlates to their twin domains. *Energy Environ. Sci.* **13**, 4168–4177 (2020).

30. Handloser, K. *et al.* Contactless visualization of fast charge carrier diffusion in hybrid halide perovskite thin films. *ACS Photonics* **3**, 255–261 (2016).

31. Tian, W., Zhao, C., Leng, J., Cui, R. & Jin, S. Visualizing carrier diffusion in individual single-crystal organolead halide perovskite nanowires and nanoplates. *J. Am. Chem. Soc.* **137**, 12458–12461 (2015).

32. Tian, W. *et al.* Limiting perovskite solar cell performance by heterogeneous carrier extraction. *Angew. Chem. Int. Ed.* **55**, 13067–13071 (2016).

33. Würfel, P. & Würfel, U. *Physics of solar cells: from basic principles to advanced concepts*. (John Wiley & Sons, 2016).

34. Xiao, Z. *et al.* Solvent annealing of perovskite-induced crystal growth for photovoltaic-device efficiency enhancement. *Adv. Mater.* **26**, 6503–6509 (2014).

35. Hermes, I. M. *et al.* Ferroelastic Fingerprints in Methylammonium Lead Iodide Perovskite. *J. Phys. Chem. C* **120**, (2016).

36. Jiang, L. *et al.* Understanding current instabilities in conductive atomic force microscopy. *Materials (Basel).* **12**, 459 (2019).

37. Leblebici, S. Y. *et al.* Facet-dependent photovoltaic efficiency variations in single grains of hybrid halide perovskite. *Nat. Energy* **1**, 1–7 (2016).

38. Docampo, P. *et al.* Influence of the orientation of methylammonium lead iodide perovskite crystals on solar cell performance. *Apl Mater.* **2**, 81508 (2014).

39. Han, W.-S., Kang, S.-O. & Suh, I.-H. An Easier Way to Calculate the Crystallographic Interplanar Angles. *Korean J. Crystallogr.* **18**, 7–9 (2007).

40. Teplin, C. W., Ginley, D. S. & Branz, H. M. A new approach to thin film crystal silicon on glass: Biaxially-textured silicon on foreign template layers. *J. Non. Cryst. Solids* **352**, 984–988 (2006).

41. Leonhard, T. *et al.* Probing the Microstructure of Methylammonium Lead Iodide Perovskite Solar Cells. *Energy Technol.* **7**, 1800989 (2019).

42. Hodes, G. & Kamat, P. V. Understanding the implication of carrier diffusion length in photovoltaic cells. (2015).

43. Yamada, Y. *et al.* Dynamic optical properties of CH3NH3PbI3 single crystals as revealed by one-and two-photon excited photoluminescence measurements. *J. Am. Chem. Soc.* **137**, 10456–10459 (2015).

44. Snaith, H. J. Perovskites: the emergence of a new era for low-cost, high-efficiency solar cells. *J. Phys. Chem. Lett.* **4**, 3623–3630 (2013).

45. Tress, W. Perovskite solar cells on the way to their radiative efficiency limit–insights into a success story of high open-circuit voltage and low recombination. *Adv. Energy Mater.* **7**, 1602358 (2017).

46. Saliba, M., Correa-Baena, J., Grätzel, M., Hagfeldt, A. & Abate, A. Perovskite solar cells: from the atomic level to film quality and device performance. *Angew. Chemie Int. Ed.* **57**, 2554–2569 (2018).

47. Kim, H. Do, Ohkita, H., Benten, H. & Ito, S. Photovoltaic performance of perovskite solar cells with different grain sizes. *Adv. Mater.* **28**, 917–922 (2016).

48. Nukunudompanich, M., Budiutama, G., Suzuki, K., Hasegawa, K. & Ihara, M. Dominant effect of the grain size of the MAPbI 3 perovskite controlled by the surface roughness of TiO 2 on the performance of perovskite solar cells. *CrystEngComm* **22**, 2718–2727 (2020).

49. Wieghold, S. *et al.* Precursor concentration affects grain size, crystal orientation, and local performance in mixed-ion lead perovskite solar cells. *ACS Appl. Energy Mater.* **1**, 6801–6808 (2018).

50. (NREL), N. R. E. L. Best Research-Cell Efficiency Chart. https://www.nrel.gov/pv/cell-efficiency.html (2021). Available at: https://www.nrel.gov/pv/cell-efficiency.html.

51. Kojima, A., Teshima, K., Shirai, Y. & Miyasaka, T. Organometal halide perovskites as visible-light sensitizers for photovoltaic cells. *J. Am. Chem. Soc.* **131**, 6050–6051 (2009).

52. Lee, M. M., Teuscher, J., Miyasaka, T., Murakami, T. N. & Snaith, H. J. Efficient hybrid solar cells based on meso-superstructured organometal halide perovskites. *Science (80-.).* **338**, 643–647 (2012).

53. Kim, H.-S. *et al.* Lead iodide perovskite sensitized all-solid-state submicron thin film mesoscopic solar cell with efficiency exceeding 9%. *Sci. Rep.* **2**, 591 (2012).

54. Zhou, H. *et al.* Interface engineering of highly efficient perovskite solar cells. *Science (80-.).* **345**, 542–546 (2014).

55. Saliba, M. *et al.* Cesium-containing triple cation perovskite solar cells: improved stability, reproducibility and high efficiency. *Energy Environ. Sci.* **9**, 1989–1997 (2016).

56. Yang, W. S. *et al.* Iodide management in formamidinium-lead-halide–based perovskite layers for efficient solar cells. *Science (80-.).* **356**, 1376–1379 (2017).

57. Brenes, R., Laitz, M., Jean, J., deQuilettes, D. W. & Bulović, V. Benefit from photon recycling at the maximum-power point of state-of-the-art perovskite solar cells. *Phys. Rev. Appl.* **12**, 14017 (2019).

58. Kirchartz, T. Photon management in perovskite solar cells. (2019).

59. Raja, W. *et al.* Photon recycling in perovskite solar cells and its impact on device design. *Nanophotonics* (2021).

60. García, I. *et al.* Back reflectors based on buried Al2O3 for enhancement of photon recycling in monolithic, on-substrate III-V solar cells. *Appl. Phys. Lett.* **105**, 133507 (2014).

61. Micha, D. N. *et al.* Development of back side technology for light trapping and photon recycling in GaAs solar cells. *Prog. Photovoltaics Res. Appl.* **27**, 163–170 (2019).

62. Miller, O. D., Yablonovitch, E. & Kurtz, S. R. Strong internal and external luminescence as solar cells approach the Shockley–Queisser limit. *IEEE J. Photovoltaics* **2**, 303–311 (2012).

63. Steiner, M. A. *et al.* Optical enhancement of the open-circuit voltage in high quality GaAs solar cells. *J. Appl. Phys.* **113**, 123109 (2013).

64. Kirchartz, T., Staub, F. & Rau, U. Impact of photon recycling on the open-circuit voltage of metal halide perovskite solar cells. *ACS Energy Lett.* **1**, 731–739 (2016).

65. Staub, F., Kirchartz, T., Bittkau, K. & Rau, U. Manipulating the net radiative recombination rate in lead halide perovskite films by modification of light outcoupling. *J. Phys. Chem. Lett.* **8**, 5084–5090 (2017).

66. Dursun, I. *et al.* Efficient photon recycling and radiation trapping in cesium lead halide perovskite waveguides. *ACS Energy Lett.* **3**, 1492–1498 (2018).

67. Ansari-Rad, M. & Bisquert, J. Insight into photon recycling in perovskite semiconductors from the concept of photon diffusion. *Phys. Rev. Appl.* **10**, 34062 (2018).

68. De Wolf, S. *et al.* Organometallic halide perovskites: sharp optical absorption edge and its relation to photovoltaic performance. *J. Phys. Chem. Lett.* **5**, 1035–1039 (2014).

5 Charge carrier extraction across heterointerfaces

Besides grain boundaries within the $MAPbI_3$ absorber layer, the main limitation for efficient charge carrier extraction and thus photocurrent are the transport layers.[1–3] Charge selective transport layers are required in PSCs due to the cells' *pin*-architecture, where $MAPbI_3$ as intrinsic semiconductor absorber is sandwiched between a metal oxide or fullerene ETL and an HTL (Figure 5.1).[4–6] To ensure a high charge selectivity, the band alignment between absorber and HTL has to facilitate the extraction of holes via a small positive offset in the valance band and block electrons via a large positive offset in the conduction band from absorber to HTL. Analogously, for ETLs, the band alignment from absorber to ETL has a small negative offset in the conduction band to extract electrons and a large negative offset in the valance band to block holes (Figure 5.2a).[2,7,8] Too large offsets for hole or electron extraction can introduce thermionic losses, effectively lowering the V_{OC} of the cells.[8]

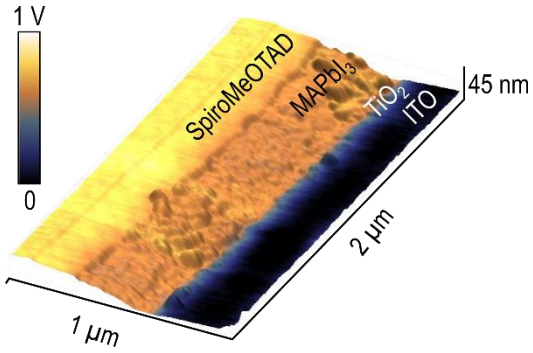

Figure 5.1: Potential distribution of PSC cross section with TiO_2 ETL under open circuit conditions with illumination imaged via KPFM overlayed onto topography.

In addition to a suitable band alignment with the $MAPbI_3$ absorber, materials for charge extraction should feature sufficiently high carrier mobilities to avoid a charge accumulation at the interfaces. For PSCs, typical HTL and ETL materials are the organic compound SpiroMeOTAD as hole conductor and inorganic metal oxides like TiO_2 and SnO_2 as electron conductors.[7] In SpiroMeOTAD, the conductivity increases upon p-doping with Li-salts to facilitate efficient hole extraction.[2,9–11] However, despite the doping, the carrier mobility of the organic compound is still up to three orders of magnitude lower than in $MAPbI_3$.[1] Likewise, TiO_2 features a relatively low intrinsic carrier mobility.[12] The combination of the consequent electronic charge accumulation with the mobile ions of the $MAPbI_3$ layers has been linked to the slow dynamic processes in PSCs that cause transient photocurrent response and *j-V* hysteresis (Chapter 1.3.1.2).[13,14] Here, a change in the external field leads to a redistribution of the charges, which causes current transients and the *j-V* hysteresis.[13,15–18] Studies that focus on these dynamic phenomena found a strong dependence of the hysteresis magnitude on the nature of the transport materials.[2,15,19–23] Particularly, the ETL material appears to determine the extent of the slow dynamic processes.[2,15,19–22] Researchers found that an exchange of a planar metal oxide ETL to a fullerene-based ETL or the introduction of a fullerene passivation layer reduces the magnitude of the *j-V* hysteresis substantially.[19–21,24] An investigation by our group suggested that defects located at the metal oxide ETL interface can lower the activation energy for the generation of mobile iodide ions. Thereby the ETL interface directly

contributes to the concentration of mobile ions in the $MAPbI_3$ layer. This higher ion concentration in turn increases the magnitude of the *j-V* hysteresis.[18]

Aside from the impact of mobile ions on the magnitude of hysteresis, some studies hypothesize that the previously observed degradation of SpiroMeOTAD[25,26] is connected to a complexation with iodide ions (Chapter 1.3.1.2).[18,27,28] This complexation can effectively lower the material's hole conductivity and thereby reduce the carrier extraction even further.[27]

In this chapter, we investigated the impact of two different ETLs displaying different magnitudes of hysteresis on the HTL and the charge carrier extraction. To this end, we imaged the potential distribution on cross sections of the two PSCs via KPFM, comparing one cell with a planar TiO_2 ETL and a strong *j-V* hysteresis to a cell with a C60-SAM ETL and minimal hysteresis. Potential distributions under open and short circuit conditions illumination revealed significant differences between both PSCs, likely related to an ion-induced degradation of the HTL in the TiO_2 cell and consequent increase in the interfacial resistance.

5.1 The interplay of contact layers: How the electron transport layer influences interfacial recombination and hole extraction in perovskite solar cells

Ilka M. Hermes,[†] Yi Hou,[‡] Victor W. Bergmann,[†] Christoph J. Brabec,[‡] and Stefan A. L. Weber[†,§]

[†] *Max Planck Institute for Polymer Research, Ackermannweg 10, 55128 Mainz, Germany*

[‡] *Department of Materials Science and Engineering, Institute of Materials for Electronics and Energy Technology (i-MEET), Friedrich-Alexander University Erlangen-Nürnberg, Martensstrasse 7, 91058 Erlangen, Germany*

[§] *Institute of Physics, Johannes Gutenberg University Mainz, Staudingerweg 10, 55128 Mainz, Germany*

-Published in the journal of physical chemistry letters (J. Phys. Chem. Lett.) 2018, 9, 6249−6256 https://doi.org/10.1021/acs.jpclett.8b02824 -

Abstract

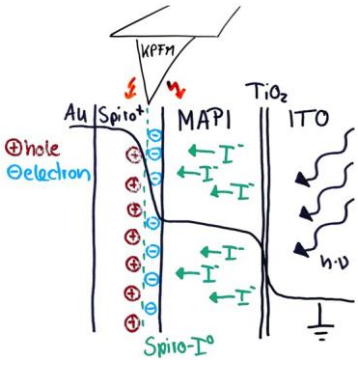

Charge-selective contact layers in perovskite solar cells influence the current density−voltage hysteresis, an effect related to ion migration in the perovskite. As such, fullerene-based electron transport layers (ETLs) suppress hysteresis by reducing the mobile ion concentration. However, the impact of different ETLs on the electronic properties of other constituent device layers remains unclear. In this Kelvin probe force microscopy study, we compared potential distributions of methylammonium lead iodide-based solar cells with two ETLs (planar TiO_2 and C60-functionalized self-assembled monolayer) with different hysteretic behavior. We found significant changes in the potential distribution of the organic hole transport layer spiroMeOTAD, suggesting the formation of a neutral spiroMeOTAD/iodide interface due to a reaction between iodide with p-

doped spiroMeOTAD in the TiO_2 cell. Our results show that the ETL affects not only the mobile ion concentration and the recombination at the perovskite/ETL interface but also the resistance and capacitance of the spiroMeOTAD.

Introduction

In this study, we correlated the electrical potential distribution of two methylammonium lead iodide ($MAPbI_3$) perovskite solar cells (PSCs) with different device architectures to the macroscopic current density-voltage (*j-V*) behavior. Interestingly, the nature of the electron transport layer (ETL) material affected not only the potential within the perovskite layer. Instead, the strongest change in the potential distribution was observed within the hole transport layer (HTL), suggesting differences in resistance and capacitance. Our results show that interfacial recombination as well as hole extraction directly depend on the choice of ETL.

Despite their recent success,[29–33] PSCs still exhibit some unfavorable properties, most significantly a rate-dependent *j-V* hysteresis, which is thought to be caused by slow processes on millisecond to minute time scales within the perovskite layer.[17,34–37] The most probable origin of the hysteresis is a combination of trapped electronic charges and the migration of iodide and iodide vacancies, which exhibit the lowest activation energies of the constituent ions.[14,38–46] The assumed density of mobile iodide is sufficient to affect the electric field distribution within a PSC significantly by accumulation at the interfaces to the contact layers.[42,47,48] Additionally, the accumulation of ions at the contact interfaces can induce band bending and, because ions act as charged traps, create nonradiative recombination sites for the photogenerated charges.[38–42,47–50] Other peculiar properties of PSCs, such as the high low-frequency capacitance under illumination in hysteretic and non-hysteretic devices, as well as a possible degradation of the organic HTL spiroMeOTAD, have also been related to mobile ionic defects.[15,20,25,27,51–54] Some ETLs can minimize the *j-V* hysteresis by suppressing the ion migration. As such, it was suggested that fullerene-based ETLs inhibit ion migration by passivating defects, binding iodide in a fullerene-iodide complex and/or blocking grain boundaries as the prevalent pathways for mobile iodide.[19,24,55–57] In 2017, Hou *et al.* introduced a phosphonic acid-based mixed C60/organic self-assembled monolayer (C60-SAM) as ETL, which significantly reduced the hysteresis compared to a conventional planar TiO_2 ETL. They also observed a decrease of the low-frequency (1-100 Hz) capacitance by an order of magnitude for the C60-SAM. They assigned the reduced hysteresis and capacitance to a lower density of mobile ions due to an enhanced crystalline quality, larger grain sizes (400-800 nm for C60-SAM compared to 300-400 nm for TiO_2), and lowered defect density of the perovskite.[19] Recently, we found that mobile ions in PSCs originate from a thin layer at the ETL interface, thus highlighting the significance of the $MAPbI_3$/ETL interface on the mobile ion concentration.[18]

Kelvin probe force microscopy (KPFM) on device cross sections directly visualizes the impact of different ETLs on the distribution of photocarriers and the interfacial capacitances in working PSCs.[3,58–62] KPFM images the local contact potential difference (*LCPD*) between an electrically connected tip-sample system by recording the DC tip bias required to nullify the electrostatic force between tip and sample.[63,64] Thereby, KPFM visualizes *LCPD* variations with a spatial resolution of 20-30 nm.[59,63,65,66] In a dark solar cell, the Fermi levels of all constituent layers align because they are in electrical contact (Figure 5.2a, b). The *LCPD* on a solar cell cross section therefore

corresponds to the negative vacuum level profile across the layers (Figure 5.2c). The inversion originates from the fact that energy level diagrams correspond to the potential energy of an electron (charge, *-e*; *e*, positive elemental charge), whereas the *LCPD* is defined as the potential energy with respect to a positive elemental charge. When the solar cell is illuminated, the quasi-Fermi levels for electrons and holes split and a photovoltage is generated across the cell. Here, KPFM can resolve the distribution of photocarriers across the cell.[3,18,58,60,65–69] To minimize topographic crosstalk, the cross sections are carefully polished with a focused ion beam (FIB) procedure prior to the measurements (SI in Appendix 8.3, Discussion 8.19 on the possible influence of FIB on KPFM).[3]

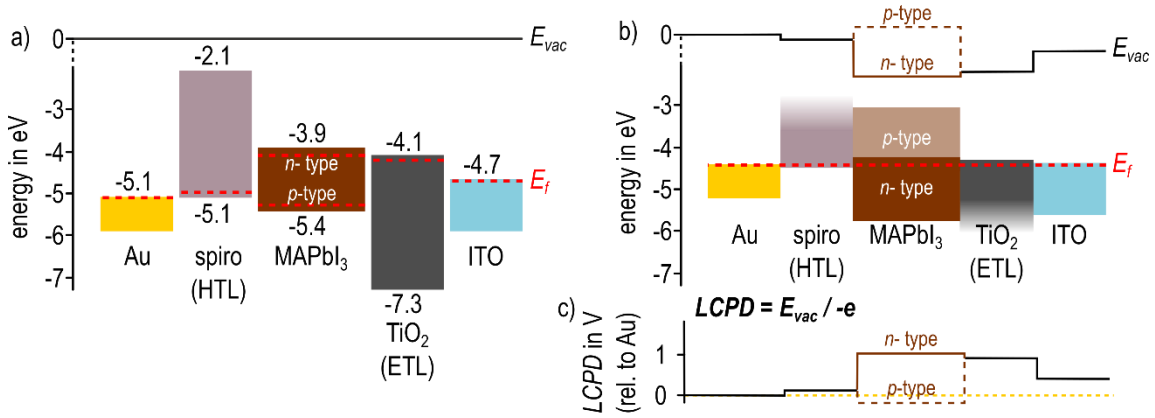

Figure 5.2: a) Energy level diagram for a PSC with a common vacuum level E_{vac} without electrical contact between the layers. b) Energy level diagram for a PSC with electrical contact between the layers, causing the alignment of the Fermi levels and shifts in the vacuum level depending on the exact value of the Fermi-level in the different layers. The effect of *p*- or *n*-type doping in the perovskite layer on E_{vac} is shown by the dashed and solid brown lines, respectively. Please note that in $MAPbI_3$, doping does not necessarily mean substitutional doping as in classic semiconductors. Instead, mobile ionic species or the stoichiometry of the perovskite can lead to a "self-doping". c) The *LCPD* as measured by KPFM on a PSC cross section corresponds to the negative vacuum level shift. Reprinted with permission from J. Phys. Chem. Lett. 2018, 9, 6249−6256. Copyright 2018 American Chemical Society.

Using cross-sectional KPFM, we compared the open- and short-circuit potential distributions in two $MAPbI_3$ PSCs with a planar TiO_2 and a C60-SAM ETL. With fullerenes assumed to passivate or bind mobile ions,[19,24,55,56] we anticipated differences in the *LCPD* distribution at the ETL interface. However, we observed the most significant *LCPD* changes within the *p*-doped spiroMeOTAD layer. We propose that the higher concentration of mobile iodide in the TiO_2 cell, as suggested by the stronger *j-V* hysteresis, led to the formation of a neutral spiroMeOTAD-iodide layer changing the resistance and capacitance of the spiroMeOTAD layer. Additionally, differences in the photopotential of the $MAPbI_3$ layer in open- and short-circuit conditions indicated an imbalance in the interfacial recombination rates rather than the extraction rates.

Results and discussion

Prior to the microscale characterization of the two PSCs with a planar TiO_2 and a C60-SAM ETL with KPFM, we observed distinct differences in the magnitude of the *j-V* hysteresis: The TiO_2 cell exhibited a strong *j-V* hysteresis with a power conversion efficiency (*PCE*) of 14.2% in reverse and 6.77% in forward scan. For the C60-SAM cell, the *j-V* hysteresis was significantly lower, with a *PCE* of 15.2% in reverse and 13.7% in forward scan (Figure 5.3). The different hysteresis strength agreed with previous observations on the same systems, which the authors attributed to an overall

reduction of mobile iodide in the C60-SAM cell.[19] While the open-circuit voltage V_{OC} and short-circuit current density j_{SC} of both cells were comparable, the lower fill factor of the TiO_2 cell suggests differences in the resistance between both cells (SI in Appendix 8.3, Table 8.20). The fill factor is more sensitive to changes in the series or shunt resistance than V_{OC} or j_{SC} (SI in Appendix 8.3, Figure 8.21).[70]

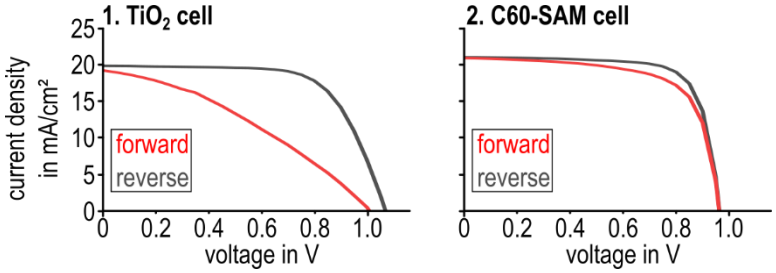

Figure 5.3: Current density-voltage characteristics of two PSCs with a TiO_2 (left) and a C60-SAM electron transport layer (right) recorded with scan rate of 0.3 V/s and 1 sun illumination. The current density measured in reverse scan direction is shown in gray, while the forward scan direction is shown in red. The cell parameters short-circuit current density j_{SC}, open-circuit voltage V_{OC}, fill factor and power conversion efficiency are given in SI in Appendix, Table 8.20. Reprinted with permission from J. Phys. Chem. Lett. 2018, 9, 6249−6256. Copyright 2018 American Chemical Society.

In subsequent KPFM measurements on the cross sections of the two PSCs, we imaged the potential in dark conditions (Figure 5.4a, b) and under white light illumination in short-circuit (both electrodes grounded, Figure 5.4c) and open-circuit conditions (Au electrode disconnected, Figure 5.4d). From the height (Figure 5.4a) and the phase signal (SI in Appendix 8.3, Figure 8.22), we identified the positions of the interfaces of each constituent layer. The semitransparent lines indicate the positions of the ETL, which were too thin to be unambiguously assigned from height or phase signal. The estimated layer thickness of the C60-SAM was a few nanometers, and the planar TiO_2 layer was between 30 and 50 nm thick. Slight distortions between the images arose from thermal drift of the sample during the measurement. In both cells, we observed a height difference of ~30 nm between the gold electrode and the $MAPbI_3$/ETL interface, which we attribute to varying sputtering rates of the materials during the polishing process. The root mean-square surface roughness of the $MAPbI_3$ layer was 7 nm in the TiO_2 cell and 4 nm in the SAM cell, thus sufficiently low to ensure crosstalk-free potential measurements. For both cells, the dark potential on the $MAPbI_3$ layer (Figure 5.4b, blue line in panel e) was higher than on the electrodes.[63] The potential difference between ITO and $MAPbI_3$ was +0.37 ± 0.05 V in the TiO_2 cell and +0.31 ± 0.02 V in the C60-SAM cell, indicating a slightly stronger *n*-doping in the TiO_2 cell (compare Figure 5.2c). Upon illuminating the samples, the distribution of photocarriers adds to the relative work function differences of the layers, allowing us to resolve the photopotential locally. In short-circuit conditions (Figure 5.4c, orange line in panel e), the potential of the $MAPbI_3$ layer increased in both cells, however, to a different extent. In the C60-SAM cell, the potential of the $MAPbI_3$ layer increased by 0.35 ± 0.05 V as compared to the TiO_2 cell, in which the potential increased by 0.18 ± 0.05 V. In open-circuit conditions (Figure 5.4d, red line in panel e), we observed an almost identical potential increase as under short circuit, with 0.38 ± 0.05 V in the C60-SAM cell and 0.20 ± 0.04 V in the TiO_2 cell, respectively. Interestingly, the dark and the illuminated potential of the $MAPbI_3$ layer were uniform, without local variations related to the position of grain boundaries. While grain boundary-related potential changes have been observed for KPFM studies on top of perovskite thin

films,[67,68] most KPFM studies on PSC cross sections did not show such a contrast, because a built-in field drives the charge carriers across the cell, superimposing surface potential changes between grains.[3,18,58,60]

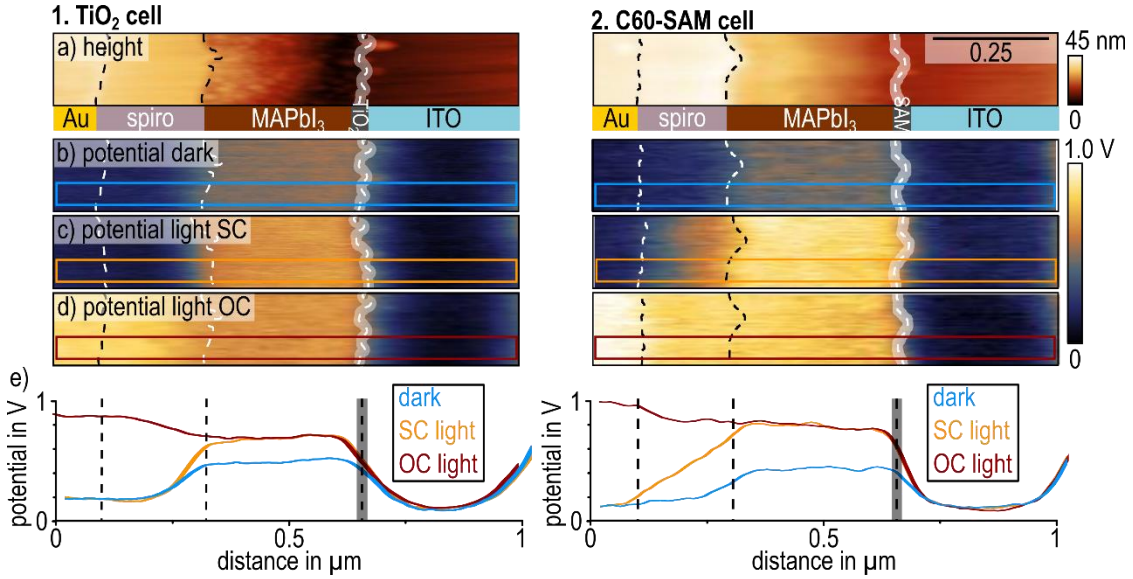

Figure 5.4: KPFM measurements on polished cross sections of two PSCs with a TiO_2 (left) and a C60-SAM electron transport layer (right). (a) Topography with assignment of layers. (b) Potential distribution without illumination. (c) Potential distribution under illumination in short circuit conditions. (d) Potential distribution under illumination in open-circuit conditions. (e) Potential profiles averaged over 15 adjacent scan lines extracted from images b, c, and d at the position of the blue, orange, and red boxes, respectively. The individual profiles are given in SI in Appendix 8.3,Figure 8.23. Reprinted with permission from J. Phys. Chem. Lett. 2018, 9, 6249−6256. Copyright 2018 American Chemical Society.

Under short-circuit conditions, the positive charge-up of the $MAPbI_3$ layer in PSCs has been observed previously. In an earlier KPFM study, we assigned the charge-up to an unbalanced charge carrier transport, in which the hole extraction through the spiroMeOTAD layer is slower than the electron extraction via the ETL.[3] Here, the spiroMeOTAD layer was nominally identical, so the electron extraction could have been more efficient in the C60-SAM cell than in the TiO_2 cell, causing a higher excess of positive photocarriers in the $MAPbI_3$ layer (Figure 5.5).[71] However, surprisingly, under open-circuit conditions, the potential of the $MAPbI_3$ layer increased by an almost identical value as under short-circuit conditions. Thus, it is probable that the positive charge-up of the $MAPbI_3$ layer has the same origin in open- and short-circuit conditions. As no charges are extracted from the cell in open-circuit conditions, extraction barriers or interfacial resistance[3] should not play a role in the open-circuit potential distribution. Instead, the positive charge-up is more likely caused by unbalanced recombination rates for electrons and holes than by different extraction rates (Figure 5.5). Because the bulk recombination of photogenerated electrons and holes in the $MAPbI_3$ will not affect the charge neutrality (Figure 5.5, white arrows), an unbalanced interfacial recombination with charge carriers from the contacts is more plausible.

Impedance spectroscopy results on comparable TiO_2 and C60-SAM PSCs indeed suggested a decrease of interfacial recombination resistance, thus increased recombination, in the TiO_2 cell, assuming a similar geometric capacitance in both cells.[19] A higher interfacial recombination in the TiO_2 cell would also manifest in different *j-V* characteristics compared to the C60-SAM cell. As such, an increase of interface recombination causes a decrease of the shunt resistance, which changes the

shape of the *j-V* curve and thus the fill factor, by lowering the current at low biases. However, the shape of the *j-V* curves (Figure 5.3) suggested that the fill factor of the TiO_2 cell was predominantly lowered by an increase of the series resistance, which can be recognized from a decreasing current density at higher biases (SI in Appendix 8.3, Figure 8.21).

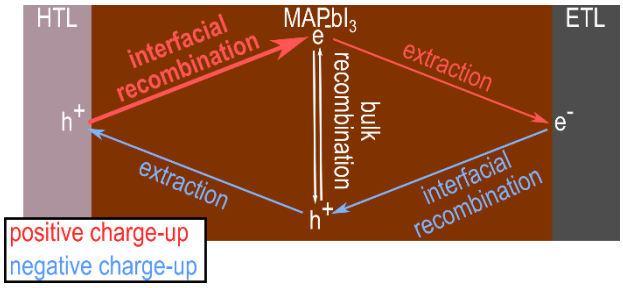

Figure 5.5: Schematic illustration of the possible origins of the light-induced charging of the $MAPbI_3$ layer. Shown in white is the bulk recombination, which does not change the net charge of the perovskite layer. Processes leading to a positive charge-up are shown in red; negative charging processes are shown in blue. The extraction of holes via the HTL and the interfacial recombination of holes with electrons at the ETL interface lead to a negative charging of the perovskite layer (blue arrows). The extraction of electrons via the ETL and the recombination of electrons with holes at the HTL interface lead to a positive charging of the perovskite layer (red arrows). We propose the interfacial recombination of electrons (in bold) at the HTL dominates for the observed positive charging of the perovskite. Reprinted with permission from J. Phys. Chem. Lett. 2018, 9, 6249−6256. Copyright 2018 American Chemical Society.

To investigate the origin of the increased series resistance, we analyzed the potential distribution in the spiroMeOTAD layer under illumination. Even though both cells used a nominally identical p-doped spiroMeOTAD layer with the same doping protocol (Experimental), we observed distinct differences: For the TiO_2 cell in short-circuit conditions, the potential sharply increased by +0.47 ± 0.05 V over ~140 nm within the spiroMeOTAD layer toward $MAPbI_3$. For the C60-SAM cell in short-circuit conditions, the potential increased linearly by +0.67 ± 0.05 V from the Au/ spiroMeOTAD interface throughout the entire ~280 nm thick spiroMeOTAD layer, resulting in a net electric field. The different potential distributions across the spiroMeOTAD suggest a change from interfacial to bulk resistance from the TiO_2 to the C60-SAM cell. Similarly, in open-circuit conditions, the potential distribution at the spiroMeOTAD/$MAPbI_3$ interface in both cells differed significantly. For the TiO_2 cell, the potential decreased by -0.15 ± 0.02 V from spiroMeOTAD to $MAPbI_3$ over ~150 nm. For the C60-SAM cell, the potential decreased by -0.12 ± 0.02 V over ~80 nm with an onset at the Au/spiroMeOTAD interface.

While the different widths of the potential increase in short-circuit conditions indicated a changed resistance of the spiroMeOTAD layer for both cells, the potential distributions in open-circuit conditions suggested a different charging behavior of the spiroMeOTAD layer and thus the overall capacitance of the cell. To understand the correlation between potential distribution and device behavior, we investigated the light-induced charge redistribution in both devices. Therefore, we subtracted the dark potential from the short- and open-circuit potential under illumination to generate the photopotential $V_{ph}(x)$ distribution (Figure 5.6, red curve). The distribution of the photocarrier density $\rho_{ph}(x)$ relates to the photopotential via its second derivative:

$$\rho_{ph}(x) = -\varepsilon_0 \varepsilon \frac{d^2}{dx^2} V_{ph}(x)$$

Equation 5.1: Photoinduced charge carrier density.

Here, ε_0 is the vacuum permittivity and ε is the relative permittivity of the material. By plotting $V_{ph}(x)$ (Figure 5.6, blue curve), we could visualize in which layers or interfaces of the device photocarriers preferably accumulate in open (Figure 5.6a) and short-circuit conditions (Figure 5.6b), respectively.[58]

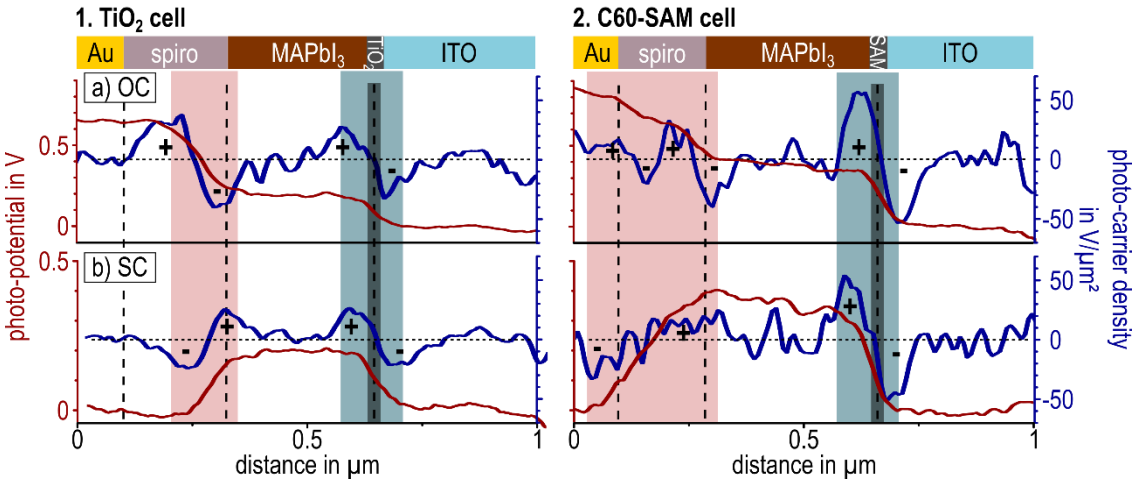

Figure 5.6: Photopotential and photocarrier density distribution in open-circuit (a) and short-circuit conditions (b) of the TiO_2 and the C60-SAM PSC in the left and right column, respectively. Data were calculated from the averaged potential profiles in Figure 5.4e. The pink and blue boxes indicate the position and width of interfacial charge layers. Positive values of the photocarrier density correspond to an accumulation of positive photocarriers at this position; negative values correspond to an accumulation of negative photocarriers. Reprinted with permission from J. Phys. Chem. Lett. 2018, 9, 6249−6256. Copyright 2018 American Chemical Society.

In open-circuit conditions, the photopotential of the TiO_2 cell decreased from the Au electrode to the ITO electrode in two distinct potential steps. The first step with an onset in the center of the spiroMeOTAD layer decreased by -0.42 ± 0.04 V over ~140 nm toward the $MAPbI_3$ layer as marked by the pink box. The charge carrier density (Figure 5.6, blue curve) revealed an accumulation of positive charges within the spiroMeOTAD layer and an accumulation of negative charges at the spiroMeOTAD/$MAPbI_3$ interface. These interfacial charge layers were shifted into the spiroMeOTAD layer by ~70 nm, with the highest density of negative charges in the spiroMeOTAD layer close to the interface. In the second potential step located at the $MAPbI_3/TiO_2$/ITO interface, the potential decreased by -0.15 ± 0.02 V over ~130 nm. Here, the arrangement of positive charges in $MAPbI_3$ and negative charges in TiO_2/ITO was located directly at the interface. The lateral shift of negative charges into the spiroMeOTAD suggests that negative charges considerably penetrated into the spiroMeOTAD layer, while the TiO_2 layer blocked positive charges efficiently at the interface. The magnitude of the shift into the spiroMeOTAD layer of 70 nm was larger than the margin of error of the spatial resolution (~20 – 30 nm). In short-circuit conditions (Figure 5.6b), the light-induced charge-up of the $MAPbI_3$ layer was visible as an accumulation of positive charges at the interfaces to both contacts. The photopotential increase at the spiroMeOTAD/$MAPbI_3$ interface in the TiO_2 cell covered a width of ~130 nm, comparable to open-circuit conditions. Here, the interfacial charge layers shifted into the spiroMeOTAD layer by around 35 nm, while the charge layers at the $MAPbI_3/TiO_2$/ITO interface were again located directly at the interface. The lateral shift of the interfacial charge layers into spiroMeOTAD under open- and short-circuit conditions

indicated that the electron-blocking interface between spiroMeOTAD and $MAPbI_3$ shifted into the spiroMeOTAD layer.

Some studies have described how *p*-doped spiroMeOTAD and mobile iodide ions accumulated at the spiroMeOTAD/$MAPbI_3$ interface can irreversibly react to a neutral spiroMeOTAD-iodide complex.[25,27,52] This reaction could give rise to the formation of a thin interfacial region, which does not exhibit the same electronic properties as the rest of the spiroMeOTAD layer and thus introduces an additional interface between the neutral and the *p*-doped spiroMeOTAD layer.

For the C60-SAM cell in open-circuit conditions, the photopotential differed significantly from the TiO_2 cell at the spiroMeOTAD/$MAPbI_3$ interface. Instead of a stepwise decay, the photopotential decreased almost linearly by -0.44 ± 0.05 V from Au to $MAPbI_3$ over ~280 nm. The accumulated positive charge had a local maximum at the Au/spiroMeOTAD interface as well as a split maximum within the spiroMeOTAD layer. While also not located directly at the interface, the charge layers shifted by only ~20 nm as compared to ~70 nm, suggesting that the penetration depth of negative charges into the spiroMeOTAD layer was reduced in the C60-SAM cell. The mechanism causing the accumulation of negative charges within the spiroMeOTAD layer therefore affected the C60-SAM cell less. Assuming a lower concentration of mobile ions in the C60-SAM cell,[19,24,55,56] the possible reaction between *p*-doped spiroMeOTAD and iodide would thus be limited as well. In short-circuit conditions (Figure 5.6b), the photopotential in the C60-SAM cell increased almost linearly from the gold electrode across the spiroMeOTAD layer to the $MAPbI_3$ layer over a total width of ~280 nm, again comparable to open-circuit conditions. The position of the highest density of positive charges was diffuse, as the maximum seemed to stretch over most of the spiroMeOTAD layer, with the negative counter charges localized at the gold electrode.

The spatial extent of the photopotential increase in short-circuit conditions can be interpreted in terms of a different type of electrical resistance of the spiroMeOTAD layer. While the sharp increase at the spiroMeOTAD/$MAPbI_3$ interface in the TiO_2 cell suggested that an interfacial potential barrier increased the interfacial resistance, the linear increase in the C60-SAM cell indicates that here, the potential barrier was comparatively low and therefore the bulk resistance of spiroMeOTAD limited the charge extraction. This observation agrees with the reduced fill factor and the shape of the *j-V* curve in the TiO_2 cell (Figure 5.3 and SI in Appendix, Table 8.20), indicating a higher series resistance of the TiO_2 cell than the C60-SAM (SI in Appendix 8.3, Figure 8.21).

The different widths of the photoinduced space charge layers at the spiroMeOTAD interface in open-circuit conditions (140 nm in the TiO_2 cell versus 280 nm in the C60-SAM cell) might also contribute to the different low-frequency capacitances of both cells. In a parallel plate capacitor, a simple model for charged interfaces in a solar cell, the capacitance is inversely proportional to the thickness of the gap between the plates. We thus suggest that the spiroMeOTAD layer contributes to the higher capacitance of the TiO_2 cell, confirming a previous study.[20] However, as reported previously,[19] the low-frequency capacitance of the TiO_2 cell was an order of magnitude higher than the low-frequency capacitance of the C60-SAM cell. We found roughly a factor of 2 between the widths of the space charge layers, corresponding to only a halving of the capacitance from the TiO_2 to the C60-SAM cell. Thus, other influences on the low-frequency capacitance were likely

dominating, such as the ionic motion and a change of the dielectric constant of the constituent layers. Zarazua *et al.* suggested that the low-frequency capacitance of PSCs originates from electronic charges accumulated at the contact interfaces and stabilized by ionic defects rather than purely from ion migration.[54] At the $MAPbI_3$/ETL interface, we found a higher charge density in the C60-SAM cell, suggesting a higher electronic capacitance. However, because the low-frequency capacitance of the C60-SAM cell was one order of magnitude smaller than that of the TiO_2 cell, we suggest that because of the lower concentration of ionic defects at the $MAPbI_3$/C60-SAM interface the stabilization of electronic charges was less efficient than in the TiO_2 cell, reducing the impact on the low-frequency capacitance.

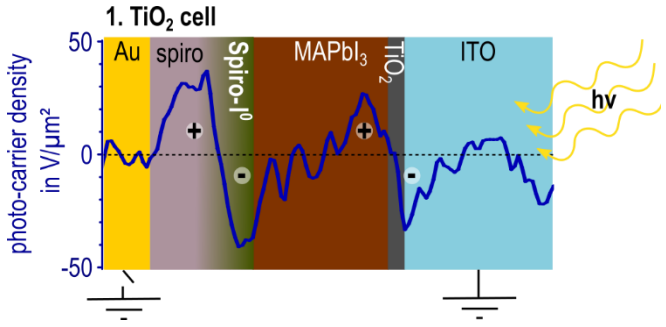

Figure 5.7: Suggested mechanism behind the shift of negative charges into the spiroMeOTAD layer in the TiO_2 cell. During device operation, mobile iodide ions penetrate into the *p*-doped spiroMeOTAD layer and react to a neutral spiroMeOTAD-iodide complex, which increases the interfacial resistance and the spiroMeOTAD/$MAPbI_3$ interface capacitance. Reprinted with permission from J. Phys. Chem. Lett. 2018, 9, 6249−6256. Copyright 2018 American Chemical Society.

As to why the spiroMeOTAD layer in both cells showed a deviating resistance and capacitance behavior, we propose spiroMeOTAD degradation by a higher density of mobile iodide ions in the TiO_2 cell (Figure 5.7). In a 300 h stability study on PSCs, Kim *et al.* observed that the photocurrent output of an encapsulated $MAPbI_3$ solar cell using spiroMeOTAD as HTL and TiO_2 as ETL continuously decreased. They linked the performance decline to an increasing resistance at the spiroMeOTAD/$MAPbI_3$ interface, suggesting an extraction barrier layer forms at this interface.[25] The instability of encapsulated cells with spiroMeOTAD HTL suggests that an internal process at the spiroMeOTAD/$MAPbI_3$ interface is responsible for the change in resistance. Another study observed an irreversible redox behavior in cycled current-voltage scans of PSCs with spiroMeOTAD as HTL and TiO_2 as ETL. They correlated the redox peak to a chemical reaction between the *p*-doped spiroMeOTAD and iodide anions resulting in the formation of a neutral spiroMeOTAD-iodide complex.[27] We propose that the different resistance and capacitance of the spiroMeOTAD layer in short- and open-circuit conditions, respectively, was caused by the irreversible formation of a neutral spiroMeOTAD-iodide layer at the spiroMeOTAD/$MAPbI_3$ interface, thus confirming the previous observations by Kim and Carrillo *et al.* (Figure 5.7).[25,27] The considerable shift of negative charges into the spiroMeOTAD layer of the TiO_2 cell in open-circuit conditions reflects how the reaction of the iodide ions with *p*-doped spiroMeOTAD creates an additional interface between the *p*-doped and neutral region within the spiroMeOTAD layer (Figure 5.6a). Furthermore, the lower fill factor (Figure 5.3) and the sharp photopotential drop at the spiroMeOTAD/$MAPbI_3$ interface (Figure 5.6a) of the TiO_2 cell illustrate the increase of the interfacial resistance by a neutral interface layer. Because we can assume from the *j*-*V* characteristics that the TiO_2 cell had a higher density of

mobile ions,[19] the neutral spiroMeOTAD-iodide layer affected the photocarrier extraction and storage more significantly than in the C60-SAM cell.

Summary

To summarize, we compared the KPFM potential distributions on cross sections of two working $MAPbI_3$ solar cells with different ETL (planar TiO_2 and C60-SAM), which differed in the magnitude of their *j-V* hysteresis: A strong hysteretic behavior was recorded for the TiO_2 cell, while the C60-SAM cell exhibited a weak hysteresis. Interestingly, we observed the most significant differences in the potential distribution at the spiroMeOTAD/$MAPbI_3$ interface, which translated into an increased interfacial resistance and capacitance for the TiO_2 cell. In the context of the previously shown suppression of ion migration in the C60-SAM cell,[19] we propose that mobile iodide ions present in the TiO_2 cell react with *p*-doped spiroMeOTAD to a neutral spiroMeOTAD-iodide complex in a thin interfacial layer between spiroMeOTAD and $MAPbI_3$ that shifts the electron-blocking interface into the spiroMeOTAD layer.[27] Hence, we conclude that the influence of the ETL material on the hole extraction needs to be considered in the device optimization.

Additionally, we observed that the light-induced positive charge-up of the $MAPbI_3$ layer had the same magnitude in open-and short-circuit conditions in both cells. This finding suggests an imbalance of the interfacial recombination at the ETL and/or the HTL interface rather than an imbalance in the carrier extraction, resulting in a surplus of positive charges within the $MAPbI_3$ layer. We suggest that the imbalance of the interfacial recombination was further increased in the C60-SAM cell because of the lower defect densities at the ETL interface.[19,24,55,56] The influence of the positive charge-up on the hysteresis, however, appeared to be negligible, considering that the SAM cell with a lower hysteresis exhibited a stronger charge-up.

Experimental

Solution Preparation. Materials and precursor solutions: Unless stated otherwise, all materials were purchased from Sigma-Aldrich and used as received. MAI and PbI_2 was purchased from Lumtec. To form a 1.4 M $MAPbI_3$ precursor solution, PbI_2 and MAI were mixed with a mole ratio of 1:1 in a mixture of DMF and DMSO (4:1 v/v).

Device Fabrication. First, the patterned ITO substrates were ultrasonically cleaned using acetone and isopropanol for 10 min each. On each cleaned ITO substrate, a dense and smooth layer of C60-SAM was deposited by dipping the ITO substrate into the C60-SAM solution for 24 h. The as-prepared perovskite precursor solution was filtered using a 0.45 μm PTFE syringe filter and coated onto substrates at a speed of 4000 rpm for 15 s. The substrate (around 2.5 cm × 2.5 cm) was quenched by blowing N_2 gas and annealed on a hot plate at 110 °C for 10 min. The doped spiroMeOTAD solution was spin-coated at 3000 rpm for 30 s. Finally, a 100 nm thick Au counter electrode was deposited onto a hole-transporting layer through a shadow mask by thermal evaporation.

SpiroMeOTAD Doping Protocol. The *p*-doped spiroMeOTAD layers were prepared with the same protocol in both cells. A spiroOMeTAD solution containing 80 mg of spiroOMeTAD, 28.5 mL of 4-tertbutylpyridine, and 17.5 mL of lithium-bis(trifluoromethanesulfonyl)imide (Li-TFSI) solution (520 mg Li-TFSI in 1 mL acetonitrile), all dissolved in 1 mL of chlorobenzene, was deposited onto

the perovskite layer via spin coating at 3000 rpm for 30 s, and the sample was then kept in a dry air box overnight.

j-V characterization. *j-V* characteristics of all the devices were measured using a source measurement unit from BoTest. Illumination was provided by a Newport Sol1A solar simulator with AM1.5G spectrum and light intensity of 100 mW cm^{-2}, which was determined by a calibrated crystalline Si-cell. During device characterization, a shadow mask with an opening of 10.4 mm^2 was used.

Cross Section Preparation. To break the solar cells so that both electrodes could be contacted during KPFM and the active layers were exposed, the samples were fixed between two glass slides and a line was scratched onto the glass side of the cells with a diamond pen. The samples were broken along this line. To minimize the surface roughness for stable KPFM imaging without topographic cross talk, the cross sections were polished with a dual beam focused ion beam (FIB; FEI NOVA60 Nanolab). In this procedure, a 45 μm long and 3.5 μm wide Pt layer was deposited onto the gold electrode parallel to the breaking edge to avoid damage of the active layers by the Ga ions of the ion beam. Here, the first step was the deposition of a 100 nm thick Pt layer via the electron beam, followed by the deposition of a 2 μm thick Pt layer via the ion beam. The protection layer was located at a distance of roughly 6 μm from the breaking edge.

To polish the cross sections, the ion beam was aligned parallel to the breaking edge and perpendicular to the Pt protection layer. The coarse polishing step was conducted with a beam current of 1 nA and acceleration voltage of 30 kV on a volume of 40 × 5 × 6 μm^3. In the final polishing step, a lower beam current of 100 pA was used on a volume of 30 × 1.5 × 6 μm^3. Following the FIB polishing, the samples were transferred into the AFM setup in less than 10 min in air.

KPFM. The KPFM measurements were performed on an Asylum Research MFP3D AFM (Oxford Instruments), which was positioned in an N_2 filled glovebox to avoid sample damage by humidity. A custom-made sample holder allowed contacting both electrodes of the solar cells while they were placed in an upright position to be illuminated from the glass side during the KPFM measurement. For illumination, a white light source (UVICO-VIS) with an illumination intensity of ~1000 W/m^2, filtered through a Schott KG 3 band-pass filter (transmission >50%, from 350 to 750 nm), was used. In short-circuit conditions, both electrodes were connected to ground. In open-circuit conditions, one of the electrodes was disconnected from ground and left floating.

KPFM was measured with conductive Pt-Ir coated cantilevers with resonance frequencies of ~70 kHz, spring constants of ~2.5 nN/nm (PPP-EFM), and scan rates of 1 Hz. For imaging, we used heterodyne KPFM,[72] which is a frequency modulation approach where the cantilever was mechanically excited on the first resonance (~70 kHz) and electrically excited (V_{AC} = 3 V) on the difference of the first and second resonances (~330 kHz). Consequently, the FM sideband coincides with the second resonance (~400 kHz), and the electrical signal is resonance-enhanced. For signal processing, we used an external Lockin amplifier HF2LI-MOD from Zürich Instruments.

For the calculation of the charge carrier density, the average of the potential was smoothed via a 7-point (10 nm per point) moving average.

Author Contributions

Y.H. prepared the perovskite solar cells and performed the *j-V* measurements under supervision of C.J.B.. I.M.H. performed the cross section preparation with the FIB and the cross sectional KPFM measurements with the support of V.W.B.. I.M.H. analyzed and interpreted the KPFM data with S.A.L.W., who supervised this project; I.M.H. wrote the manuscript under supervision of S.A.L.W. with help of C.J.B. and Y.H..; All Authors contributed to the scientific discussion and revision of the manuscript.

Associated Content

Supporting Information

The Supporting Information can be found in Appendix 8.3:

Discussion on focused ion beam treatment, cell parameters derived from *j-V* measurement in Figure 5.3, schematic of influence of shunt and series resistances on *j-V* characteristics, phase image corresponding to Figure 5.4c, and single LCPD profiles before averaging for Figure 5.4e.

Acknowledgements

I.M.H. acknowledges ERC Grant No. 340391 SuPro for funding. We thank Rüdiger Berger and Alexander Klasen for helpful discussions.

-Publication end-

5.2 Heterointerfaces – concluding remarks and outlook

In this chapter, we investigated the influence of heterointerfaces to the charge transport layers on the carrier extraction from the $MAPbI_3$ layer. Therefore, we compared the charge distribution within two PSCs that use different ETL and exhibit different magnitudes in *j-V* hysteresis. One cell featured a strong *j-V* hysteresis, which indicates a high concentration of mobile iodide ions within the $MAPbI_3$ layer.[14,16,18,73] For this cell under open circuit conditions and illumination, negative charges of the interfacial space charge layer penetrated into the organic HTL SpiroMeOTAD. Based on previous reports,[20,25,27] this shift of the space charge layer into the HTL likely originated from a reaction between mobile iodide ions and the p-doped SpiroMeOTAD. This reaction consequently lowered the conductivity of the HTL and thus impeded the hole extraction. The correlated increase in the interfacial resistance corresponds to the observed shape of the *j-V* curve, suggesting a high series resistance.

This study highlights that the choice of transport layers is a determining factor for the charge carrier extraction and therefore the generated photocurrent. For performance optimization of PSCs, extraction layers still have to be considered as crucial bottlenecks. A barrier-free carrier extraction not only requires a high conductivity but also an increase in stability of heterointerfaces with respect to mobile ions via passivation layers[9,74] or a chemically inert HTL .[25]

For future study of the chemical reactivity between transport layers and $MAPbI_3$, nano-IR measurements could provide a nanoscale visualization of the material composition particularly of organic compounds. Likewise, EDX images the presence of iodide atoms in the transport layers. Moreover, the study could be complemented by transient photocurrent and time-resolved KPFM measurements[18] to correlate the ion motion layer and infiltration into the HTL and the increase in interfacial resistance.

Bibliography

1. Grill, I. *et al.* Charge transport limitations in perovskite solar cells: the effect of charge extraction layers. *ACS Appl. Mater. Interfaces* **9**, 37655–37661 (2017).

2. Le Corre, V. M. *et al.* Charge transport layers limiting the efficiency of perovskite solar cells: how to optimize conductivity, doping, and thickness. *ACS Appl. Energy Mater.* **2**, 6280–6287 (2019).

3. Bergmann, V. W. *et al.* Real-space observation of unbalanced charge distribution inside a perovskite-sensitized solar cell. *Nat. Commun.* **5**, 1–9 (2014).

4. Valadi, K. *et al.* Metal oxide electron transport materials for perovskite solar cells: a review. *Environ. Chem. Lett.* **19**, 2185–2207 (2021).

5. Saliba, M. *et al.* How to Make over 20% Efficient Perovskite Solar Cells in Regular (n–i–p) and Inverted (p–i–n) Architectures. *Chem. Mater.* **30**, 4193–4201 (2018).

6. Miyano, K., Tripathi, N., Yanagida, M. & Shirai, Y. Lead halide perovskite photovoltaic as a model p–i–n diode. *Acc. Chem. Res.* **49**, 303–310 (2016).

7. Green, M. A., Ho-Baillie, A. & Snaith, H. J. The emergence of perovskite solar cells. *Nat. Photonics* **8**, 506–514 (2014).

8. Schulz, P. *et al.* Interface energetics in organo-metal halide perovskite-based photovoltaic cells. *Energy Environ. Sci.* **7**, 1377–1381 (2014).

9. Ye, M. *et al.* Recent advances in interfacial engineering of perovskite solar cells. *J. Phys. D. Appl. Phys.* **50**, 373002 (2017).

10. Jiménez-López, J., Cambarau, W., Cabau, L. & Palomares, E. Charge injection, carriers recombination and HOMO energy level relationship in perovskite solar cells. *Sci. Rep.* **7**, 1–10 (2017).

11. Juarez-Perez, E. J. *et al.* Role of the dopants on the morphological and transport properties of spiro-MeOTAD hole transport layer. *Chem. Mater.* **28**, 5702–5709 (2016).

12. Cheng, M. *et al.* Charge-transport layer engineering in perovskite solar cells. *Sci. Bull.* **65**, 1237–1241 (2020).

13. García-Rosell, M., Bou, A., Jiménez-Tejada, J. A., Bisquert, J. & Lopez-Varo, P. Analysis of the influence of selective contact heterojunctions on the performance of perovskite solar cells. *J. Phys. Chem. C* **122**, 13920–13925 (2018).

14. van Reenen, S., Kemerink, M. & Snaith, H. J. Modeling anomalous hysteresis in perovskite solar cells. *J. Phys. Chem. Lett.* **6**, 3808–3814 (2015).

15. Almora, O. *et al.* Capacitive dark currents, hysteresis, and electrode polarization in lead halide perovskite solar cells. *J. Phys. Chem. Lett.* **6**, 1645–1652 (2015).

16. Almora, O., Aranda, C., Zarazua, I., Guerrero, A. & Garcia-Belmonte, G. Noncapacitive hysteresis in perovskite solar cells at room temperature. *ACS Energy Lett.* **1**, 209–215 (2016).

17. Snaith, H. J. *et al.* Anomalous hysteresis in perovskite solar cells. *J. Phys. Chem. Lett.* **5**, 1511–1515 (2014).

18. Weber, S. A. L. *et al.* How the formation of interfacial charge causes hysteresis in perovskite solar cells. *Energy Environ. Sci.* **11**, (2018).

19. Hou, Y. *et al.* Suppression of hysteresis effects in organohalide perovskite solar cells. *Adv. Mater. Interfaces* **4**, 1700007 (2017).

20. Kim, H.-S. *et al.* Control of I–V hysteresis in CH3NH3PbI3 perovskite solar cell. *J. Phys. Chem. Lett.* **6**, 4633–4639 (2015).

21. Wojciechowski, K. *et al.* C60 as an efficient n-type compact layer in perovskite solar cells. *J. Phys. Chem. Lett.* **6**, 2399–2405 (2015).

22. Ravishankar, S. *et al.* Influence of charge transport layers on open-circuit voltage and hysteresis in perovskite solar cells. *Joule* **2**, 788–798 (2018).

23. Wolff, C. M., Caprioglio, P., Stolterfoht, M. & Neher, D. Nonradiative recombination in perovskite solar cells: the role of interfaces. *Adv. Mater.* **31**, 1902762 (2019).

24. Fang, Y., Bi, C., Wang, D. & Huang, J. The functions of fullerenes in hybrid perovskite solar cells. *ACS Energy Lett.* **2**, 782–794 (2017).

25. Kim, H.-S., Seo, J.-Y. & Park, N.-G. Impact of selective contacts on long-term stability of CH3NH3PbI3 perovskite solar cells. *J. Phys. Chem. C* **120**, 27840–27848 (2016).

26. Sanchez, R. S. & Mas-Marza, E. Light-induced effects on Spiro-OMeTAD films and hybrid lead halide perovskite solar cells. *Sol. Energy Mater. Sol. Cells* **158**, 189–194 (2016).

27. Carrillo, J. *et al.* Ionic reactivity at contacts and aging of methylammonium lead triiodide perovskite solar cells. *Adv. Energy Mater.* **6**, 1502246 (2016).

28. Kim, S. J., Choi, K., Lee, B., Kim, Y. & Hong, B. H. Materials for Flexible, Stretchable Electronics: Graphene and 2D Materials. *Annu. Rev. Mater. Res.* **45**, 63–84 (2015).

29. Kim, H.-S. *et al.* Lead iodide perovskite sensitized all-solid-state submicron thin film mesoscopic solar cell with efficiency exceeding 9%. *Sci. Rep.* **2**, 591 (2012).

30. Kojima, A., Teshima, K., Shirai, Y. & Miyasaka, T. Organometal halide perovskites as visible-light sensitizers for photovoltaic cells. *J. Am. Chem. Soc.* **131**, 6050–6051 (2009).

31. Yang, W. S. *et al.* High-performance photovoltaic perovskite layers fabricated through intramolecular exchange. *Science (80-.).* **348**, 1234–1237 (2015).

32. Lee, M. M., Teuscher, J., Miyasaka, T., Murakami, T. N. & Snaith, H. J. Efficient hybrid solar cells based on meso-superstructured organometal halide perovskites. *Science (80-.).* **338**, 643–647 (2012).

33. Tan, H. *et al.* Efficient and stable solution-processed planar perovskite solar cells via contact passivation. *Science (80-.).* **355**, 722–726 (2017).

34. Tress, W. *et al.* Understanding the rate-dependent J–V hysteresis, slow time component, and aging in CH 3 NH 3 PbI 3 perovskite solar cells: the role of a compensated electric field. *Energy Environ. Sci.* **8**, 995–1004 (2015).

35. Kim, H.-S. & Park, N.-G. Parameters affecting I–V hysteresis of CH3NH3PbI3 perovskite solar cells: effects of perovskite crystal size and mesoporous TiO2 layer. *J. Phys. Chem. Lett.* **5**, 2927–2934 (2014).

36. Unger, E. L. *et al.* Hysteresis and transient behavior in current–voltage measurements of hybrid-perovskite absorber solar cells. *Energy Environ. Sci.* **7**, 3690–3698 (2014).

37. Sanchez, R. S. *et al.* Slow dynamic processes in lead halide perovskite solar cells. Characteristic times and hysteresis. *J. Phys. Chem. Lett.* **5**, 2357–2363 (2014).

38. O'Regan, B. C. *et al.* Optoelectronic studies of methylammonium lead iodide perovskite solar cells with mesoporous TiO2: separation of electronic and chemical charge storage, understanding two recombination lifetimes, and the evolution of band offsets during J–V hysteresis. *J. Am. Chem. Soc.* **137**, 5087–5099 (2015).

39. Azpiroz, J. M., Mosconi, E., Bisquert, J. & De Angelis, F. Defect migration in methylammonium lead iodide and its role in perovskite solar cell operation. *Energy Environ. Sci.* **8**, 2118–2127 (2015).

40. Belisle, R. A. *et al.* Interpretation of inverted photocurrent transients in organic lead halide perovskite solar cells: proof of the field screening by mobile ions and determination of the space charge layer widths. *Energy Environ. Sci.* **10**, 192–204 (2017).

41. Richardson, G. *et al.* Can slow-moving ions explain hysteresis in the current–voltage curves of perovskite solar cells? *Energy Environ. Sci.* **9**, 1476–1485 (2016).

42. Eames, C. *et al.* Ionic transport in hybrid lead iodide perovskite solar cells. *Nat. Commun.* **6**, 1–8 (2015).

43. Frost, J. M. & Walsh, A. What is moving in hybrid halide perovskite solar cells? *Acc. Chem. Res.* **49**, 528–535 (2016).

44. Li, C. *et al.* Iodine migration and its effect on hysteresis in perovskite solar cells. *Adv. Mater.* **28**, 2446–2454 (2016).

45. Yang, T., Gregori, G., Pellet, N., Grätzel, M. & Maier, J. The significance of ion conduction

in a hybrid organic–inorganic lead-iodide-based perovskite photosensitizer. *Angew. Chemie Int. Ed.* **54**, 7905–7910 (2015).

46. Delugas, P., Caddeo, C., Filippetti, A. & Mattoni, A. Thermally activated point defect diffusion in methylammonium lead trihalide: anisotropic and ultrahigh mobility of iodine. *J. Phys. Chem. Lett.* **7**, 2356–2361 (2016).

47. Levine, I. *et al.* Interface-dependent ion migration/accumulation controls hysteresis in MAPbI3 solar cells. *J. Phys. Chem. C* **120**, 16399–16411 (2016).

48. Yuan, Y. & Huang, J. Ion migration in organometal trihalide perovskite and its impact on photovoltaic efficiency and stability. *Acc. Chem. Res.* **49**, 286–293 (2016).

49. Lopez-Varo, P. *et al.* Effects of ion distributions on charge collection in perovskite solar cells. *ACS Energy Lett.* **2**, 1450–1453 (2017).

50. Sherkar, T. S. *et al.* Recombination in perovskite solar cells: significance of grain boundaries, interface traps, and defect ions. *ACS energy Lett.* **2**, 1214–1222 (2017).

51. Zhao, Y. *et al.* Mobile-ion-induced degradation of organic hole-selective layers in perovskite solar cells. *J. Phys. Chem. C* **121**, 14517–14523 (2017).

52. Kim, S. *et al.* Relationship between ion migration and interfacial degradation of CH 3 NH 3 PbI 3 perovskite solar cells under thermal conditions. *Sci. Rep.* **7**, 1–9 (2017).

53. Peng, W. *et al.* Quantification of ionic diffusion in lead halide perovskite single crystals. *ACS Energy Lett.* **3**, 1477–1481 (2018).

54. Zarazua, I., Bisquert, J. & Garcia-Belmonte, G. Light-induced space-charge accumulation zone as photovoltaic mechanism in perovskite solar cells. *J. Phys. Chem. Lett.* **7**, 525–528 (2016).

55. Shao, Y., Xiao, Z., Bi, C., Yuan, Y. & Huang, J. Origin and elimination of photocurrent hysteresis by fullerene passivation in CH3NH3PbI3 planar heterojunction solar cells. *Nat. Commun.* **5**, 1–7 (2014).

56. Hou, Y. *et al.* Low-temperature and hysteresis-free electron-transporting layers for efficient, regular, and planar structure perovskite solar cells. *Adv. Energy Mater.* **5**, 1501056 (2015).

57. Xu, J. *et al.* Perovskite–fullerene hybrid materials suppress hysteresis in planar diodes. *Nat. Commun.* **6**, 1–8 (2015).

58. Bergmann, V. W. *et al.* Local Time-Dependent Charging in a Perovskite Solar Cell. *ACS Appl. Mater. Interfaces* **8**, (2016).

59. Guerrero, A., Juarez-Perez, E. J., Bisquert, J., Mora-Sero, I. & Garcia-Belmonte, G. Electrical field profile and doping in planar lead halide perovskite solar cells. *Appl. Phys. Lett.* **105**, 133902 (2014).

60. Cai, M. *et al.* Control of electrical potential distribution for high-performance perovskite

solar cells. *Joule* **2**, 296–306 (2018).

61. Lan, F., Jiang, M., Tao, Q. & Li, G. Revealing the working mechanisms of planar perovskite solar cells with cross-sectional surface potential profiling. *IEEE J. Photovoltaics* **8**, 125–131 (2017).

62. Dymshits, A., Henning, A., Segev, G., Rosenwaks, Y. & Etgar, L. The electronic structure of metal oxide/organo metal halide perovskite junctions in perovskite based solar cells. *Sci. Rep.* **5**, 1–6 (2015).

63. Melitz, W., Shen, J., Kummel, A. C. & Lee, S. Kelvin probe force microscopy and its application. *Surf. Sci. Rep.* **66**, 1–27 (2011).

64. Nonnenmacher, M., o'Boyle, M. P. & Wickramasinghe, H. K. Kelvin probe force microscopy. *Appl. Phys. Lett.* **58**, 2921–2923 (1991).

65. Berger, R., Domanski, A. L. & Weber, S. A. L. Electrical characterization of organic solar cell materials based on scanning force microscopy. *Eur. Polym. J.* **49**, 1907–1915 (2013).

66. Jiang, C.-S. *et al.* Carrier separation and transport in perovskite solar cells studied by nanometre-scale profiling of electrical potential. *Nat. Commun.* **6**, 1–10 (2015).

67. Collins, L. *et al.* Breaking the time barrier in Kelvin probe force microscopy: fast free force reconstruction using the G-Mode platform. *ACS Nano* **11**, 8717–8729 (2017).

68. Garrett, J. L. *et al.* Real-time nanoscale open-circuit voltage dynamics of perovskite solar cells. *Nano Lett.* **17**, 2554–2560 (2017).

69. Panigrahi, S. *et al.* Imaging the anomalous charge distribution inside CsPbBr3 perovskite quantum dots sensitized solar cells. *ACS Nano* **11**, 10214–10221 (2017).

70. Nelson, J. A. *The physics of solar cells*. (World Scientific Publishing Company, 2003).

71. Will, J. *et al.* Evidence of Tailoring the Interfacial Chemical Composition in Normal Structure Hybrid Organohalide Perovskites by a Self-Assembled Monolayer. *ACS Appl. Mater. Interfaces* **10**, (2018).

72. Garrett, J. L. & Munday, J. N. Fast, high-resolution surface potential measurements in air with heterodyne Kelvin probe force microscopy. *Nanotechnology* **27**, 245705 (2016).

73. Meloni, S. *et al.* Ionic polarization-induced current–voltage hysteresis in CH 3 NH 3 PbX 3 perovskite solar cells. *Nat. Commun.* **7**, 1–9 (2016).

74. Moriya, M. *et al.* Architecture of the Interface between the Perovskite and Hole-Transport Layers in Perovskite Solar Cells. *ChemSusChem* **9**, 2634–2639 (2016).

6 Conclusion and outlook

In this work, I explored the influence of boundary structures on different length scales on the charge carrier transport in $MAPbI_3$ single crystals, thin films and full PSCs. The studied boundary structures include subcrystalline ferroelastic domain walls, grain boundaries and heterointerfaces to the charge extraction layers. My investigations revealed that all of these interfacial structures can affect the carrier transport in different ways: Domain walls appeared to control the directionality of the charge carrier diffusion, unpassivated grain boundaries introduced a substantial series resistance and the charge carrier transport across heterointerfaces displayed a distinct dependence on the concentration of mobile ions and the chemical stability of the extraction layer. For future optimization of $MAPbI_3$-based solar cells and other optoelectronic devices, such as light-emitting diodes or photodetectors, these findings can directly be applied to facilitate a barrier-free charge carrier transport.

As I have shown in Chapter 3, subcrystalline twin domains form during $MAPbI_3$'s ferroelastic cubic-tetragonal phase transition to release internal strain (Chapter 3.1.1).[1] The crystallographic anomalies at the position of the domain walls can introduce a localized flexoelectric polarization or energetic barriers.[2,3] Both of these phenomena explain the observed anisotropy in the charge carrier diffusion (Chapter 3.2.2) by accelerating the diffusion parallel to the domain walls or the delaying the diffusion perpendicular to the domain walls, respectively.[4] The consequent directionality in the charge carrier transport can be exploited for PSC optimization. For example, with bulk domains oriented 90° to the (110) surface layer (Chapter 3.1.2), the charge extraction on $MAPbI_3$ films with (110) texture should be more efficient than for non-textured films.[5] Moreover, the ferroelastic nature of the domains allows tailoring domain patterns or reducing the domain density as required by mechanical stress or heat (Chapter 3.1.3); thus, the functional properties of the subcrystalline domains can directly be controlled via strain engineering.

The exact mechanism of the domain wall influence on the charge carriers should be studied in detail in the future. Particularly, the acceleration of charge carriers due to the local flexoelectric polarization bear great potential – not only for $MAPbI_3$-based optoelectronics but also for other functional ferroelastic materials. To determine which of the two mechanisms governs, future investigations via pump-probe time-resolved KPFM could aid to distinguish preferential charge pathways. Moreover, by reducing the domain walls density via the application of stress, an in-situ, correlative PFM and PL study could directly link the amount of domain walls to a rise or drop in diffusivity. Particularly, the recent success of flexible PSCs, now reaching *PCE*s of ~20%[6] requires a systematic analysis, of how a change in the strain state will affect the domains and the charge carrier diffusion in the $MAPbI_3$ layer. Furthermore, an extension of the research to charge carrier drift, using spatial and time-resolved PL microscopy under the application of an external field, could provide a wholistic understanding of how domain walls affect the charge carrier transport in ferroelastic solar cell absorbers.

As shown in Chapter 4.1, grain boundaries feature a largely adverse effect on the carrier dynamics in polycrystalline $MAPbI_3$. Particularly in measurements of the drift current across several connected grains, I observed that grain boundaries impose a substantial series resistance in

the range of several giga-Ohms (Chapter 4.1.1). These large resistance values suggest that future devices will benefit from an overall reduction in the grain boundary density by increasing the grain sizes to match the layer thickness of the absorber layer.[7] Moreover, both the inter-grain drift and the inter-grain diffusion showed a dependence of the carrier transport on the grain boundary morphology, including the presence of gaps between adjacent grains and likely the crystallinity at the boundary: Large gaps and potentially amorphous material at grain boundaries limited the carrier transport (Chapters 4.1.1 and 4.1.2).

A future study on the impact of passivation strategies on the grain boundary resistance and diffusion transparency could further illuminate the role of morphological anomalies on the inter-grain carrier transport.[8,9] Moreover, high resolution TEM could aid to reveal a possible presence of amorphous material in grain boundaries and thereby allow evaluating the effect of crystallinity on the charge dynamics in polycrystalline films. The influence of possible facet-dependence on the inter-grain carrier transport[10] could be investigated by introducing an in-plane texture using epitaxial film growth on a suitable substrate prior to CAFM or PL characterization.

Additional to the inter-grain carrier transport, I explored the influence of grain boundaries on confined photons (Chapter 4.2), which can add understanding on efficient photon management in PSCs to push their *PCE* towards the radiative limit.[11] Here, those boundaries with large contact area and no gaps reduced the light outcoupling from the $MAPbI_3$ grains. Minimized outcoupling is important to increase the reabsorption probability via photon recycling. Hence, for PSCs, large grains with low density of grain boundaries as possible scattering centers are likely to facilitate loss-free light propagation. In future studies on the photon transfer, a spectral analysis of the PL signal will help to identify energetic losses caused by inelastic scattering in bulk grains or at grain boundaries. These energetic losses reduce the reabsorption probability.

Finally, the impact of heterointerfaces on the charge extraction was focus of Chapter 5.1. Here, I found that transport layers affect the charge carrier extraction in PSCs in dependence of the mobile ion concentration.[12] In a device with an apparently high concentration of mobile ions, results suggest a penetration of mobile ions into the organic HTL. Here, the ions lower the p-doping of the HTL,[13,14] which leads to a consequent increase in interfacial resistance. Since this degradation of the HTL introduces an additional bottleneck for the charge carrier extraction, the stabilization of transport layers with respect to mobile ions is crucial for PSC optimization.

Cross-sectional nano-IR AFM could provide further insights on the possible reaction between the HTL and mobile ions in the $MAPbI_3$ absorber. Nano-IR AFM can image local changes in the chemical composition in real space with nanometer resolution and thus may be able to resolve the interfacial degradation of SpiroOMeTAD. As demonstrated previously,[15] time-resolved KPFM can additionally be employed to image the ion drift across the $MAPbI_3$ layer and thereby capture the diffusion into the HTL. Moreover, the correlation of KPFM data with simultaneous transient photo-current measurements could directly capture the degradation of the HTL an increase in the series resistance of the solar cell. Finally, with the successful application of PSCs in Si tandems,[16] the influence of heterointerfaces on the carrier extraction will become even more important. Hence, an extension of the research to cross sections of tandem solar cells will add to the targeted interface optimization for highly efficient tandems.

1 I. M. Hermes, S. A. Bretschneider, V. W. Bergmann, D. Li, A. Klasen, J. Mars, W. Tremel, F. Laquai, H.-J. Butt, M. Mezger, R. Berger, B. J. Rodriguez and S. A. L. Weber, *J. Phys. Chem. C.*

2 A. R. Warwick, J. Íñiguez, P. D. Haynes and N. C. Bristowe, *J. Phys. Chem. Lett.*, 2019, **10**, 1416–1421.

3 E. K. H. Salje, *Annu. Rev. Mater. Res.*, 2012, **42**, 265–283.

4 I. M. Hermes, A. Best, L. Winkelmann, J. Mars, S. M. Vorpahl, M. Mezger, L. Collins, H.-J. Butt, D. S. Ginger, K. Koynov and S. A. L. Weber, *Energy Environ. Sci.*, 2020, **13**, 4168–4177.

5 P. Docampo, F. C. Hanusch, N. Giesbrecht, P. Angloher, A. Ivanova and T. Bein, *Apl Mater.*, 2014, **2**, 81508.

6 J. Chung, S. S. Shin, K. Hwang, G. Kim, K. W. Kim, D. S. Lee, W. Kim, B. S. Ma, Y.-K. Kim, T.-S. Kim and J. Seo, *Energy Environ. Sci.*, 2020, **13**, 4854–4861.

7 H. Do Kim, H. Ohkita, H. Benten and S. Ito, *Adv. Mater.*, 2016, **28**, 917–922.

8 D. W. DeQuilettes, S. Jariwala, S. Burke, M. E. Ziffer, J. T.-W. Wang, H. J. Snaith and D. S. Ginger, *ACS Nano*, 2017, **11**, 11488–11496.

9 D. W. de Quilettes, S. M. Vorpahl, S. D. Stranks, H. Nagaoka, G. E. Eperon, M. E. Ziffer, H. J. Snaith and D. S. Ginger, *Science (80-.).*, 2015, **348**, 683–686.

10 S. Y. Leblebici, L. Leppert, Y. Li, S. E. Reyes-Lillo, S. Wickenburg, E. Wong, J. Lee, M. Melli, D. Ziegler and D. K. Angell, *Nat. Energy*, 2016, **1**, 1–7.

11 T. Kirchartz, 2019.

12 I. M. Hermes, Y. Hou, V. W. Bergmann, C. J. Brabec and S. A. L. Weber, *J. Phys. Chem. Lett.*, , DOI:10.1021/acs.jpclett.8b02824.

13 J. Carrillo, A. Guerrero, S. Rahimnejad, O. Almora, I. Zarazua, E. Mas-Marza, J. Bisquert and G. Garcia-Belmonte, *Adv. Energy Mater.*, 2016, **6**, 1502246.

14 H.-S. Kim, J.-Y. Seo and N.-G. Park, *J. Phys. Chem. C*, 2016, **120**, 27840–27848.

15 S. A. L. Weber, I. M. Hermes, S.-H. Turren-Cruz, C. Gort, V. W. Bergmann, L. Gilson, A. Hagfeldt, M. Graetzel, W. Tress and R. Berger, *Energy Environ. Sci.*, , DOI:10.1039/c8ee01447g.

16 M. Jošt, L. Kegelmann, L. Korte and S. Albrecht, *Adv. Energy Mater.*, 2020, **10**, 1904102.

7 Acknowledgements

8 Appendix

8.1 Supporting information: Ferroelastic fingerprints in methylammonium lead iodide perovskite

Ilka M. Hermes,† Simon A. Bretschneider,† Victor W. Bergmann,† Dan Li,† Alexander Klasen,†,‡ Julian Mars,†,∥ Wolfgang Tremel,‡ Fredéric Laquai,†,§ Hans-Jürgen Butt,† Markus Mezger,†,∥ Rüdiger Berger,† Brian J. Rodriguez,⊥ and Stefan A. L. Weber†,∥

† Max Planck Institute for Polymer Research, Ackermannweg 10, 55128 Mainz, Germany

‡ Institute of Inorganic Chemistry and Analytical Chemistry, Johannes Gutenberg University Mainz, Duesbergweg 10-14, 55128 Mainz, Germany

§ Solar and Photovoltaics Engineering Research Center (SPERC), King Abdullah University of Science and Technology (KAUST), Thuwal, Kingdom of Saudi Arabia

∥ Institute of Physics, Johannes Gutenberg University Mainz, Staudingerweg 10, 55128 Mainz, Germany

⊥ School of Physics and Conway Institute of Biomolecular and Biomedical Research, University College Dublin, Belfield, Dublin 4, Ireland

Published in the Journal of Physical Chemistry C (J. Phys. Chem. C) 2016, 120, 5724–5731, https://doi.org/10.1021/acs.jpcc.5b11469

Figure 8.1

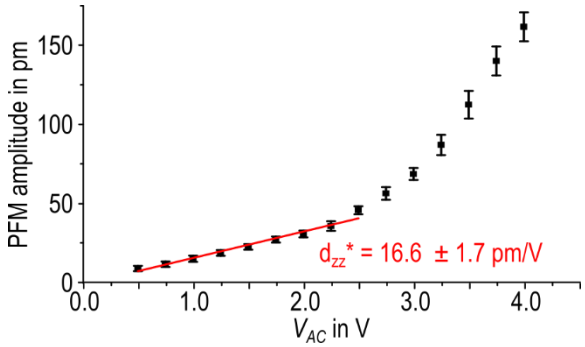

Figure 8.1: Vertical piezoresponse amplitude on $MAPbI_3$ film in dependence of externally applied AC voltage at f_{Drive}=300 kHz (scan angle = 0°). The linear fit (red line) was applied until 2.5 V AC voltage and exhibited slope of 16.6 ± 1.7 pm/V corresponding to the resonance enhanced piezoelectric coefficient d_{zz}*. Reprinted with permission from J. Phys. Chem. C 2016, 120, 10, 5724–5731. Copyright 2016 American Chemical Society.

The vertical piezoresponse amplitude was measured as a function of the applied AC voltage on a domain oriented in a 115° angle with respect to the cantilever. Up until an AC voltage of 2.5 V the response is linear with a slope of 16.6 ± 1.7 pm/V. AC voltages higher than 3 V caused damages of the sample surface. With 16.6 ± 1.7 pm/V the piezoelectric coefficient d_{zz}* measured here is higher than the previously reported value of 5 pm/V. But as we measured at 300 kHz, close to the contact

resonance frequency of 315 kHz, it is likely that the piezoresponse is further enhanced by the resonance.

Figure 8.2

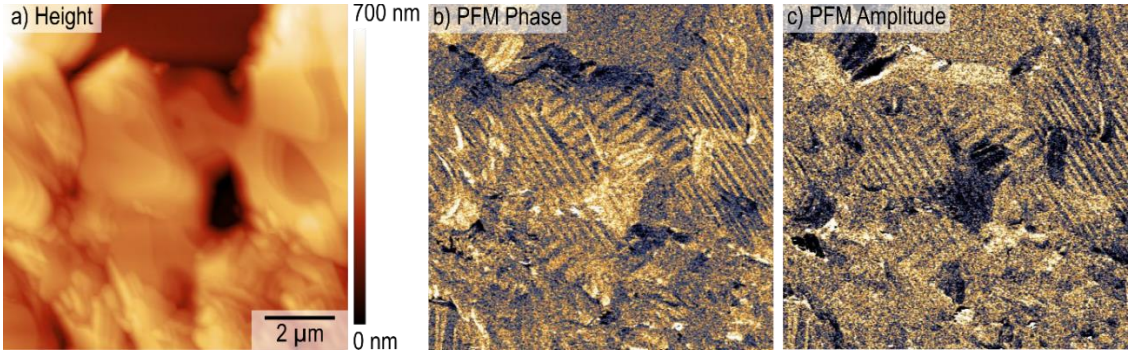

Figure 8.2: Lateral PFM measurement on $MAPbI_3$ film on ITO without PEDOT:PSS (a) Topography, (b) PFM phase, (c) PFM amplitude (V_{AC} = 2.5 V; f_{Drive} = 600 kHz). Reprinted with permission from J. Phys. Chem. C 2016, 120, 10, 5724–5731. Copyright 2016 American Chemical Society.

The lateral piezoresponse was measured on a $MAPbI_3$ film prepared without the PEDOT:PSS layer directly on ITO to get information in the influence of the substrate on the twin domain formation. On the grains that crystallized directly on ITO we observed the same periodic pattern in the piezoresponse as on grains that crystallized on PEDOT:PSS.

Figure 8.3

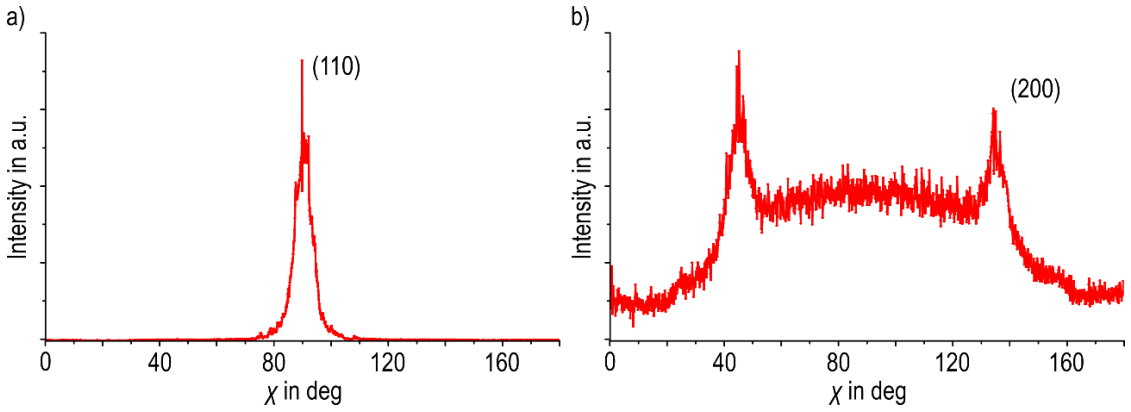

Figure 8.3: Intensity distributions of a) the (110) and b) the (200) Bragg reflections of $MAPbI_3$ vs. the azimuthal angle χ. Reprinted with permission from J. Phys. Chem. C 2016, 120, 10, 5724–5731. Copyright 2016 American Chemical Society.

The intensity distribution of the (110) Bragg reflection shows an intensity maximum at $\chi = 90°$ i.e., close to the specular condition. For the (200) reflection two intensity maxima at $\chi = 90° \pm 45°$. These results suggest that the (110) crystal planes of the $MAPbI_3$ are preferentially orientated parallel to the surface.

Figure 8.4

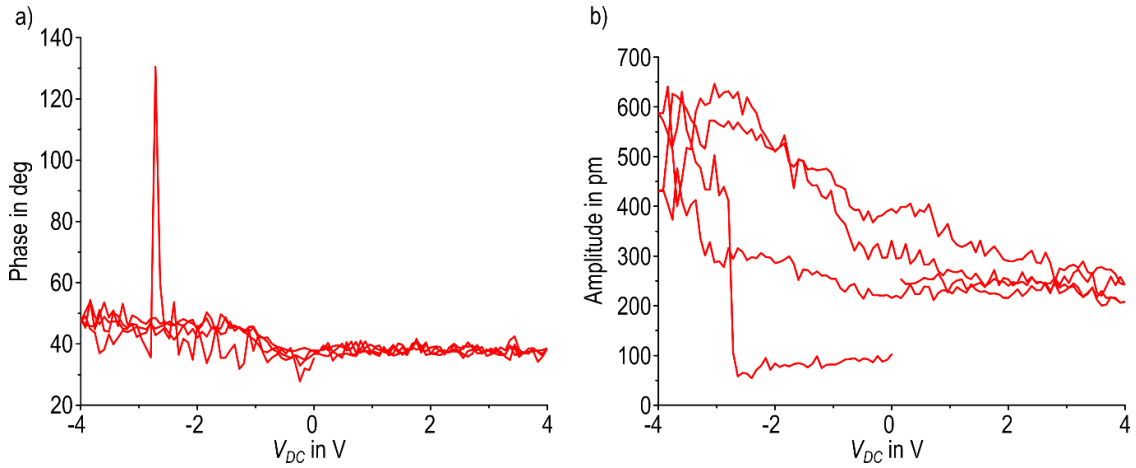

Figure 8.4: Ferroelectric switching experiment on $MAPbI_3$ film with a scan rate of 0.8 V/s. a) PFM phase and b) PFM amplitude in dependence of the applied DC voltage. Reprinted with permission from J. Phys. Chem. C 2016, 120, 10, 5724–5731. Copyright 2016 American Chemical Society.

The ferroelectric switching experiments on the $MAPbI_3$ films were performed with a scan rate of 0.8 V/s. We did not observe a ferroelectric switching event in the PFM phase. The absence of a ferroelectric hysteresis loop in the PFM phase indicates the absence of out-of-plane switchable polarization in the (110) plane of the $MAPbI_3$ grains.

Figure 8.5

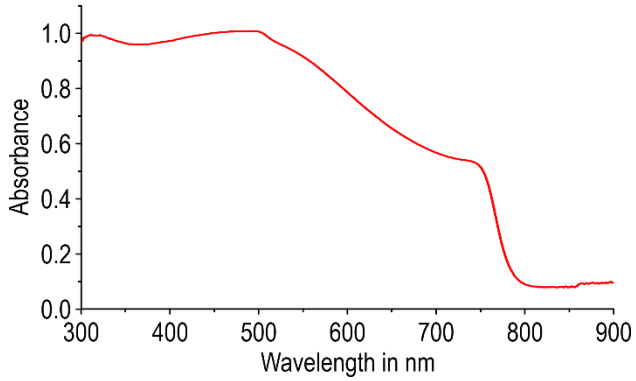

Figure 8.5: UV-vis absorption spectra of $MAPbI_3$ film. Reprinted with permission from J. Phys. Chem. C 2016, 120, 10, 5724–5731. Copyright 2016 American Chemical Society.

Figure 8.5 shows the UV-vis absorption spectra of the perovskite film. The broad absorption of the film covers the visible spectrum with an absorption onset at 800 nm and a peak at 750 nm characteristic for $MAPbI_3$. An additional peak at around 500 nm is probably caused by the presence of crystalline lead iodide, which was also observed in the XRD measurement in Chapter 3.1.1 Figure 3.4.

8.2 Supporting information: Anisotropic charge carrier diffusion in single $MAPbI_3$ grains correlates to their twin domains

Ilka M. Hermes,[a, *] Andreas Best,[a] Leonard Winkelmann,[a,c] Julian Mars,[a] Sarah M. Vorpahl,[b] Markus Mezger,[a, c] Liam Collins,[d] Hans-Jürgen Butt,[a] David S. Ginger,[b] Kaloian Koynov[a] and Stefan A. L. Weber[a, c, *]

[a] *Max Planck Institute for Polymer Research, Ackermannweg 10, 55128 Mainz, Germany.*

[b] *Department of Chemistry, University of Washington, Seattle, Washington 98105, United States.*

[c] *Institute of Physics, Johannes Gutenberg University Mainz, Duesbergweg 10-14, 55128 Mainz, Germany*

[d] *Center for Nanophase Materials Sciences, Oak Ridge National Laboratory, 1 Bethel Valley Rd., Oak Ridge, Tennessee 37830, USA*

Published in Energy & Environmental Science (Energy Environ. Sci.) 2020, 13, 4168-4177 https://doi.org/10.1039/D0EE01016B

Figure 8.6

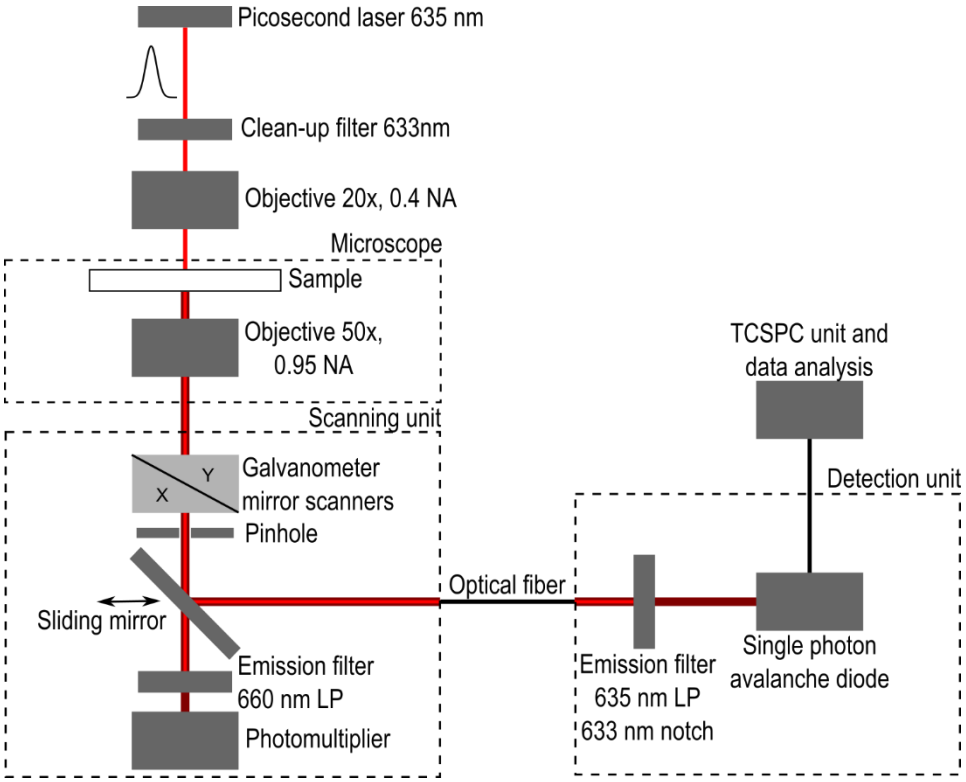

Figure 8.6: Beam path schematic of the spatial- and time-resolved PL setup with the optical excitation with a picosecond laser from the top and the detection of the PL emission in transmission either by a photomultiplier for the static PL distribution, scanned by XY galvanometer-mirrors, or by a detection unit from PicoQuant with a τ-SPAD avalanche diode followed by TCSPC unit. The experimental setup is described in depth in the methods section. Reprinted with permission from Energy Environ. Sci., 2020, Advance Article. - Published by The Royal Society of Chemistry.

Calculation 8.7

For the calculation of the approximate initial carrier density, we measured the average laser power for each of the experimental settings to calculate the respective fluence (energy density) given in the table below.

To calculate the initial carrier density N_0 from the fluence we used the following equation according to Richter *et al.*[1]

$$N_0 = \frac{fluence * a}{E_{ph} * t}$$

With an absorbtance a~0.5, a photon energy E_{ph}= 3.14 *10^{-19} J and a thickness t of ~1000 nm. The penetration depth was around 400 nm.[2]

Average power Repetition rate: 2 MHz	Pulse energy	Energy density	Carrier density
23.6 nW	11.8 fJ	0.772 µJ/cm²	1.23 * 10^{16} 1/cm³
26.6 nW	13.3 fJ	0.870 µJ/cm²	1.39 * 10^{16} 1/cm³
27.3 nW	13.7 fJ	0.893 µJ/cm²	1.43 * 10^{16} 1/cm³
28.6 nW	14.3 fJ	0.936 µJ/cm²	1.49 * 10^{16}1/cm³
Average power Repetition rate: 20 MHz	**Pulse energy**	**Energy density**	**Carrier density**
214 nW	10.7 fJ	0.7oo µJ/cm²	1.12 * 10^{16} 1/cm³
254 nW	12.7 fJ	0.831 µJ/cm²	1.33 * 10^{16} 1/cm³
260 nW	13.0 fJ	0.851 µJ/cm²	1.36 * 10^{16} 1/cm³
267 nW	13.3 fJ	0.874 µJ/cm²	1.40 * 10^{16}1/cm³

Figure 8.8

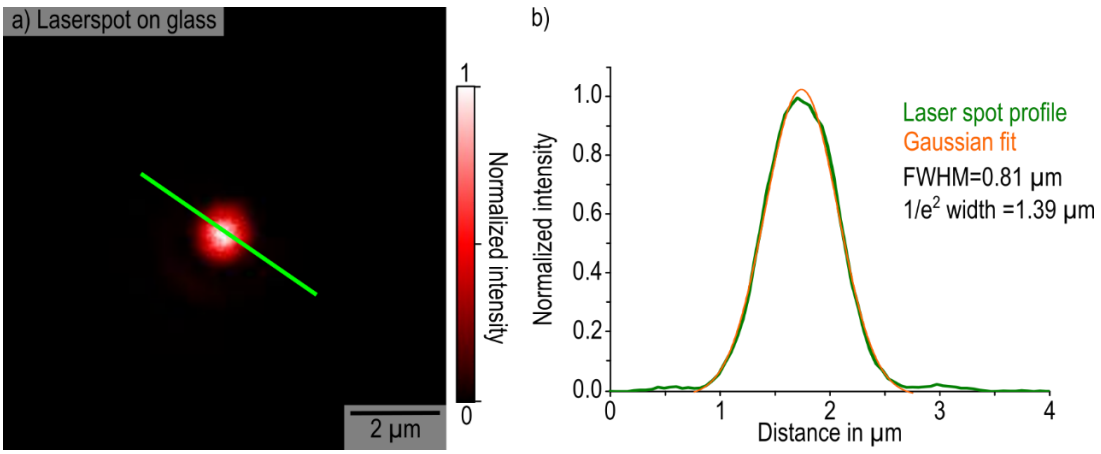

Figure 8.8: Diameter of the excitation spot measured on glass in transmission with the galvanometer mirror scanners without the 660 nm LP emission filter (excitation fluence of 0.77 µJ/cm², repetition rate of 2 MHz, pinhole 60 µm - comparable to the excitation during the time-resolved PL measurements). The intensity profile in b) was extracted at the

positions of the green line in a) and fitted with a Gaussian function to determine the spot diameter at FWHM. Reprinted with permission from Energy Environ. Sci., 2020, Advance Article. - Published by The Royal Society of Chemistry.

The diameter of the laser spot at full width half-maximum (FWHM) was determined by focusing the excitation spot onto the glass substrate next to the characterized $MAPbI_3$ grain with the same excitation parameters used during the time-resolved PL measurements. We fitted the intensity profile extracted at the position of the green line in Figure 8.8a with a Gaussian peak function and found a beam diameter of 0.81 µm at FWHM (Figure 8.8b).

Figure 8.9

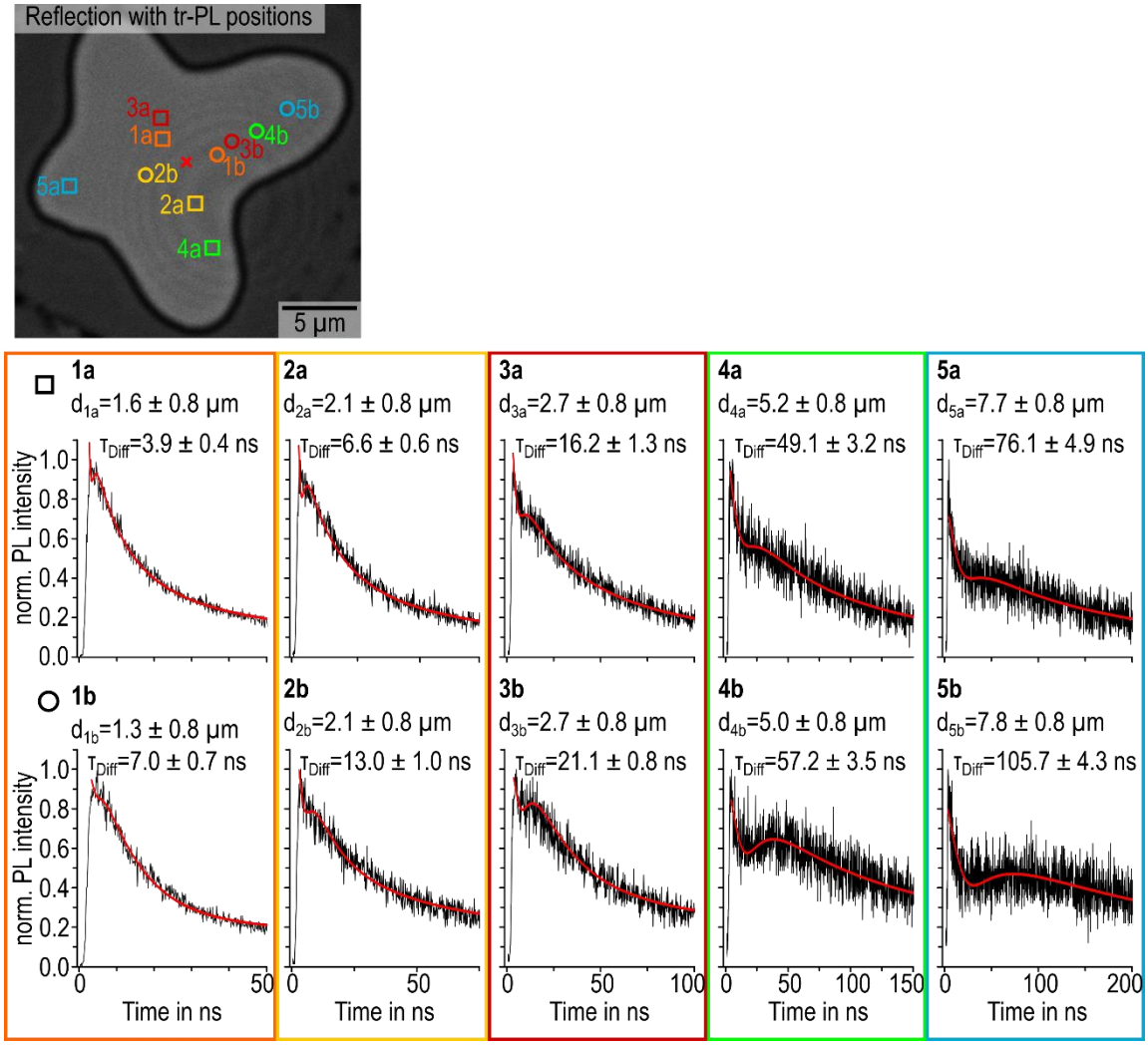

Figure 8.9: Additional time-resolved PL decays measured in various distances from the excitation spot detected along different directions of the grain marked in the PL reflection image by the colored squares and circles. Each color represents two detection positions at comparable distances, with the squares (a) marking the direction of shorter diffusion times and the circles (b) marking the direction of longer diffusion times. The red lines in b-d represent the corresponding fits according to Equation 3.1 in Chapter 3.2.2. Please note that the scales of the time-axis were changed to increase the comprehensibility of the shift of the diffusion peak. Excitation with 633 nm wavelength, a fluence of 0.77 µJ/cm², a repetition rate of 2 MHz and 0.81 µm beam diameter (Figure 8.8). Reprinted with permission from Energy Environ. Sci., 2020, Advance Article. - Published by The Royal Society of Chemistry.

The additional time-resolved PL decays in Figure 8.9 detected at two comparable distances from the excitation position, each, visualize the anisotropy of the diffusion time τ_{Diff}. These decay curves are consistent with the findings presented in the main manuscript.

Figure 8.10

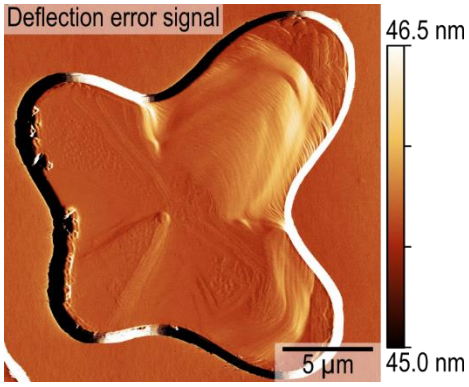

Figure 8.10: Deflection error signal of PFM measurement shown in Figure 3.21 in Chapter 3.2.2 in the main manuscript. Reprinted with permission from Energy Environ. Sci., 2020, Advance Article. - Published by The Royal Society of Chemistry.

The deflection error signal in Figure 8.10 corresponding to the lateral PFM measurement Figure 3.21 in Chapter 3.2.2 shows the defined terrace steps indicating a high crystallinity.

Figure 8.11

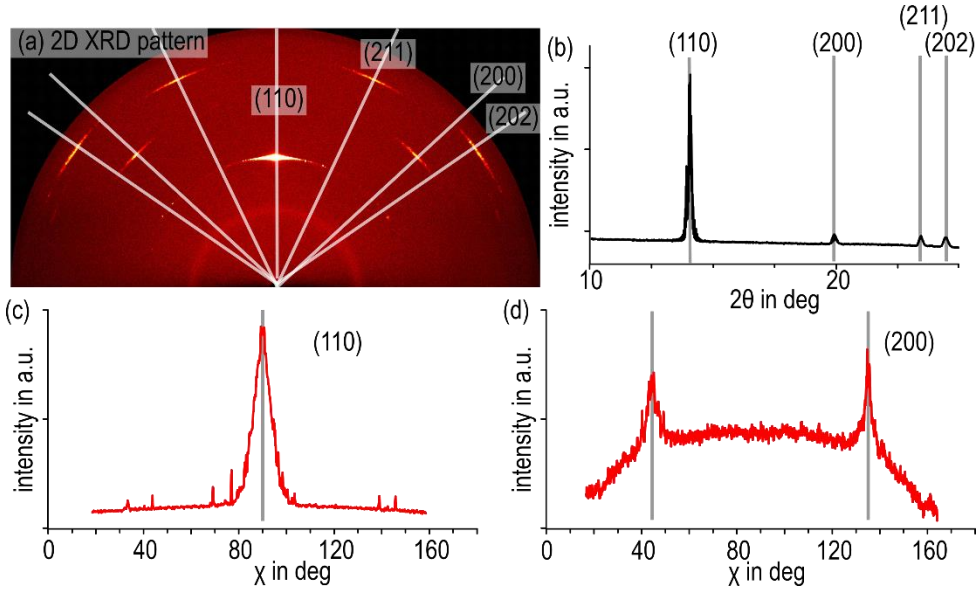

Figure 8.11: 2D XRD characterization of a $MAPbI_3$ thin film from the same batch as the sample in the main manuscript. a) 2D XRD pattern. b) 1D diffraction pattern from radially averaging the 2D pattern in a). c) Intensity distribution of the (110) and d) the (200) Bragg reflection vs. the azimuthal angle. Reprinted with permission from Energy Environ. Sci., 2020, Advance Article. - Published by The Royal Society of Chemistry.

The 2D XRD pattern of a $MAPbI_3$ thin film from the same batch studied by PFM and PL shows distinct and pronounced Bragg reflections at the position of the (110), (200), (202) and (211) crystal planes (Figure 8.11 a and b). The radially averaged diffraction pattern (Figure 8.11b) exhibits a strong (110) reflection at 14.1° and weak reflections of the (200), (211) and (202) crystal plane at 19.9°, 23.5° and 24.5°, respectively. These Bragg angles 2θ are in good agreement with literature values reported for tetragonal $MAPbI_3$ perovskite.[3–5] The absence of the characteristic PbI_2 reflection between 12° and 13° suggests the absence of degradation products, despite the solvent annealing on air.

The intensity distributions of the (110) and (200) reflections show intensity maxima at the azimuthal angles X of 90° and 45° and 135°, respectively (Figure 8.11c and d). Measurements at various incident angles confirm that the maximum of the (110) reflection was located around specular condition. This implies, that the (110) crystal plane is predominantly oriented parallel to the sample surface. Accordingly, the (202) and (211) Bragg reflections are positioned at the azimuthal angles expected for the sample surface oriented parallel to the (110) plane (white lines in Figure 8.11a). We observed the same texture previously on similar $MAPbI_3$ perovskite films.[6]

Figure 8.12

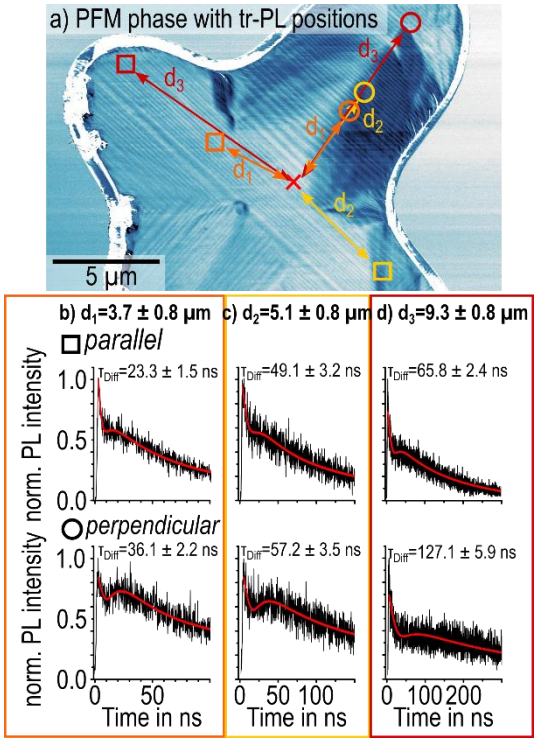

Figure 8.12: a) Lateral PFM phase image of the grain illustrating the detection positions of the six PL decays shown in b, c and d. These positions were selected at defined distances d_i from the excitation spot (red cross) in direction either parallel (squares) or perpendicular (circles) to the twin domains. b) PL decays detected at the position of the orange square and circle in a, with d_1=3.7±0.8 µm. c) PL decays detected at the position of the yellow square and circle in a, with d_2=5.1±0.8 µm. d) PL decays detected at the position of the red square and circle in a, with d_3=9.3±0.8 µm. The red lines in b-d represent the corresponding fits according to Equation 3.1 in Chapter 3.2.2. Please note that the scales of the time-axis change to increase the comprehensibility of the diffusion peak shift. Excitation with 633 nm wavelength, a fluence of 0.77 µJ/cm², a repetition rate of 2 MHz and 0.81 µm beam diameter (Figure 8.8). Reprinted with permission from Energy Environ. Sci., 2020, Advance Article. - Published by The Royal Society of Chemistry.

Figure 8.13

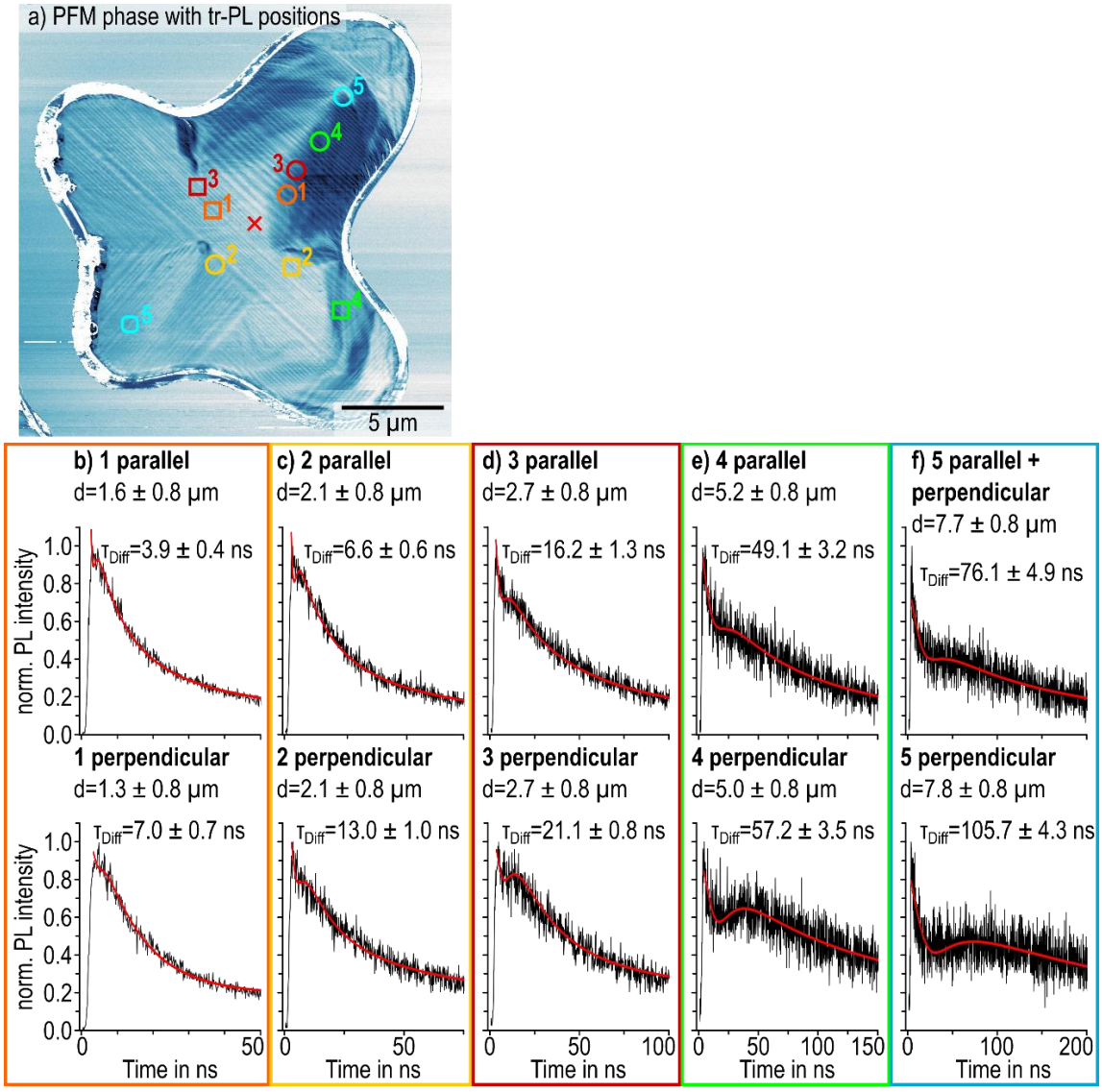

Figure 8.13: Correlation of time-resolved PL decays from Figure 8.9 with the ferroelastic domain pattern imaged in the lateral PFM phase in a. PL decays were measured in various distances from the excitation spot detected along different directions of the grain marked in the PFM phase by the colored squares and circles. Each color represents two detection positions at comparable distances, with the squares marking a detection position parallel to the domains and the circles marking a detection position perpendicular to the domains. The data fits via Equation 3.1 in Chapter 3.2.2 of the according PL decays are displayed in red. Please note that the scales of the time-axis were changed to increase the comprehensibility of the shift of the diffusion peak. Excitation with 633 nm wavelength, a fluence of 0.77 µJ/cm², a repetition rate of 2 MHz and 0.81 µm beam diameter (Figure 8.8). Reprinted with permission from Energy Environ. Sci., 2020, Advance Article. - Published by The Royal Society of Chemistry.

Figure 8.14

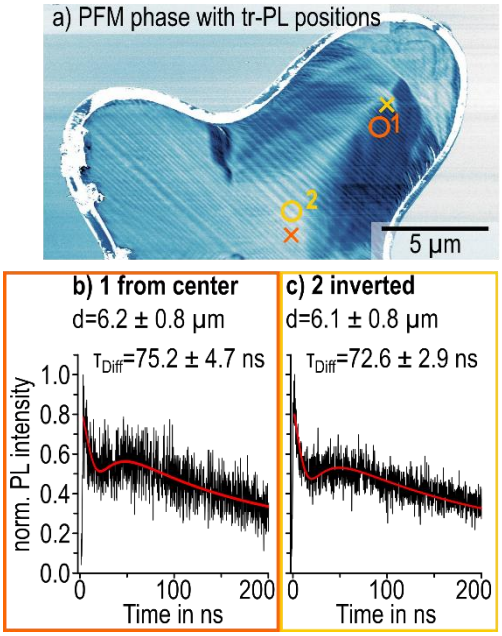

Figure 8.14: a) Lateral PFM phase with the detection positions of time-resolved PL decays marked by the orange and yellow numbered circles and the excitation positions marked by the orange and yellow cross for excitation from center and the inverted excitation and detection, respectively. Time-resolved PL decays detected from center in b and inverted excitation and detection locations in c. The red lines in b-d represent the corresponding fits according to Equation 3.1 in Chapter 3.2.2. Excitation with 633 nm wavelength, a fluence of 0.77 µJ/cm², a repetition rate of 2 MHz and 0.81 µm beam diameter (Figure 8.8). Reprinted with permission from Energy Environ. Sci., 2020, Advance Article. - Published by The Royal Society of Chemistry.

We find that diffusion times extracted from the PL decays with excitation position in the grain center and with inverted excitation and detection positions coincide. Thus, an influence of a macroscopic drift originating from the grain boundaries on the carrier diffusion can be excluded.

Figure 8.15

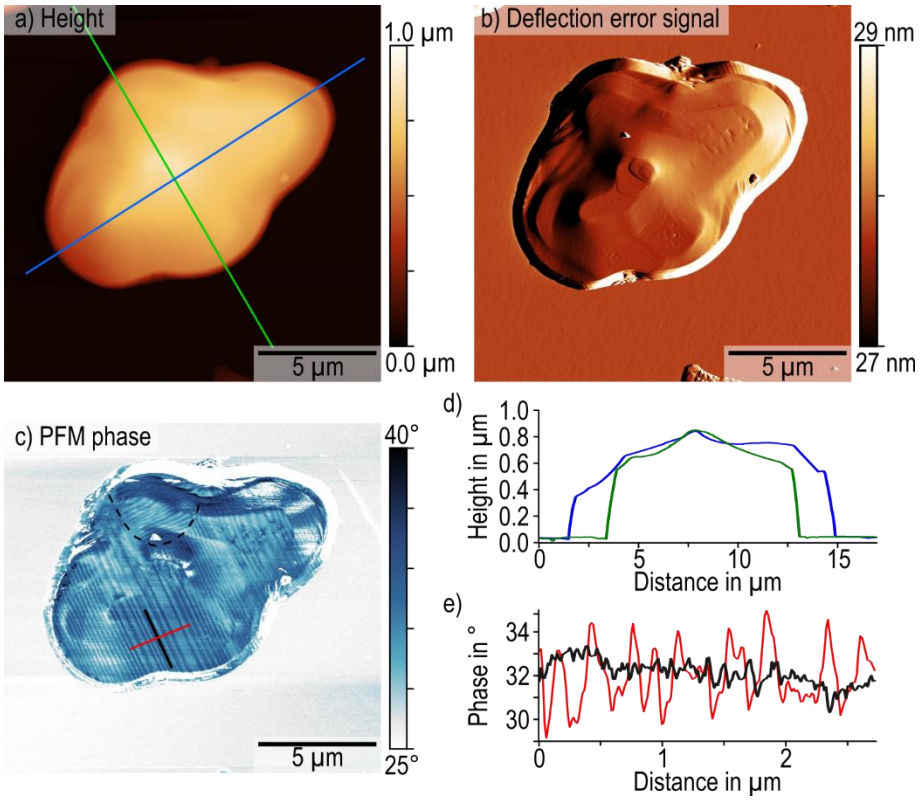

Figure 8.15: Lateral PFM measurement (1.5 V AC excitation, 736 kHz, 48 nN) on another large isolated $MAPbI_3$ grain of a thin film sample from the same batch as the sample characterized in the main manuscript and the sample used for XRD in Figure 8.11. a) Height signal with positions of profiles (green and blue line) shown in d. b) Deflection error signal of PFM measurement. c) Lateral PFM phase imaging periodic twin domains with position of the profiles (solid black and red line) shown in e. The area with a 90° direction change is outlined with the dashed black line. d) Height profiles extracted at the position of the blue and green line in a show some step edges over a height of 0.3 - 0.4 µm in both profiles. e) PFM phase profiles extracted at the positions of the red and black line in c showing the absence of periodicity in the profile parallel to the domains along the black line and varying periodicities between 0.15 and 0.47 µm in the profile extracted perpendicular to the domains along the red line. Reprinted with permission from Energy Environ. Sci., 2020, Advance Article. - Published by The Royal Society of Chemistry.

The PFM data of another $MAPbI_3$ grain from a sample of the same batch are summarized in Figure 8.15. Similar to the crystallite characterized in the main manuscript, we chose a large isolated grain to avoid additional inter-grain diffusion effects due to shared grain walls. The grain in Figure 8.15 is around 9 µm in diameter along its shorter axis (green line in a and d) and 13 µm along its long axis (blue line in a and d) with a surface area of 91 µm². The grain exhibits a terrace-like surface structure with smooth terrace surfaces and step edges located close to the center of the grain as well as close to the grain boundaries (Figure 8.15b and d). The PFM phase in Figure 8.15c clearly visualizes the periodic piezoresponse of the twin domains with a periodicity of 0.15 - 0.47 µm (Figure 8.15e).

Figure 8.16

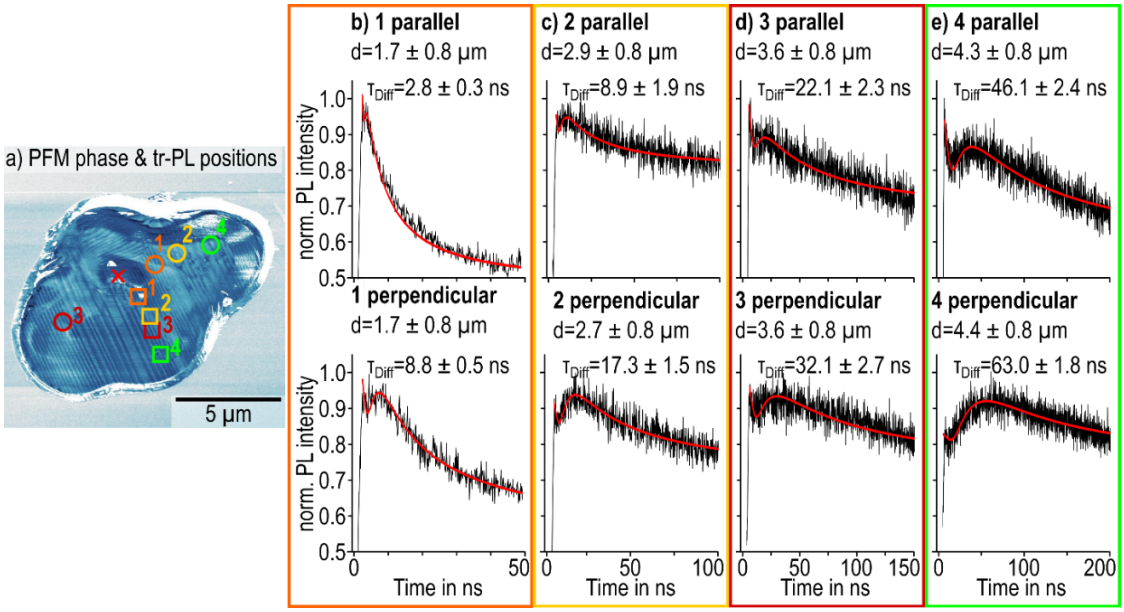

Figure 8.16: Time-resolved PL decays measured on a $MAPbI_3$ grain of another sample from the same batch, previously characterized via PFM in Figure 8.15. a) PFM phase with the detection positions of the time–resolved PL decays marked by the colored and numbered circles and squares in various distances from the excitation spot marked with the red cross. The circles represent detection positions perpendicular to the twin domains and the squares represent detection positions parallel to the twin domains. The red lines in b-e represent the corresponding fits according to Equation 3.1 in Chapter 3.2.2. Please note that the scales of the time-axis were changed to increase the comprehensibility of the shift of the diffusion peak. Excitation with 633 nm wavelength, a fluence of 0.77 µJ/cm², a repetition rate of 2 MHz and 0.81 µm beam diameter (Figure 8.8). Reprinted with permission from Energy Environ. Sci., 2020, Advance Article. - Published by The Royal Society of Chemistry.

The time-resolved PL decays measured on a second large isolated $MAPbI_3$ grain of another sample from the same batch consistently exhibit a shift of the diffusion time to longer times for the carrier diffusion perpendicular to the twin domains, thus agreeing with the data presented in the main manuscript. Analogously to the PL decays in Figure 3.19 in Chapter 3.2.2, the shape of the PL decay originates from a superposition of an exponential decay wave-guided from the initial PL emission at the position of the excitation spot and a peak function from the carrier diffusion. The diffusion times τ_{Diff} are derived from the data fit as described in the main manuscript.

Simulation 8.17

To clarify the impact of photon recycling on the deviations of the diffusion times at larger distances from a classical diffusion model, we performed a simple 1D Monte Carlo simulation. Starting from an initial ensemble of $N=10^8$ particles with a random Gaussian position distribution corresponding to the Gaussian beam profile, we iterated the distribution in timesteps of for 100 iterations (500 ns). We implemented the $\tau_{Step} = 5\ ns$ simulation in the software IgorPro 6.27 (Wavemetrics) using the built-in gnoise and expnoise functions. These functions generate random numbers with a Gaussian probability distribution of given characteristic width around zero (gnoise), or random positive numbers with an exponentially decaying probability distribution with characteristic decay length (expnoise).

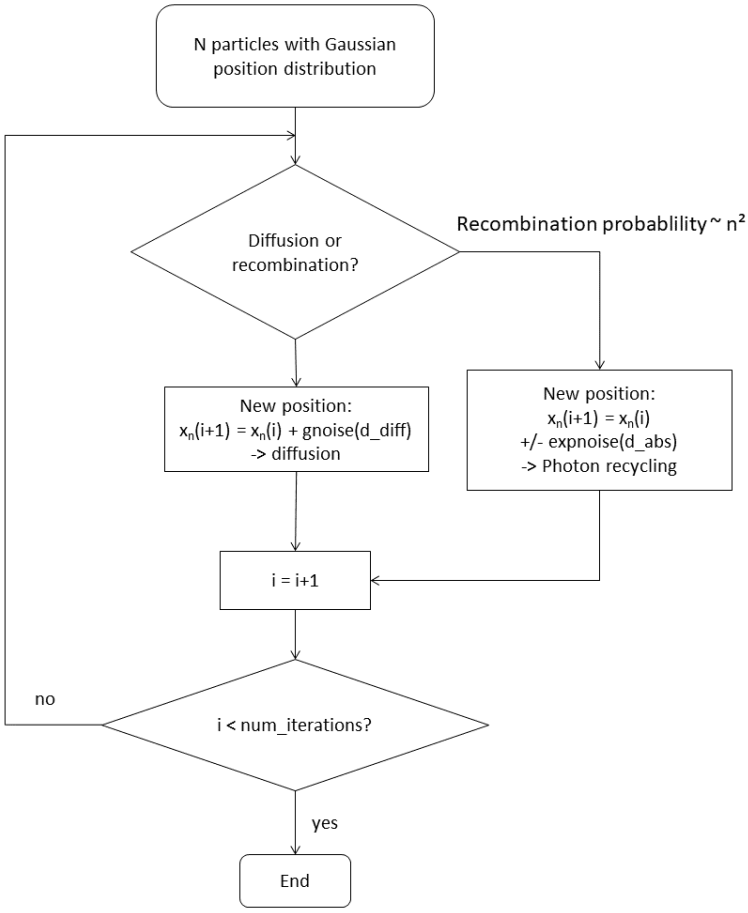

Figure 8.17-1: Sequence of 1D Monte-Carlo simulation on the influence of photon recycling o the detected diffusion times for large excitation-detection distances. Reprinted with permission from Energy Environ. Sci., 2020, Advance Article. - Published by The Royal Society of Chemistry.

The sequence of the simulation is illustrated in Figure 8.17-1. For each step, the probability of bimolecular recombination p_{BMrec} for a given particle is calculated from the particle density in the vicinity:

$$p_{BMrec} = k * n^2$$

With a numerical prefactor k. If the particle falls into the recombination branch, the new position can be calculated via a Lambert-Beer absorption law with a characteristic absorption length of λ_{Abs}=1µm. We assume that all the photons generated by bimolecular recombination are re-absorbed (i.e., photon recycling probability = 1), creating new particles at position

$$x_n(i+1) = x_n(i) \pm expnoise(\lambda_{Abs})$$

We want to point out that a photon-recycling probability of unity is unlikely, as many photons will escape the perovskite film via photoluminescence. Thus, our simulation captures a scenario with strong photon recycling.

All the particles that fall into the diffusion branch will diffuse over a characteristic distance $d_{Diff} = \sqrt{(2D\tau_{Step}}$) (with diffusion constant D=1 cm²/s):

$$x_n(i+1) = x_n(i) + gnoise(d_{Diff})$$

After each iteration in time, a histogram of the particle distribution is generated and added to a 2D contour plot of the particle density as a function of position and time (Figure 8.17-2). From these contour plots, we extracted particle density transients for given distances from the excitation. From the position of the maximum in these transients, we calculated the diffusion time for a given distance, similar to the analysis of the PL transients in the experimental data.

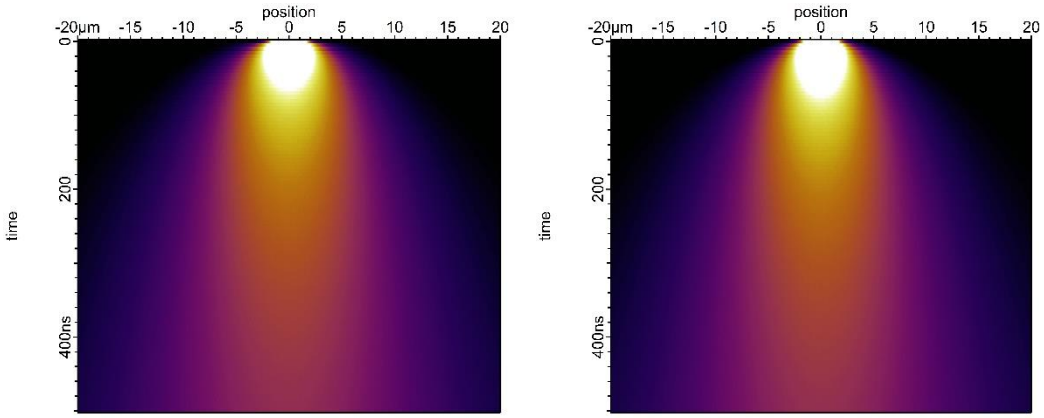

Figure 8.17-2: Particle density plots as function of position (horizontal) and time (vertical axis) for pure diffusion (left) and diffusion plus photon recycling (right). The brighter the color, the higher is the particle density. Reprinted with permission from Energy Environ. Sci., 2020, Advance Article. - Published by The Royal Society of Chemistry.

From comparing the diffusion data with (k>0) and without (k=0) photon recycling we found that photon recycling slightly accelerates the effective diffusion. However, the effect is comparatively small (Figure 8.17-3), despite the fact that we used a rather high prefactor k to calculate the bimolecular recombination probability. We chose k to be high enough that after the first timestep, almost all particles recombine. Nevertheless, the particle density, n, decreases so rapidly within the first couple of nanoseconds that photon recycling due to the n^2- dependence of bimolecular recombination becomes so unlikely, that it does not affect the effective diffusion times any more (Figure 8.17-3). Therefore, the fits of the diffusion times versus the distance with and without photon recycling almost coincide. They yielded similar values for the effective bimolecular recombination coefficient k_2=9352±23 with photon recycling and k_2=9882±23 without photon recycling.

Concluding, we found that the influence of photon recycling at the given excitation energies on the effective diffusion times is minor and likely does not account for the observed deviation from the classic diffusion model at larger distances (Figure 3.22 in Chapter 3.2.2.).

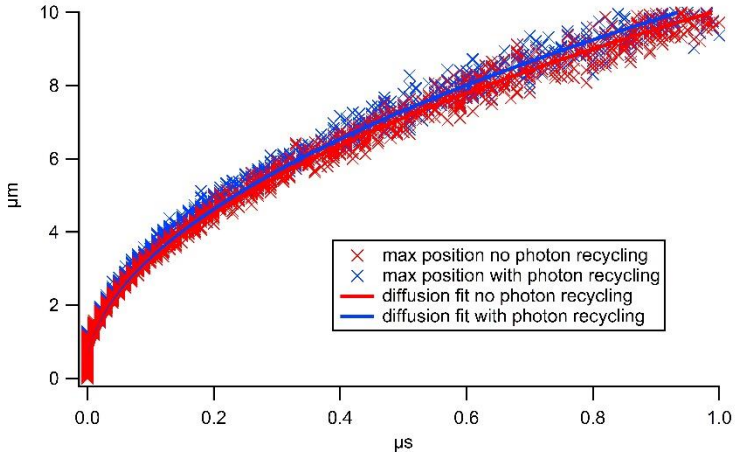

Figure 8.17-3: Diffusion times vs. distance between excitation and detection without photon recycling (red) and with photon recycling (blue). Reprinted with permission from Energy Environ. Sci., 2020, Advance Article. - Published by The Royal Society of Chemistry.

Figure 8.18

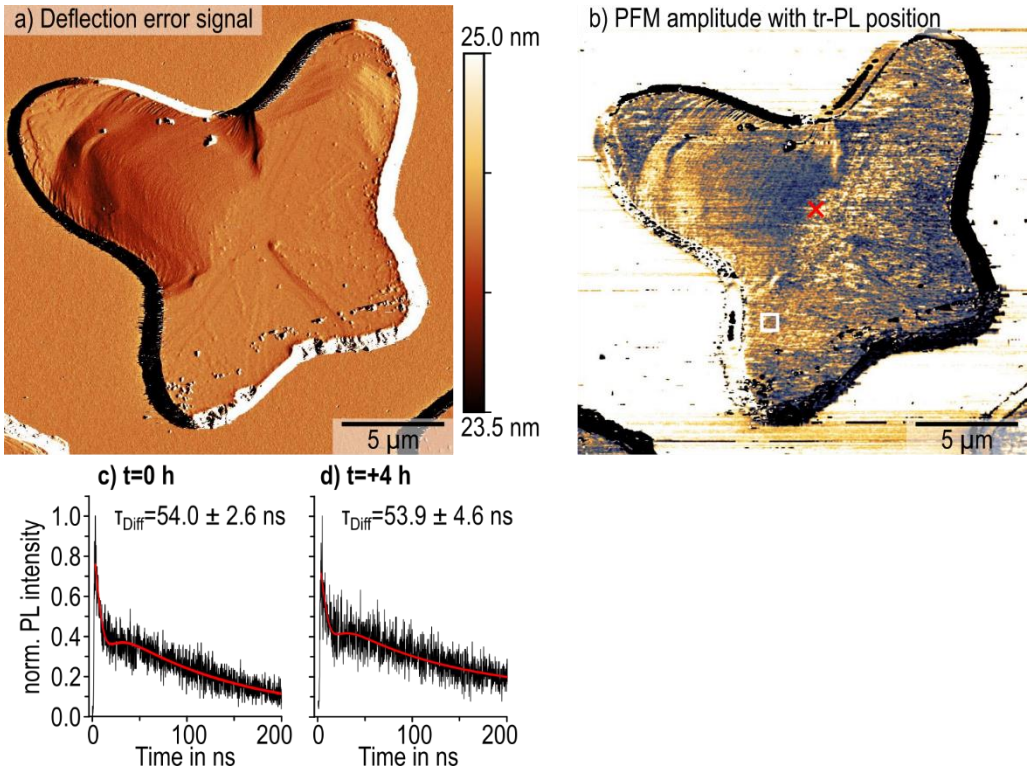

Figure 8.18: Lateral PFM measurement (1.5 V AC excitation, 777 kHz, 48 nN) after the PL measurements with the deflection error signal in a) and the PFM amplitude in b). Time-resolved PL decays measured at the same position of the white square in b from the excitation after a time of 0 (c) and 4 hours (d). The red lines in c and d represent the corresponding fits according to Equation 3.1 in Chapter 3.2.2. Excitation with 633 nm wavelength, a fluence of 0.77 µJ/cm², a repetition rate of 2 MHz and 0.81 µm beam diameter (Figure 8.8). Reprinted with permission from Energy Environ. Sci., 2020, Advance Article. - Published by The Royal Society of Chemistry.

To study the influence of possible degradation over the measurement time, we measured PFM on the same grain following the PL experiments. In the deflection error signal in Figure 8.18a, we observe that the surface of the sample became rougher, compared to the measurement prior to the

PL experiments in Figure 3.19 in Chapter 3.2.2. The PFM signal in Figure 8.18b shows an increase in topographic crosstalk with PFM measurement due to the rougher sample surface. While the PFM signal becomes weaker, the overall structure of the twin domain remains unchanged. We suggest that the passivation of the sample surface weakened the resulting PFM signal. Since the domain arrangement remains and we detect the PL emission in transmission, we are confident that the surface passivation does not influence the PL data collection. To further confirm the benign influence of the surface passivation, we compared the PL decay of the same positions at the beginning and the end of the experiment. While we observe an increase in the noise level after 4 hours, the overall shape and the diffusion time of the PL decay remain unchanged, confirming negligible influence of degradation over the course of the experiments.

8.3 Supporting information: The interplay of contact layers: How the electron transport layer influences interfacial recombination and hole extraction in perovskite solar cells

Ilka M. Hermes,[†] Yi Hou,[‡] Victor W. Bergmann,[†] Christoph J. Brabec,[‡] and Stefan A. L. Weber[†,§]

[†] *Max Planck Institute for Polymer Research, Ackermannweg 10, 55128 Mainz, Germany*

[‡] *Department of Materials Science and Engineering, Institute of Materials for Electronics and Energy Technology (i-MEET), Friedrich-Alexander University Erlangen-Nürnberg, Martensstrasse 7, 91058 Erlangen, Germany*

[§] *Institute of Physics, Johannes Gutenberg University Mainz, Staudingerweg 10, 55128 Mainz, Germany*

Published in the journal of physical chemistry letters (J. Phys. Chem. Lett.) 2018, 9, 6249−6256
https://doi.org/10.1021/acs.jpclett.8b02824

Discussion 8.19

To avoid topographic crosstalk during the KPFM measurements cross sections of the solar cells were polished with a dual beam focused ion beam (FIB). We used several precautionary steps to protect the active layers from incorporation of Ga ions from the ion beam. As such, we deposited a 2.1 µm thick protective Pt layer onto the gold electrode parallel and in a 6 µm distance to the breaking edge in two consecutive steps:

1. A 100 nm thick Pt layer was deposited with the electron beam at a low current of 1.6 nA
2. A 2 µm thick Pt layer via the ion beam at a current of 100 pA.

For the polishing step, the ion beam was aligned parallel to the breaking edge and perpendicular to the Pt protection layer. We milled 6 µm deep into the sample so that if any Ga ions are incorporated, they will accumulate either in the Pt protective layer or in the glass substrate far away (>3µm) from the active layers. Again, we used low currents for the polishing to protect the active layers: The first coarse polishing step was conducted with a beam current of 1 nA and the second, final polishing step was conducted with a beam current of 100 pA. To assure that no Ga ions are

incorporated following this procedure, we performed EDX measurements showing the absence of Ga ions for a previous study on perovskite cross sections.[7]

To exclude effects from surface charges or defect states at the cross-sectional surface, we either compare potential profiles of different devices prepared with the same protocol, or we evaluate the photopotential (difference between illuminated and dark potential), where the effect of surface charges and/or work function changes are subtracted.

Table 8.20

Table 8.20: Cell parameters short circuit current density j_{SC}, open circuit voltage V_{OC}, fill factor (*FF*) and *PCE* determined from the *j-V* curves of the TiO_2 cell and the C60-SAM cell in Figure 5.3 in Chapter 5.1.

	TiO_2 CELL (FORWARD)	TiO_2 CELL (REVERSE)	C60-SAM CELL (FORWARD)	C60-SAM CELL (REVERSE)
J_{SC}	19.2 mA/cm²	19.8 mA/cm²	20.8 mA/cm²	21.0 mA/cm²
V_{OC}	1.00 V	1.07 V	0.98 V	0.98 V
FF	0.35	0.67	0.68	0.74
PCE	6.77%	14.2%	15.2%	13.7%

After breaking and polishing the solar cells as preparation the KPFM measurements, an open circuit voltage decreased to ~0.8 V for the TiO_2 cell and to ~0.9 V on the C60-SAM cell, measured with a voltmeter. With the slight decrease in open circuit voltage, we can assume that the devices are operational.

Figure 8.21

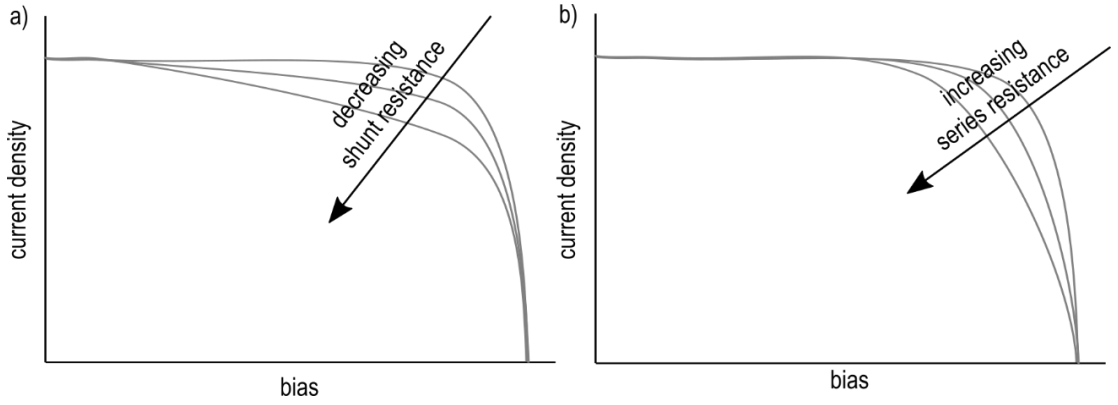

Figure 8.21: Influence of shunt (a) and series resistance (b) on the fill factor in the *j-V* characteristics of a solar cell, sketched after[8]. Reprinted with permission from J. Phys. Chem. Lett. 2018, 9, 6249−6256. Copyright 2018 American Chemical Society.

Figure 8.22

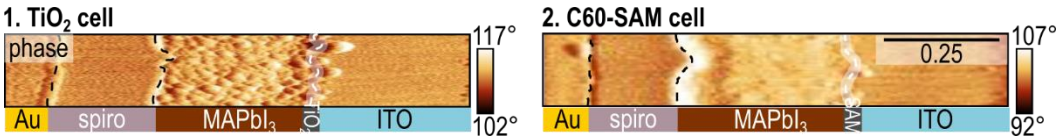

Figure 8.22: Phase signal corresponding to height and LCPD signal in Figure 1a and b on cross sections of $MAPbI_3$ solar cells with TiO_2 as ETL in the left column and C60-SAM as ETL in the right column. The phase signal was used to identify interfaces in the different solar cell layers as indicated by the dashed lines and the position of the ETL highlighted by the

semitransparent line. Reprinted with permission from J. Phys. Chem. Lett. 2018, 9, 6249−6256. Copyright 2018 American Chemical Society.

Figure 8.23

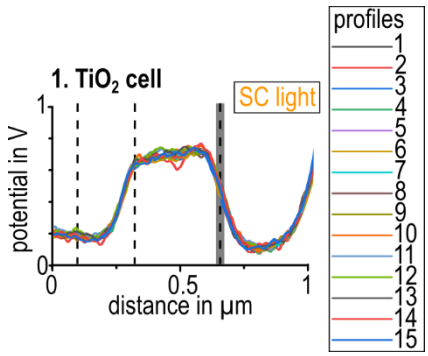

Figure 8.23: The 15 single LCPD profiles of the TiO_2 cell in short circuit conditions under illumination that were used in the averaged profiles shown in Figure 5.4d in Chapter 5.1. We derived standard deviations of the potential on the gold electrode between 10 mV and 30 mV as representation of the noise level. Reprinted with permission from J. Phys. Chem. Lett. 2018, 9, 6249−6256. Copyright 2018 American Chemical Society.

Bibliography

1. Richter, J. M. *et al.* Enhancing photoluminescence yields in lead halide perovskites by photon recycling and light out-coupling. *Nat. commun.* **7**, 1–8 (2016).

2. De Wolf, S. *et al.* Organometallic halide perovskites: sharp optical absorption edge and its relation to photovoltaic performance. *J. Phys. Chem. Lett.* **5**, 1035–1039 (2014).

3. Baikie, T. *et al.* Synthesis and crystal chemistry of the hybrid perovskite (CH3NH3) PbI3 for solid-state sensitised solar cell applications. *J. Mater. Chem. A* **1**, 5628–5641 (2013).

4. Song, Z. *et al.* Impact of processing temperature and composition on the formation of methylammonium lead iodide perovskites. *Chem. Mater.* **27**, 4612–4619 (2015).

5. Christians, J. A., Miranda Herrera, P. A. & Kamat, P. V. Transformation of the excited state and photovoltaic efficiency of CH3NH3PbI3 perovskite upon controlled exposure to humidified air. *J. Am. Chem. Soc.* **137**, 1530–1538 (2015).

6. Hermes, I. M. *et al.* Ferroelastic Fingerprints in Methylammonium Lead Iodide Perovskite. *J. Phys. Chem. C* **120**, (2016).

7. Bergmann, V. W. *et al.* Real-space observation of unbalanced charge distribution inside a perovskite-sensitized solar cell. *Nat. Commun.* **5**, 1–9 (2014).

8. Nelson, J. A. *The physics of solar cells*. (World Scientific Publishing Company, 2003).

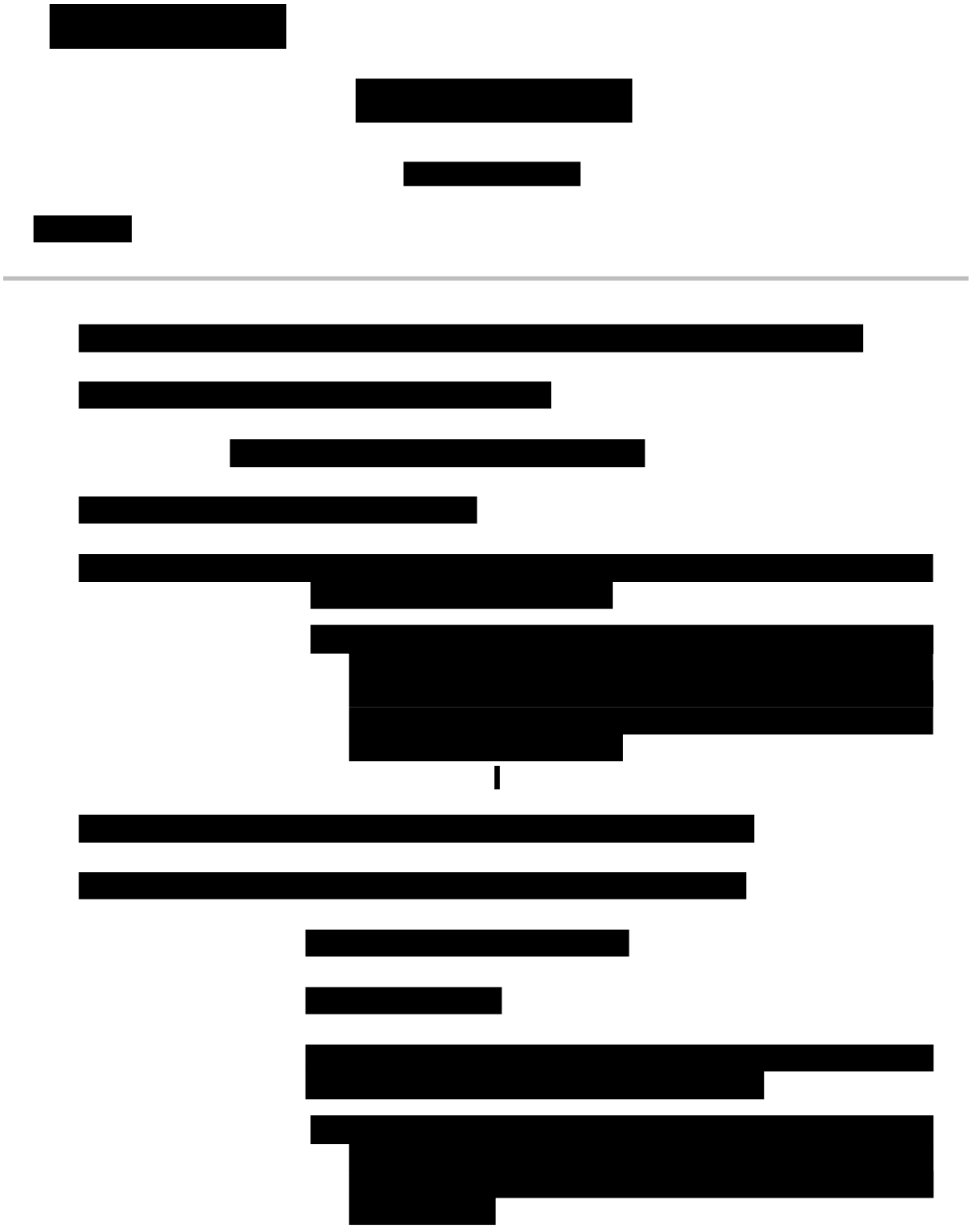

List of Publications

Truitt, R.; **Hermes, I.M.;** Main, A.; Sendecki, A.; Lind, C. Low Temperature Synthesis and Characterization of $AlScMo_3O_{12}$. *Materials* **2015**, *8*, 700-716, https://doi.org/10.3390/ma8020700

Marutschke, C.; Walters, D.; Cleveland, J.; **Hermes, I.M.;** Bechstein, R.; Kühnle, A. Three-dimensional hydration layer mapping on the (10.4) surface of calcite using amplitude modulation atomic force microscopy. *Nanotechnology* **2014**, 25, 335703, https://doi.org/10.1088/0957-4484/25/33/335703

Söngen, H.; Marutschke, C.; Spijker, P.; Holmgren, E.; **Hermes, I.M.;** Bechstein, R.; Klassen, S.; Tracey, J.; Foster, A.S.; Kühnle, A. Chemical Identification at the Solid–Liquid Interface. *Langmuir* **2017**, 33, 1, 125-129, https://doi.org/10.1021/acs.langmuir.6b03814

Söngen, H.; Jaques, Y.M.; Spijker, P.; Marutschke, C.; Klassen, S.; **Hermes, I.M.;** Bechstein, R.; Zivanovic, L.; Tracey, J.; Foster, A.S.; Kühnle, A. Three-dimensional solvation structure of ethanol on carbonate minerals. *Beilstein J. Nanotechnol.* **2020**, 11, 891–898, https://doi.org/10.3762/bjnano.11.74

Hermes, I.M.; Bretschneider, S.A.; Bergmann, V.W; Li, D.; Klasen, A.; Mars, J.; Tremel, W.; Laquai, F.; Butt, H.-J.; Mezger, M.; Berger, R.; Rodriguez, B.; Weber, S.A.L. Ferroelastic Fingerprints in Methylammonium Lead Halide Perovskite, *J. Phys. Chem. C,* **2016**, 120, 10, 5724-5731, https://doi.org/10.1021/acs.jpcc.5b11469

Li, D.; Bretschneider, S.A.; Bergmann, V.W; **Hermes, I.M.**; Mars, J.; Klasen, A.; Lu, H.; Tremel, W.; Mezger, M.; Butt, H.-J.; Weber, S.A.L.; Berger, R Humidity-Induced Grain Boundaries in $MAPbI_3$ Perovskite Films, *J. Phys. Chem. C,* **2016**, 120, 12, 6363-6368, https://doi.org/10.1021/acs.jpcc.6b00335

Bergmann, V.W; Guo, Y.; Tanaka, H.; **Hermes, I.M.**; Li, D.; Klasen, A.; Bretschneider, S.A.; Nakamura, E.; Berger, R.; Weber, S.A.L. Local time-dependent charging in a perovskite solar cell, *ACS Appl. Mater. Interfaces* **2016**, 8, 30, 19402–19409, https://doi.org/10.1021/acsami.6b04104

Weber, S.A.L.; **Hermes, I.M.**; Turren-Cruz, S.-H.; Gort, C.; Bergmann, V.W.; Gilson, L.; Hagfeldt, A.; Graetzel, M.; Tress, W.; Berger, R. How the formation of interfacial charge causes hysteresis in perovskite solar cells. *Energy Environ. Sci.,* **2018**, 11, 2404-2413, https://doi.org/10.1039/C8EE01447G

Will, J.; Hou, Y.; Scheiner, S.; Pinkert, U.; **Hermes, I.M.**; Weber, S.A.L.; Hirsch, A.; Halik, M.; Brabec, C.J; Unruh, T. Evidence of Tailoring the Interfacial Chemical Composition in Normal Structure Hybrid Organohalide Perovskites by a Self-Assembled Monolayer. *ACS Appl. Mater. Interfaces* **2018,** 10, 6, 5511–5518, https://doi.org/10.1021/acsami.7b15904

Vorpahl, S.M.; Giridharagopal, R.; Eperon, G.E.; **Hermes, I.M.**; Weber, S.A.L.; Ginger, D.S. Orientation of ferroelectric domains and disappearance upon heating methylammonium lead triiodide perovskite from tetragonal to cubic phase. *ACS Appl. Energy Mater*. **2018**, 1, 4, 1534–1539, https://doi.org/10.1021/acsaem.7b00330

Axt, A.; **Hermes, I.M.**; Bergmann, V.W.; Tausendpfund, N.; Weber, S.A.L. Know your full potential: Quantitative Kelvin probe force microscopy on nanoscale electrical devices, *Beilstein J. Nanotechnol.,* **2018**, 9, 1809–1819, https://doi.org/10.3762/bjnano.9.172

Hermes, I.M.; Hou, Y.; Bergmann, V.W.; Brabec, C.J.; Weber, S.A.L. The interplay of contact layers: How the electron transport layer influences interfacial recombination and hole extraction in perovskite solar cells. *J. Phys. Chem. Lett.,* **2018**, 9, 21, 6249-6256, https://doi.org/10.1021/acs.jpclett.8b02824

Klasen, A.; Baumli, P.; Sheng, Q.; Ewald, J.; Bretschneider, S.A.; **Hermes, I.M.**; Bergmann, V.W.; Gort, C.; Axt, A.; Weber, S.A.L.; Kim, H.; Butt, H.-J.; Tremel, W.; Berger, R. Removal of Surface Oxygen Vacancies Increases Conductance Through TiO2 Thin Films for Perovskite Solar Cells. *J. Phys. Chem. C,* **2019**, 123, 22, 13458-13466, https://doi.org/10.1021/acs.jpcc.9b02371

Hermes, I.M.; Best, A.; Winkelmann, L.; Mars, J.; Vorpahl, S.M.; Mezger, M.; Collins, L.; Butt, H.-J.; Ginger, D.S.; Koynov, K.; Weber, S.A.L. Anisotropic carrier diffusion in single $MAPbI_3$ grains correlates to their twin domains. *Energy Environ. Sci.,* **2020**, 13, 11, 4168-4177, https://doi.org/10.1039/D0EE01016B